

Stephen F. Austin State University

SFA ScholarWorks

Electronic Theses and Dissertations

Winter 12-16-2023

Comparative Lineament and Geomorphic Analysis of Chaotic Terrains and Noctis Labyrinthus, Mars

Sarah A. Walton

Stephen F Austin State University, sarah.a.walton@nasa.gov

Follow this and additional works at: <https://scholarworks.sfasu.edu/etds>



Part of the [Geology Commons](#), [Geomorphology Commons](#), [Other Earth Sciences Commons](#), and the [Tectonics and Structure Commons](#)

[Tell us](#) how this article helped you.

Repository Citation

Walton, Sarah A., "Comparative Lineament and Geomorphic Analysis of Chaotic Terrains and Noctis Labyrinthus, Mars" (2023). *Electronic Theses and Dissertations*. 525.

<https://scholarworks.sfasu.edu/etds/525>

This Thesis is brought to you for free and open access by SFA ScholarWorks. It has been accepted for inclusion in Electronic Theses and Dissertations by an authorized administrator of SFA ScholarWorks. For more information, please contact cdsscholarworks@sfasu.edu.

Comparative Lineament and Geomorphic Analysis of Chaotic Terrains and Noctis Labyrinthus, Mars

Creative Commons License



This work is licensed under a [Creative Commons Attribution-Noncommercial-No Derivative Works 4.0 License](https://creativecommons.org/licenses/by-nc-nd/4.0/).

**COMPARATIVE LINEAMENT AND GEOMORPHIC ANALYSIS OF CHAOTIC
TERRAINS AND NOCTIS LABYRINTHUS, MARS**

By

Sarah A. Walton, Bachelor of Science

Presented to the Faculty of the Graduate School of

Stephen F. Austin State University

In Partial Fulfillment

Of the Requirements

For the Degree of

Master of Science

STEPHEN F. AUSTIN STATE UNIVERSITY

December 2023

**COMPARATIVE LINEAMENT AND GEOMORPHIC ANALYSIS OF CHAOTIC
TERRAINS AND NOCTIS LABYRINTHUS, MARS**

By

Sarah A. Walton, Bachelor of Science

APPROVED:

Dr. Kevin Stafford, Thesis Director

Dr. Melinda Faulkner, Committee Member

Dr. Zachariah Fleming, Committee Member

Dr. Daniel Unger, Committee Member

Lorenzo M. Smith, PhD.
Acting Dean of Research and Graduate Studies

ABSTRACT

Noctis Labyrinthus (NL) is an extensional trough network connecting the Tharsis rise and Valles Marineris on Mars. Chaotic terrains are a group of polygonally-fractured surface features commonly associated with subsidence due to rapid fluid loss within the subsurface. Polygonal surface patterns are seen at both sites, where geometric topographic highs are bounded by low troughs. Lineaments, topography, and geomorphology of NL and chaotic terrains were analyzed to determine tectonics and fluid influence in the formation and evolution of both sites. NL shows preferential fracture patterns associated with regional extension. Lineaments within chaotic terrains do not show cumulative preferential trends but demonstrate irregular fracture networks associated with collapse structures. Theoretical models for the evolution of both systems were produced, developing a better understanding of processes that shaped the Martian landscape

ACKNOWLEDGEMENTS

Thanks are extended to the members of my committee, Dr. Zach Fleming, Dr. Mindy Faulkner, and Dr. Daniel Unger. A thanks to my advisor, Dr. Kevin Stafford, for allowing me to explore my passion for planetary science and providing hours of guidance. I would also like to thank my fellow graduate student cohort to whom I am in debt for the comradery and laughs over the years.

TABLE OF CONTENTS

ABSTRACT	iii
ACKNOWLEDGEMENTS	iv
TABLE OF CONTENTS	v
LIST OF FIGURES	vii
LIST OF TABLES	xv
INTRODUCTION	1
GEOLOGIC SETTING	6
General Geology	6
Geologic History	8
Pre-Noachian	8
Noachian	11
Hesperian	12
Amazonian	14
Tectonics	14
Hydrology	17
Fluvial activity	17
Hydrated minerals	18
Groundwater and potential periodic recharge	18
Noctis Labyrinthus	20
Origin Theories	20
Morphology and Structure	21
Chaotic Terrains	26
Origins	27

METHODOLOGY	28
Data Collection	28
Image and Terrain Analysis	32
Topographic Analyses	35
Lineament Analyses	36
Hydrated Mineral Mapping.....	39
RESULTS	40
Image and Terrain Analysis	40
Topographic Analyses	64
Elevation.....	64
Slope Analysis	108
Lineament Analysis Phase I: Noctis Labyrinthus	148
Lineament Analysis Phase II: Chaotic Terrains	151
Lineament Analysis Phase III: Statistical Analyses.....	166
Hydrated Mineral Mapping.....	172
DISCUSSION	175
Comparative Analysis	175
CONCLUSIONS	182
FUTURE WORK.....	185
Contributions and Constraints	185
CTX DEM Generation.....	187
In-Depth Analysis	187
REFERENCES	189
VITA	194

LIST OF FIGURES

Figure 1. Elevation model of major regions within the Tharsis rise, Mars (MOLA 200mpp DEM overlain on 200mpp HRSC global hillshade map).	3
Figure 2. Global Map of the Martian surface with major geologic provinces labeled. The global dichotomy is highlighted and separates the flat northern lowlands and the rugged southern highlands. Chaotic terrains are found at the headwaters of massive outflow channels east of the Tharsis rise.	5
Figure 3. Theorized stratigraphy of the Martian crust (From Clifford, 1993).	7
Figure 4. Geologic timescale of Mars with major processes and associated mineral group deposits (From Ehlmann & Edwards, 2014).	9
Figure 5. Example of layered LTD's within NL. Light toned deposits are common on the surface of Mars and can be composed of hydrated mineral deposits. The deposits stand out against the typical dark-toned surface within greyscale imagery. Some interpret LTD's as pyroclastic material such as ash flow and ash fall that has undergone hydrologic weathering.....	23
Figure 6. Example of a pit crater chain within NL. Collapse pits are rimless depressions formed due to subsidence and induced collapse within the subsurface. Collapse pits often form along a directional plane, forming a pit crater chain.	25
Figure 7. Mars Reconnaissance Orbiter (MRO) inserted into Martian orbit in 2006, where the orbiter has provided several years of continuous image, mineral, and science observations of the surface of Mars (From NASA Jet Propulsion Laboratory, 2023).	29
Figure 8. The context camera (CTX) that is currently aboard the MRO before it was assembled on the spacecraft. The CTX camera allows for images to be captured with an average resolution of ~6 meters per pixel (mpp) (From Malin Space Science Systems, 2023).	30
Figure 9. The CRISM instrument in three parts: the (A) Optical Sensor Unit (OSU) which includes optics, a gimbal to remove image smear to due spacecraft movement, two visible and infrared detectors for producing images, and cryocoolers and radiators to cool and to keep the CRISM cold, the (B) Gimbal	

Motor Electronics (GME), which commands and powers the gimbal, and the (C) Data Processing Unit (DPU) ,which accepts and processes commands from MRO and accepts data from the OSU to return back to the spacecraft (From NASA/ John Hopkins Applied Physics Laboratory, 2023).....	31
Figure 10. Locations and names of the chaotic terrains analyzed east of the Valles Marineris.	33
Figure 11. Digitized troughs and mesas within NL. Troughs are represented by low elevation areas bounded by mesas; mesas are represented by high elevation flat-topped plateaus.....	41
Figure 12. Smooth trough floors within NL. Dune structures are common due to extensive eolian processes occurring in recent geologic times.	42
Figure 13. Scattered LTD within a trough floor.	44
Figure 14. Layered and scattered LTD's in a trough floor associated with patterned ground. Slump debris (boulders) are seen to the west and interpreted solifluction lobes to the east.	45
Figure 15. Layered LTD's within a trough wall and associated patterned ground seen at the top of the layers, showing peaks of LTD's.	46
Figure 16. Layered LTD's in a stratified mesa wall, this stratigraphic pattern is common throughout NL.	47
Figure 17. Interpreted solutional holes within a trough in NL.	48
Figure 18. Interpreted patterned ground within NL, patterned ground is a periglacial morphology, a result of thawing and re-freezing of permafrost near the surface.....	49
Figure 19. Un-evolved graben in western NL.	50
Figure 20. Example of a pit crater chain forming a new trough within NL.	51
Figure 21. Large crater on the outskirts of NL, rough terrain surrounding the crater is the blanket ejecta, common of large and young craters. Craters are common within NL terrain and are distinguished by their raised rim and symmetrical nature.	53
Figure 22. Differences in morphology between mesas and knobs within Ister Chaos. (A) Mesas are flat plateaus of high elevations, whereas knobs (B) appear	

to have undergone a different degree of erosion where the high elevation is peaked with a cap and lacks a flat area.....	54
Figure 23. Knobs within Aurorae Chaos capped with LTD. LTD caps and layered deposits are common within chaotic terrain knobs. Within the floor of this image, pattered ground is seen to the south.....	55
Figure 24. Interpreted patterned ground in Baetis Chaos.....	56
Figure 25. Unusual textured ground outside of Echus Chaos.	57
Figure 26. Patterned ground within Xanthe Chaos infilled by LTD's.....	58
Figure 27. Outflow channel examples along chaotic terrain floors in (A) Baetis Chaos and (B) Eos Chaos with flow directions labeled.	60
Figure 28. Pit crater chains seen outside of Eos Chaos. Pit craters and pit chains are found throughout the chaotic terrain, similar to morphology seen in NL.....	61
Figure 29. Interpreted collapsed mesas within Candor Chaos. LTD rims surround polygonal shapes that show similar spatial patterns to in-tact mesas but appear to be collapsed in around the LTD's.	62
Figure 30 (A) Echus Chaos and (B) Nilus Chaos, appear to be more structurally controlled than other analyzed chaotic terrains toward the east.....	63
Figure 31. Location of NL (dashed box) compared to the 19 analyzed chaotic terrains (solid boxes) on the surface of Mars.	65
Figure 32. Map of topographic profile lines taken within NL.	66
Figure 33. NL topographic profiles A – A', B- B', and C -C'. Mesas are identified as high elevation flat topographic features and troughs are low elevation areas bounded by mesas.	67
Figure 34. NL topographic profiles D – D', E -E' and F- F'.....	68
Figure 35. NL topographic profiles G – G' and H – H'.	69
Figure 36. Topographic profiles taken in Arsinoes Chaos.	70
Figure 37. Topographic profiles of Arsinoes Chaos.....	71
Figure 38. Topographic profiles taken in Aurorae Chaos.	72

Figure 39. Topographic profiles of Aurorae Chaos.....	73
Figure 40. Topographic profiles taken in Aram Chaos.....	74
Figure 41. Topographic profiles of Aram Chaos.	75
Figure 42. Topographic profiles taken in Aureum Chaos.....	76
Figure 43. Topographic profiles of Aureum Chaos.	77
Figure 44. Topographic profile taken in Baetis Chaos.	78
Figure 45. Topographic profile of Baetis Chaos.....	79
Figure 46. Topographic profile taken in Candor Chaos.	80
Figure 47. Topographic profile of Candor Chaos.....	81
Figure 48. Topographic profiles taken in Chryse Chaos.	82
Figure 49. Topographic profiles of Chryse Chaos.	83
Figure 50. Topographic profile taken in Echus Chaos.	84
Figure 51. Topographic profile of Echus Chaos.....	85
Figure 52. Topographic profiles taken in Eos Chaos.	86
Figure 53. Topographic profiles of Eos Chaos.....	87
Figure 54. Topographic profile taken in Hydrae Chaos.	88
Figure 55. Topographic profile of Hydrae Chaos.....	89
Figure 56. Topographic profiles taken in Hydaspis Chaos.	90
Figure 57. Topographic profiles of Hydaspis Chaos.....	91
Figure 58. Topographic profiles taken in Hydraotes Chaos.....	92
Figure 59. Topographic profiles of Hydraotes Chaos.	93
Figure 60. Topographic profile taken in Iamuna Chaos.	94
Figure 61. Topographic profile of Iamuna Chaos.....	95
Figure 62. Topographic profiles taken in Iani Chaos.	96
Figure 63. Topographic profiles of Iani Chaos.....	97

Figure 64. Topographic profile taken in Ister Chaos.	98
Figure 65. Topographic profile of Ister Chaos.	99
Figure 66. Topographic profiles taken in Margaritifer Chaos.	100
Figure 67. Topographic profiles of Margaritifer Chaos.....	101
Figure 68. Topographic profile taken in Nilus Chaos.	102
Figure 69. Topographic profile of Nilus Chaos.....	103
Figure 70. Topographic profiles taken in Pyrrhae Chaos.....	104
Figure 71. Topographic profiles of Pyrrhae Chaos.	105
Figure 72. Topographic profile taken in Xanthe Chaos.....	106
Figure 73. Topographic of Xanthe Chaos.....	107
Figure 74. Slope profiles within west NL.....	109
Figure 75. Slope profiles within central NL.	110
Figure 76. Slope profiles within east NL.	111
Figure 77. Slope profiles within Arsinoes Chaos.	112
Figure 78. Slope profiles within Aurorae Chaos.....	113
Figure 79. Slope profiles within Aram Chaos.....	114
Figure 80. Slope profiles within Aureum Chaos.....	115
Figure 81. Slope profiles within Baetis Chaos.	116
Figure 82. Slope profiles within Candor Chaos.....	117
Figure 83. Slope profiles within Chryse Chaos.	118
Figure 84. Slope profiles within Echus Chaos.	119
Figure 85. Slope profiles within Eos Chaos.	120
Figure 86. Slope profiles within Hydrae Chaos.....	121
Figure 87. Slope profiles within Hydaspis Chaos.....	122
Figure 88. Slope profiles within Hydraotes Chaos.	123

Figure 89. Slope profiles within Iamuna Chaos.	124
Figure 90. Slope profiles within Iani Chaos.	125
Figure 91. Slope profiles within Ister Chaos.	126
Figure 92. Slope profiles within Margaritifer Chaos.	127
Figure 93. Slope profiles within Nilus Chaos.	128
Figure 94. Slope profiles within Pyrrhae Chaos.....	129
Figure 95. Slope profiles within Xanthe Chaos.	130
Figure 96. Cumulative plot of percent area for defined slope breaks at 2, 5, 15, 25, 45, and 60 degrees for all chaotic terrains and NL. Four maturities of chaotic terrains were able to be discerned from slope comparisons.	142
Figure 97. Group 1 of similar slope values within the chaotic terrains. This group represents immature or un-evolved chaotic terrains due to the low relative percentages of slopes between 2 and 15 degrees.....	144
Figure 98. Group 2 of similar slope values within the chaotic terrains. This group represents a second group of immature or un-evolved chaotic terrains but is more evolved than group 1 due a higher number of slopes between . 2 – 15 degrees.....	145
Figure 99. Group 3 of similar slope values within the chaotic terrains. This group represents a more evolved group of chaotic terrains with medium maturity, where slopes dominantly fall between 2 – 15 deg. The compiled dataset of all chaotic terrains also averages to this group.	146
Figure 100. Group 4 of similar slope values within the chaotic terrains. This group represents the evolved, mature, chaotic terrains that are likely to have wide, eroded chaos floors as well as shallow mesa and knob walls.....	147
Figure 101. Comparative slope percent area of NL and composite chaotic terrain slopes. The bulk of chaotic terrain slopes are below 30 degrees, while slopes in NL are nominally > 60. These high slope values within NL are likely attributed to steep mesa walls, while low slope values are attributed to mesa plateaus, trough floors, and surrounding flat terrain.	149
Figure 102. Groupings of chaotic terrains defined based on slope percent area analysis.	150

Figure 103. Rose diagram plot and statistics for digitized NL lineaments. Lineaments in NL show a preferential NNE direction.	153
Figure 104. Results of the lineament analysis for NL. Three dominant regional fracture patterns are seen in the NNE, NNW, and radial fractures (NW and NE directions).....	154
Figure 105. Cumulative rose diagram plot for all 19 analyzed chaotic terrains. The mean vector has a value of ~315 but does not show strong preferential orientation of lineaments within all chaos.	155
Figure 106. Cumulative rose diagram plot for Arsinoes Chaos.	156
Figure 107. Cumulative rose diagram plot for Aurorae Chaos.....	156
Figure 108. Cumulative rose diagram plot for Aram Chaos.....	157
Figure 109. Cumulative rose diagram plot for Aureum Chaos.	157
Figure 110. Cumulative rose diagram plot for Baetis Chaos.	158
Figure 111. Cumulative rose diagram plot for Candor Chaos.....	158
Figure 112. Cumulative rose diagram plot for Chryse Chaos.	159
Figure 113. Cumulative rose diagram plot for Echus Chaos.	159
Figure 114. Cumulative rose diagram plot for Eos Chaos.	160
Figure 115. Cumulative rose diagram plot for Hydaspiis Chaos.....	160
Figure 116. Cumulative rose diagram plot for Hydrae Chaos.....	161
Figure 117. Cumulative rose diagram plot for Hydraotes Chaos.	161
Figure 118. Cumulative rose diagram plot for Iamuna Chaos.	162
Figure 119. Cumulative rose diagram plot for Iani Chaos.....	162
Figure 120. Cumulative rose diagram plot for Ister Chaos.	163
Figure 121. Cumulative rose diagram plot for Margaritifer Chaos.	163
Figure 122. Cumulative rose diagram plot for Nilus Chaos.	164
Figure 123. Cumulative rose diagram plot for Pyrrhae Chaos.....	164
Figure 124. Cumulative rose diagram plot for Xanthe Chaos.	165

Figure 125. Result of the comparative two-sample Kolmogorov-Smirnov test between NL lineation orientations (nl_az) and chaotic terrain lineation orientations (chaos_az).	169
Figure 126. Groupings of chaotic terrains based on similarity of lineament orientation. Four discrete groups are defined.	171
Figure 127. Hydrated mineral mapping within NL. Dominant observations are hydrated poly and mono- sulfates, although, hydrated silica (opal), and hydrated phyllosilicates are also detected.	173
Figure 128. Aqueous mineral distribution within analyzed chaotic terrains. Hydrated phyllosilicates are the most abundant hydrated mineral within the region, with sulfates also appearing, and hydrated silica observations being confined to Valles Marineris areas.....	174

LIST OF TABLES

Table 1. Names and locations for the 19 chaotic terrains analyzed.....	34
Table 2. Slope classifications measured by percent area within NL.	131
Table 3. Slope classifications measured by percent area within all chaotic terrains.	131
Table 4. Slope classifications measured by percent area within Arsinoes Chaos.	132
Table 5. Slope classifications measured by percent area within Aurorae Chaos.	132
Table 6. Slope classifications measured by percent area within Aram Chaos.	133
Table 7. Slope classifications measured by percent area within Aureum Chaos.	133
Table 8. Slope classifications measured by percent area within Baetis Chaos.	134
Table 9. Slope classifications measured by percent area within Candor Chaos.	134
Table 10. Slope classifications measured by percent area within Chryse Chaos.	135
Table 11. Slope classifications measured by percent area within Echus Chaos.	135
Table 12. Slope classifications measured by percent area within Eos Chaos.	136
Table 13. Slope classifications measured by percent area within Hydaspis Chaos.	136

Table 14. Slope classifications measured by percent area within Hydrae	
Chaos.....	137
Table 15. Slope classifications measured by percent area within Hydraotes	
Chaos.....	137
Table 16. Slope classifications measured by percent area within Iamuna	
Chaos.....	138
Table 17. Slope classifications measured by percent area within Iani	
Chaos.....	138
Table 18. Slope classifications measured by percent area within Ister	
Chaos.....	139
Table 19. Slope classifications measured by percent area within Margaritifer	
Chaos.....	139
Table 20. Slope classifications measured by percent area within Nilus	
Chaos.....	140
Table 21. Slope classifications measured by percent area within Pyrrhae	
Chaos.....	140
Table 22. Slope classifications measured by percent area within Xanthe	
Chaos.....	141
Table 23. P-value results from the two sample Kolmogorov-Smirnov test comparing the similarity between the azimuths of two lineament datasets. Each chaotic terrain, as well as a compiled chaotic terrain dataset, was tested against all other terrains and NL. A p-value above 0.05 (highlighted in red stripes) indicates the azimuths of two lineament datasets are similar from a statistical standpoint.....	167
Table 24. Simplified p-value results from Table 23.1. Red boxes reject the null hypothesis of similarity (p-value < 0.05), while green boxes indicate a p-value > 0.05, indicating the input datasets are similar.....	168

INTRODUCTION

Our planetary neighbor, Mars, is presently the most explored planetary body in the solar system apart from Earth. Missions to Mars have been exceedingly successful within recent years, with eight active orbiters continuously collecting data of the Martian surface, subsurface and atmosphere. On the surface, six rovers have been successful in operations, collecting close-up imagery and performing sophisticated in-situ geologic investigations.

Nicknamed 'The Red Planet,' the terrestrial planet is the fourth planet from the Sun in our solar system. Mars has a predominantly basaltic crust, a mantle and a solid metallic core. Atmospheric composition is 95% gaseous CO₂ and trace amounts of water vapor that experience rapid atmospheric escape, but it is theorized the atmosphere once may have been thick enough to support the presence of liquid water on the surface (Carr & Head, 2009). Evidence for the flow of water is present due to interpreted fluvial morphologies and rich hydrated surficial mineral deposits. The planet is cold and arid, with yearly surface temperatures averaging -27°C due to the distance from the Sun and the absence of a thick atmosphere. Liquid water is not stable on the surface of Mars but is found frozen in layered deposits at the poles and locked within the subsurface as ice (Clifford, 2010). The proximity to Earth and geomorphological evidence for

the flow of liquid on the surface allows Mars to remain the target of many past and current missions to space. Understanding the unique geology of Mars will not only begin to unravel the complex geologic history of the red planet but will also be essential in the steps toward planetary body exploration and habitation.

This study focuses on the structural and hydrologic controls within unique geomorphologic regions seen on Mars, and more specifically within Noctis Labyrinthus (NL), a ~1,000-km-wide extensional trough network within the Phoenicis Lacus quadrangle. NL lies on the northern edge of Syria Planum, a large volcanic province with several low shield volcanoes, and connects the Tharsis rise tectonic province to the Valles Marineris (Figure 1). NL hosts a complicated mix of volcanic, tectonic, hydrologic, and glacial morphologies, which makes understanding the evolution of the system challenging. The presence of aqueously-altered mineral assemblages within strata in NL suggests that hydrologic activity may have contributed more of a diagenetic influence than originally theorized. Spatial patterns seen at the surface also coincide with polygonal fracturing commonly associated with hydrologic processes (Johnson et al., 2006).

Outflow channels on the eastern side of Valles Marineris are interpreted to be caused by the catastrophic release of groundwater within the subsurface (Figure 2). Seen at the headwaters of the outflow channels are chaotic terrains, a

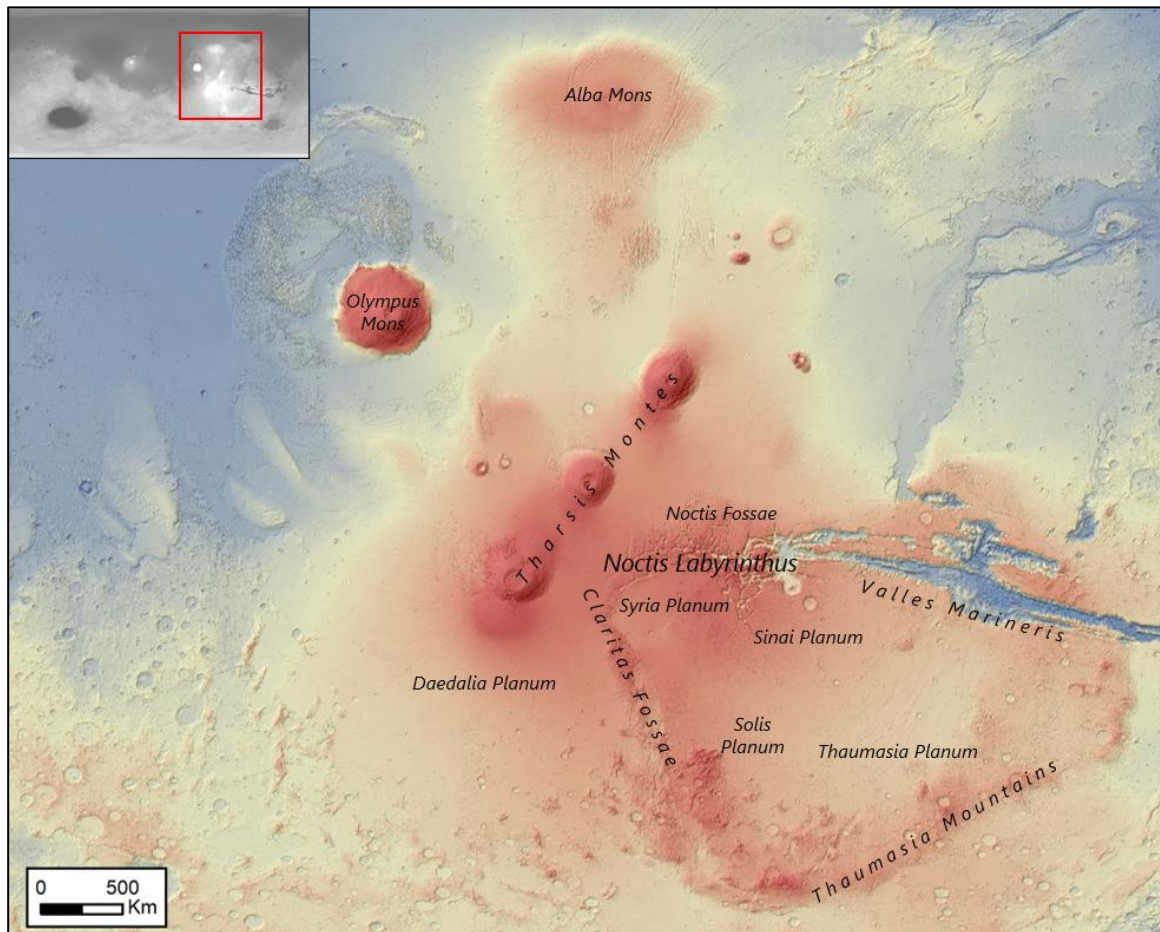


Figure 1: Elevation model of major regions within the Tharsis rise, Mars (MOLA 200m DEM overlain on HRSC global hillshade map).

degradation theoretically based on amount of fluid released at time of collapse, series of depressions bounded by polygonal mesas, which have been interpreted as the origin of the outflow (Sharp & Malin, 1975). Chaos morphology is attributed to large-scale regional subsidence due to rapid fluid loss within the subsurface (Carr, 1979). The distinction between chaotic terrain and outflow channel topographically varies with locality, where chaos shows differing levels of erosion in proximity to defined outflow channels.

Similar surficial polygonal patterns are seen within chaotic terrains and NL, where low troughs bound geometric topographic mesas, which suggests a common origin and evolution of both morphologies. This research analyzes lineament patterns, topography, and geomorphology of NL to determine the role of fluid in the evolution of the network and links the chaotic terrains typically associated with hydrologic induced subsidence to NL. Using geographic information systems (GIS) and planetary image analyses, further understanding of the geologic and origins of both unique morphologies was established.

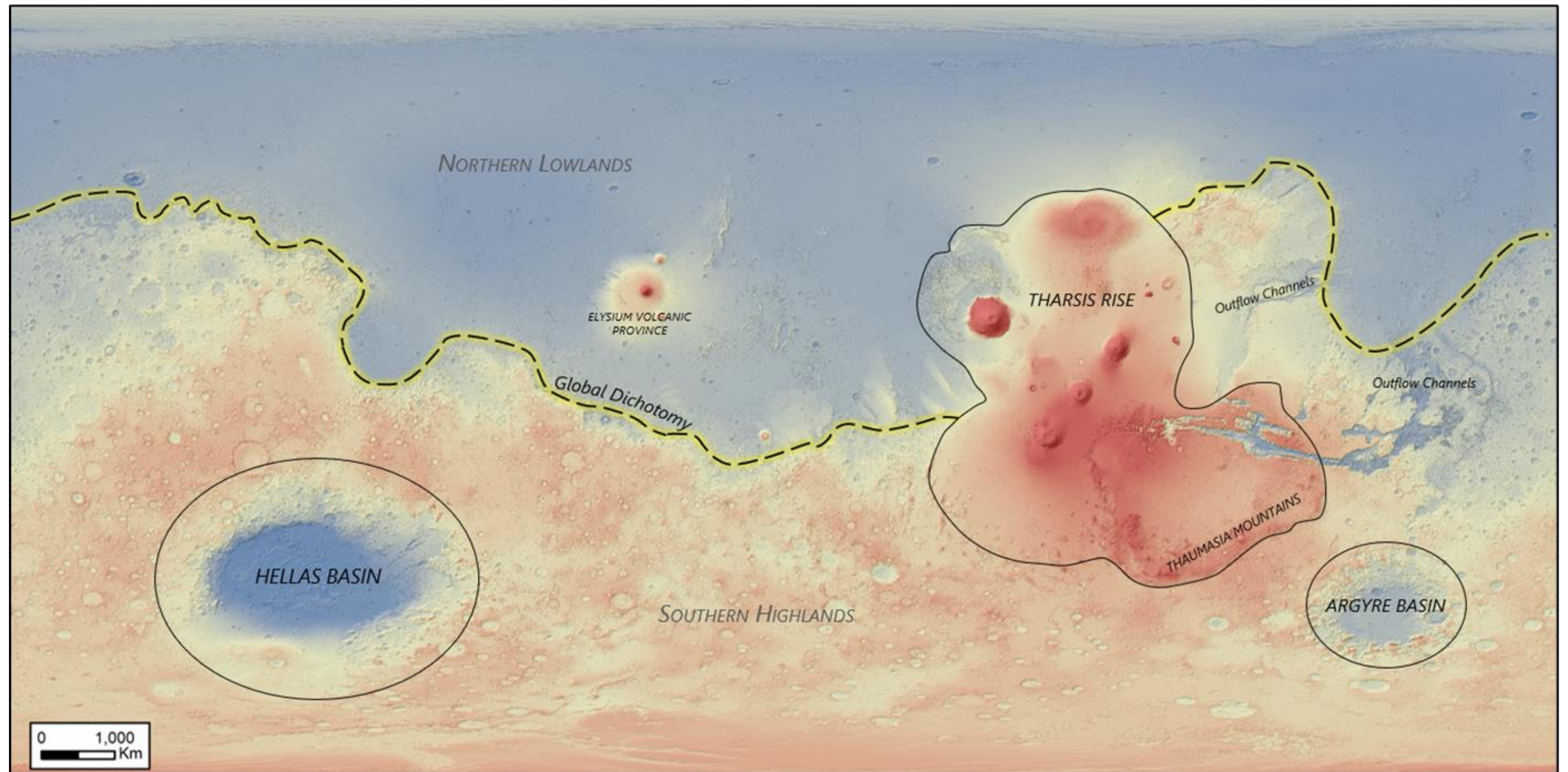


Figure 2: Global Map of the Martian surface with major geologic provinces labeled. The global dichotomy is highlighted and separates the flat northern lowlands and the rugged southern highlands. Chaotic terrains are found at the headwaters of massive outflow channels east of the Tharsis rise.

GEOLOGIC SETTING

General Geology

Martian geology is dominated by the complicated intermixing of igneous, sedimentary, and impact processes. Most rock is igneous with volcanic origins where basalt lava / sheet flows and pyroclastic deposits are the dominate subtypes (Tanaka et al., 2014). Other deposits are directly related to the weathering, erosion, and alteration of igneous deposits. Volcanic deposits are commonly tectonically-altered based on locality. Units related to impacts of bolides, such as impact ejecta, are also globally common. Stratigraphically, Martian crust would consist of layers of volcanic deposits and products, alternating in composition and extent based on the nature of the volcanic or igneous process that occurred. Basement rock within the crust is likely highly fractured in-situ, due to large-scale tectonic stresses and/or continuous bombardment by bolides on the surface. With increasing depth, the fractures would reach a self-compaction where the fractures have no further effect on the nature of the strata (Clifford, 1993). Figure 3 shows a theoretical model for the stratigraphy of the Martian crust.

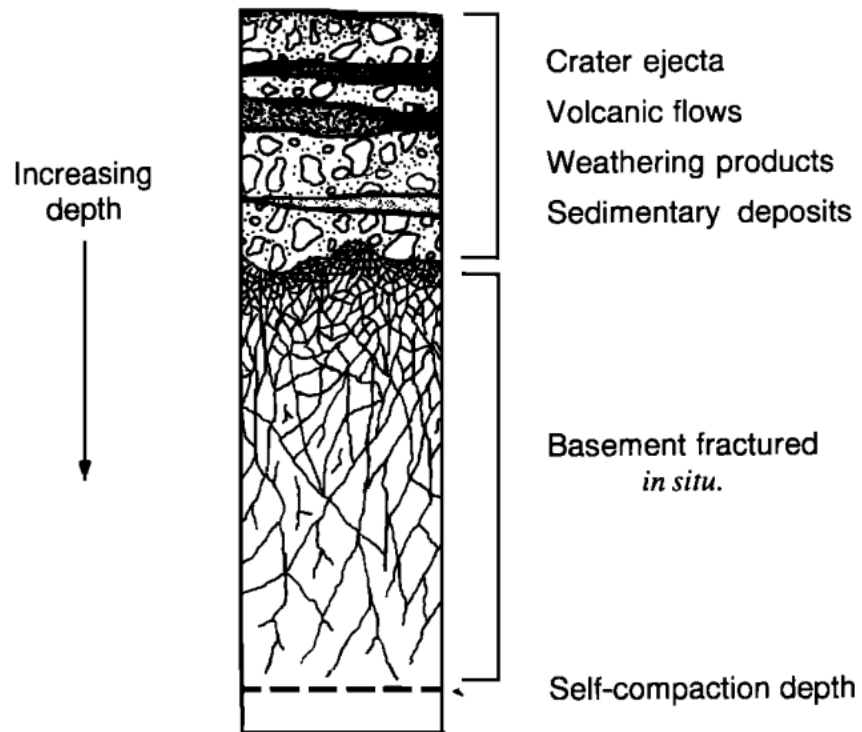


Figure 3: Theorized stratigraphy of the Martian crust (From Clifford, 1993).

Geologic History

The geologic history of Mars is described within four periods, where crater size-frequency distribution, surficial lava flow superposition and mineralogical trends have been some of the tools used to define them (Carr & Head, 2009). These periods emphasize planetary-wide geologic processes and the evolution of the surface with geologic time as a function of the general life-cycle of non-Earth-like terrestrial bodies. Activity within the geologic record is confined to the first billion years post planetary accretion and differentiation where geologic processes have slowed significantly following those first billion years. Figure 4 shows an estimated geologic timescale, associated mineral assemblage deposition and active processes during each period. Unlike our Earth-based geologic time scale, the periods defined in the Martian time scale are rough estimates of millions to billions of years of geologic time without accurate dating techniques. Periods are named pre-Noachian, Noachian, Hesperian and Amazonian (Carr & Head, 2009).

Pre-Noachian

The pre-Noachian began 4.5 billion years ago (Gya) at the formation of the solar system, reflects the time of planetary accretion, to a quick differentiation of the core, mantle and crust, and ends with the formation of the Hellas impact

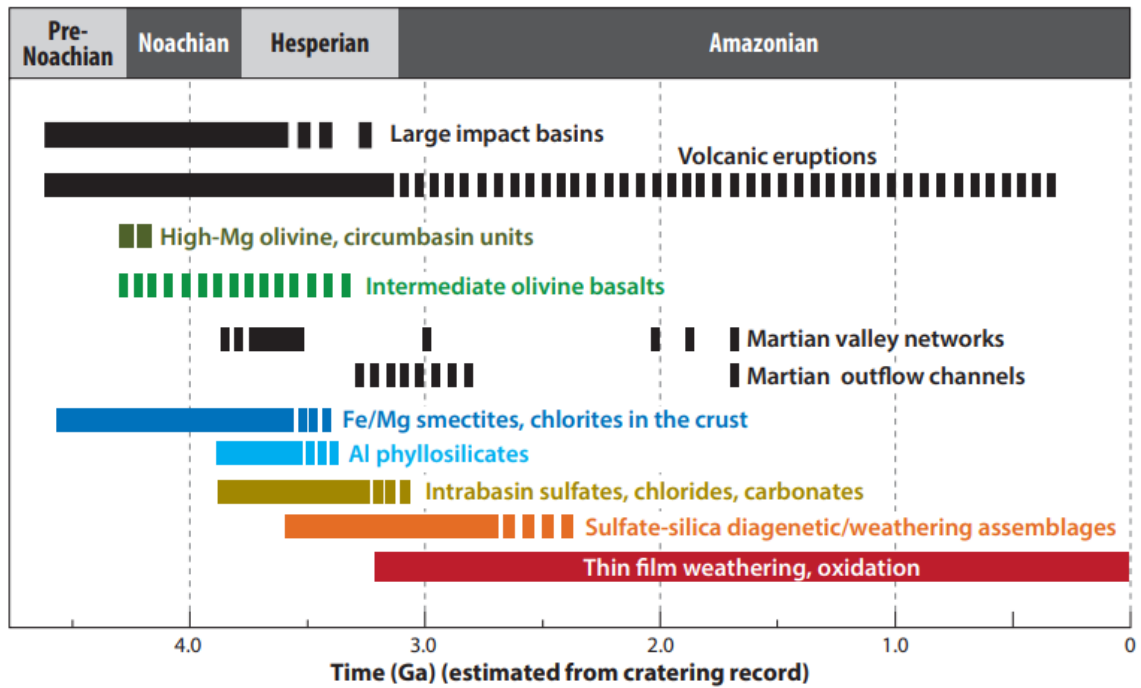


Figure 4: Geologic timescale of Mars with major processes and associated mineral group deposits (From Ehlmann & Edwards, 2014).

basin (~ 4.1 Gya) (Figure 2). High impact and erosional rates in the Noachian significantly erased the pre-Noachian geologic record and due to the limited exposed surface units, this period is obscure. Similar to the formation of Earth, Mars is estimated to have had a large planet-wide magma ocean shortly following accretion and differentiation (Carr & Head, 2009). Remanent, localized magnetic crustal anomalies found in the southern highlands also indicate that Mars had a magnetic field similar to Earth at some point in its geologic history, but the exact nature of the field is still relatively unknown. Due to the unclear nature of the pre-Noachian, it is not well defined in the literature.

The global dichotomy between the northern lowlands and the southern highlands of Mars is believed to have formed during the pre-Noachian, and the preservation of the dichotomy boundary indicates that there was likely no crustal recycling or rearrangement (Figure 2) (Andrews-Hanna & Bottke, 2017). There is no evidence for large-scale, Tharsis-style volcanism, but smaller, more localized volcanics may have been present and any volcanic activity during this period would have been accompanied by the outgassing of volatiles like sulfur compounds and water (Carr & Head, 2009). Based on impact crater mapping and superposition, impact rates were less than 17% of that of the Noachian period, indicating a comparatively low bombardment period. Evidence may exist for large impact basins that pre-date the Hellas basin, in the form of quasi-circular depressions, which may have contributed to the formation and

development of the global dichotomy (Nimmo & Tanaka, 2005). Again, the geologic record has been widely altered, degraded, and overlain by younger Noachian rock, so determining the climate and atmospheric conditions during this period is difficult.

Noachian

The Noachian sustained the most intense prolonged activity throughout the geologic record. The Noachian period begins with the formation of the Hellas impact basin at the end of the pre-Noachian (~4.1 Gya) and ends ~ 3.7 Gya. This period is mostly characterized by the high impact rates, the presence of liquid water at the surface and in the subsurface, and comparatively high erosional rates as a result of fluvial processes. Anomalous high impact rates during the Noachian correlate to the Late Heavy Bombardment period of the solar system and are likely related to the increased post-accretion collisions. The Noachian also experienced the formation of large-scale volcanics, primarily located within the Tharsis rise (Figure 2). Further development of the Tharsis rise continued through the late Noachian (Carr & Head, 2009).

Evidence for the flow of liquid on the surface during the Noachian is present globally. Exposed Noachian units show erosional features directly related to the flow of liquid, and the presence of Fe and Mg phyllosilicate deposits in aqueously-altered Noachian units imply the alteration of primary igneous rock by

an aqueous solution (Carr & Head, 2009). Erosional features in Noachian terrains coupled with the presence of surface runoff patterns indicate episodic precipitation and warm surface conditions. Hydrous weathering produced aqueous-altered secondary minerals in the early to middle Noachian rock record, but late Noachian units show little to no deposition of aqueous-altered rock. This may have been due to changes in the climate during the late Noachian, where the climate could have been colder and drier, suppressing conditions needed for hydrous weathering to occur. Widespread impacts would have distributed ejecta planet-wide and would have likely caused hydrothermal activity surrounding the impact sites. Continuous large-scale impacts may have contributed to the climate and surface conditions during the Noachian. Bolide impacts would have warmed the surface and ejected large amounts of volatiles into the atmosphere, which would have been precipitated and collected at topographic lows on the surface (Carr & Head, 2009).

Hesperian

The Hesperian period (3.7 ~ 3 Gya) is characterized by low erosion rates and extensive widespread volcanism (Carr & Head, 2009). Volcanism dominated the period, following the formation of the Tharsis and Elysium volcanic provinces (Figure 3). Volcanism was so prevalent that nearly 30% of the Martian landscape was resurfaced by volcanic activity. The steep decline in erosional rates from the

Noachian to the Hesperian suggests a cessation of surface conditions that would favor aqueous activity and fluvial morphology development. Continuing from the late-Noachian to early-Hesperian, most of the surficial water would have been locked within the newly generated cryosphere as subsurface ice (Carr & Head, 2009).

However, geomorphic evidence of large-scale episodic flood events is found in Hesperian-aged immense outflow channels. Episodic ocean conditions may have been present where fluid released from the subsurface accumulated in the northern lowlands. Floods producing outflow channels of this scale would likely be due to the rapid release of groundwater from deeply buried aquifers, caused by impact melting or tectonic-volcanic processes (Carr, 1979). The formation of the Valles Marineris, Noctis Labyrinthus and surrounding chaotic terrains is estimated to have occurred during this period, and possibly being a product of large-scale flooding. Transitional surface changes from the early and middle-Noachian to the late-Noachian and Hesperian decreased the widespread deposits of phyllosilicates and the presence of sulfate-rich deposits increased. Increased atmospheric concentrations of volcanically-degassed sulfur compounds contributed to increased deposition of sulfates and would aid in explaining the shift in climate from the Noachian to the Hesperian. Late-Hesperian saw a different transition, with deposits consisting of anhydrous ferric oxides becoming dominant (Carr & Head, 2009).

Amazonian

The Amazonian, extending from ~3 Gya to present, combines the last three billion years of Martian geologic history into a single period. Characterized by extremely limited and slow geologic processes, the Amazonian saw a decrease in volcanic activity, and continuously low erosion rates (Carr & Head, 2009). Impact rates continued to decrease from the Hesperian, so much so that Amazonian-aged rock is only lightly cratered, an exceedingly different condition from the heavily cratered Noachian terrain. Volcanics were largely confined to Tharsis and Elysium provinces. General hydrologic activity was limited but it is estimated that flooding continued into the Amazonian at a smaller, more local scale than in the Hesperian. Morphological features attributed to the accumulation of ice and glacial flow are prevalent in the Amazonian, indicating a relatively continuous cold and arid climate, similar to the present-day conditions on Mars (Carr & Head, 2009). Eolian processes dominate the surface of Mars today, sweeping sediment across the planet in giant dust storms, creating common sand dune surface morphologies.

Tectonics

Exceptional preservation of the rock record on Mars equivalent to Archean-aged rock indicates there is no form of large-scale crustal recycling

such as a plate tectonic cycle similar to that of Earth (Andrews-Hanna & Bottke, 2017). Although there is no cyclical tectonics occurring, tectonic forces contribute to much of the unique morphology seen on the surface. Three general tectonic provinces can be characterized from elevation data: the southern highlands, the northern lowlands, and the Tharsis rise (Figure 2). A global dichotomy separates the northern lowlands from the southern highlands, representing a change in elevation of 1-3 km between the two provinces. The northern lowlands are characterized by uniform, low topography of the region, low crater density and contain volcanic rock Hesperian to Amazonian in age, presumably a result of the global resurfacing that occurred in the Hesperian. Northern lowlands lack any crustal flexure indicators, implying the plains may be in isostatic equilibrium (Wise et al., 1979). The southern highlands are elevated in topography, heavily cratered, and dominantly Noachian in age (Nimmo & Tanaka, 2005).

The Tharsis rise is a large, elevated plateau, containing some of the most tectonically-influenced morphology on Mars. Large-scale shield volcanoes dominate, contributing to the buildup of anomalously thick lithosphere characteristic of the region. Based on crater density and deformation age estimations, the Tharsis rise began uplift during the late Noachian - early Hesperian and continued until the latter part of the Amazonian (Bouley et al., 2018). Emplacement of such a large uplift within the lithosphere would result in large-scale tectonic deformation, which is seen in compressional and tensional

faulting, radial and concentric to the uplift. Fossae, large narrow graben and linear wrinkle ridges, are common (Watters & Schultz, 2010).

Many large-scale structures, such as the Tharsis volcanic complexes (Olympus Mons; Tharsis Montes volcanoes), Syria Planum, Valles Marineris, and the Noctis Labyrinthus are all results of the development of the Tharsis rise (Anderson, 2001). Tharsis origin models discuss mantle plume upwelling in the lithosphere and spherical elastic shell loading (Banerdt et al., 1982). Plume development could have been a result of a deep-rooted mantle plume or impact driven thermochemical plume emplacement and contributed to rapid isostatic rise within the Tharsis province (Reese et al., 2004; Schubert et al., 1990; Wise et al., 1979). Following initial upwelling, underplating of the plume and the planetary geotherm remnant of accretion would have provided a heat source to sustain long periods of continuous extrusive and intrusive volcanism within the province. Proposed models must account for the scale of deformation accompanying the rise, where extrusive and intrusive magmatic deposits load and extensively deform the lithosphere (Watters & Schultz, 2010).

The Yin (2012) model for global Martian tectonics diverts from traditionally accepted models and essentially defines the Tharsis rise as a result of slab subduction near the Argyre impact basin and Thaumasia Mountains (Figure 2) that initiated slab-rollback and loading the lithosphere due to extensive volcanic

rock deposition. Yin (2012) delineates four distinct volcanic zones, which coincide with the development and rollback of a slab as slow creep towards the global dichotomy was engaged. Structures related to the development of the rise are categorized as classical regional subduction features, with compressional thrust faulting occurring closer to the plate boundary and backarc extension and conjugate strike-slip zones occurring within the Noctis Labyrinthus extensional zone and the Valles Marineris transtensional zone (Yin, 2012).

Hydrology

Fluvial activity

Substantial evidence for liquid on the surface of Mars is present in aqueously-altered mineral deposits and geomorphology that exists only by the modification of terrain by moving fluid. Channels of fluvial origin identified and categorized by Sharp and Malin (1975) are grouped into two categories: outflow channels and runoff channels. Fretted channels referred to in this text are chaotic terrains and are not of fluvial origin, rather a product of mass-wasting and aqueous subsurface seepage, which will be discussed in detail further. Runoff channels include multi-channel networks and gullies that dissect older terrains, indicating surface runoff flow. Runoff channels are analogous to typical fluvial processes occurring in streams and rivers on Earth. Outflow channels are the

product of catastrophic flooding during the Hesperian and early-Amazonian, originating within the chaotic terrains and flowing outwards towards the northern lowlands. The size of these channels indicates liquid was released rapidly at great pressure, possibly originating from confined, deeply buried aquifers (Sharp & Malin, 1975).

Hydrated minerals

Hydrated mineral deposits are also a major indicator for the presence of a hydrologic cycle on Mars. Iron-bearing phyllosilicates are found globally, pointing to fluvial activity as a major source of clay mineral growth and deposition (Ehlmann et al., 2013). Soluble sulfates are found within altered layered strata and could indicate groundwater as an important diagenetic and depositional influence (Johnston et al., 2006). Minerals formed by the presence of hydrologic activity are found at localities, where hydrated silica, hematite, various salts, olivine and zeolites are common.

Groundwater and potential periodic recharge

The formation of aquifers in fractured, porous volcanic and brecciated rock is highly feasible. Rodriguez and others (2016) propose an elevated groundwater table located within the Tharsis rise, with an associated structurally-controlled groundwater flow path traveling eastward through NL. As climate cooled throughout the late-Hesperian and Amazonian, subsequent confinement of an

aquifer due to cryosphere growth could have occurred. The presence of a global groundwater system confined by a thick cryosphere (Carr, 1979), would have immense implications for morphology evolution on Mars, and more locally, within NL. Subsidence and collapse morphology of the chaotic terrains suggests massive subsurface erosion and/or solution, which could implicate episodic release of groundwater from a confined aquifer (Carr, 1995). These episodic conditions could be indicative of short-term, excessively warm conditions, where volcanic activity or impact melting developed rapid sublimation within the subsurface where volatiles trapped within were forced to rapidly escape.

Due to gravitational perturbations, Mars experiences large scale variations in its obliquity and as a result there are cyclical effects on climate conditions. The rotational axial tilt is currently about 25° but is estimated to vary between 14° and 35° (Ward, 1973). Ice deposits are currently located at the N/S poles, but changes in the obliquity allows melting of polar ice deposits and promotes glacial movement inwards toward the equator. As obliquity shifts, insolation driven ice melt would have occurred and contributed to recharge of potential subsurface aquifers (Holo et al., 2018). Permafrost has been identified at many locations, where a dry layer of permafrost may already exist within the subsurface, it is hypothesized that a “wet” active layer of permafrost was active during the Amazonian and contributed to higher degrees of sublimation and active hydrologic weathering of features in the mid-latitudes (Kreslavsky et al., 2008)

Noctis Labyrinthus

Noctis Labyrinthus (NL) is a complicated, interconnected, linear trough network connecting the Valles Marineris to the Tharsis Montes volcanic province in the southern highlands of Mars (Figure 1). NL can be observed directly from orbit with a diameter of ~1,000 km, and despite its grandiose nature, NL remains severely understudied. The region is dominated by the interconnection of kilometer-deep troughs and pits, producing bounded polygonal-like mesas, that give the structure its unique shape (Tanaka & Davis, 1987). NL is estimated to be late Hesperian to early Amazonian in age and cuts through Hesperian to Noachian-aged basalt flows (Tanaka & Davis, 1988). The troughs are discontinuous and surface patterns seen from orbit coincide with polygonal fracture patterns commonly associated with collapse structures on Earth. NL is anomalously domical, suggesting uplift of the area.

Origin theories

Many models arise for the origins of NL, but two models are more widely accepted: one model suggests formation of NL due to structurally-controlled groundwater circulation and induced collapse (Rodriguez et al., 2016; Tanaka & Davis, 1988). Others suggest magma withdrawal and deflation-induced surface collapse (Mège et al., 2003). Extensional tectonics is theorized to be the initial sequence that allowed for continuous evolution and collapse. Presence of

stratified, hydrated minerals within the trough walls gives basis for induced collapse due to large-scale fluid loss of a cryosphere during active extension and could indicate that hydrologic activity was more of an influence on the evolution of NL than originally theorized (Kling et al., 2021).

Morphology and Structure

Normal faulting and graben structures are widespread within and around NL (Tanaka & Davis, 1988). Noctis Fossae bounds NL to the north (Figure 1), which consists of series of extensional faulting pre-dating the formation of NL. Likely formed in the late Noachian to late Hesperian, these fossae are long and narrow, and oriented radial to Syria Planum. Syria Planum, a volcanic plateau, defines the southern boundary of NL (Figure 1) and contains concentric-orientated extensional faulting that formed post-Noctis Fossae but predate the formation of NL, likely forming during the late Hesperian. The normal faulting within NL has a dominant north-south orientation and is estimated late Hesperian in age. NL faulting is controlled mainly by pre-existing radial and concentric faulting surrounding the area, but tangential WNW - NNW trending faults were also produced (Tanaka & Davis, 1988).

Geomorphologically, NL is dominated by the interconnection of large troughs and pits, producing bounded polygonal mesas that divide the troughs. Troughs are characterized by their linear nature and have been interpreted as

graben, or a dropped down surface situated between two normal faults. At most points along NL, troughs express an elevation difference of ~ 2,000 – 4,000 m from the top of the mesa to the bottom of the trough (Rodriguez et al., 2016). The massive size and depth of these troughs suggests that extensional tectonics cannot be the only formation mechanism (Kling et al., 2018). Troughs within NL have deep canyon floors, and typically show signs of slump and collapse within the canyon walls. Mudflows, landslide debris and boulders are common. In preserved sites, layered strata can be found in the steep canyon walls. Within this stratum is found the most critical insights into the lithology of NL and of Mars itself.

Thollot and others (2012) identified a unique trough within NL, which reveals strata with some of the greatest mineralogical diversity on the planet. Hydrated minerals are most easily detected making up the light-toned deposits (LTDs) which stand out against the dark-toned surface and strata (Figure 5). LTDs are composed of Fe sulfates, Fe smectites, hydrated silicates and aluminosilicates, and hydrated sulfates. The presence of these hydrated minerals, without morphological evidence for a sustained body of water within the trough, favors groundwater circulation as a mechanism for these deposits. Such diverse mineralogy has yet to be found anywhere else in NL, but similar hydrated mineral deposits have been found within the troughs across the network (Thollot et al., 2012).

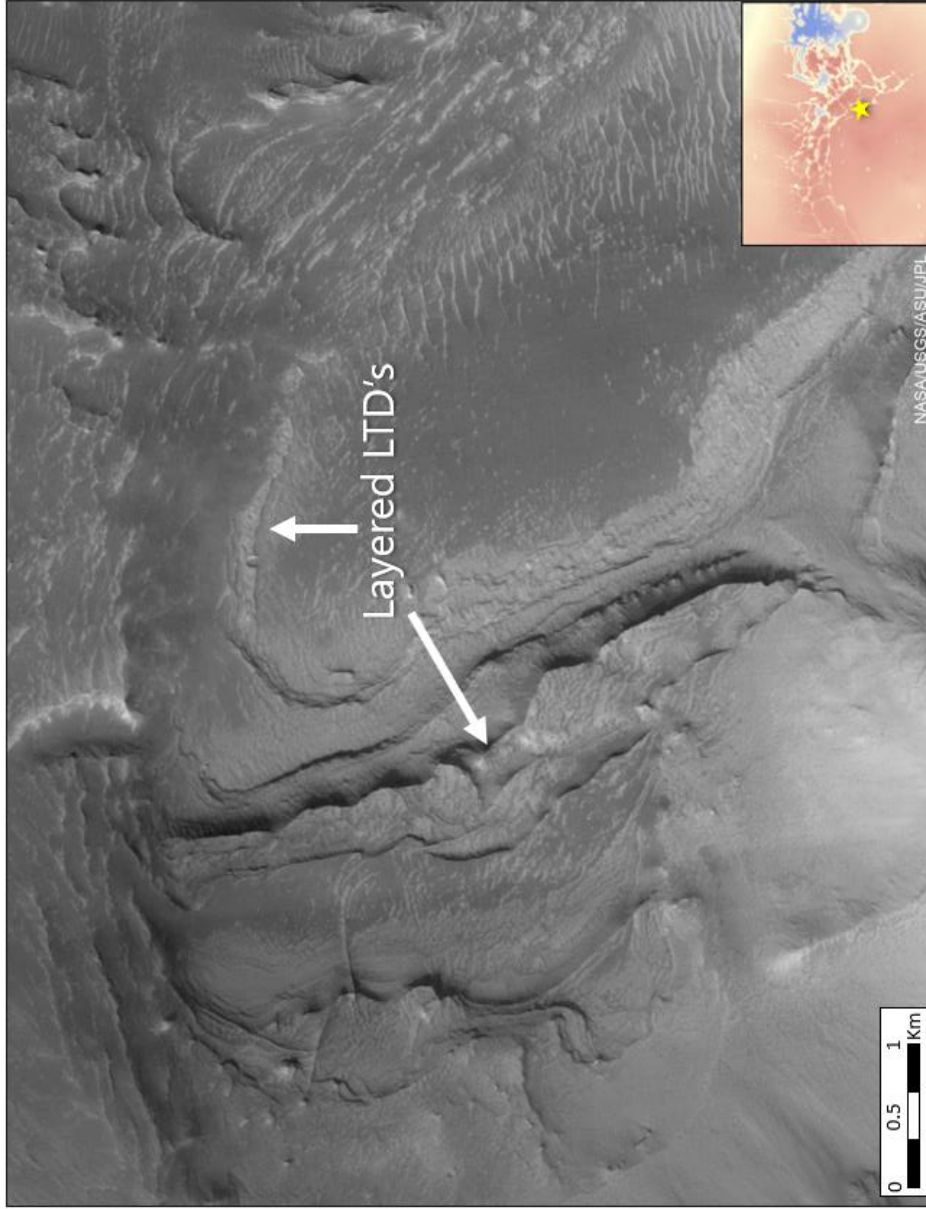


Figure 5: Example of layered LTD's within NL. Light toned deposits are common on the surface of Mars and can be composed of hydrated mineral deposits. The deposits stand out against the typical dark-toned surface within greyscale imagery. Some interpret LTD's as pyroclastic material such as ash flow and ash fall that has undergone hydrologic weathering.

Collapsed pits are rimless circular to elliptical depressions on the surface and are formed due to collapse into a subsurface cavity (Figure 6). They lack raised rims, a feature that distinguishes collapsed pits from impact craters. Collapse pits are formed from subsidence and collapse within the subsurface. The mechanism of these cavities is unknown, but could be sourced from dissolution, dike extrusion and magma withdrawal, tectonic activity, or a combination of processes. Pit-chains, or pits found in alignment with one another are also common, with most of the pit-chains in NL align with graben directional trends. The individual pit-crater chains appear to increase in size (both diameter and depth) with proximity to the central region of NL (Kling et al., 2018).

Several interpreted periglacial landforms can be found within the trough floors of NL, such as thermokarst, polygon ice wedges and solifluction lobes (Kling et al., 2021). In most places, these features are superimposed by landslide debris, suggesting that ground ice had some role in the formation of NL (Kling et al., 2021). If we accept the glaciation theory, the equatorial regions of Mars would have been covered in thick ice deposits, as seen at the poles today. Insolation driven ice melt as obliquity changed could have promoted recharge within a deeply buried aquifer system.

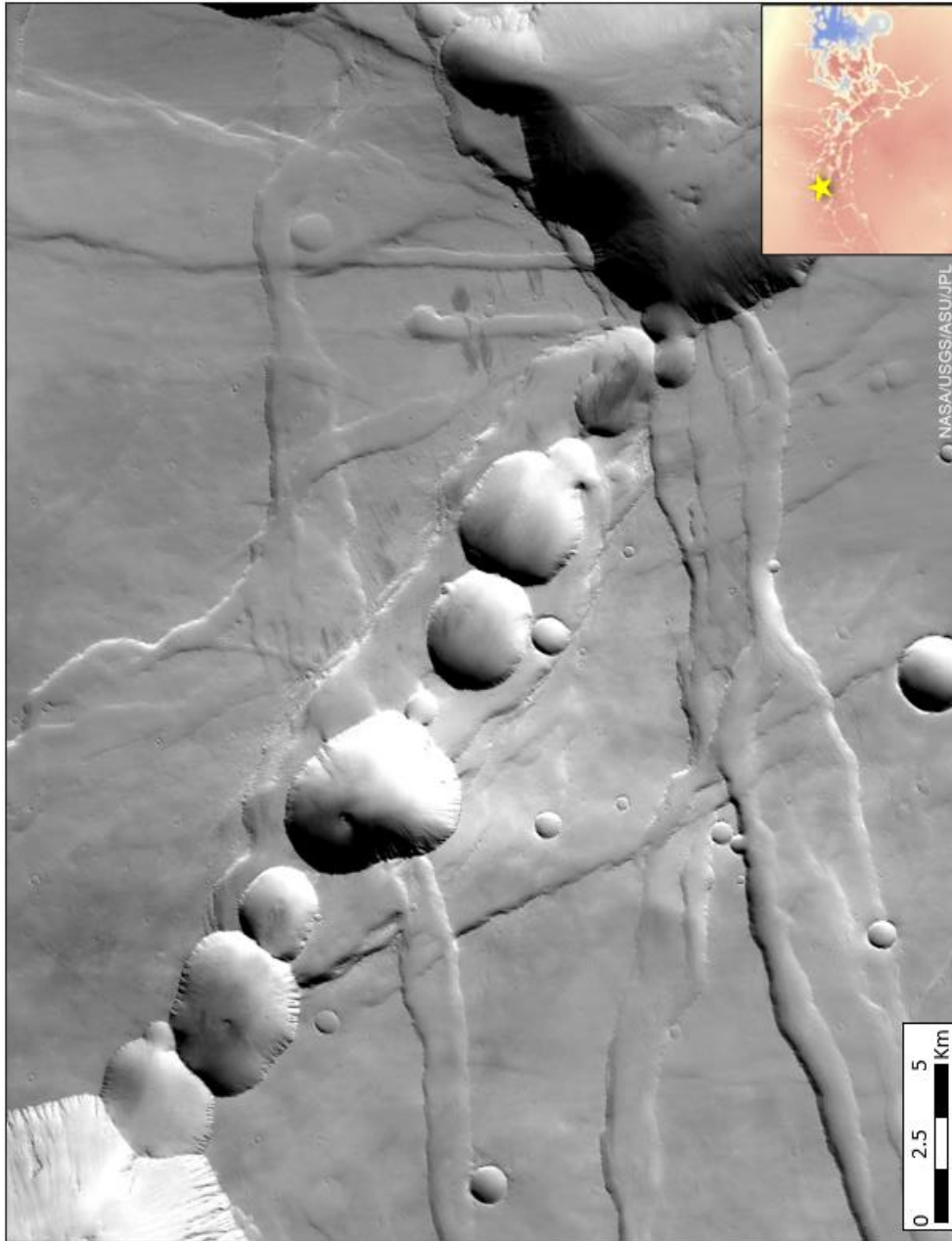


Figure 6: Example of a pit crater chain within NL. Collapse pits are rimless depressions formed due to subsidence and induced collapse within the subsurface. Collapse pits often form along a directional plane, forming a pit crater chain.

Karstic morphologies have been interpreted at several sites in NL (Baioni et al., 2017). Several shallow rimless depressions are observed and distinguished from identified collapsed pits and pit-chains due to their random nature and are seemingly unassociated with tectonic lineaments. These shallow depressions have been interpreted as doline landforms, with their formation processes being analogous to the development of dolines in evaporite rock on Earth (Stafford & Boston, 2005). Polygonal-like terrain can be observed within LTD deposits on trough floors. This terrain is characterized by well-defined polygonal shapes with sharp divides that display an irregular topography, forming the terrain into a cellular mesh-like pattern. Polygonal karst terrain is commonly found in soluble evaporitic rock on Earth as a result of solutional widening of endokinetic fissures and could serve as an analog for the polygonal terrain found in NL (Baioni et al., 2017).

Chaotic Terrains

The chaotic terrains are series of blocky, polygonal, surface features seen at the head of major outflow channels just east of the Tharsis rise (Figure 2). The terrain is a jumbled assemblage of large irregular blocks bounding lowland troughs (Sharp, 1973). These structures are theorized to be a product of localized collapse and subsidence due to rapid release of subsurface fluid or deflation within the subsurface (Carr, 1979). Degradation of terrains correlates

with the amount of fluid released from the system. If a particular chaos went through a multi-phase release and subsidence, the area appears heavily degraded. LTD's are found within some chaos and are interpreted as crystalline hematite associated with hydrous sulfate layers. These layers are somewhat correlated with the placement of chaotic terrains, where some pre-date formation stratigraphically and others serve as caps for the chaos blocks (Glotch & Rogers, 2007).

Origins

The main theories presented for a possible triggering mechanism of the expulsion of material within the subsurface at rapid rates involve volcano-ice interactions in the cryosphere (Chapman and Tanaka, 2002) and the release of water from subterranean caverns due to a destabilized aquifer system (Carr, 1979). An initial structural control on evolution is proposed where chaos is formed at the intersection of major fault systems of the Tharsis rise. Continuous bombardment of the Martian surface would have hydrologic effects on the geomorphology of the area. Impacts may have provided the initial melting mechanism for the release of subsurface fluid and could provide an explanation for episodic outflow conditions (Rodriguez et al., 2005). Whatever the mechanism for formation of these chaotic terrains, it is apparent that subsurface fluid had a large role in the evolution of the terrain.

METHODOLOGY

Data Collection

Images and data collected by the Mars Reconnaissance Orbiter (MRO) (Figure 7) were the primary resource of this research. The MRO operates a powerful onboard instrument suite: the Context Camera (CTX) and the Compact Reconnaissance Imaging Spectrometer (CRISM). MRO was launched on August 12, 2005, from Cape Canaveral, Florida and was inserted into the Martian orbit on March 10, 2006, where it has been continuously collecting and providing key insights into mineralogy and features of the surface (NASA Jet Propulsion Laboratory, 2023). CTX provides geologic context or “big picture” images across the planet with a camera resolution of 6m per pixel over a 30km-wide swath. CTX produces grayscale images with a broad band of visible light wavelengths ranging from 500-800 nm (Figure 8) (Malin et al., 2007).

CRISM is a visible-infrared imaging spectrometer that maps spectral signatures of water-related mineral deposits, which ceased data gathering in mid-2023. The instrument covered a hyperspectral range from 362-3920 nm at 6.55 nm per channel, observing the surface in both the visible wavelengths and shorter, near and mid infrared wavelengths (Figure 9) (NASA/John Hopkins Applied Physics Laboratory, 2023). This allowed CRISM to detect a wide

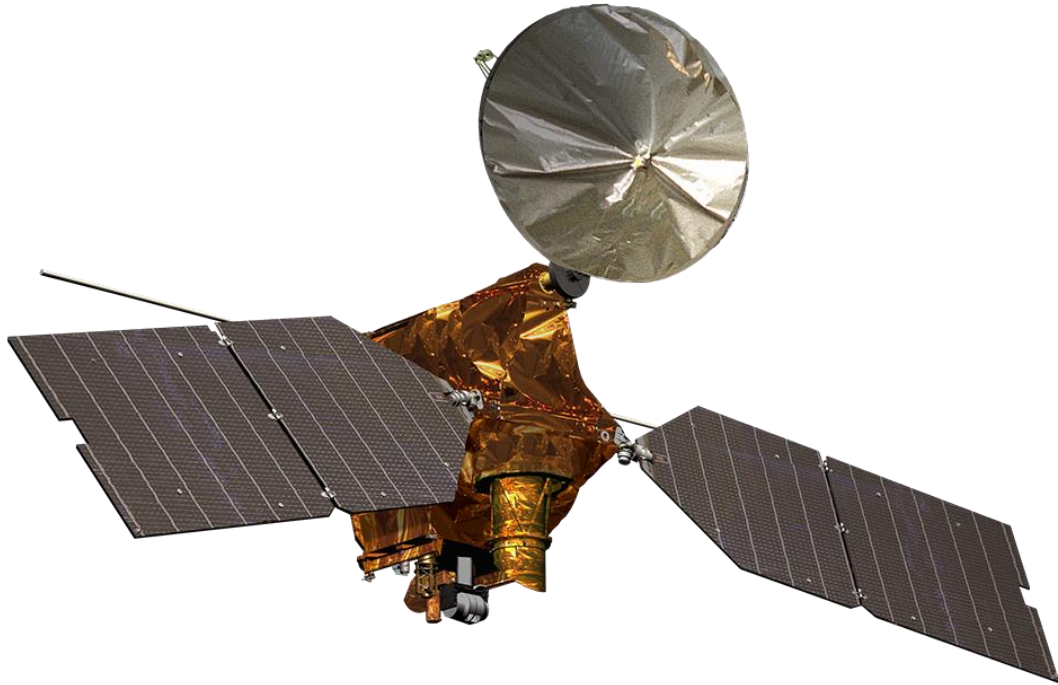


Figure 7: Mars Reconnaissance Orbiter (MRO) inserted into Martian orbit in 2006, where the orbiter has provided several years of continuous image, mineral, and science observations of the surface of Mars (From NASA Jet Propulsion Laboratory, 2023).

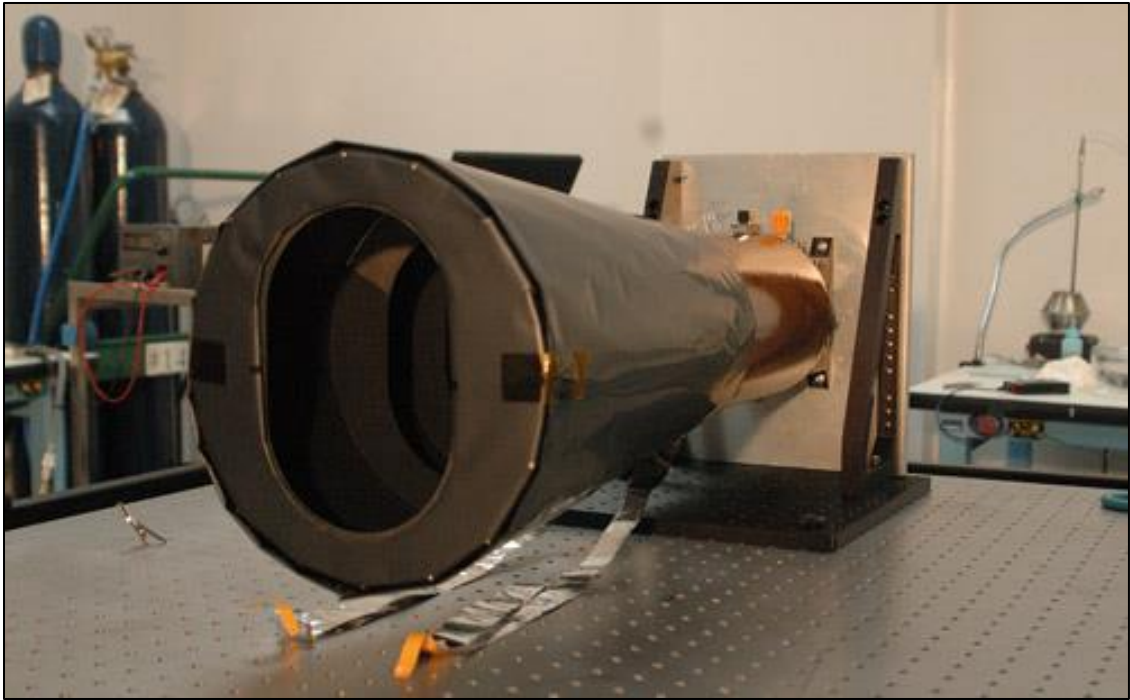


Figure 8: The context camera (CTX) that is currently aboard the MRO before it was assembled on the spacecraft. The CTX camera allows for images to be captured with an average resolution of ~6 meters per pixel (mpp) (From Malin Space Science Systems, 2023).

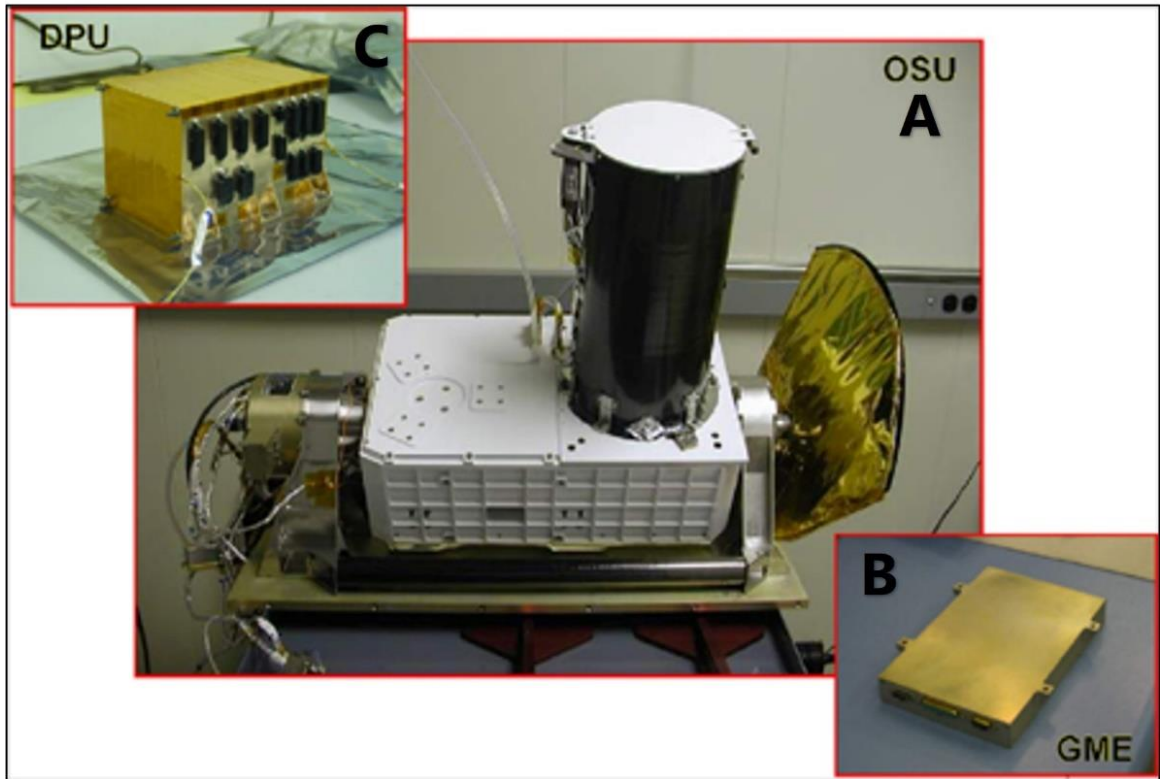


Figure 9: The CRISM instrument in three parts: the (A) Optical Sensor Unit (OSU) which includes optics, a gimbal to remove image smear due to spacecraft movement, two visible and infrared detectors for producing images, and cryocoolers and radiators to cool and to keep the CRISM cold, the (B) Gimbal Motor Electronics (GME), which commands and powers the gimbal, and the (C) Data Processing Unit (DPU), which accepts and processes commands from MRO and accepts data from the OSU to return back to the spacecraft (From NASA/ John Hopkins Applied Physics Laboratory, 2023).

assemblage of minerals, notably sulfate, carbonate, hydroxyl, and other hydrated minerals (Murchie et al., 2007).

All data is publicly available through NASA via the Planetary Data System (PDS), specific datasets used were the global aqueous mineral index (Elhman & Edwards., 2014) and the CTX mosaics generated by the Bruce Murray Laboratory for Planetary Visualization at California Institute of Technology. The global CTX mosaic covers > 99.5% of the surface, concentrated at mid-latitudes, and is comprised of 86,571 separate images co-registered by 3,147,169 control points (Dickson et al., 2023). Global mosaics used were obtained from Astropedia, a public planetary data database that is a combined effort by the USGS and NASA to push public access of planetary data. All analyses utilized geographic information systems (GIS) software, ESRI's ArcMap and Arizona State University's (ASU) JMARS (Java Mission-planning and Analysis for Remote Sensing).

Image and Terrain Analysis

Out of 30 documented chaotic terrains, 19 were chosen based on locality and resolvability in the imagery (Figure 10). Table 1 shows the analyzed chaotic terrains with assigned coordinates and area. Image analysis was done using several CTX mosaics to cover the areas of NL and the 19 chaotic terrains

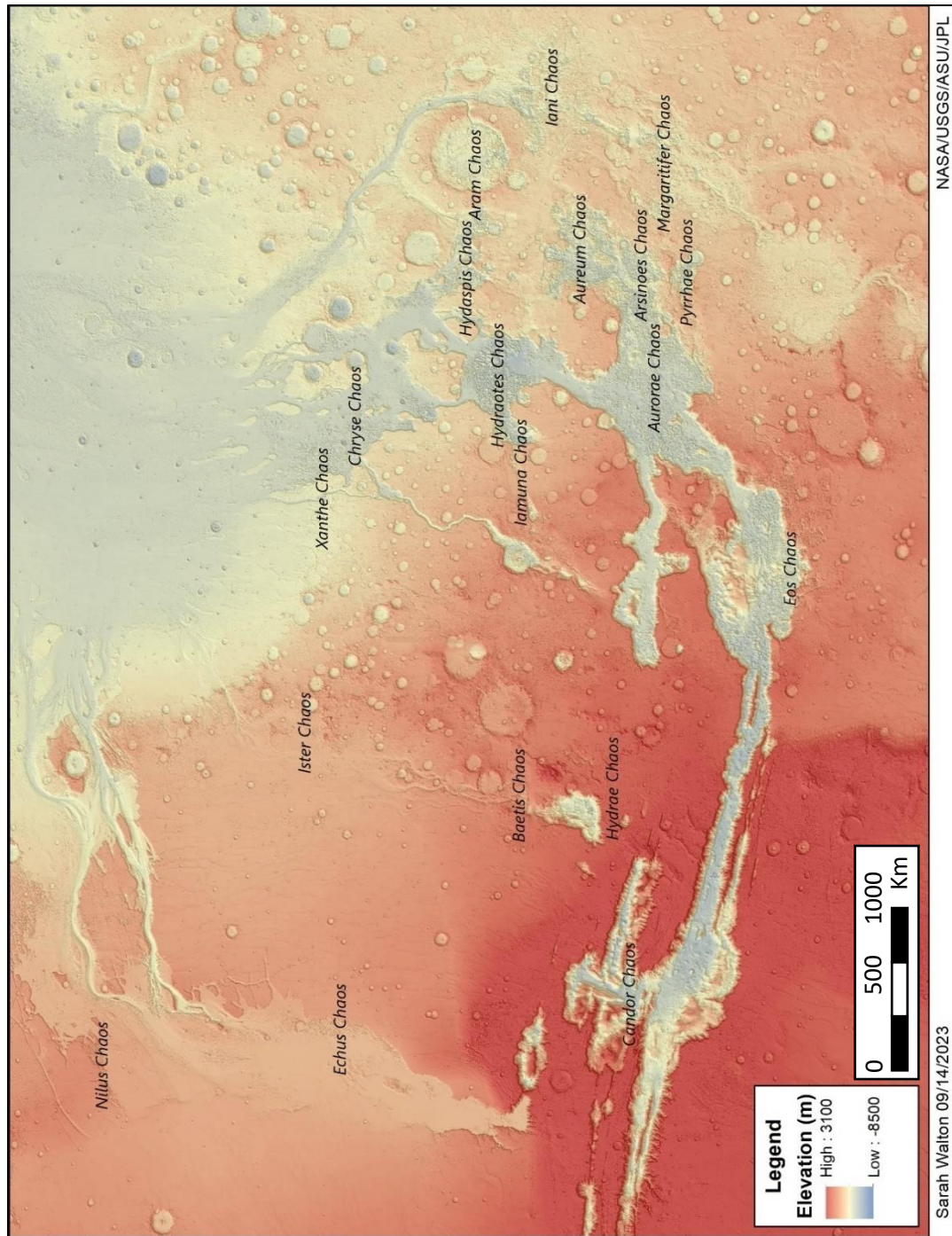


Figure 10: Locations and names of the chaotic terrains analyzed east of the Valles Marineris.

Table 1: Names and locations for the 19 chaotic terrains analyzed.

Chaos ID	Chaos Name	Map Code	Center Longitude (deg E)	Center Latitude (deg N)
1	Aram Chaos	ARA	337.6084	2.5233
2	Arsinoes Chaos	ANO	332.084	-7.6574
3	Aureum Chaos	AUR	333.0366	-3.8947
4	Aurorae Chaos	AOE	325.1851	-8.4693
5	Baetis Chaos	BTS	299.6008	-0.1671
6	Candor Chaos	CDO	287.415	-6.9367
7	Chryse Chaos	CHR	322.8104	9.8646
8	Echus Chaos	ECH	285.281	10.7879
9	Eos Chaos	EOS	313.478	-16.8183
10	Hydaspis Chaos	HYP	333.071	3.0875
11	Hydrae Chaos	HDE	300.0262	-5.9023
12	Hydraotes Chaos	HYT	324.7085	1.1179
13	Iamuna Chaos	IMU	319.3896	-0.2825
14	Iani Chaos	INA	342.958	-2.1921
15	Ister Chaos	IST	303.4371	12.9536
16	Margaritifer Chaos	MRG	338.2954	-9.3015
17	Nilus Chaos	NLU	283.0453	25.3871
18	Pyrrhae Chaos	PYR	331.6006	-10.4609
19	Xanthe Chaos	XNT	317.7831	11.874

analyzed. Mosaics were used to characterize major geomorphologies seen in both regions and to investigate unique local geologic features. The image mosaics have a ~5mpp resolution, where each pixel is about the size of a typical vehicle parking space in the United States. Within NL, CTX images were used to digitize troughs and mesas as polygons in ArcMap. Images were individually inspected for geologic features and trends, which were used for comparative geomorphic analysis across NL and the chaotic terrains.

Topographic Analyses

Topographic analysis was conducted with topographic profiling and slope analyses. Topographic profile lines and plots were generated with JMARS using MOLA 200m DEM at 128 ppd for each profile. Topographic profiling of the 200mpp MOLA DEM was used for comparison of elevation contrast between localities within NL and the chaotic terrains, and as a metric to compare elevation profiles with certain morphologies seen on the surface. Plots for NL and the 19 chaotic terrains attempted to maintain scale respectively, where all profiles for NL maintain the same scale and all profiles for the chaotic terrains maintain scale.

Slope rasters were generated from the MOLA 200m DEM using ESRI's ArcMap and symbolizes six slope classifications from 0-2, 2-5, 5-15, 15-25, 25-45, and 45-60 degrees to visualize dramatic changes in slope. No slopes of

greater than 60 degrees were found within the study areas, thus slope breaks were defined to exclude these values. Maps of slope values were displayed with a THEMIS IR Day 100mpp basemap. Individual slope rasters were reclassified to reflect the six slope breaks defined above using ArcMap's reclassify raster tool. The reclassified raster was then converted to a multi-polygon shapefile using the raster to polygon tool. This was done to quantitatively assess and compare the percent area of each slope break between NL and the chaotic terrains.

Lineament Analyses

A comparative lineament analysis was performed on the linear morphology of NL and several chaotic terrains. A THEMIS IR Day 100mpp basemap was used to insure accurate interpretation at a continuous large scale. Lineaments interpreted could be classified as continuous troughs, fractures or other linear geomorphic features and were classed as polylines within ArcMap. The length of the line in meters and orientation in azimuth was recorded. This process was done for both NL and each of the 19 chaotic terrains selected for analyses. Azimuth was restricted to 270 – 360 and 0 – 90 degrees or quadrants 1 and 4 on a typical rose diagram plot using a basic python restriction of the data using ArcMaps' built-in python functions. Completed lineaments for each site were exported into .csv files and imported into Rick Allmendinger's Stereonet 11

for orientation analyses. Within Stereonet, half-rose diagrams were generated to show preferred orientation of lineaments with respect to North.

Statistical analyses of lineament data from all sites were done using a two sample Kolmogorov Smirnov test, a statistical test that measures the dissimilarity of two samples if the samples were to be drawn from the same probability. This was performed using a simple python script, leveraging pandas and scipy packages for reading and analyzing the data, and seaborn, a matplotlib wrapper, to visualize the result of the analyses. The script is as written below:

```
import pandas as pd
```

```
import seaborn as sns
```

```
import scipy
```

```
PATH = r'/path/to/my/dataset.csv'
```

```
COLUMN1 = 'my_first_column'
```

```
COLUMN2 = 'my_second_column'
```

```
data = pd.read_csv(PATH)
```

```
result = scipy.stats.ks_2samp(data[COLUMN1], data[COLUMN2])

result.pvalue # if this is less than 0.05, two samples are significantly
different at the alpha = 0.05 level
```

```
# to plot
```

```
variable_name = 'Lineaments'
```

```
value_name = 'Azimuth'
```

```
tmp = pd.melt(data[[COLUMN1, COLUMN2]], value_vars = [COLUMN1,
COLUMN2]).rename(
```

```
columns = {'variable': variable_name, 'value': value_name})
```

```
tmp.head()
```

```
sns.kdeplot(tmp, x = value_name, hue = variable_name)
```

Hydrated Mineral Mapping

Two hydrated mineral maps of NL and the chaotic terrains were produced from the Ehlmann and Edwards (2014) global aqueous mineral distribution data set. This data set was derived from CRISM observations and globally compiled into a point data set. The point data was brought into ArcMap and displayed on a MOLA 200M DEM and hillshade basemap, using three symbologies to represent different mineral composition observations. The three hydrated minerals displayed were hydrated phyllosilicates, silica, and sulfates.

When comparing NL and the chaotic terrains, the presence of hydrated minerals in general points to a history of fluid interaction within the region. This was qualitatively performed to analyze the presence of hydrated minerals and determine what type, if any, were present. Observations of hydrated sulfates could point to a more sulfate-rich deposition history within each locality. Similar premise stands when looking for hydrated phyllosilicates, where silica-rich material came into contact with fluid.

RESULTS

Image and Terrain Analysis

Characterization of general geomorphology for NL yielded five major categories: troughs, mesas, faults, pits and pit chains, and craters.

Troughs are identified as wide, relatively-flat, low-lying areas between mesas, where some of the most notable geomorphic features of NL are exposed within trough floors. Collapse material, such as boulder fields and major sediment cover, is prominent with proximity to the trough walls. Figure 11 shows digitized troughs found within NL. For the purposes of this research, troughs were only characterized as such if they had major depth differences and showed significant widening of the troughs. The evolution of troughs increases grid-east towards the Valles Marineris transition zone. Evolution is a qualitative function of depth and width, where a deep and wide trough would be classified as evolved and a shallow, slim trough would be classified as unevolved.

Within the troughs, two major types arise, smooth troughs, where dust cover and sediment dominate, creating smooth trough floors with dune fields common (Figure 12). The other type of trough is more common, where the trough floors are exposed and feature rough floors, where each rough trough exhibits

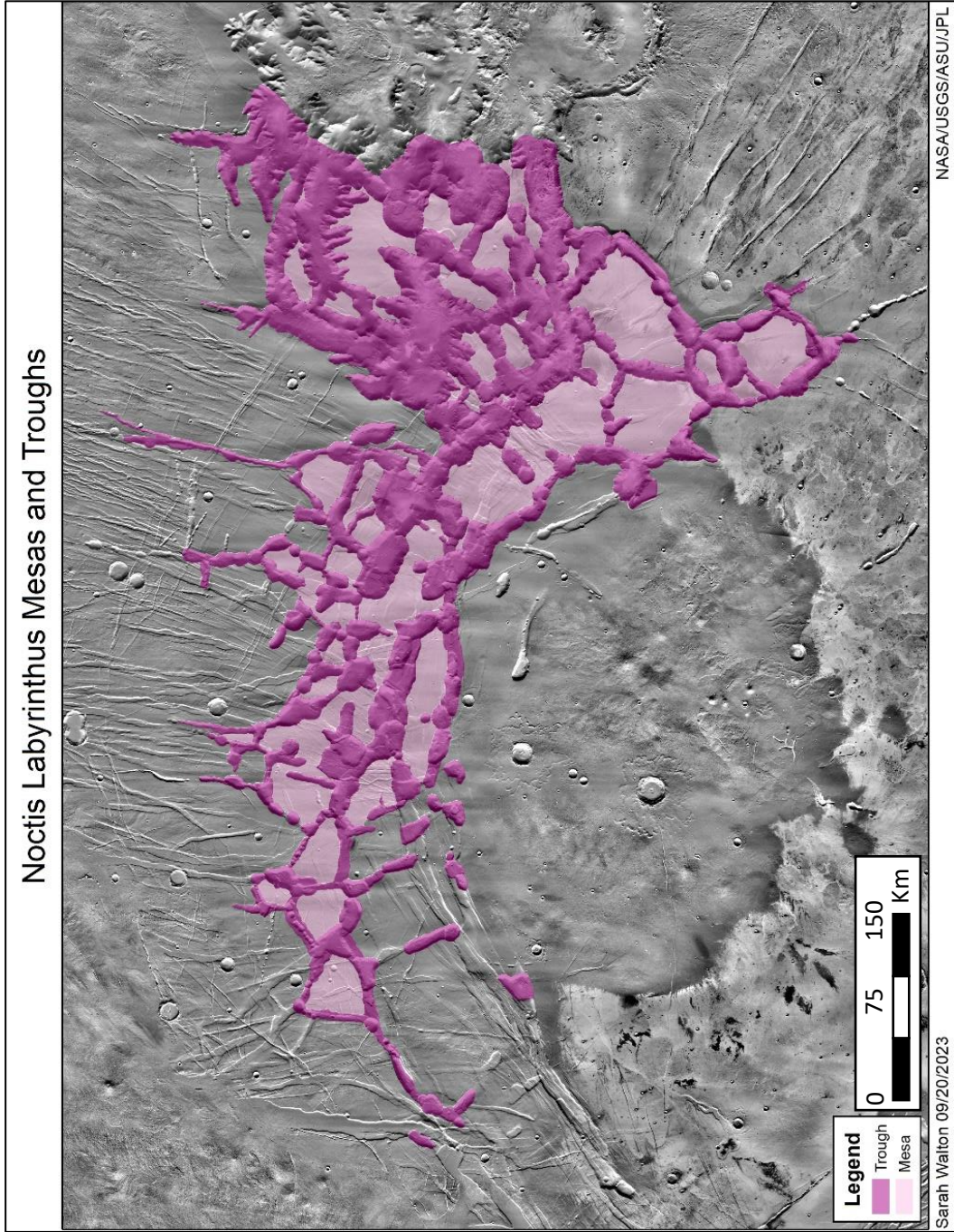


Figure 11: Digitized troughs and mesas within NL. Troughs are represented by low elevation areas bounded by mesas; mesas are represented by high elevation flat-topped plateaus.

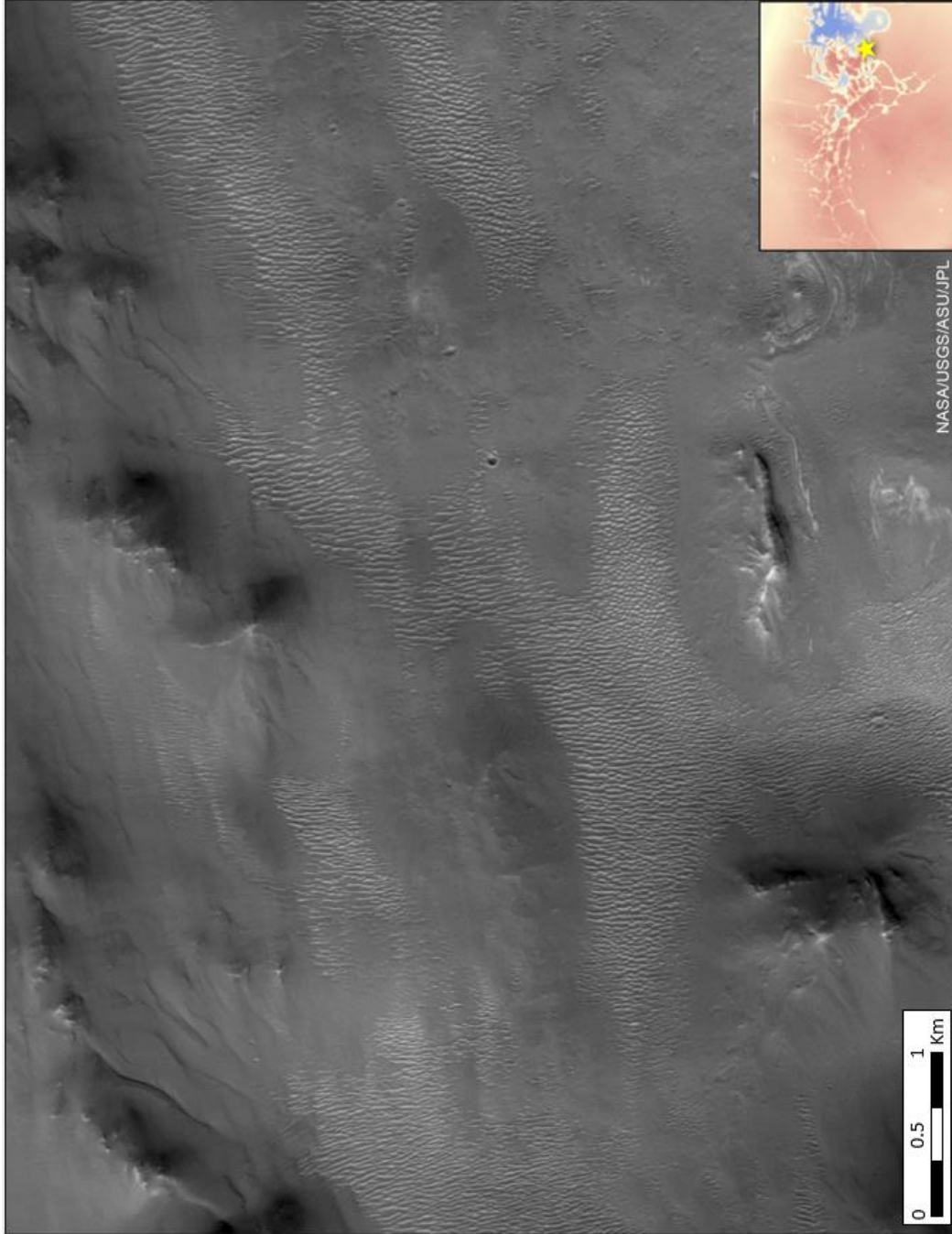


Figure 12: Smooth trough floors within NL. Dune structures are common due to extensive eolian processes occurring in recent geologic times.

unique morphology. Most rough floors show common exposed layered or scattered LTD's (Figures 13 - 16). Other interpreted morphologies include patterned ground and collapse features possibly due to solutional processes (Figure 17). Patterned ground is interpreted as periglacial in origins, where the upper cryosphere went through periods of thaw and re-freeze cycles (Figure 18).

Mesas are high ground terrain features that bound troughs (Figure 11). Mesas are typically flat and wide, showing some overprinting of grabens where collapse has not been induced. Mesa walls are layered at most localities with a hard dark cap rock, various pyroclastic and lava flow deposits, and LTD's.

Faults are linear non-circular features trending in a certain orientation. Normal faults are most common within NL, where two normal faults will create a drop-down block between faults also known as a graben. Faulting within NL follows preferential directions to the NW, NNE and NE. Figure 19 shows an example of an un-evolved graben, which is different from evolved troughs based on width and depth of the trough.

Pits and *Pit Chains* are flat circular features that lack a raised rim, where some pit chains appear to be forming new troughs on the outskirts of NL (Figure 20). Some pit chains follow trough directional trends, while others appear random in nature. Pits are interpreted as collapse features, where subsurface material was removed along a preferential orientation to create pits.

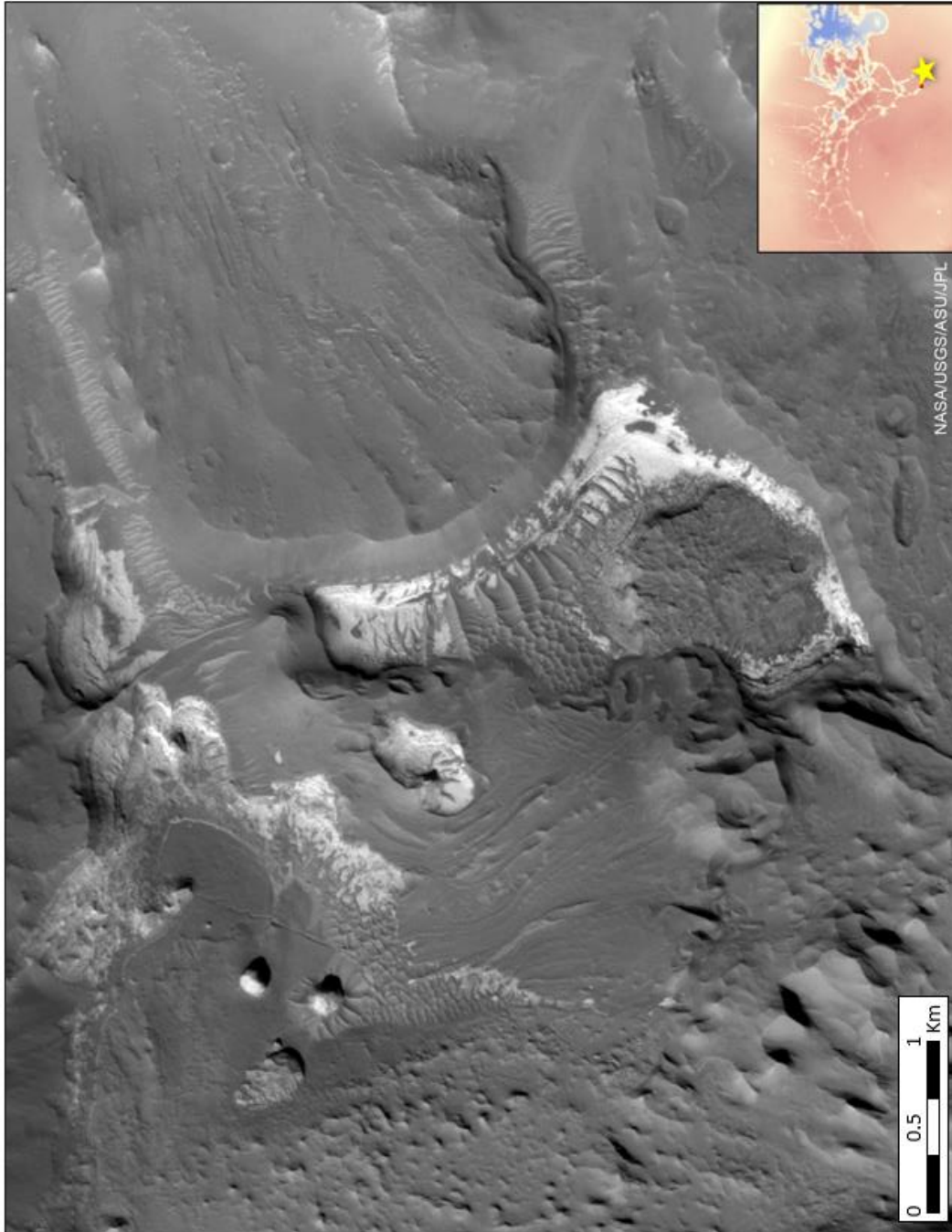


Figure 13: Scattered LTD within a trough floor.

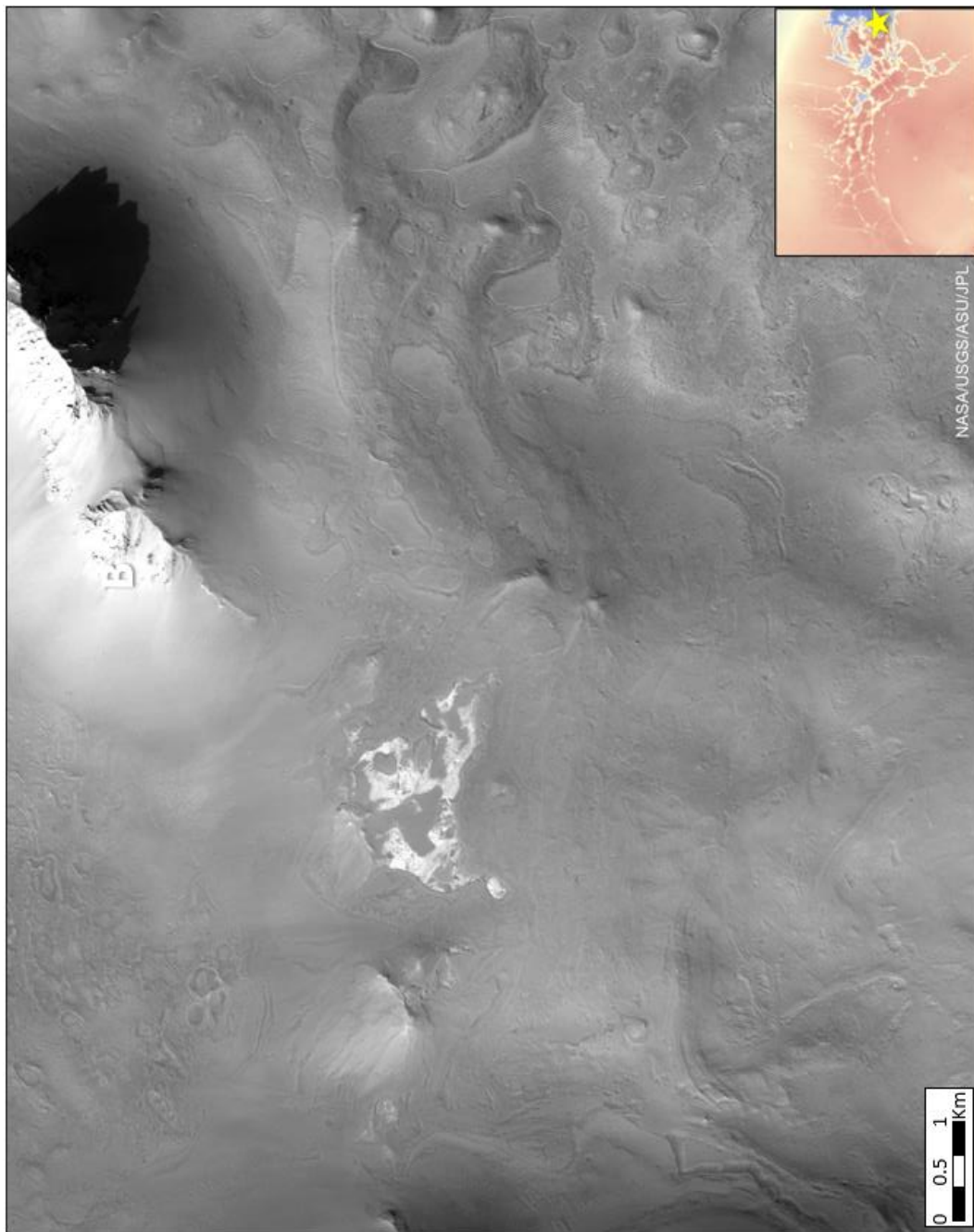


Figure 14: Layered and scattered LTD's in a trough floor associated with patterned ground. Slump debris (boulders) are seen to the west and interpreted solifluction lobes to the east.

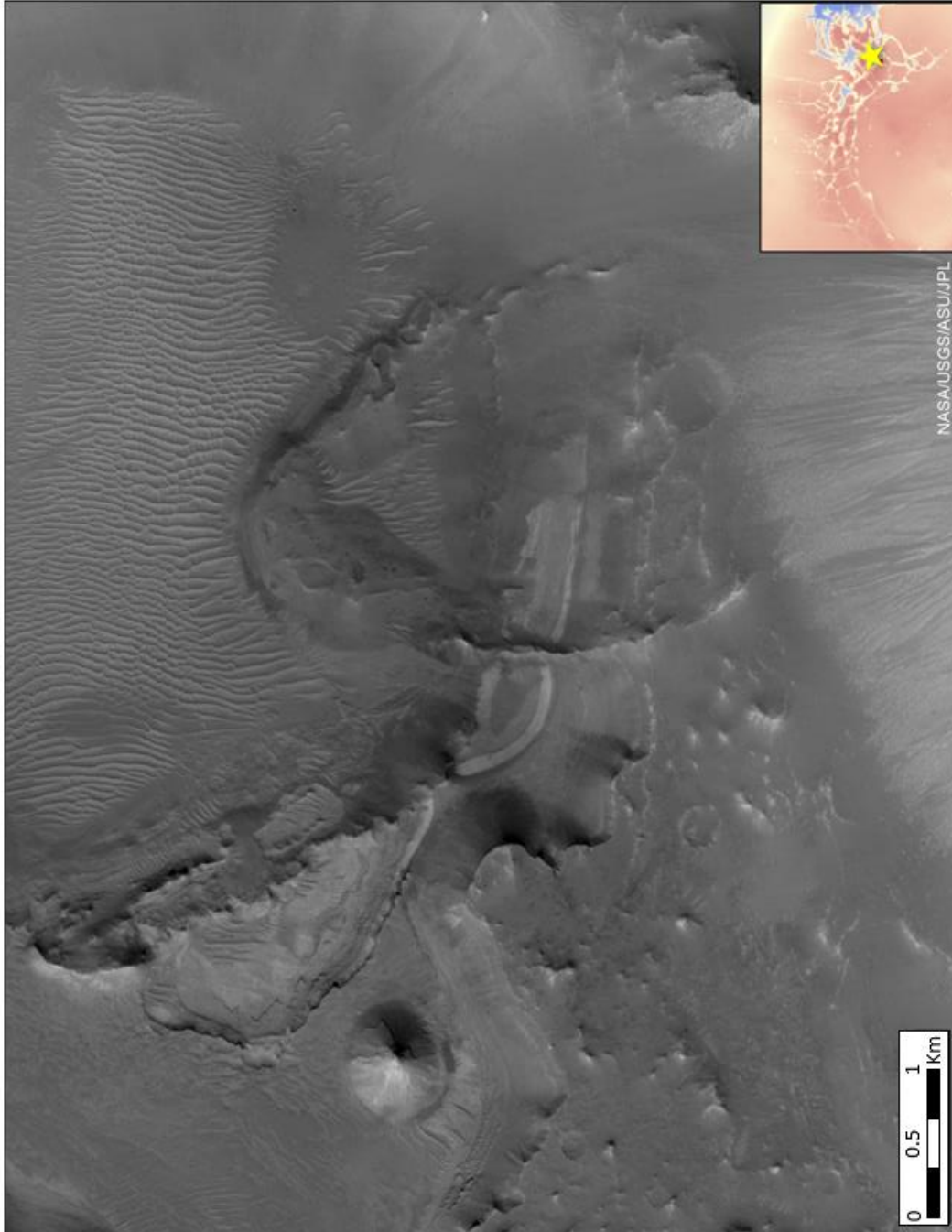


Figure 15: Layered LTD's within a trough wall and associated patterned ground seen at the top of the layers, showing peaks of LTD's.



Figure 16: Layered LTD's in a stratified mesa wall, this stratigraphic pattern is common throughout NL.

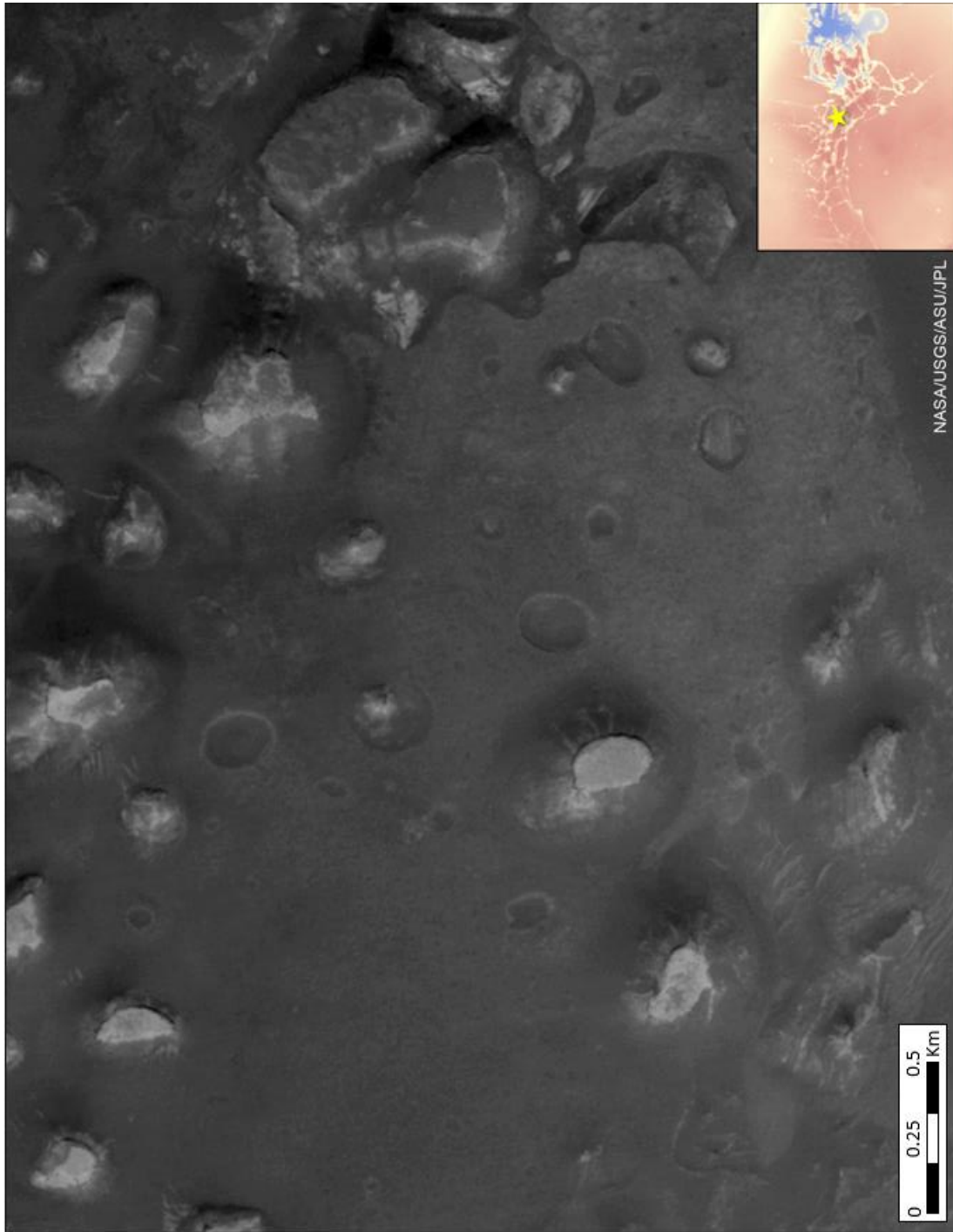


Figure 17: Interpreted solutional holes within a trough in NL.

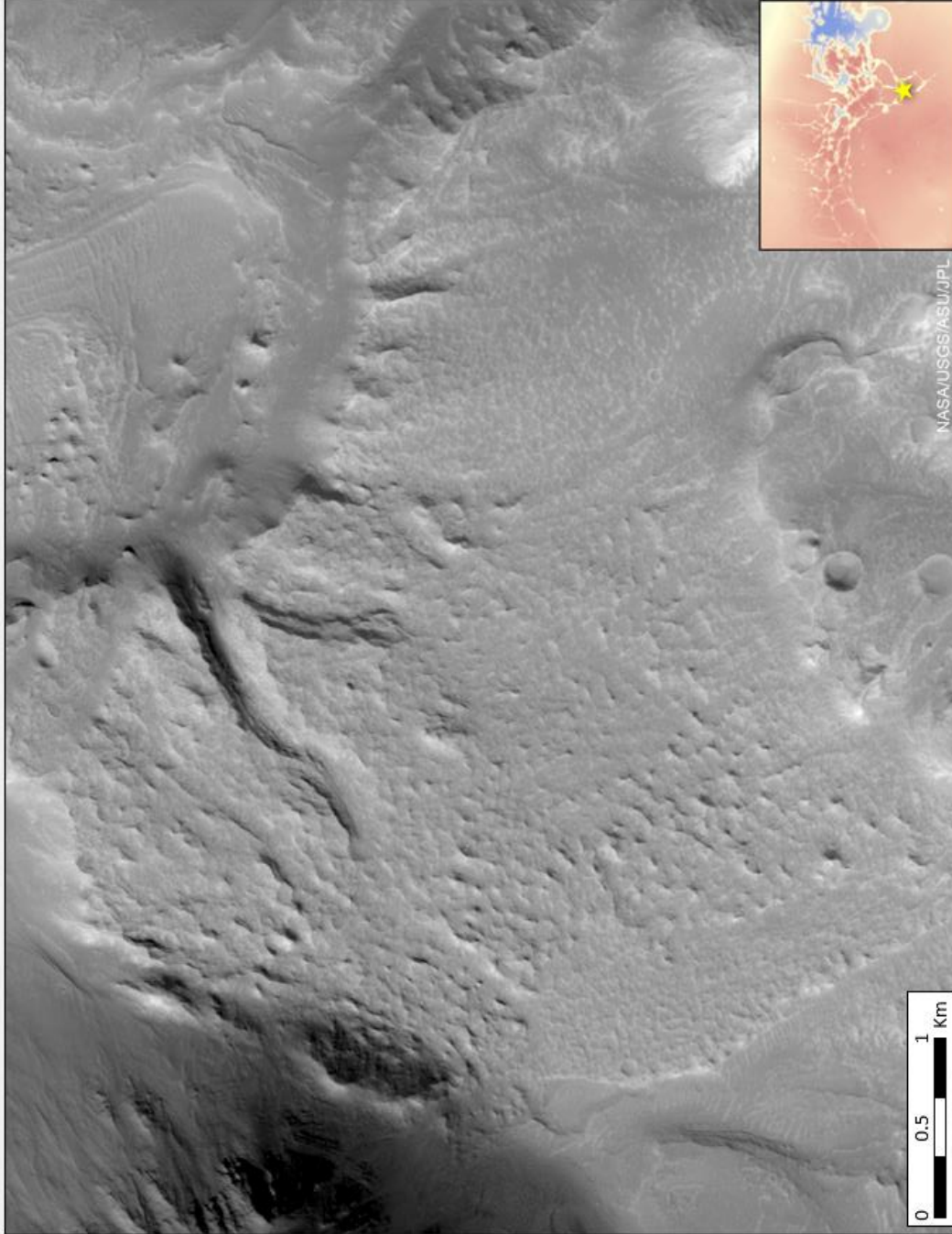


Figure 18: Interpreted patterned ground within NL, patterned ground is a periglacial morphology, a result of thawing and re-freezing of permafrost near the surface.

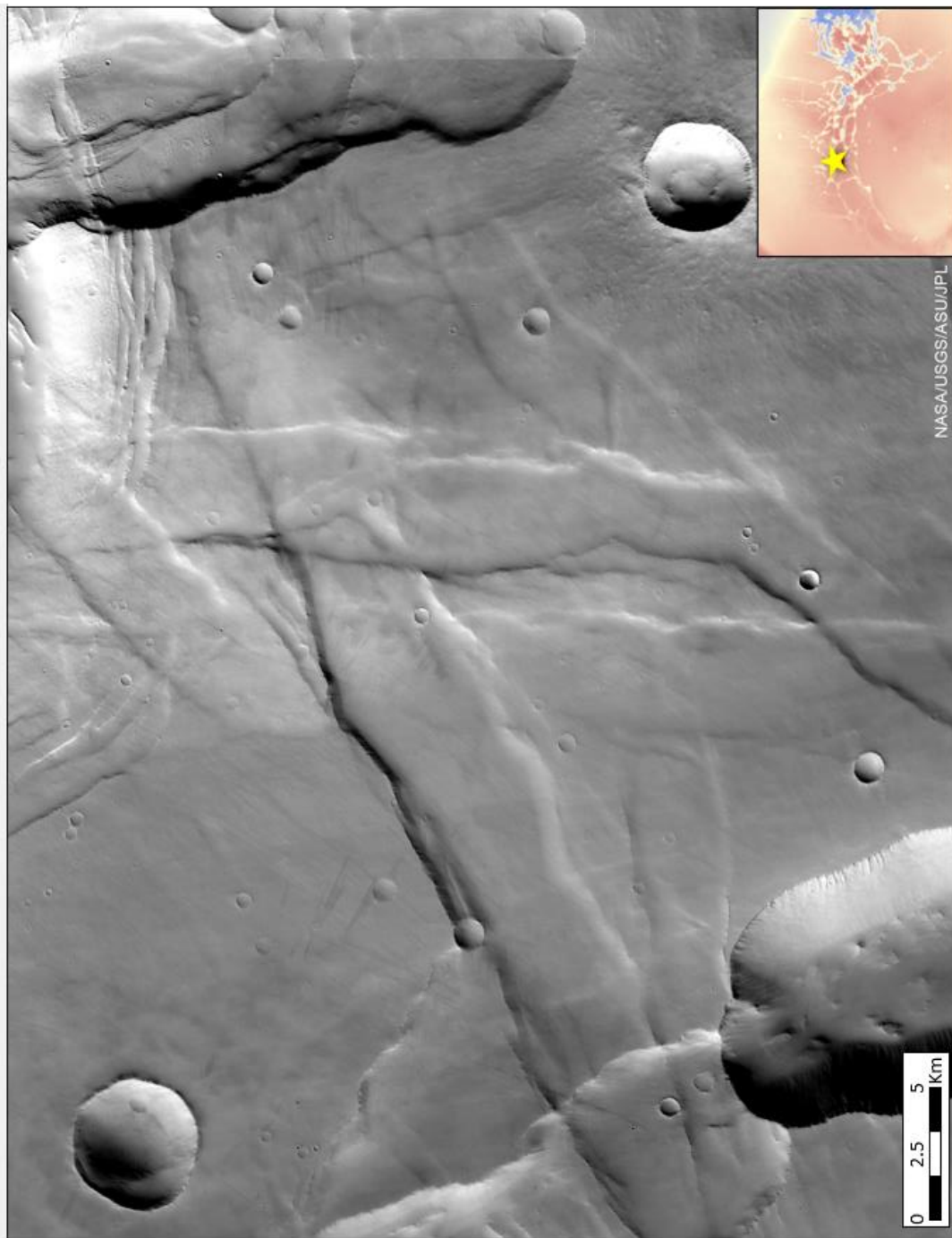


Figure 19: Un-evolved graben in western NL.

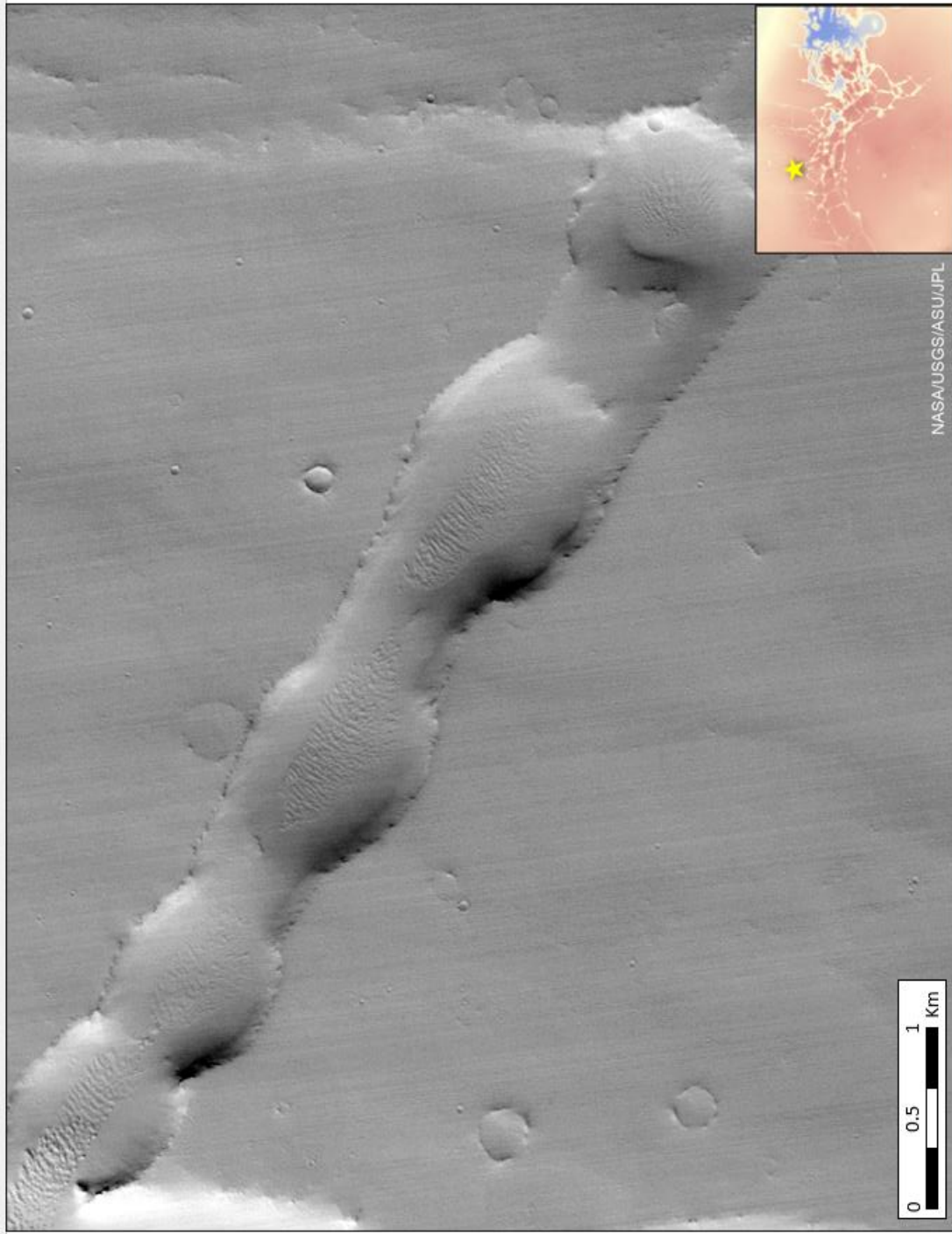


Figure 20: Example of a pit crater chain forming a new trough within NL.

Craters are rimmed (usually) symmetrical circular features, where large complex craters feature flat floors and a central high point where isostatic rebound occurred post- impact (Figure 21). Craters are common throughout Noachian Southern Highland terrain, a remnant of the LHB period of the solar system. Ejecta is sometimes present within fresh craters but because of the amount of sediment transportation on the surface of Mars, infill is common.

Major morphologies found within the analyzed chaotic terrains are placed into four broad categories: mesas and knobs, floors, fractures, and craters.

Mesas and *knobs* are blocky and indistinct high elevation terrain features, where mesas have a more distinct flat plateau and knobs have peaked caps (Figure 22). Mesa size can be closely related to spatial position, where larger mesas seemed to be grouped together, which could be largely a product of differential weathering or spatial degree of degradation of material. Many knobs appear to be capped with LTD's and LTD's can be found layered in mesa walls (Figure 23).

Chaos floors are low elevation features where floors can be trough-like low points between mesas and knobs or flat, open areas of terrain. Within the chaos floors, patterned ground is found at numerous localities and can expose LTD's in a polygonal shape at the surface (Figures 24 – 26). The chaos floor also



Figure 21: Large crater on the margin of NL, rough terrain surrounding the crater is the blanket ejecta, common of large and young craters. Craters are common within NL terrain and are distinguished by their raised rim and symmetrical nature.

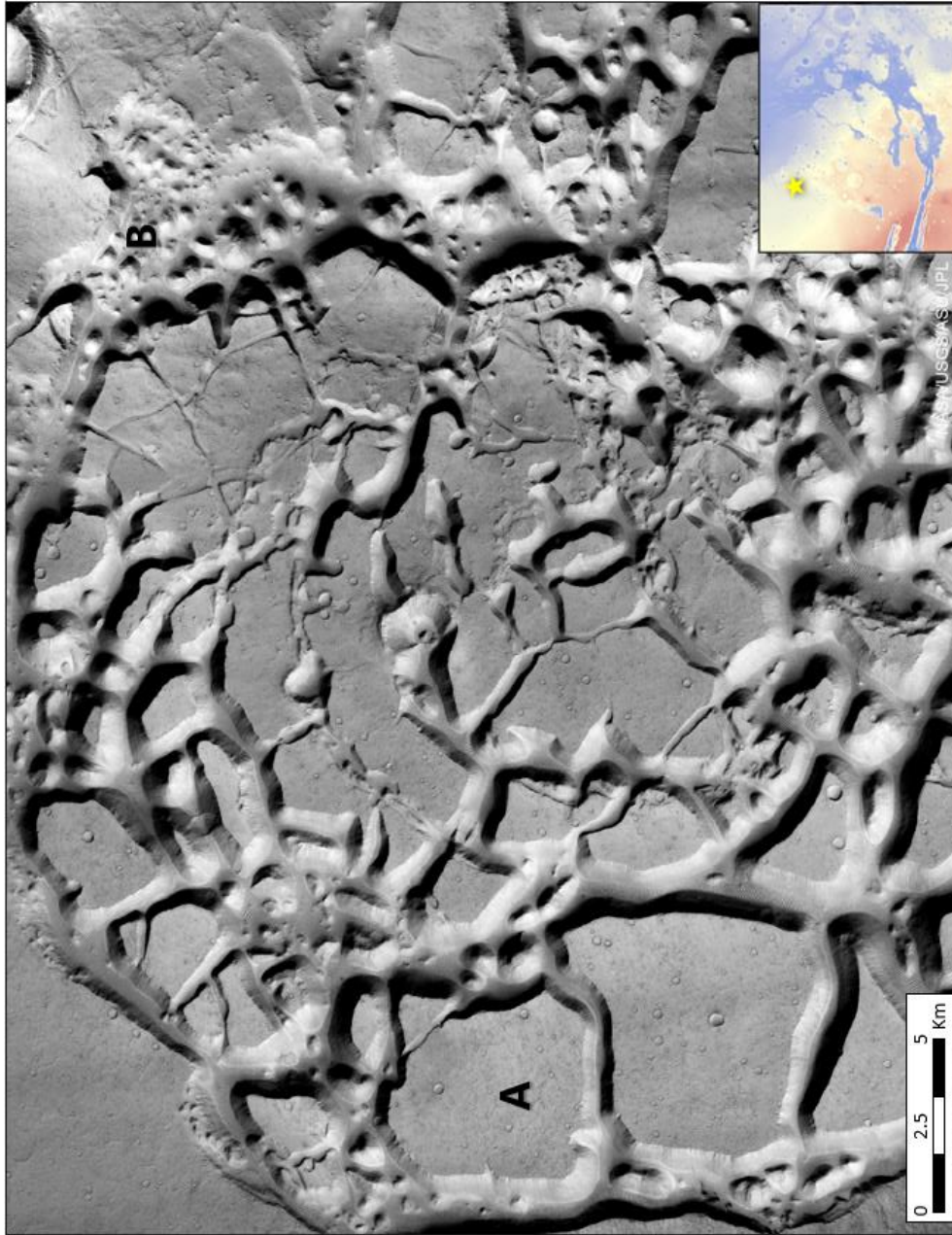


Figure 22: Differences in morphology between mesas and knobs within Ister Chaos. (A) Mesas are flat plateaus of high elevations, whereas knobs (B) appear to have undergone a different degree of erosion where the high elevation is peaked with a cap and lacks a flat area.

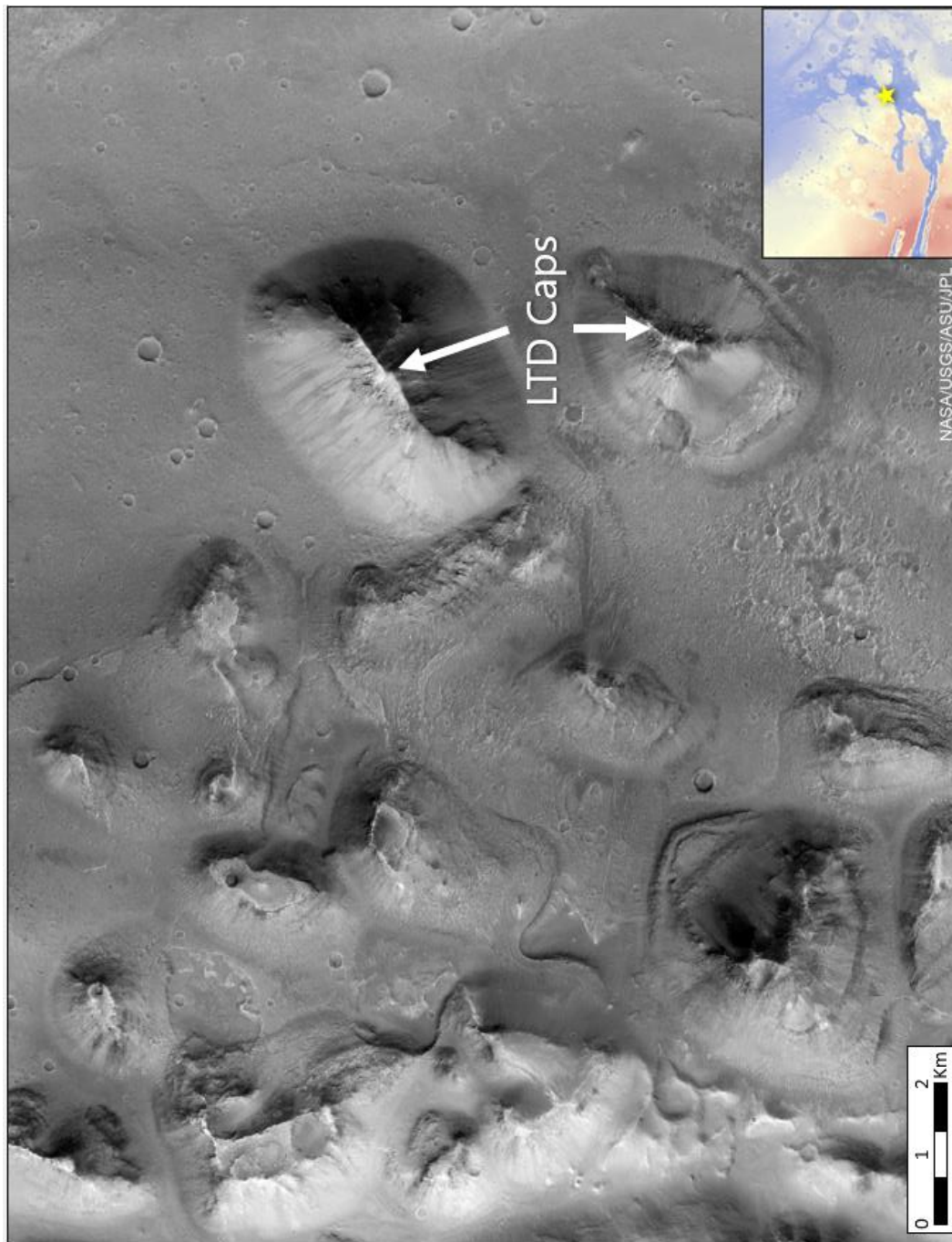


Figure 23: Knobs within Aurorae Chaos capped with LTD. LTD caps and layered deposits are common within chaotic terrain knobs. Within the floor of this image, pattered ground is seen to the

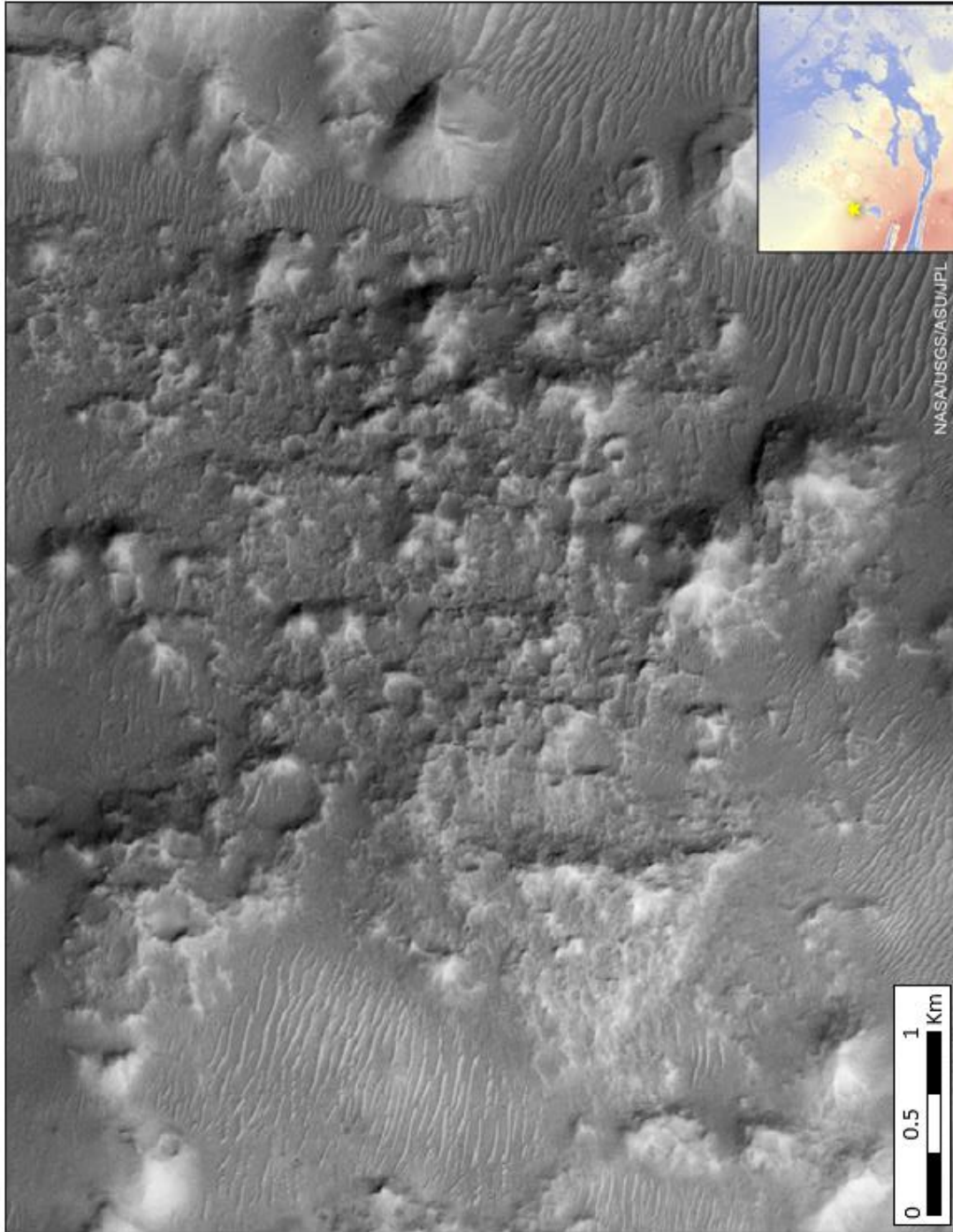


Figure 24: Interpreted patterned ground in Baeis Chaos

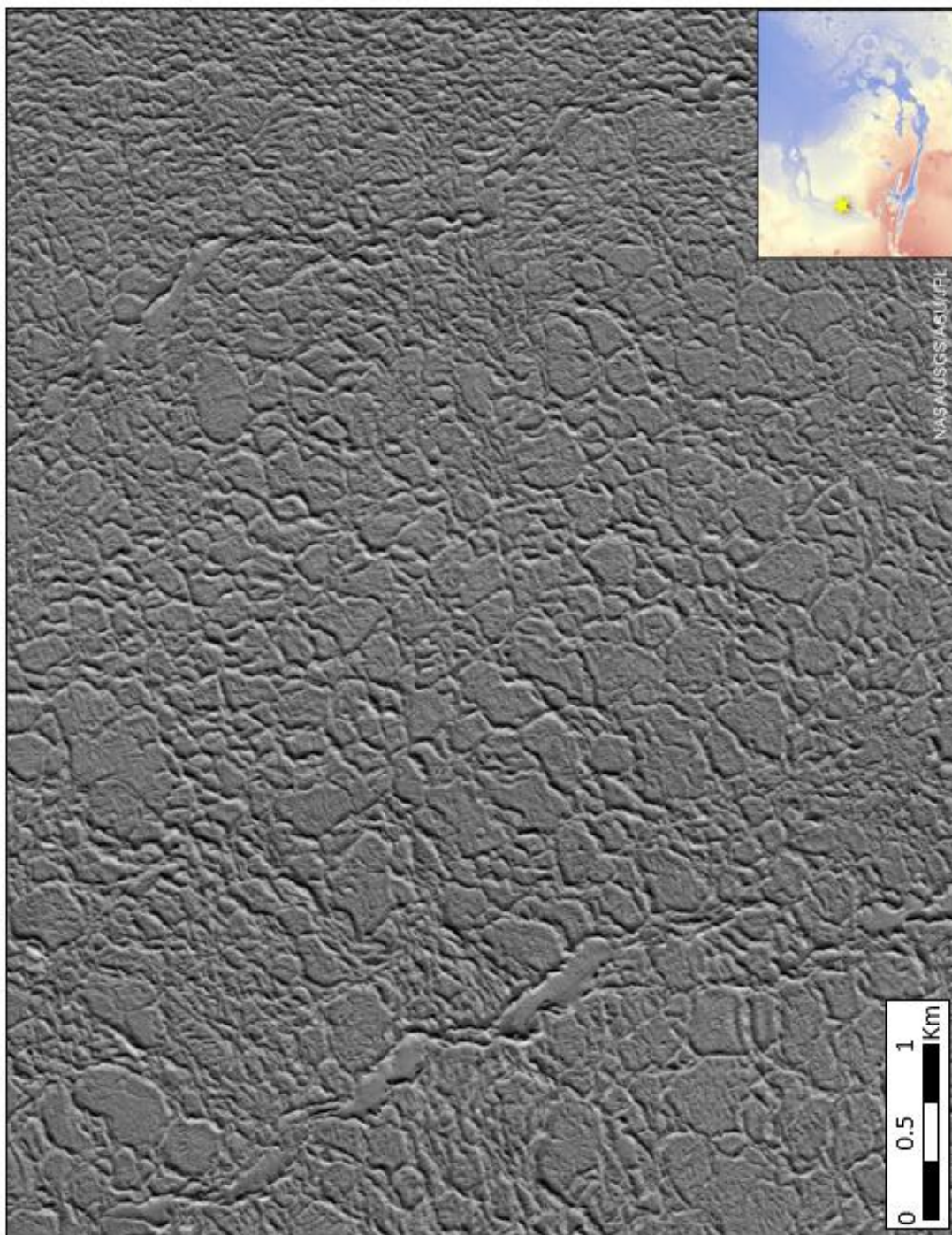


Figure 25: Unusual textured ground outside of Echus Chaos

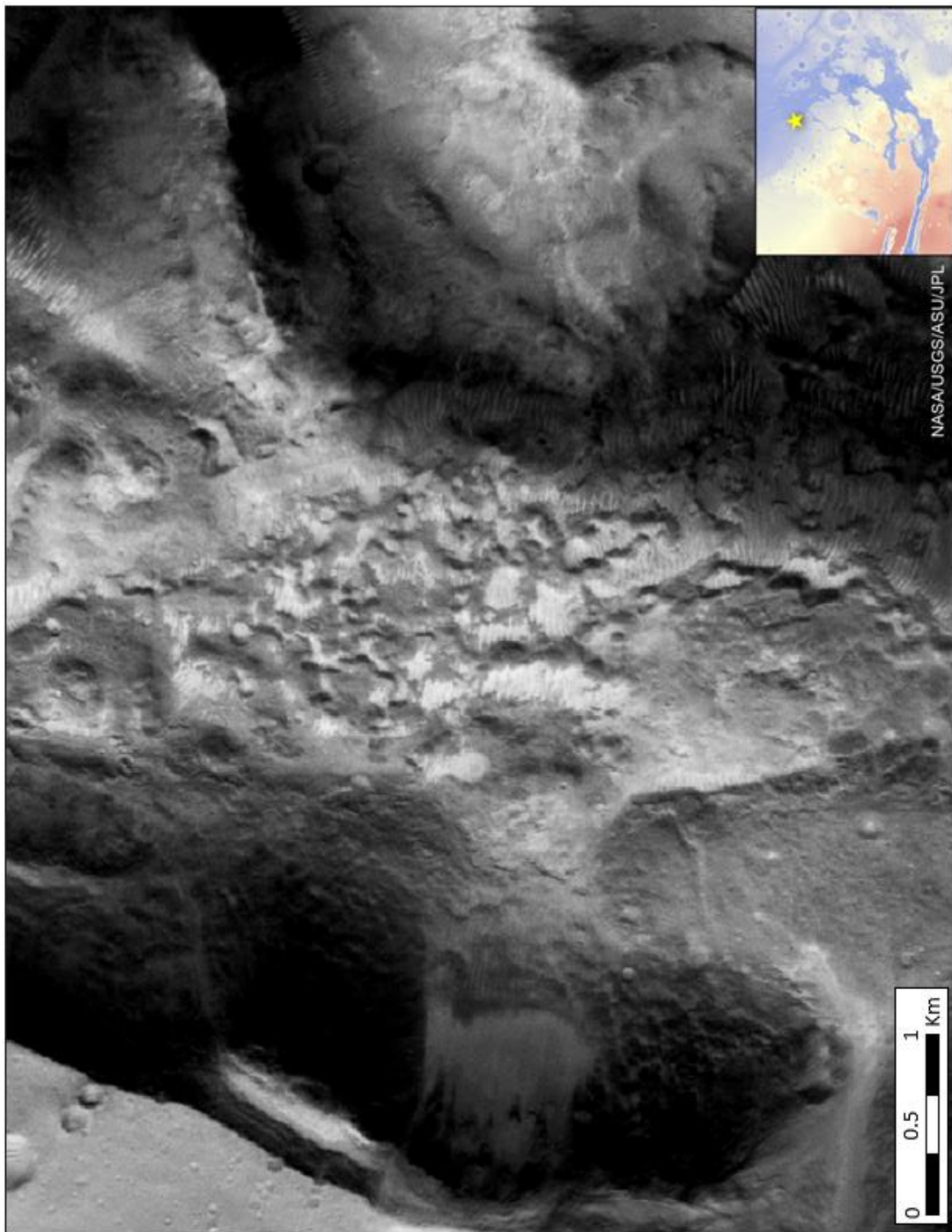


Figure 26: Patterned ground within Xanthe Chaos infilled by LTD's.

shows evidence of induced massive fluid flow across multiple chaotic terrain floors, where floors can show flow scarps in a directional preference (Figure 27).

Both the mesas/knobs and floors within chaotic terrain show evolved collapse structures, such as subsidence-induced collapse pits and pit chains (Figure 28). Figure 29 shows interpreted collapsed mesas, seen in Candor Chaos.

Fractures are caused by outbreak and collapse events and are not heavily influenced by regional tectonic processes. These are found throughout the chaotic terrain and have no preferential fracture orientation. Chaotic terrains toward the west (Echus Chaos and Nilus Chaos) appear to be more geomorphologically-controlled by surficial faulting than the remainder of the chaos (Figure 30).

Craters are also found within the chaotic terrains, as seen in most Noachian age, southern highland terrain, the description remains the same from the NL morphological classification.

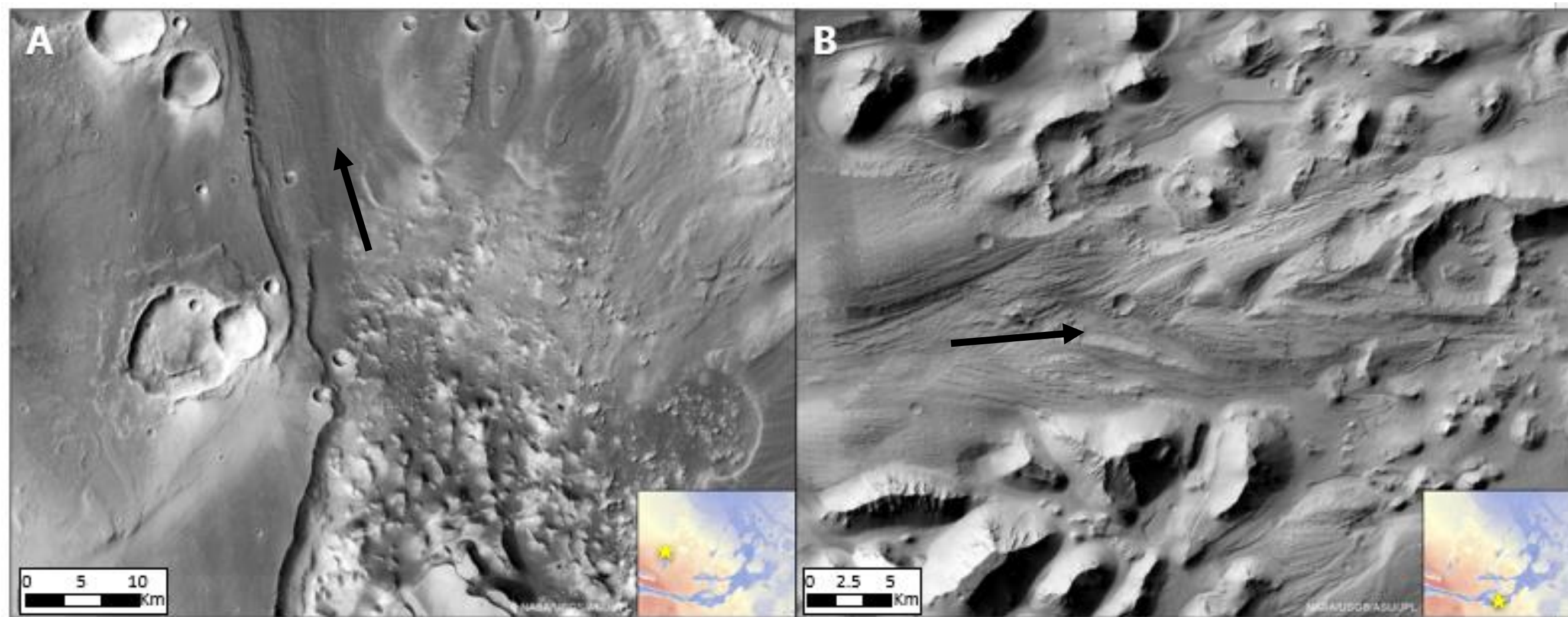


Figure 27: Outflow channel examples along chaotic terrain floors in (A) Baetis Chaos and (B) Eos Chaos with flow directions labeled.

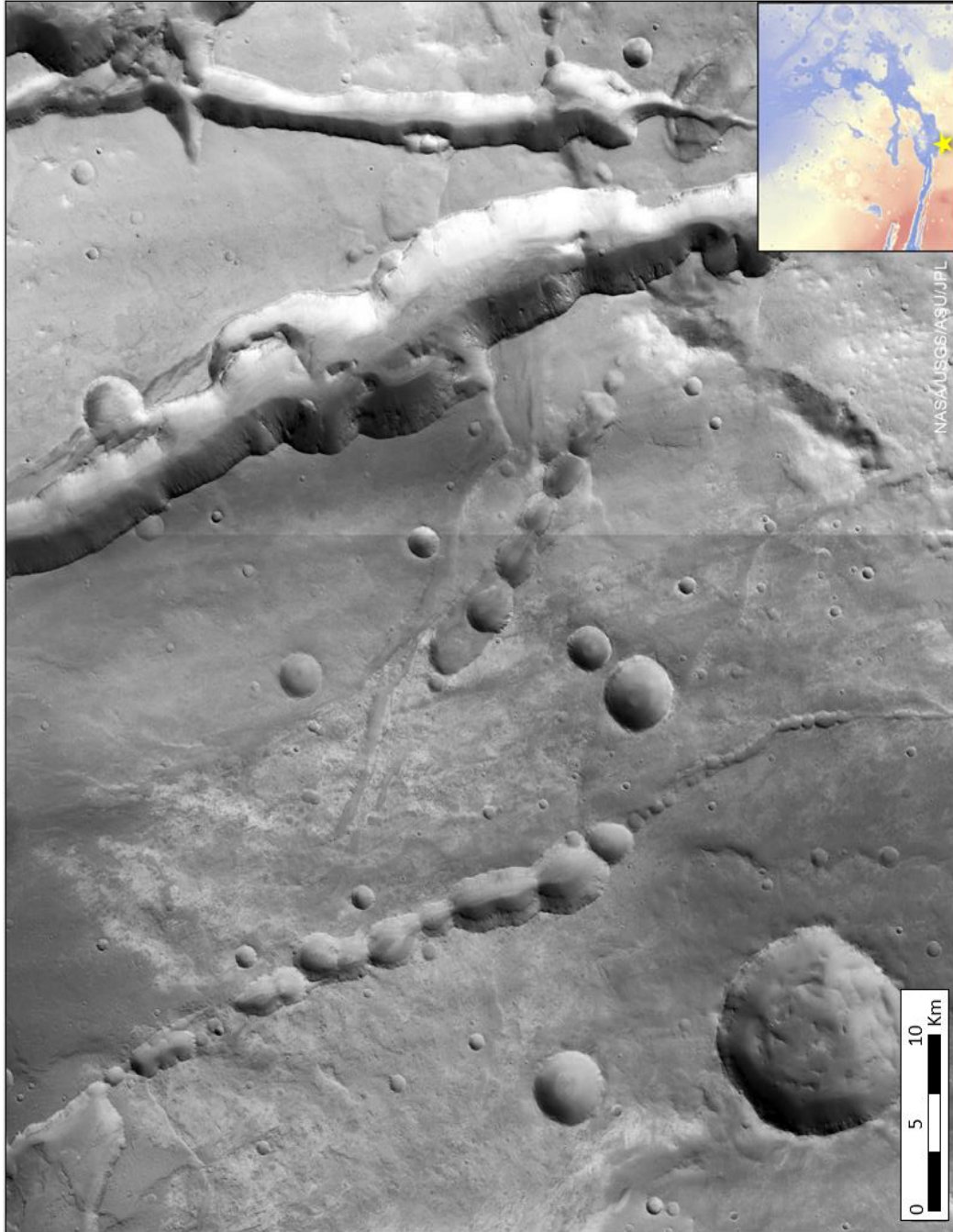


Figure 28: Pit crater chains seen outside of Eos Chaos. Pit craters and pit chains are found throughout the chaotic terrain, similar to morphology seen in NL.

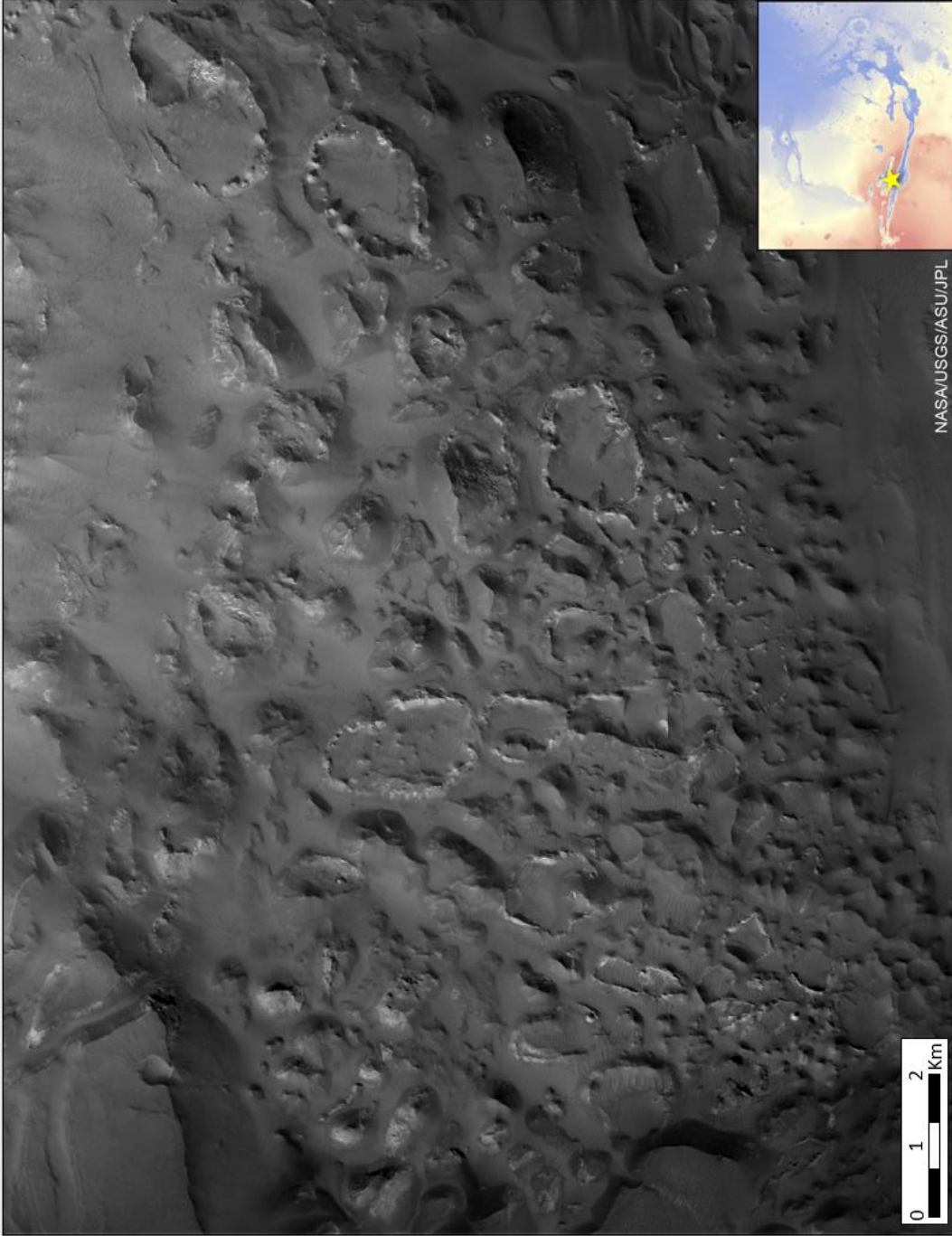


Figure 29: Interpreted collapsed mesas within Candor Chaos. LTD rims surround polygonal shapes that show similar spatial patterns to in-tact mesas but appear to be collapsed

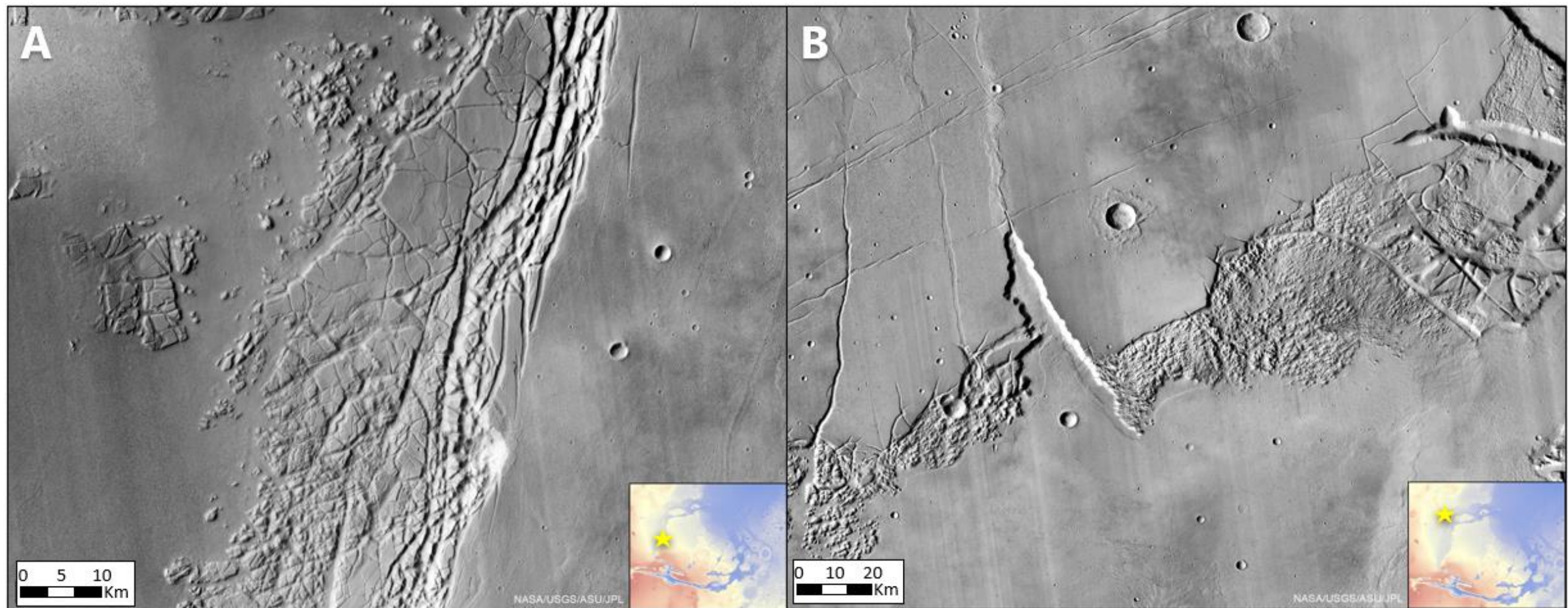


Figure 30: (A) Echus Chaos and (B) Nilus Chaos, appear to be more structurally controlled than other analyzed chaotic terrains toward the east.

Topographic Analysis

Elevation

Topographic profiles were conducted for both NL and the 19 chaotic terrains analyzed (Figure 31). Profiles are seen in Figures 32 through 73. NL plots show distinct changes in elevation reflecting the characteristic morphology of the troughs and plateaus of NL (Figures 32 – 35) with a maximum elevation change of ~ 5,000m between the top of the plateau to bottom of the trough (Figure 33). It is of note, troughs near the west limb of NL (towards Tharsis Montes), show a significantly smaller elevation relief from top of the mesa to bottom of the trough. Topographic profiles of chaotic terrains yield small scale similarities to NL morphology. With a maximum difference over profiles taken of ~2,500m in a preserved site with distinct mesas. High peaks in elevation are classified as mesas within the terrains and followed by steep elevation drops into the chaos floor. Profiles in the chaotic terrains are less pronounced and show less dramatic changes in elevation between mesas and troughs. Mesas are also more infrequent, where most of the chaotic terrains analyzed are bulk trough morphology. Smaller chaotic terrains fail to show distinct topographic change due to the coarse resolution of input data (MOLA 200mpp DEM), and the need to preserve scale over observable features.

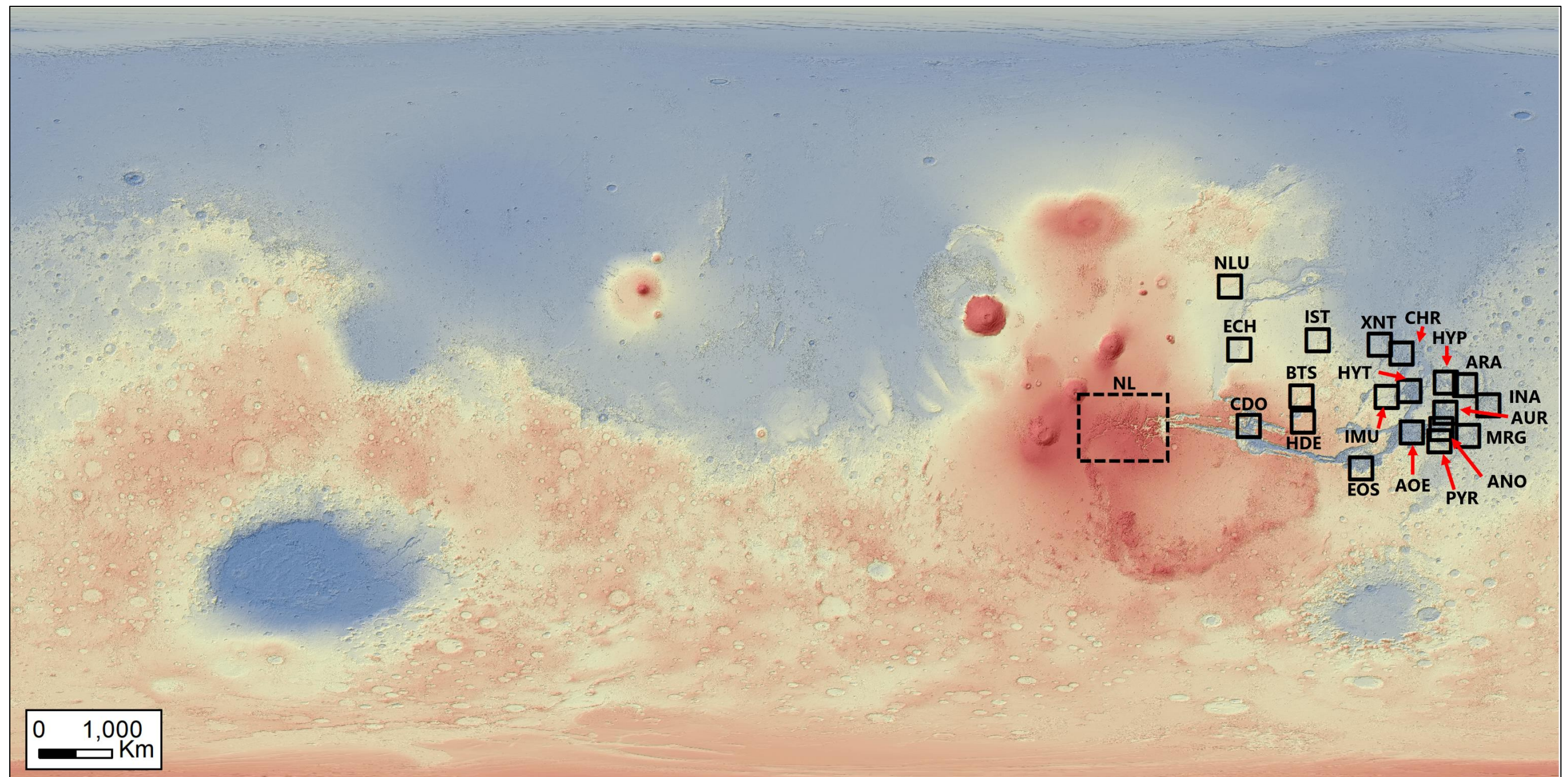


Figure 31: Location of NL (dashed box) compared to the 19 analyzed chaotic terrains (solid boxes) on the surface of Mars.

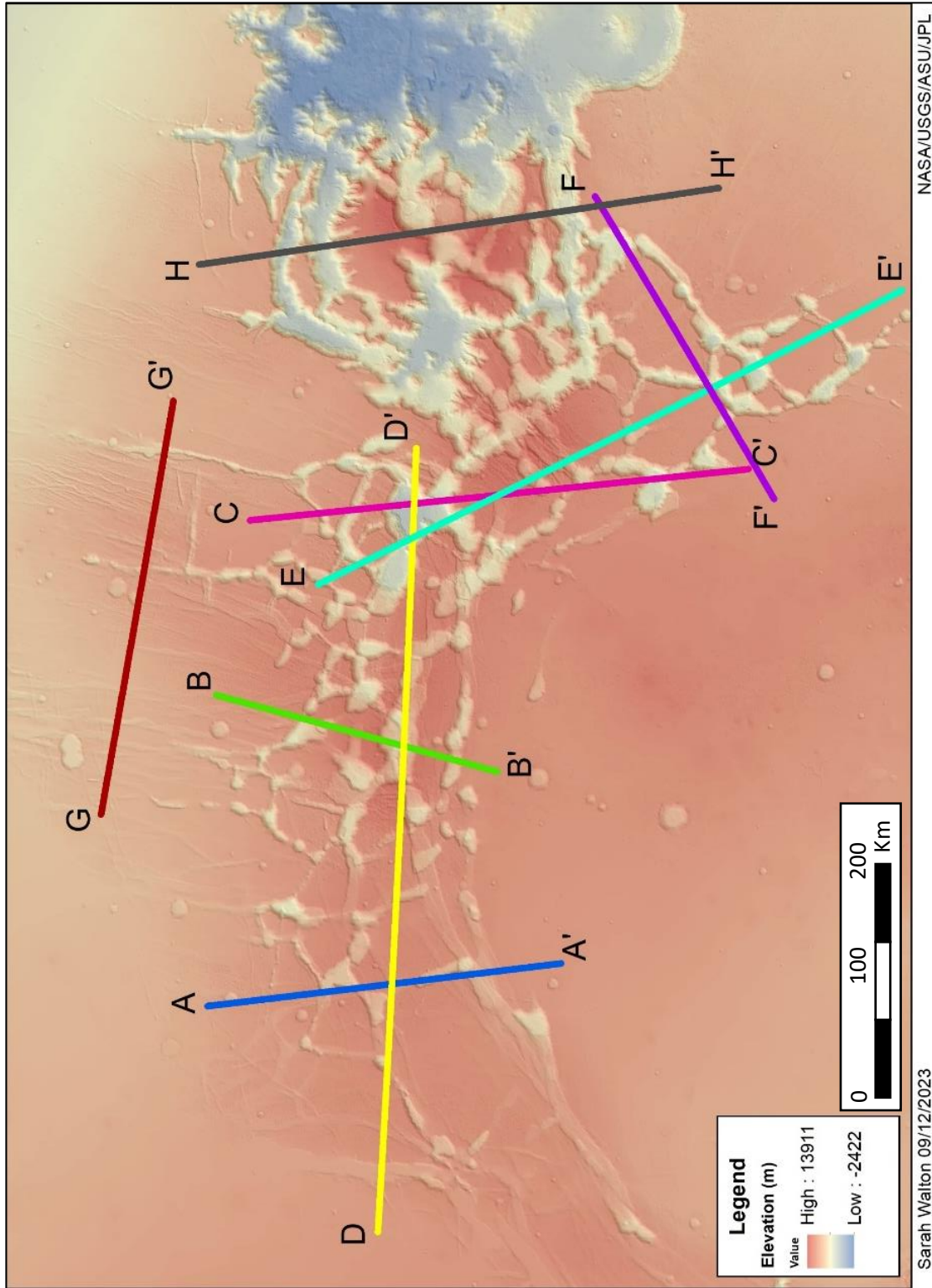


Figure 32: Map of topographic profile lines taken within NL.

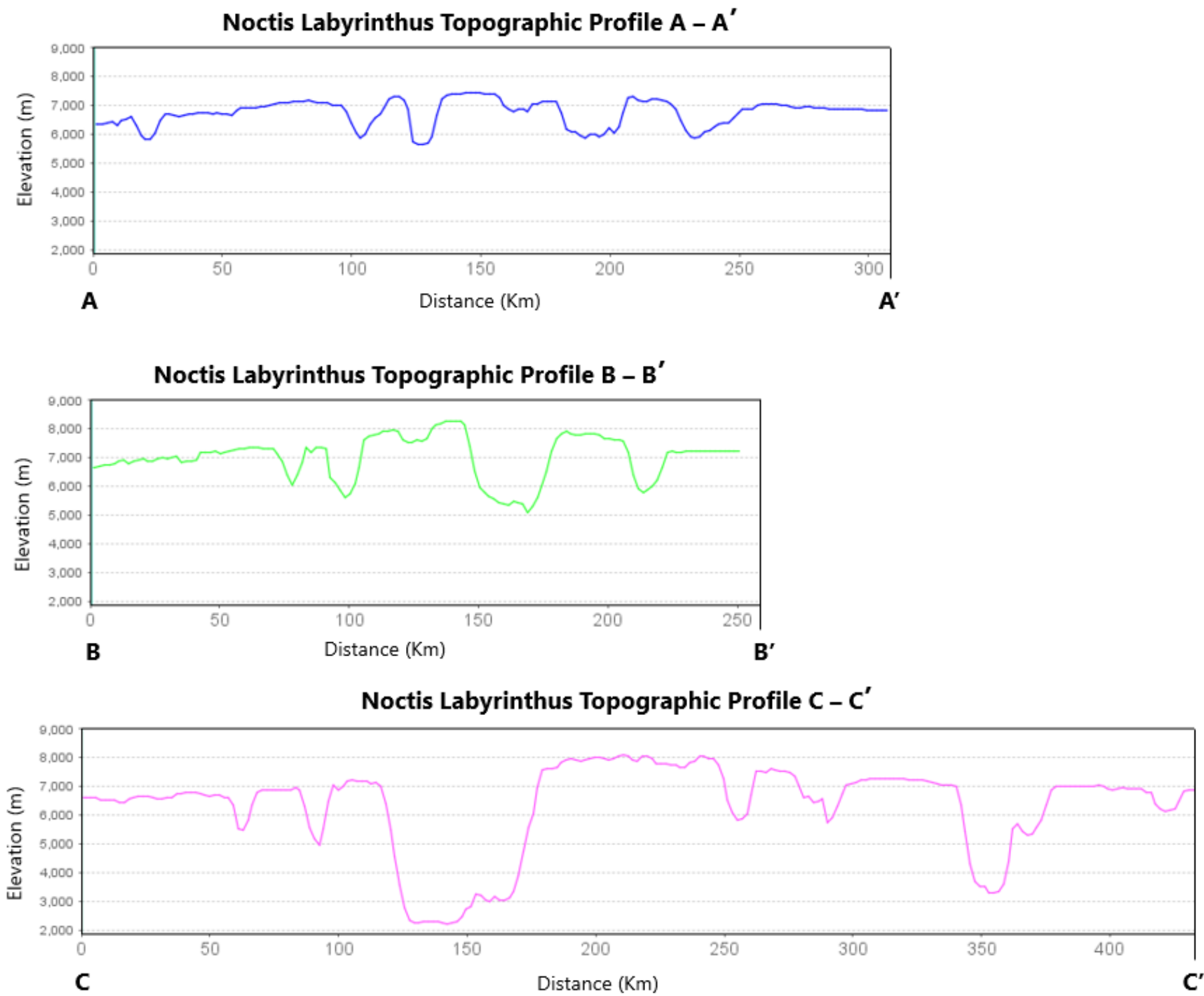


Figure 33: NL topographic profiles A – A', B- B', and C -C'. Mesas are identified as high elevation flat topographic features and troughs are low elevation areas bounded by mesas.

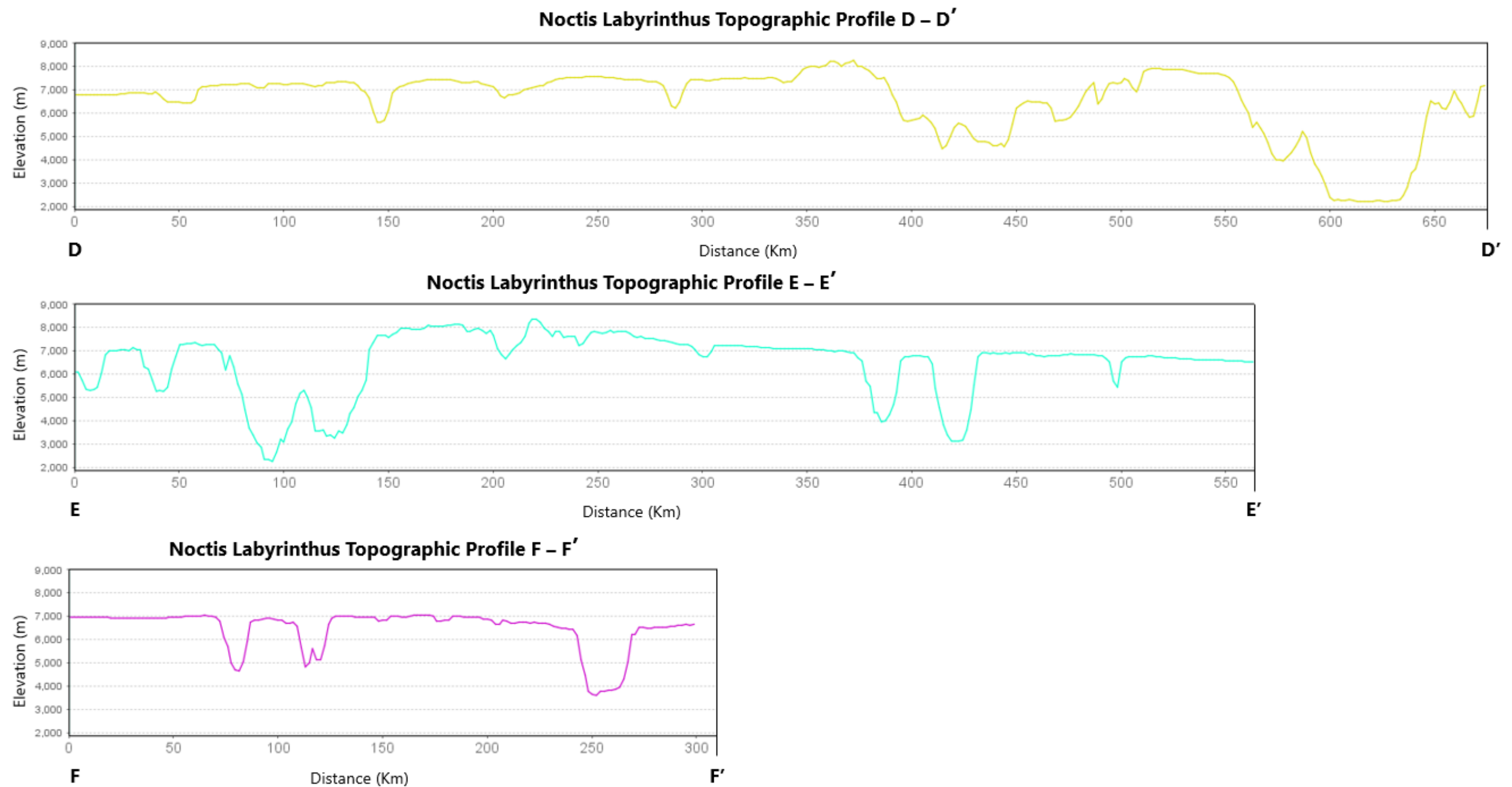


Figure 34: NL topographic profiles D – D', E -E' and F- F'.

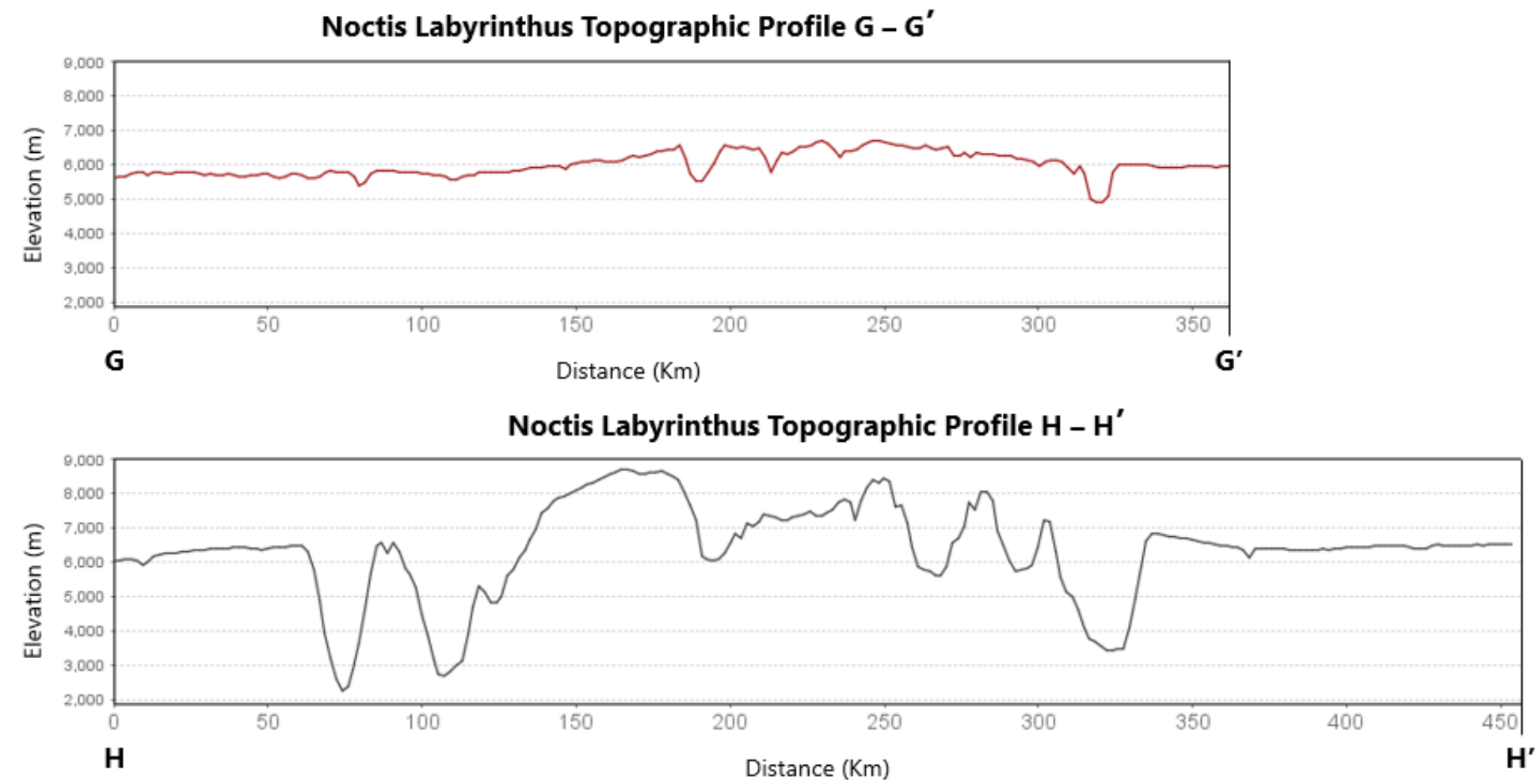


Figure 35: NL topographic profiles G – G' and H – H'.

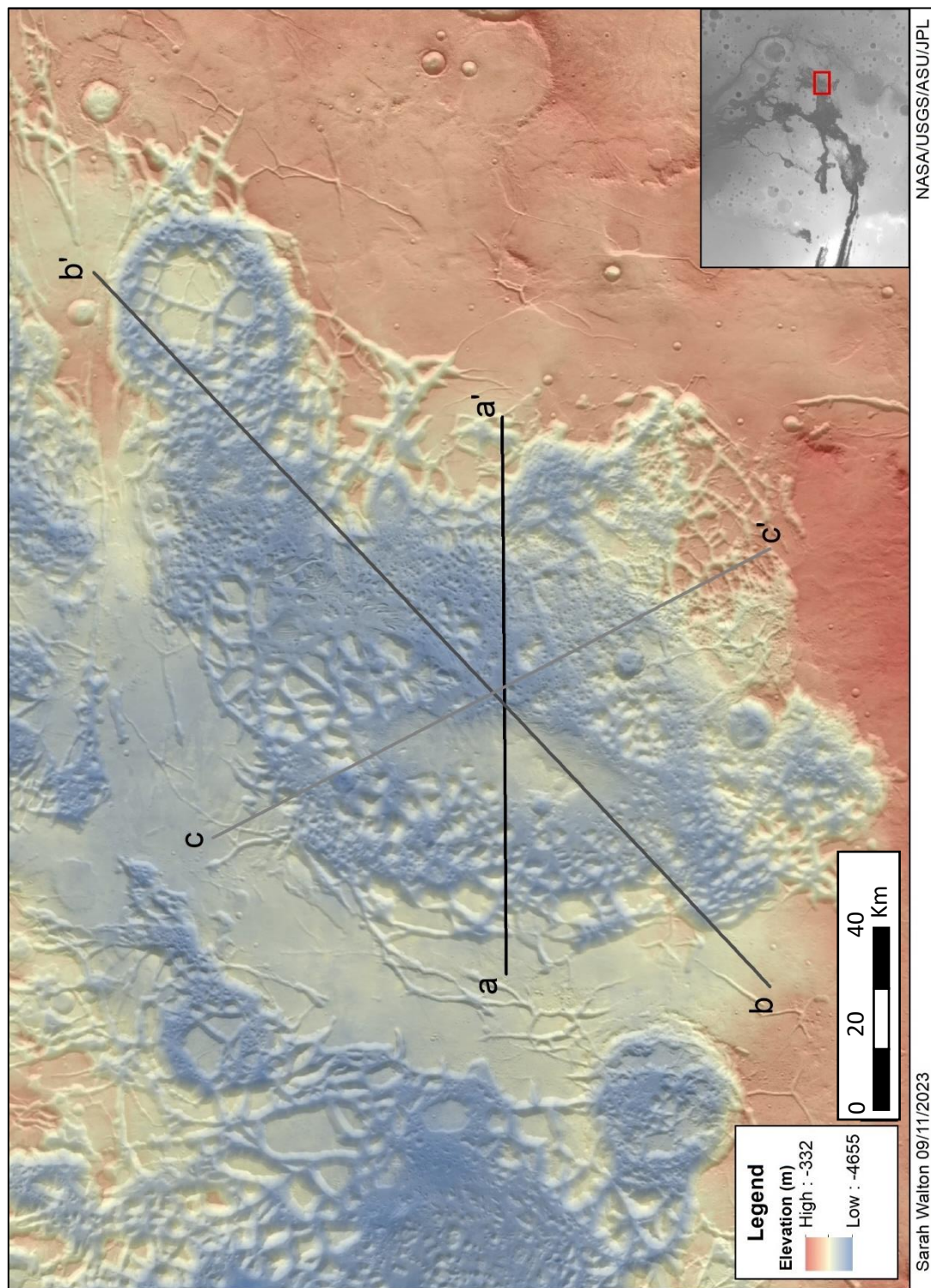


Figure 36: Topographic profiles taken in Arsinoe Chaos.

Arsinoes Chaos Topographic Profiles a - a', b - b', and c - c'

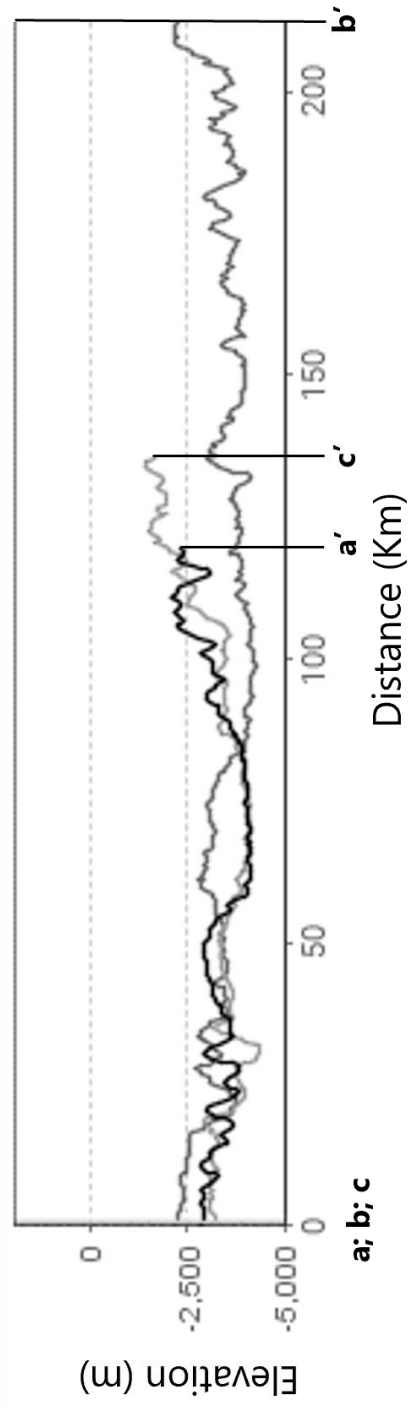


Figure 37: Topographic profiles of Arsinoes Chaos.

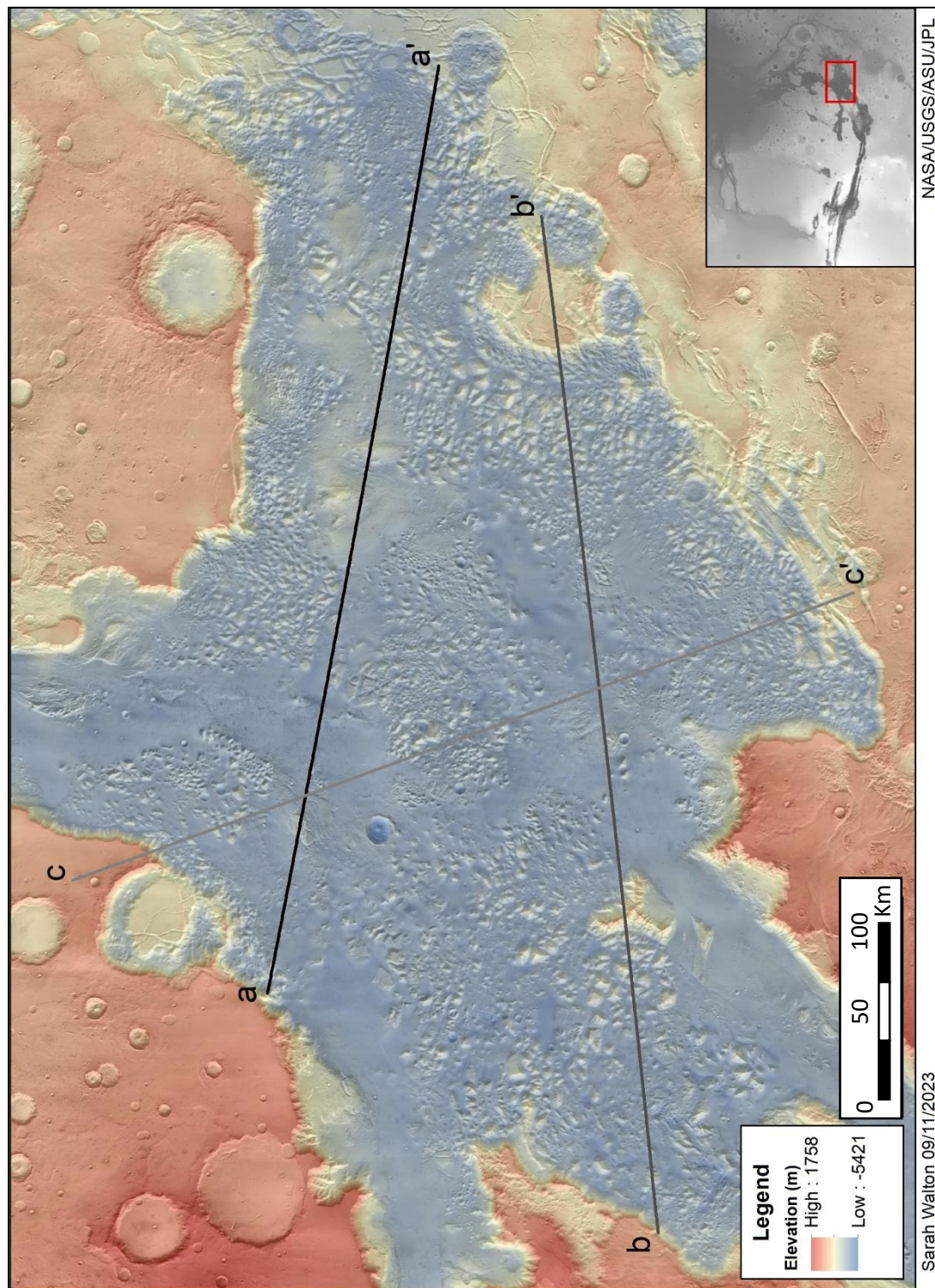


Figure 38: Topographic profiles taken in Aurorae Chaos.

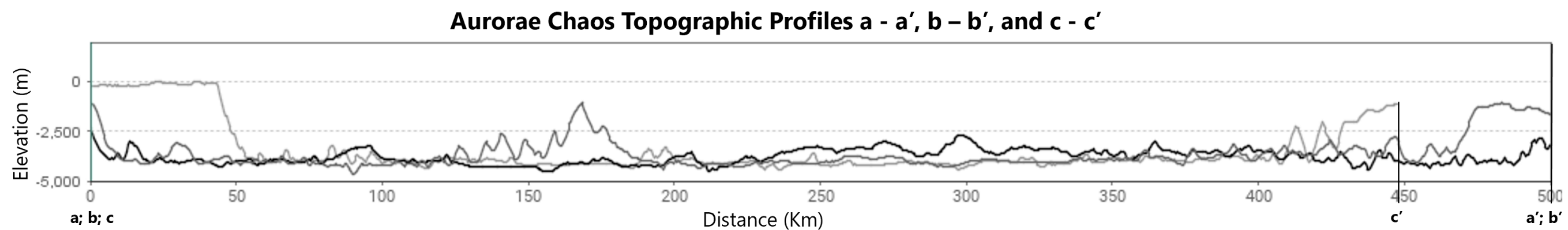


Figure 39: Topographic profiles of Aurorae Chaos.

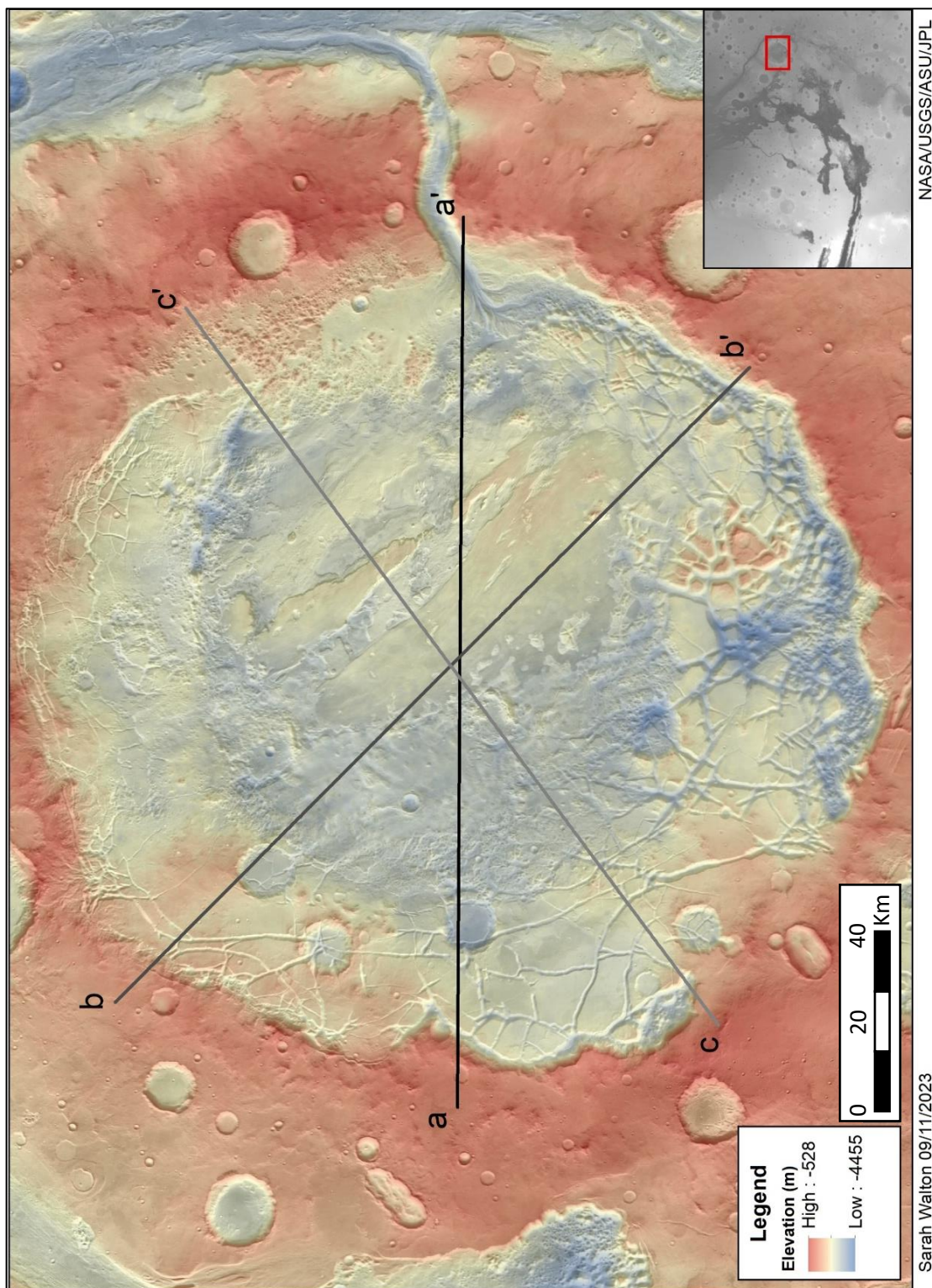


Figure 40: Topographic profiles taken in Aram Chaos.

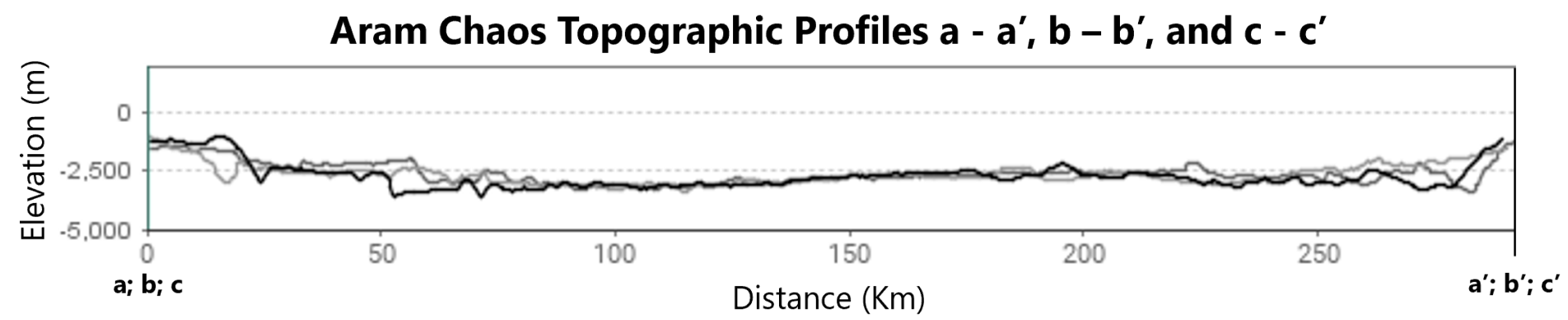


Figure 41: Topographic profiles of Aram Chaos.

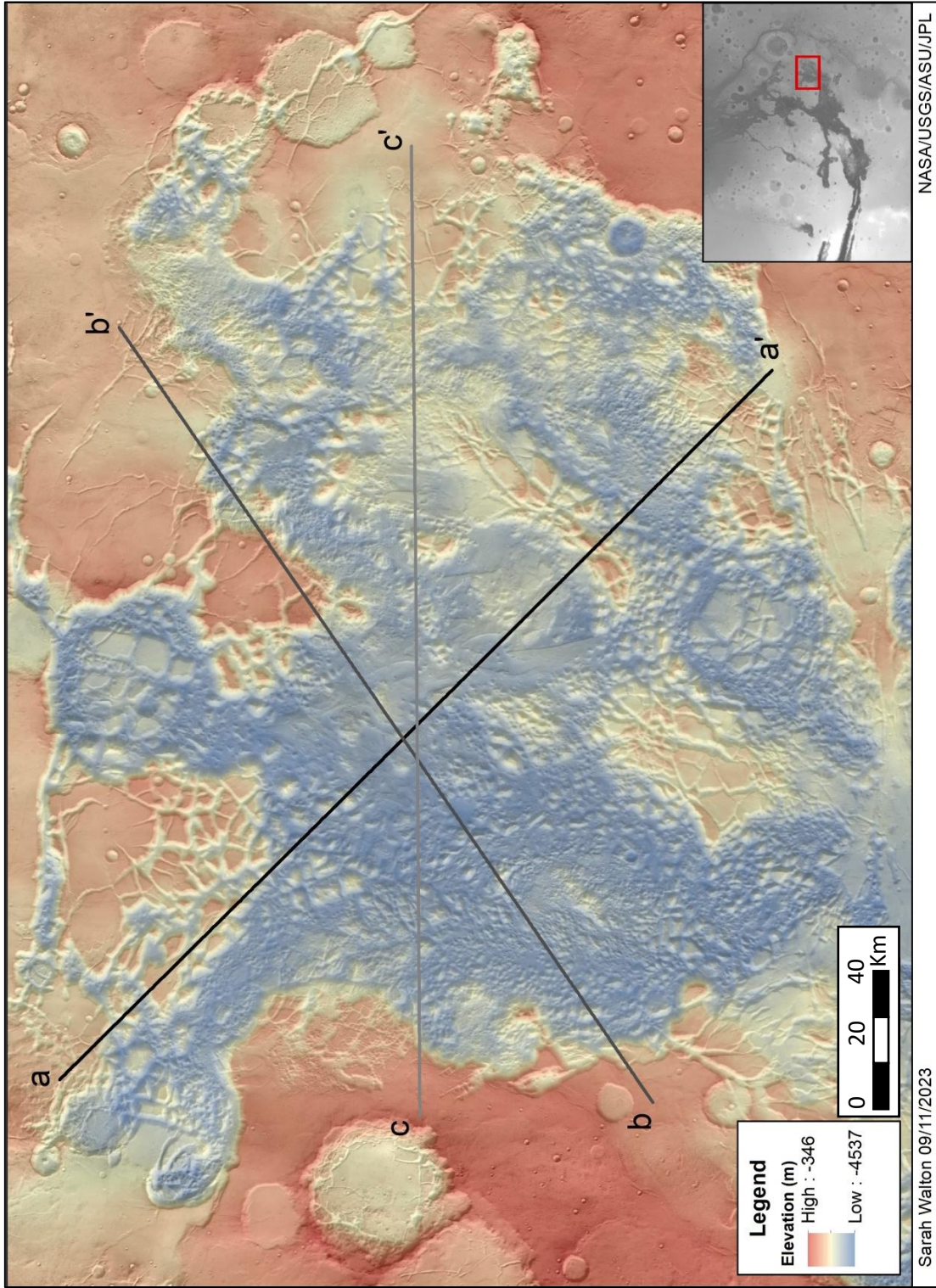


Figure 42: Topographic profiles taken in Aureum Chaos.

Sarah Walton 09/11/2023

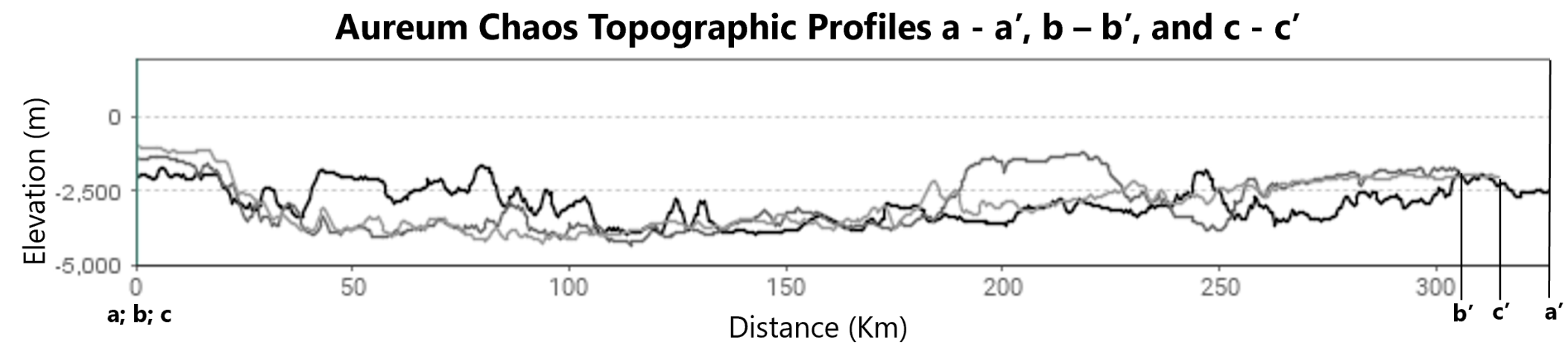


Figure 43: Topographic profiles of Aureum Chaos.

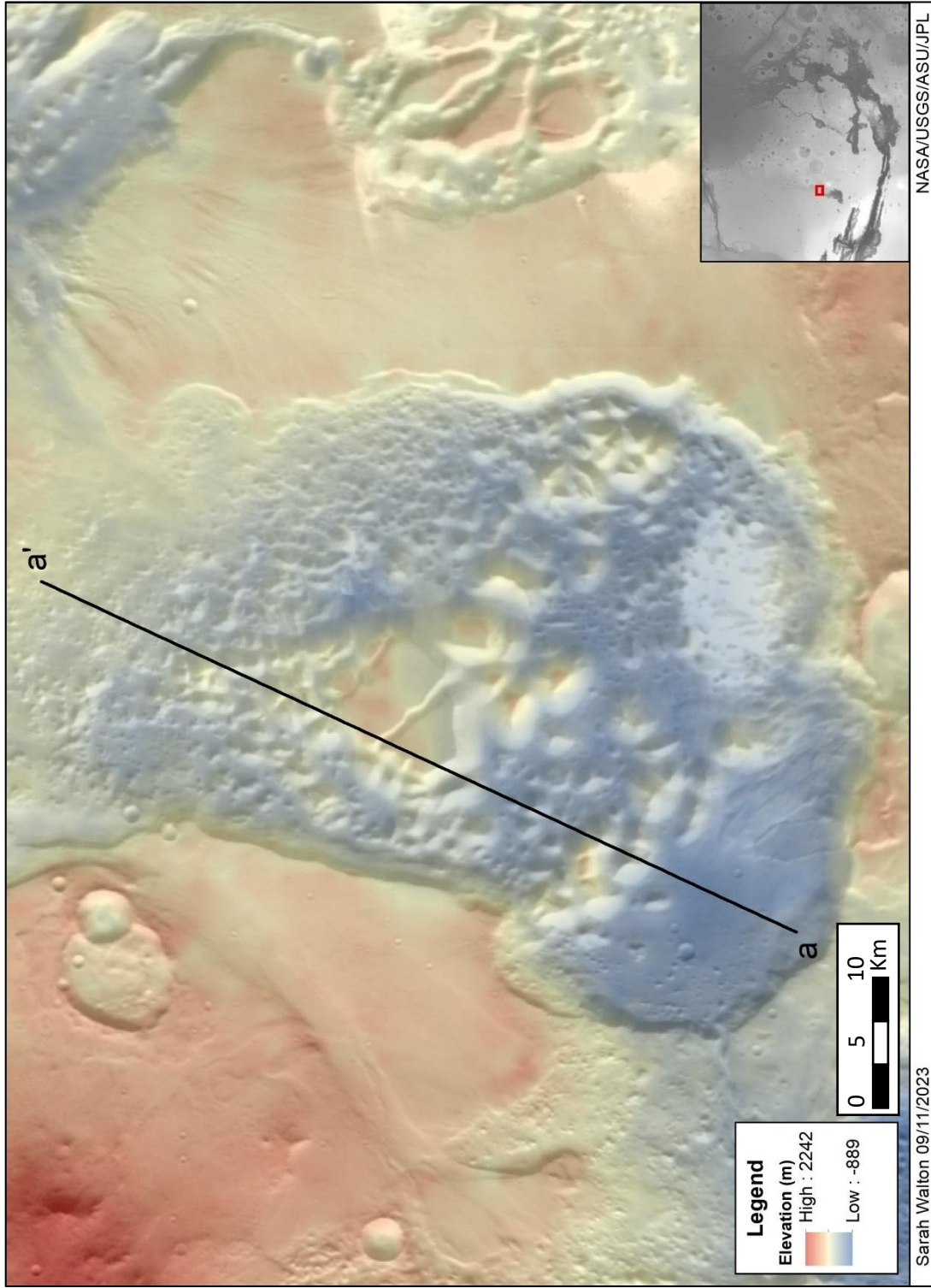


Figure 44: Topographic profile taken in Baetis Chaos.

Baetis Chaos Topographic Profile a – a'

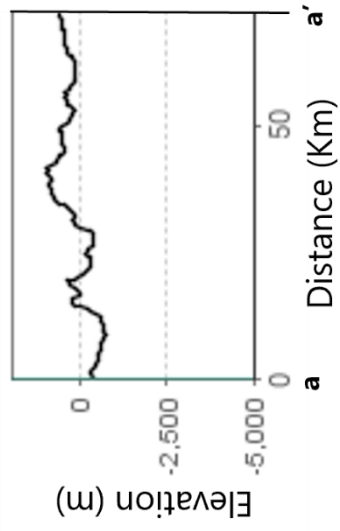


Figure 45: Topographic profile of Baetis Chaos.

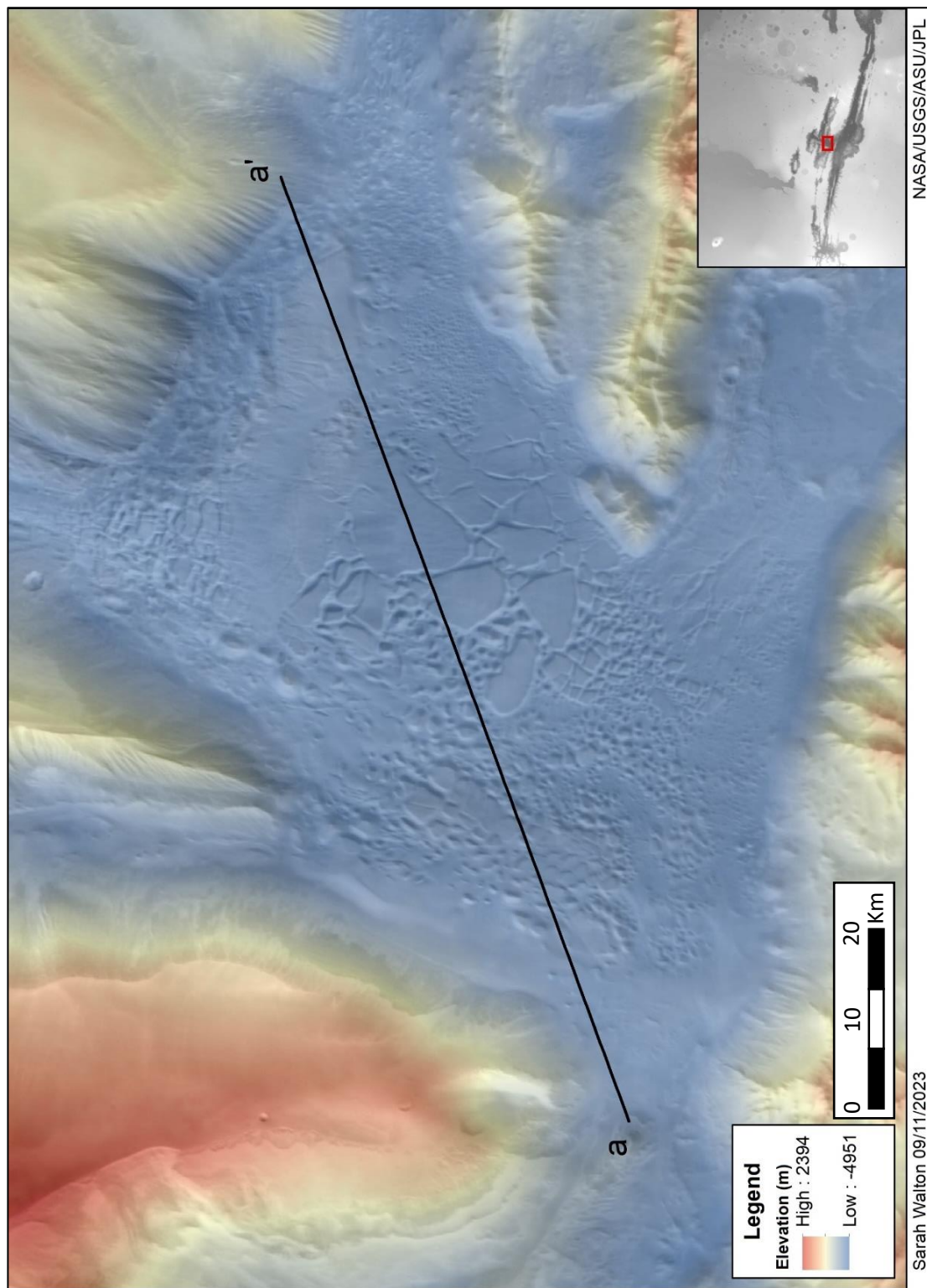


Figure 46: Topographic profile taken in Candor Chaos.

Candor Chaos Topographic Profile a – a'

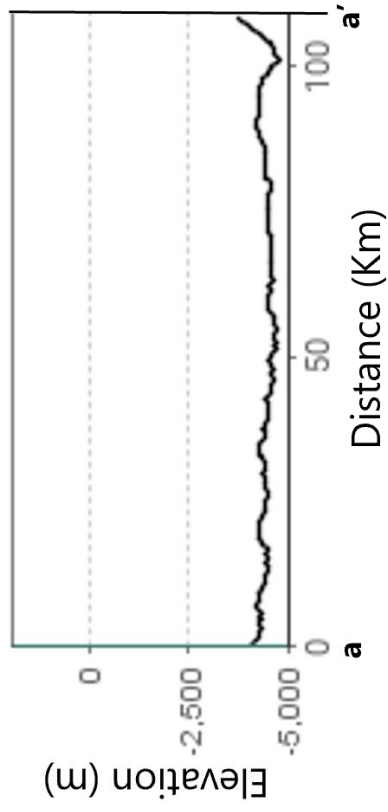


Figure 47: Topographic profile of Candor Chaos.

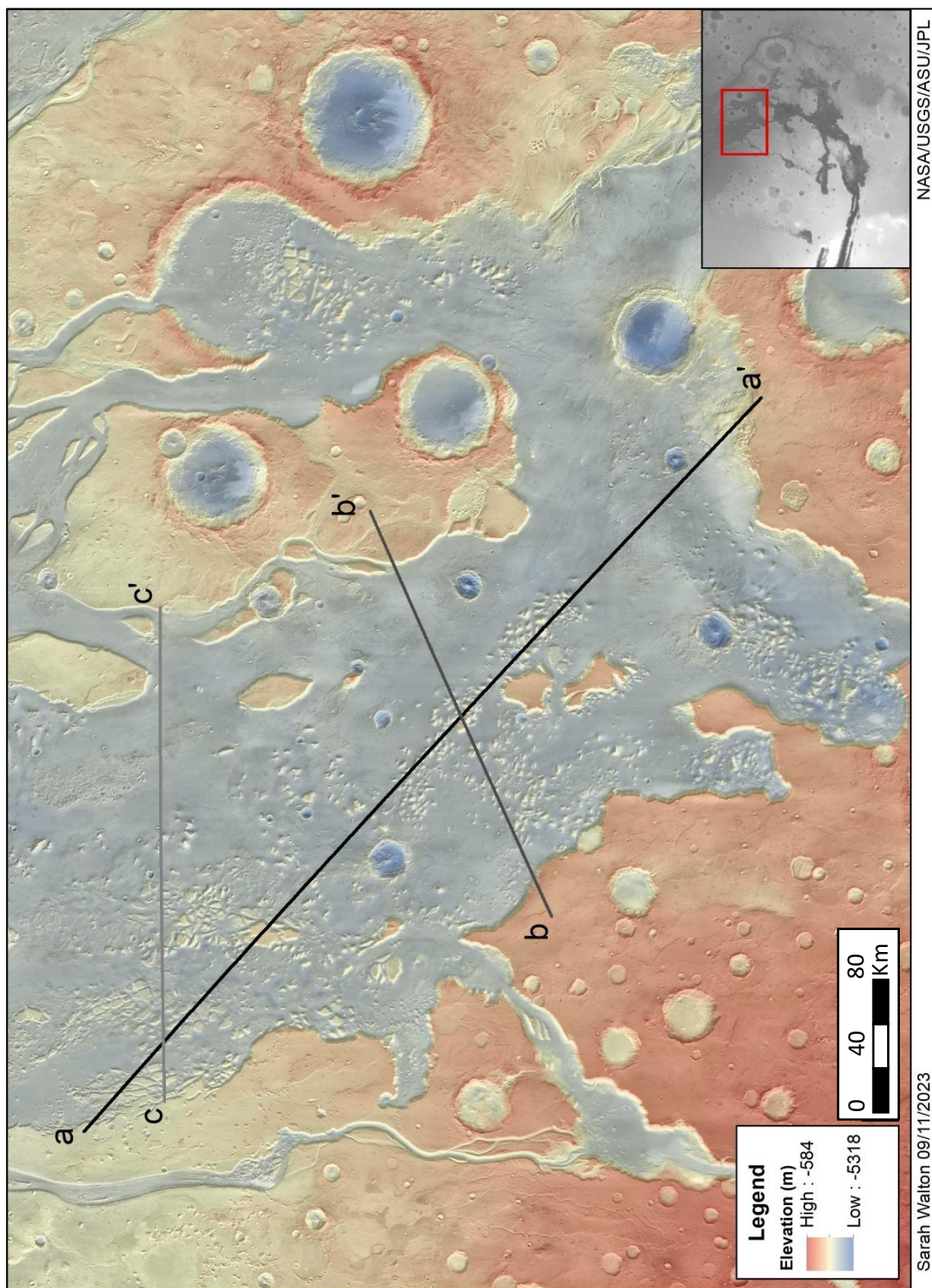


Figure 48: Topographic profiles taken in Chryse Chaos.

Chryse Chaos Topographic Profiles a - a', b - b', and c - c'

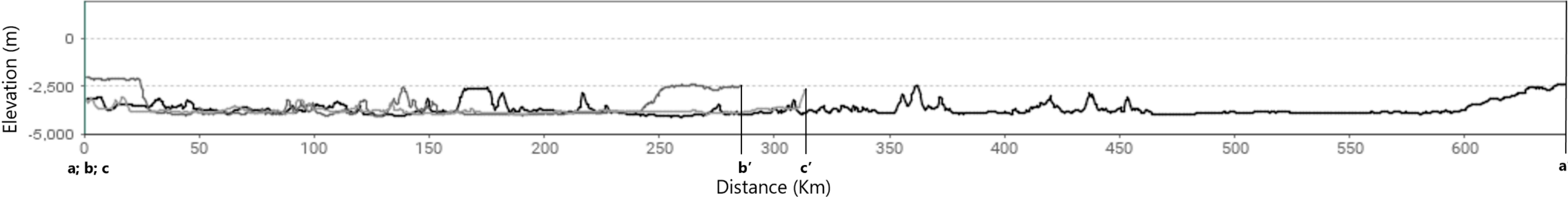


Figure 49: Topographic profiles of Chryse Chaos.

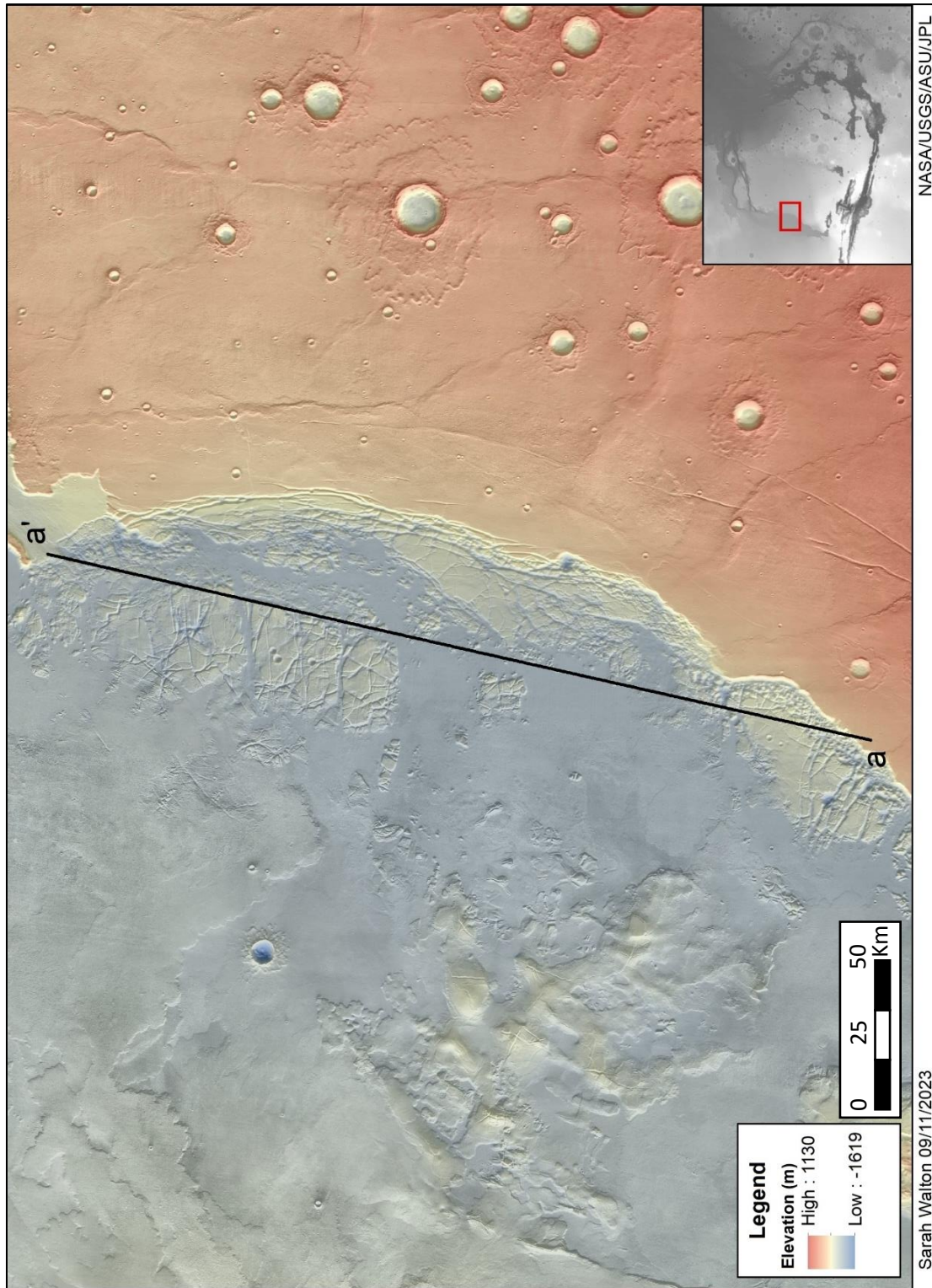


Figure 50: Topographic profile taken in Echus Chaos.

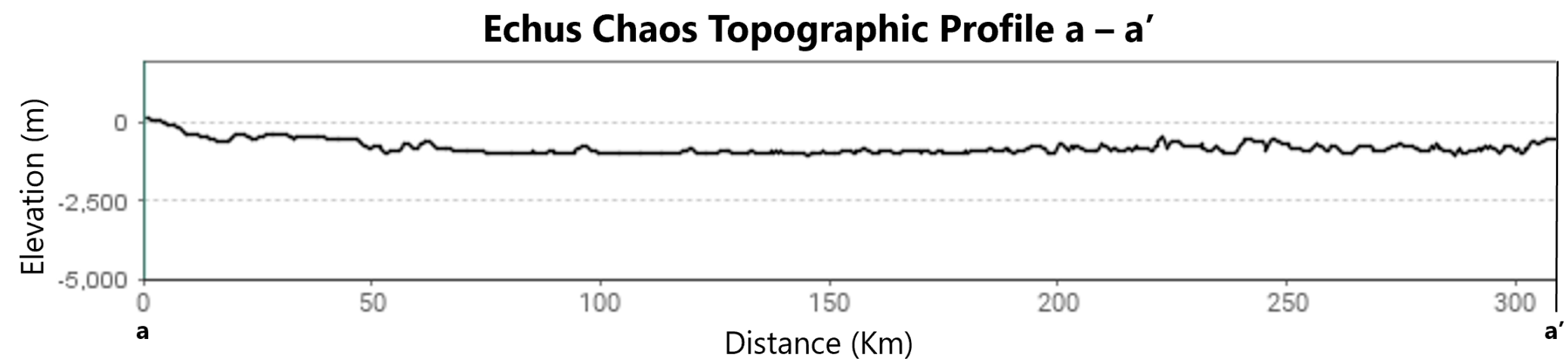


Figure 51: Topographic profile of Echus Chaos.

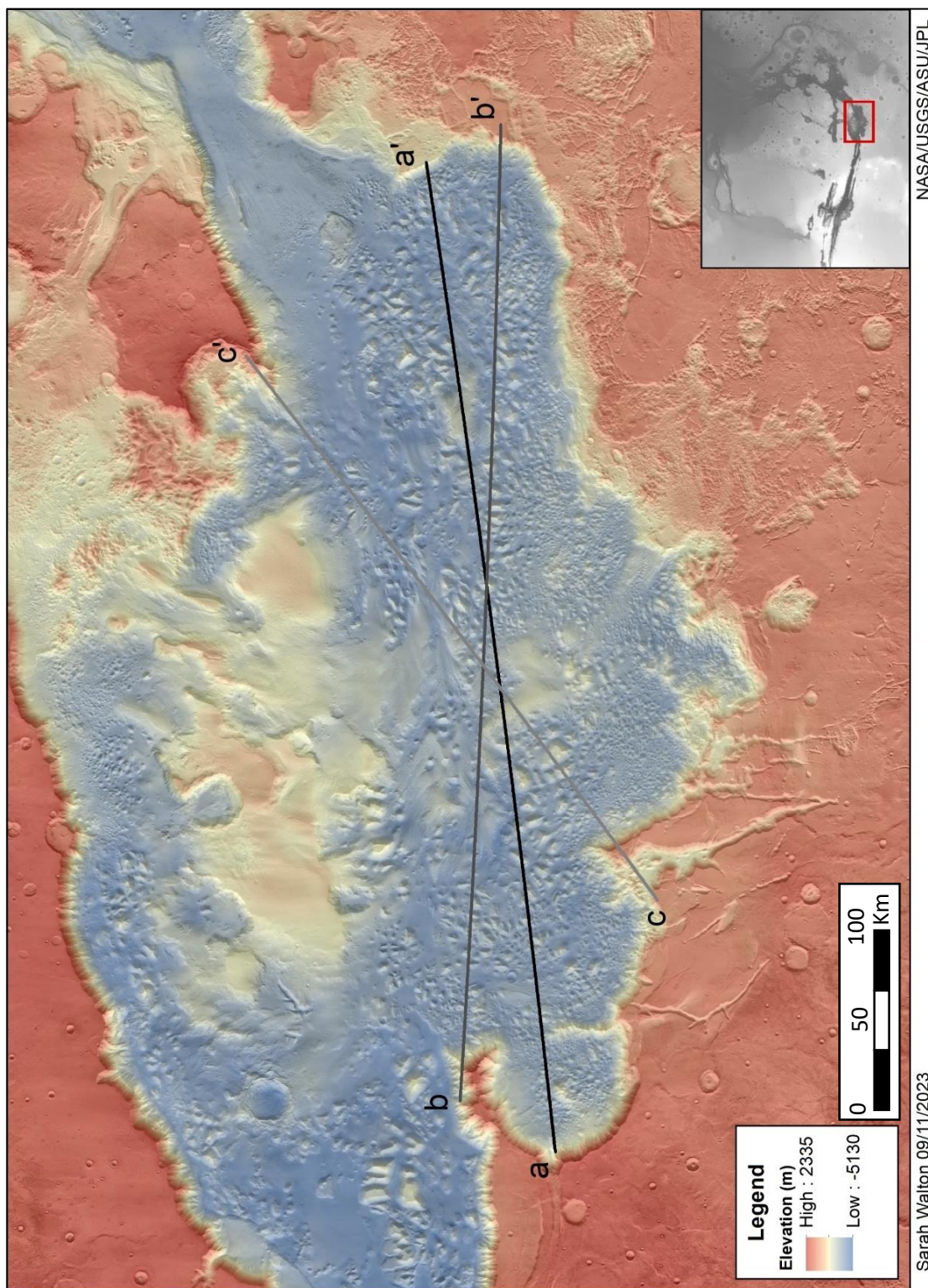


Figure 52: Topographic profiles taken in Eos Chaos.

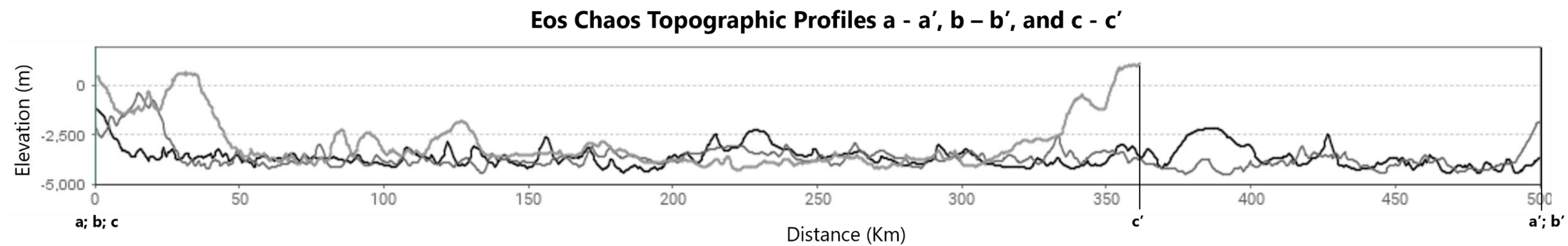


Figure 53: Topographic profiles of Eos Chaos.

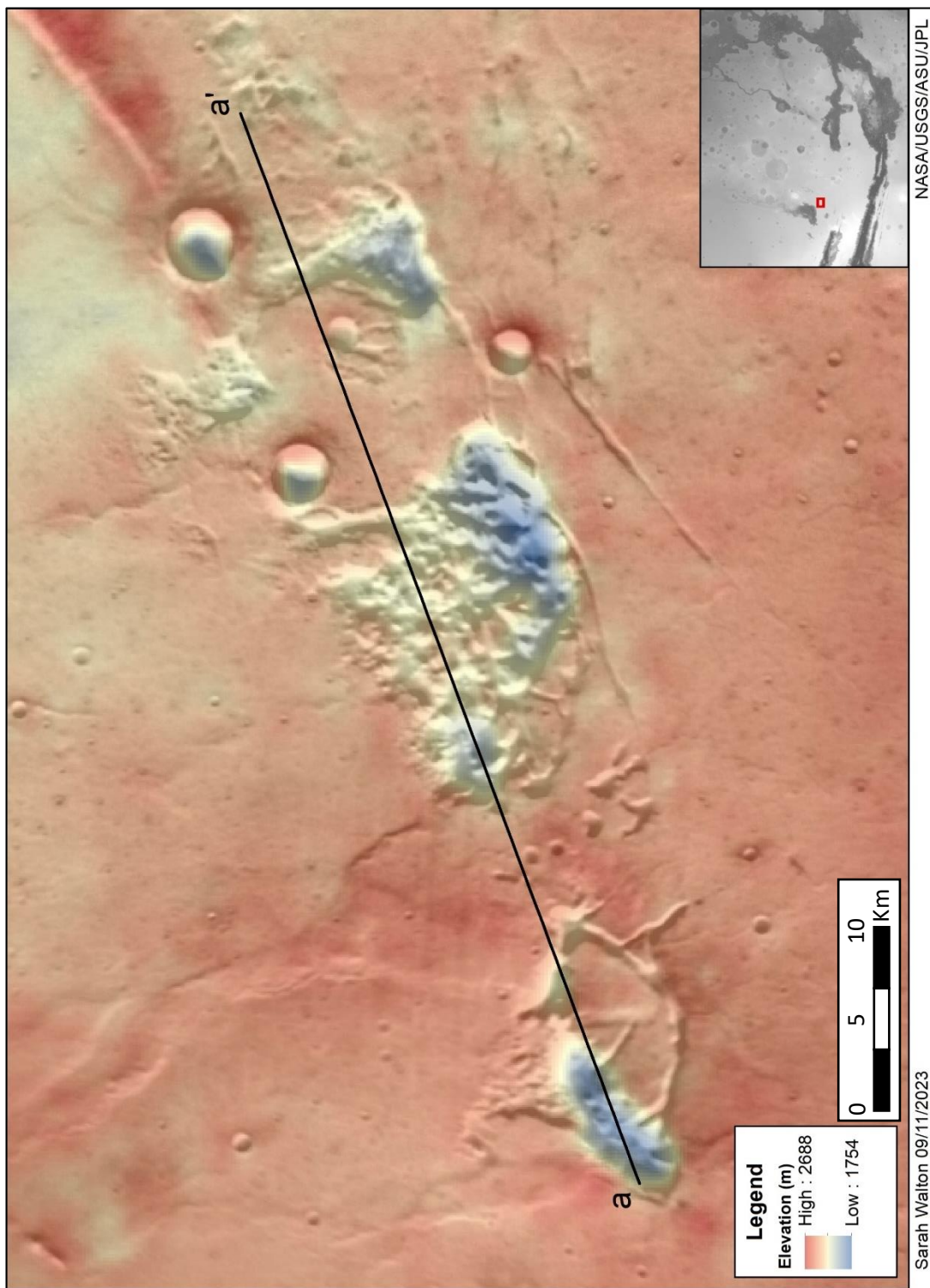


Figure 54: Topographic profile taken in Hydræ Chaos.

Hydrae Chaos Topographic Profile a – a'

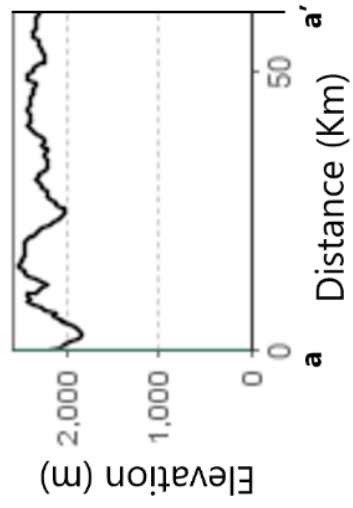


Figure 55: Topographic profile of Hydrae Chaos.

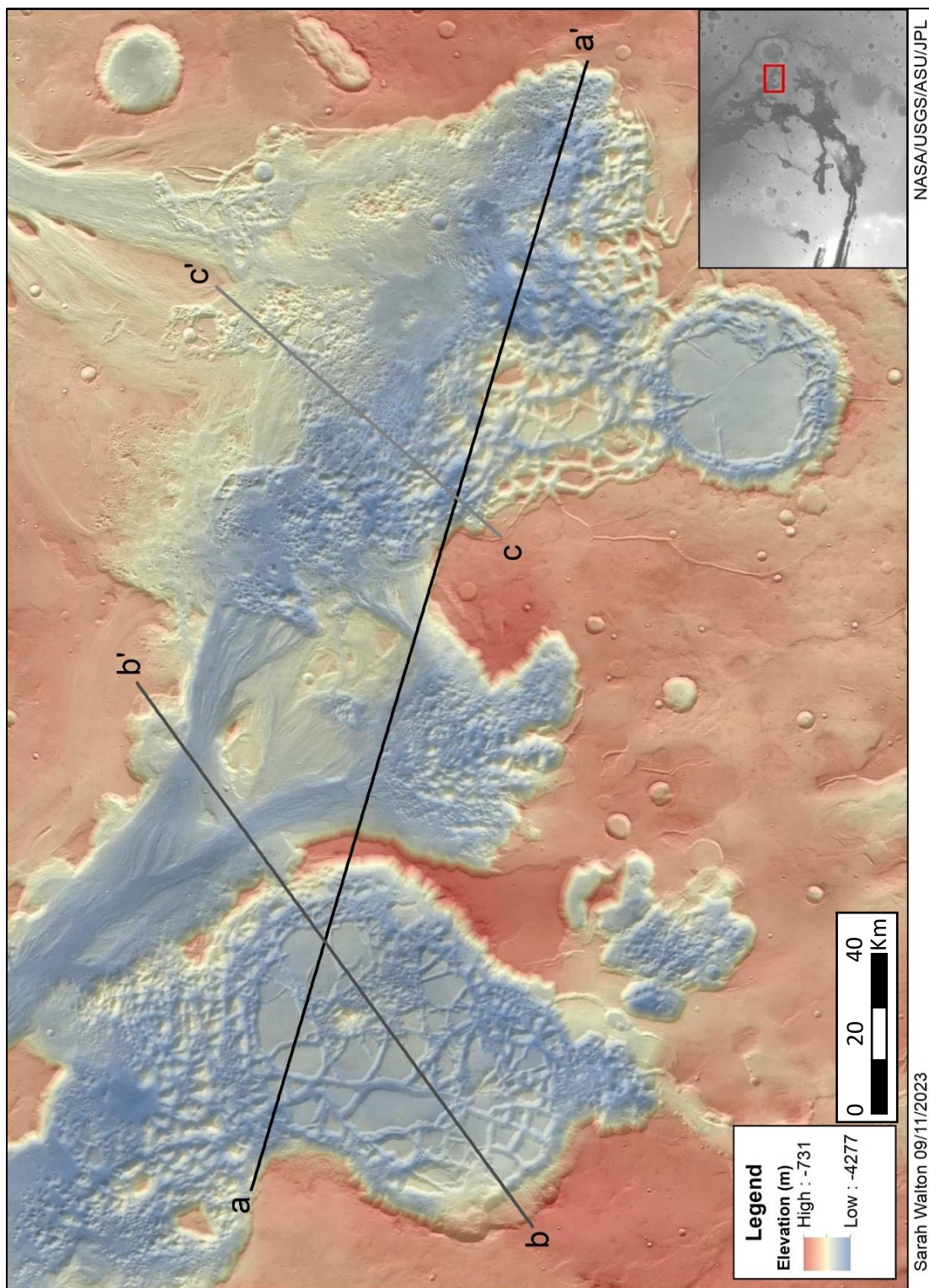


Figure 56: Topographic profiles taken in Hydaspis Chaos.

Hydaspis Chaos Topographic Profiles a - a', b - b', and c - c'

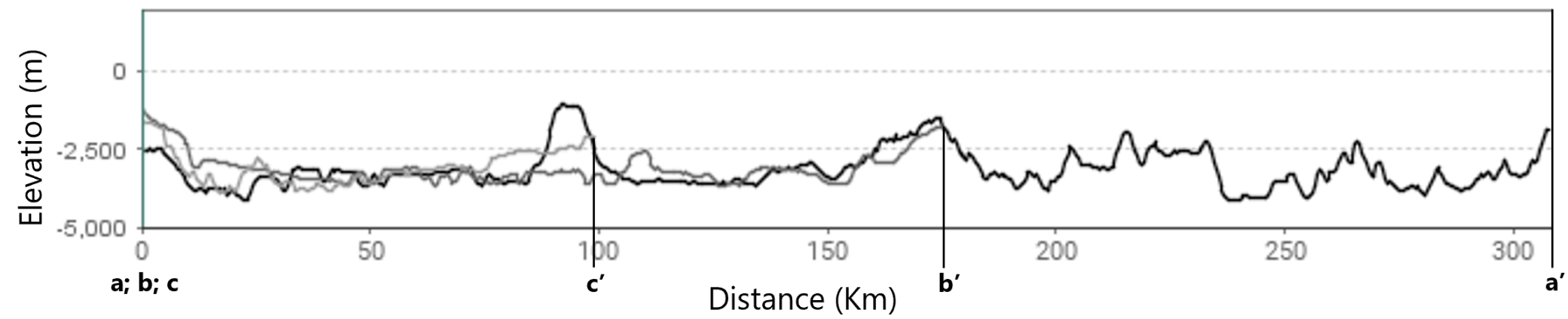


Figure 57: Topographic profiles of Hydaspis Chaos.

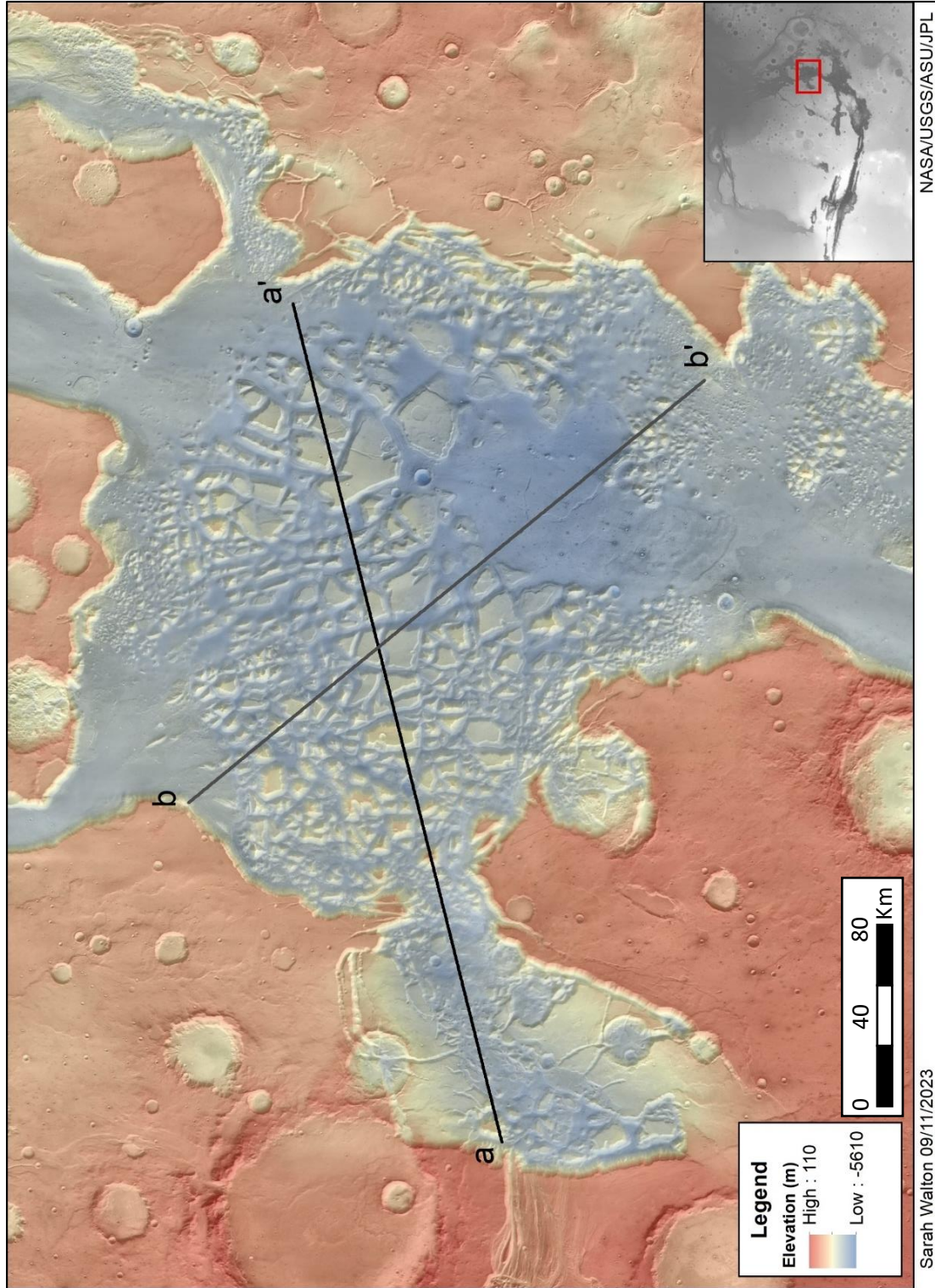


Figure 58: Topographic profiles taken in Hydrates Chaos.

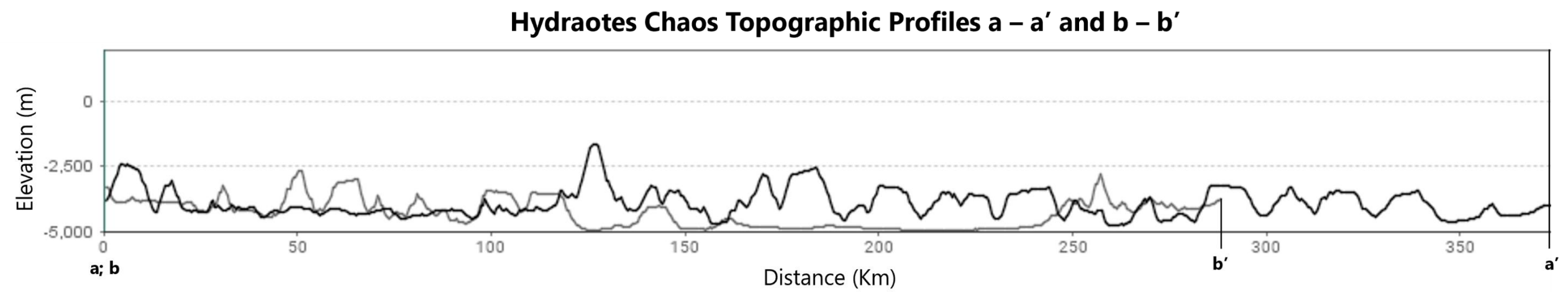


Figure 59: Topographic profiles of Hydraotes Chaos.

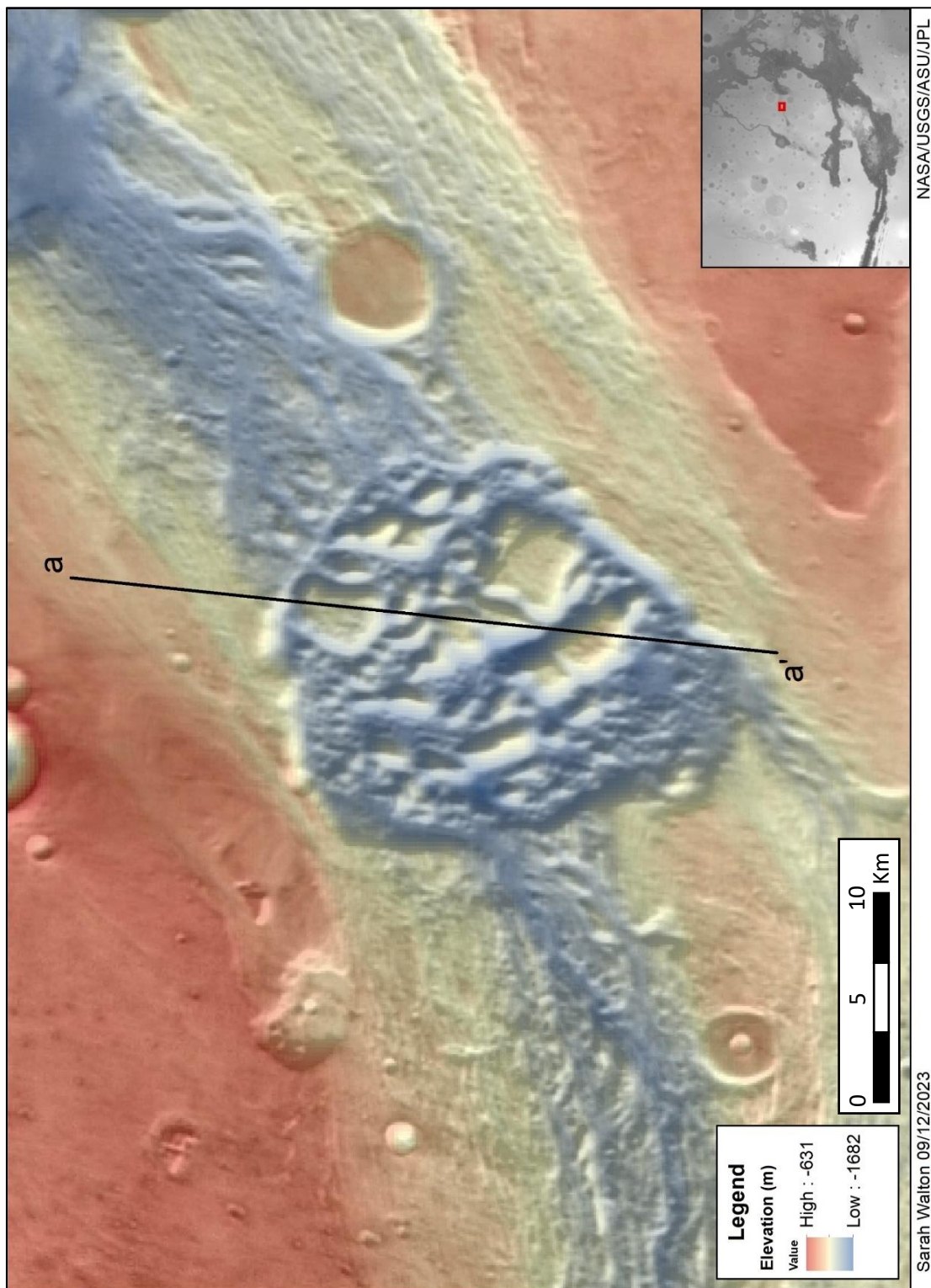


Figure 60: Topographic profile taken in lamuna Chaos.

lamuna Chaos Topographic Profile a – a'

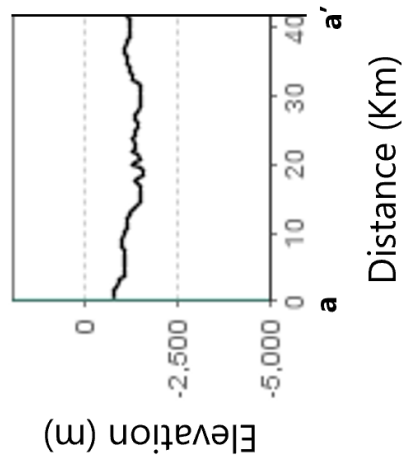


Figure 61: Topographic profile of lamuna Chaos.

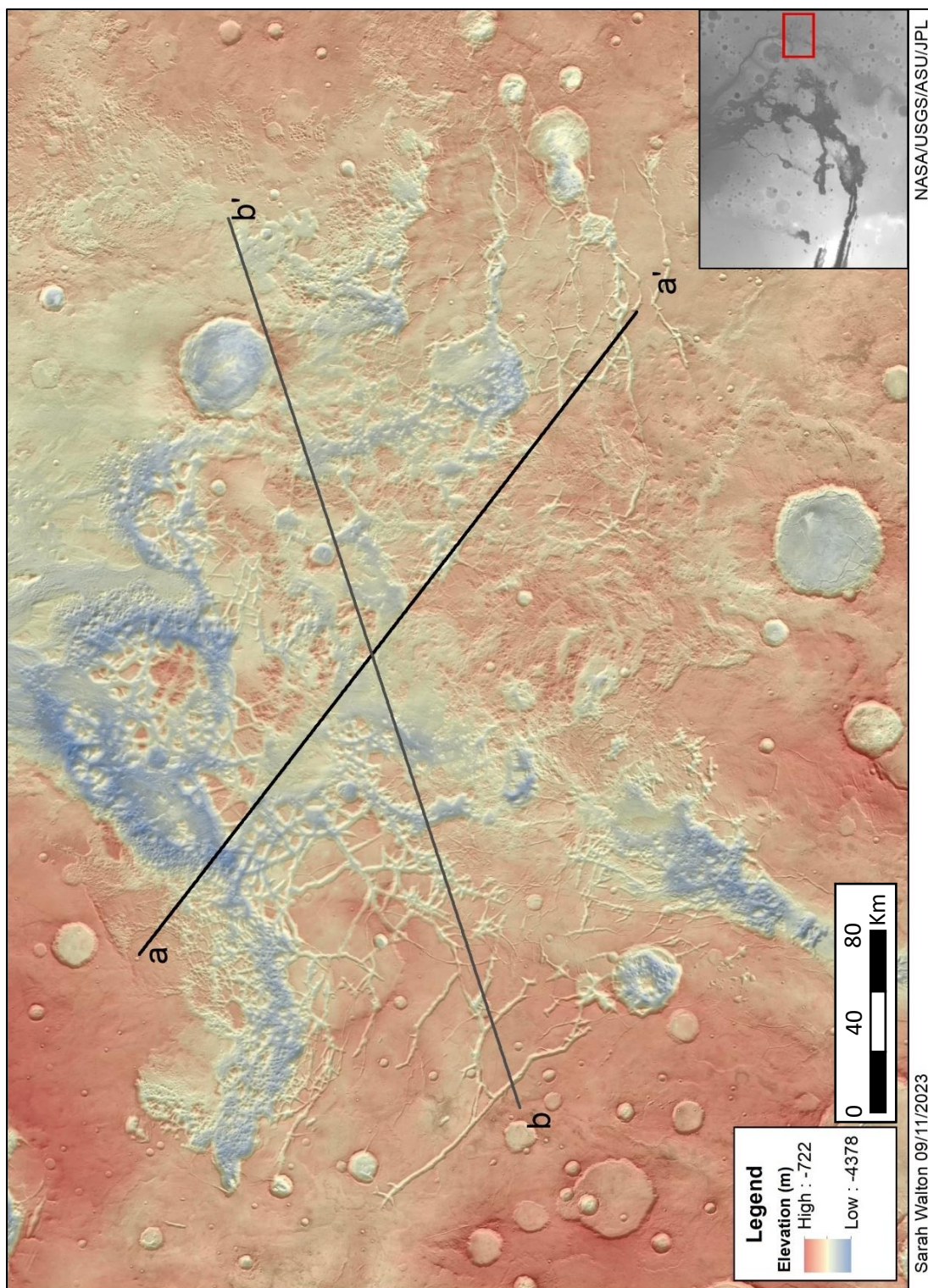


Figure 62: Topographic profiles taken in Iani Chaos.

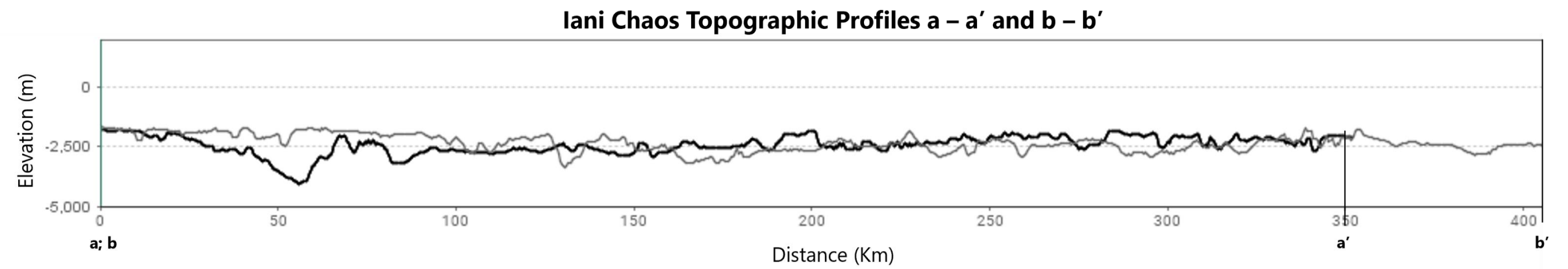


Figure 63: Topographic profiles of Iani Chaos.

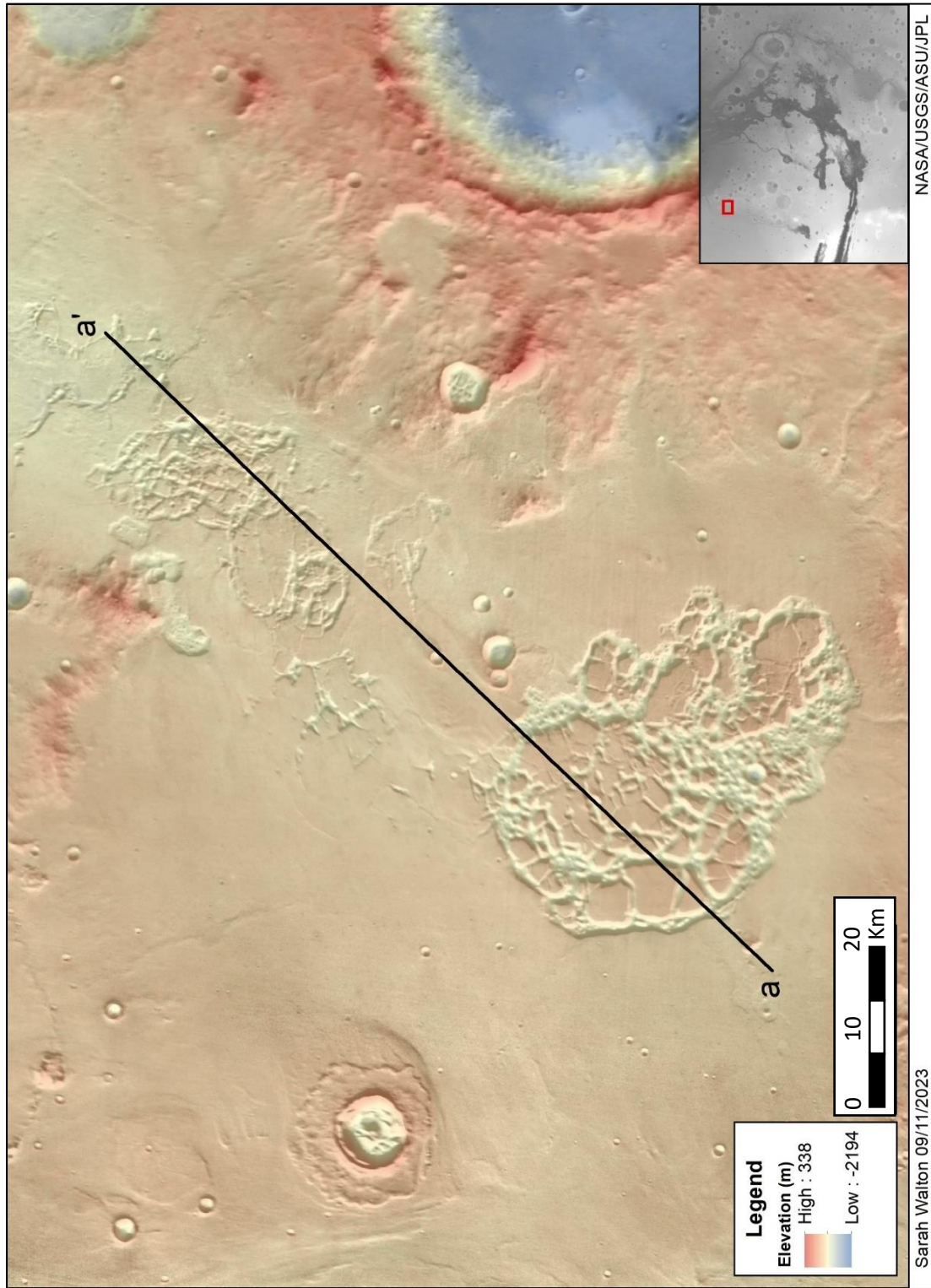


Figure 64: Topographic profile taken in Ister Chaos.

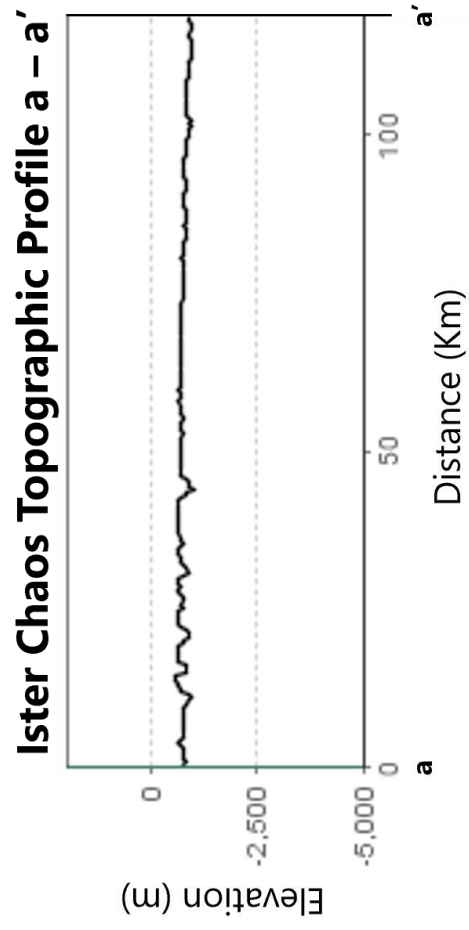


Figure 65: Topographic profile of Ister Chaos.

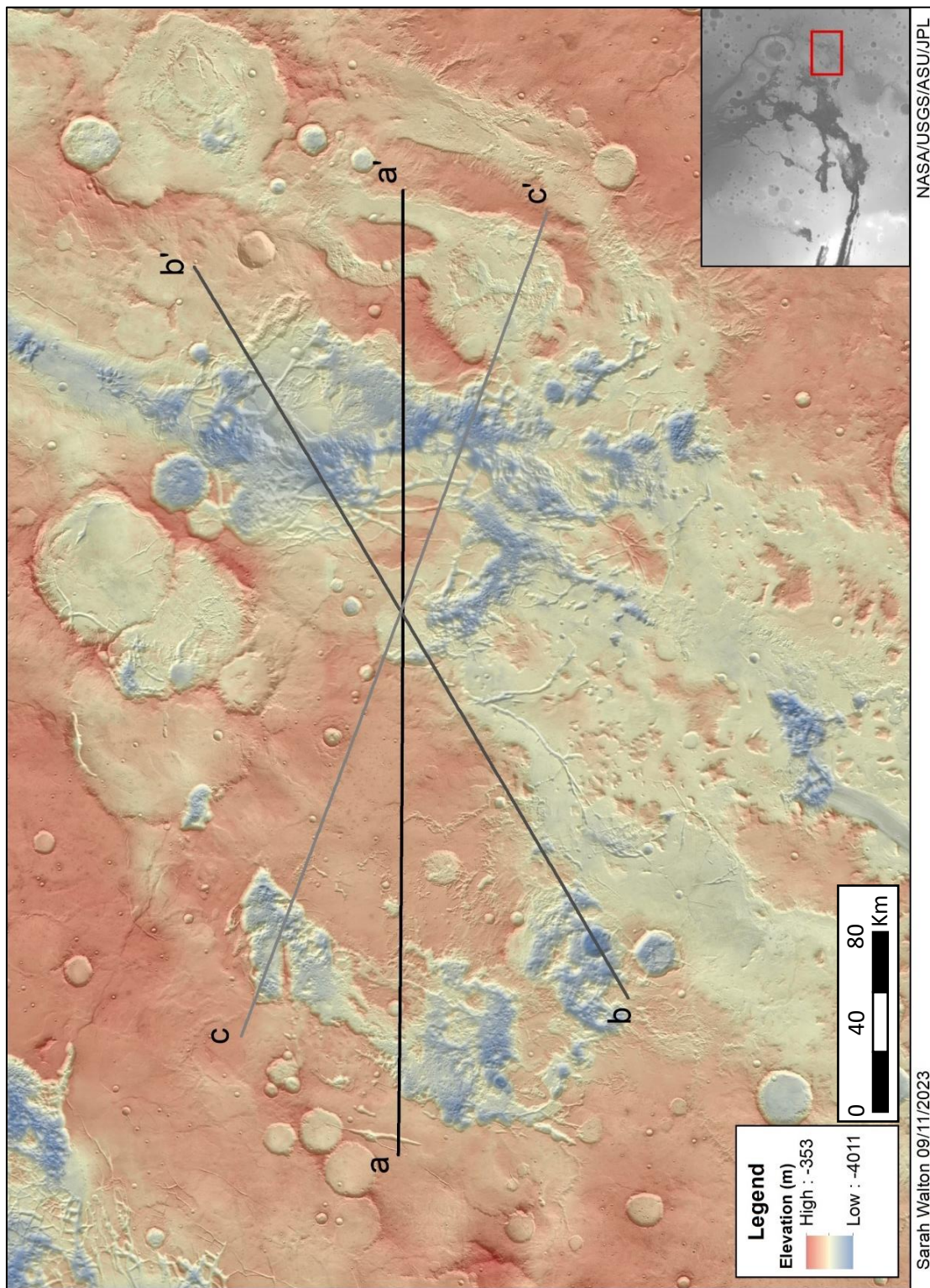


Figure 66: Topographic profiles taken in Margaritifer Chaos.

Sarah Walton 09/11/2023

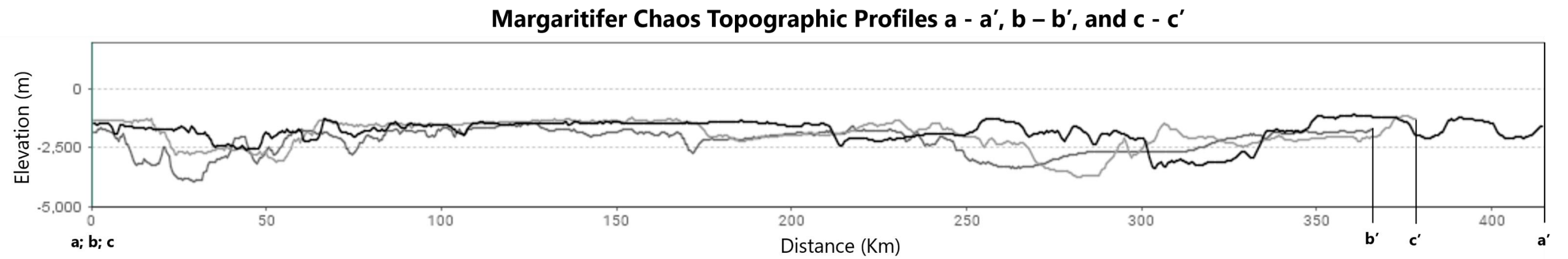


Figure 67: Topographic profiles of Margaritifer Chaos.

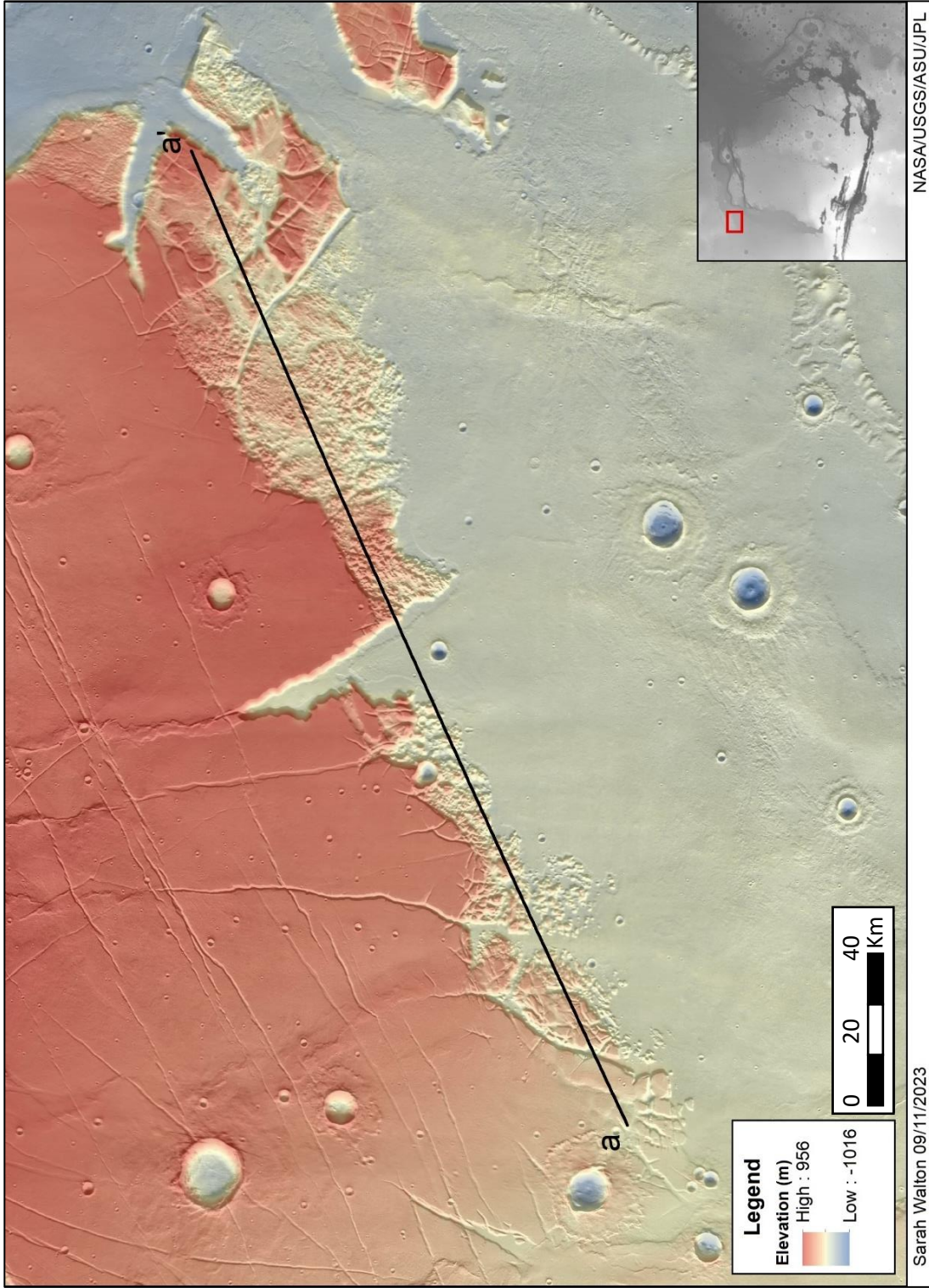


Figure 68: Topographic profile taken in Nilus Chaos.

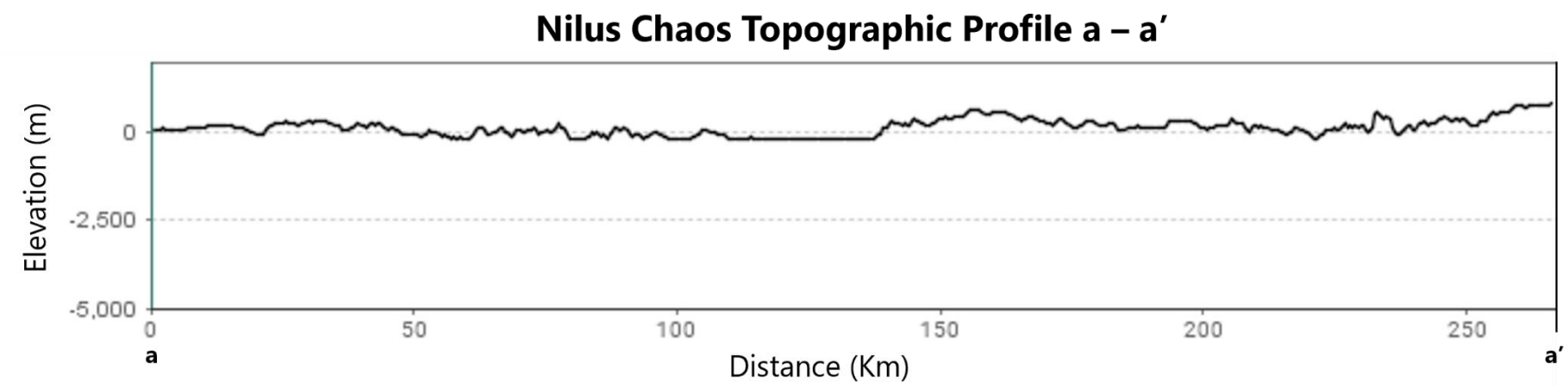


Figure 69: Topographic profile of Nilus Chaos.

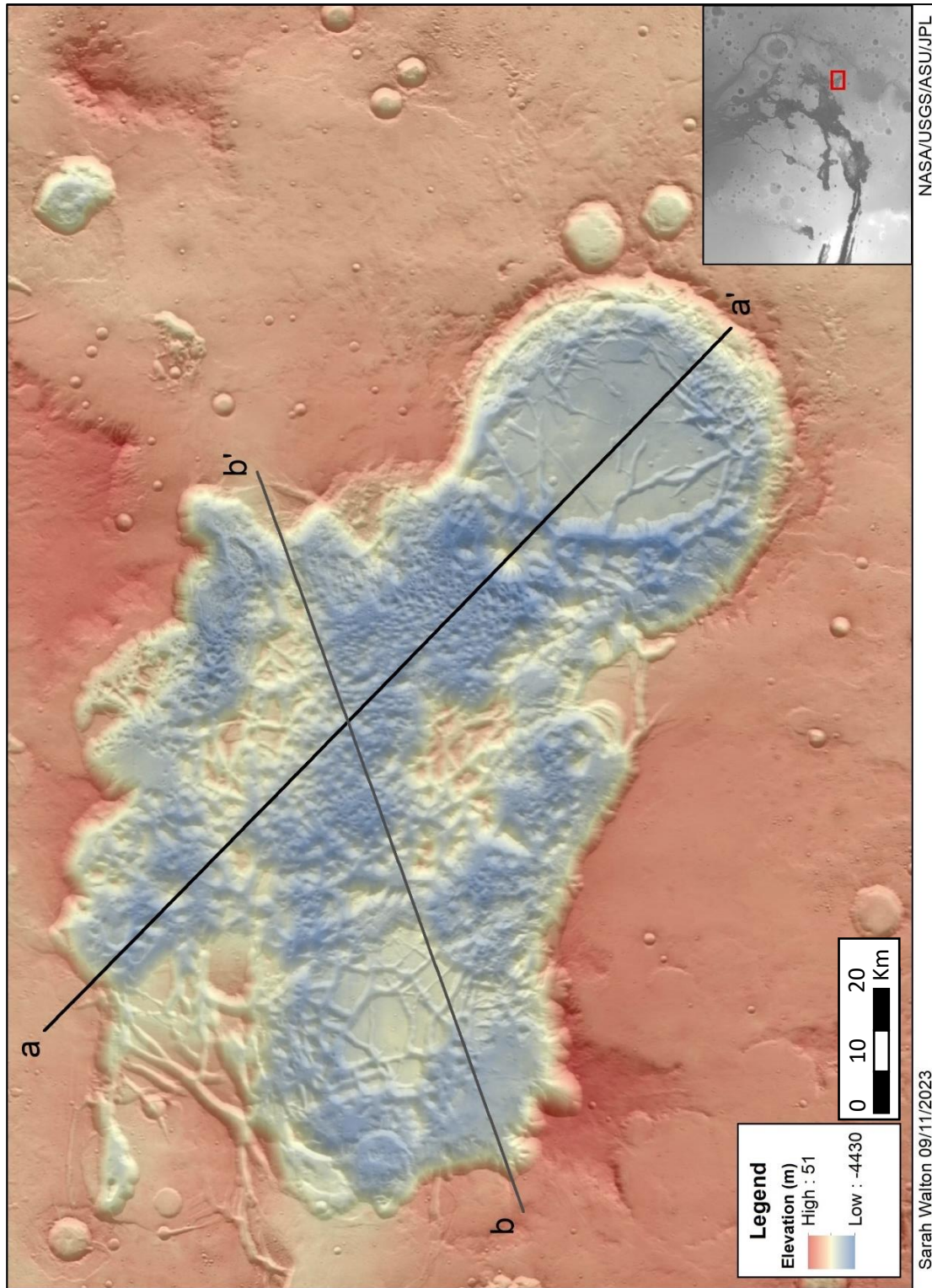


Figure 70: Topographic profiles taken in Pyrrhae Chaos.

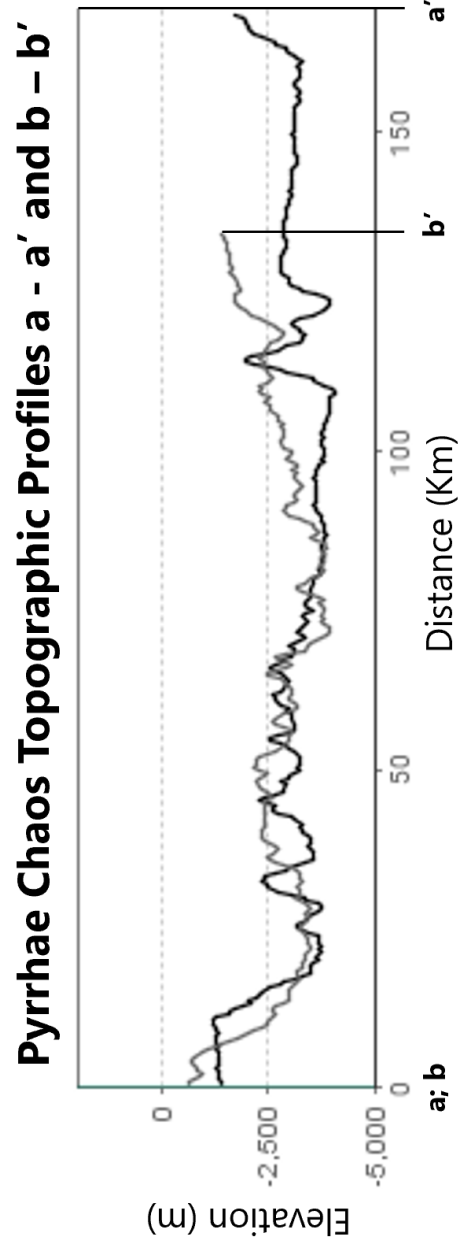


Figure 71: Topographic profiles of Pyrrhae Chaos.

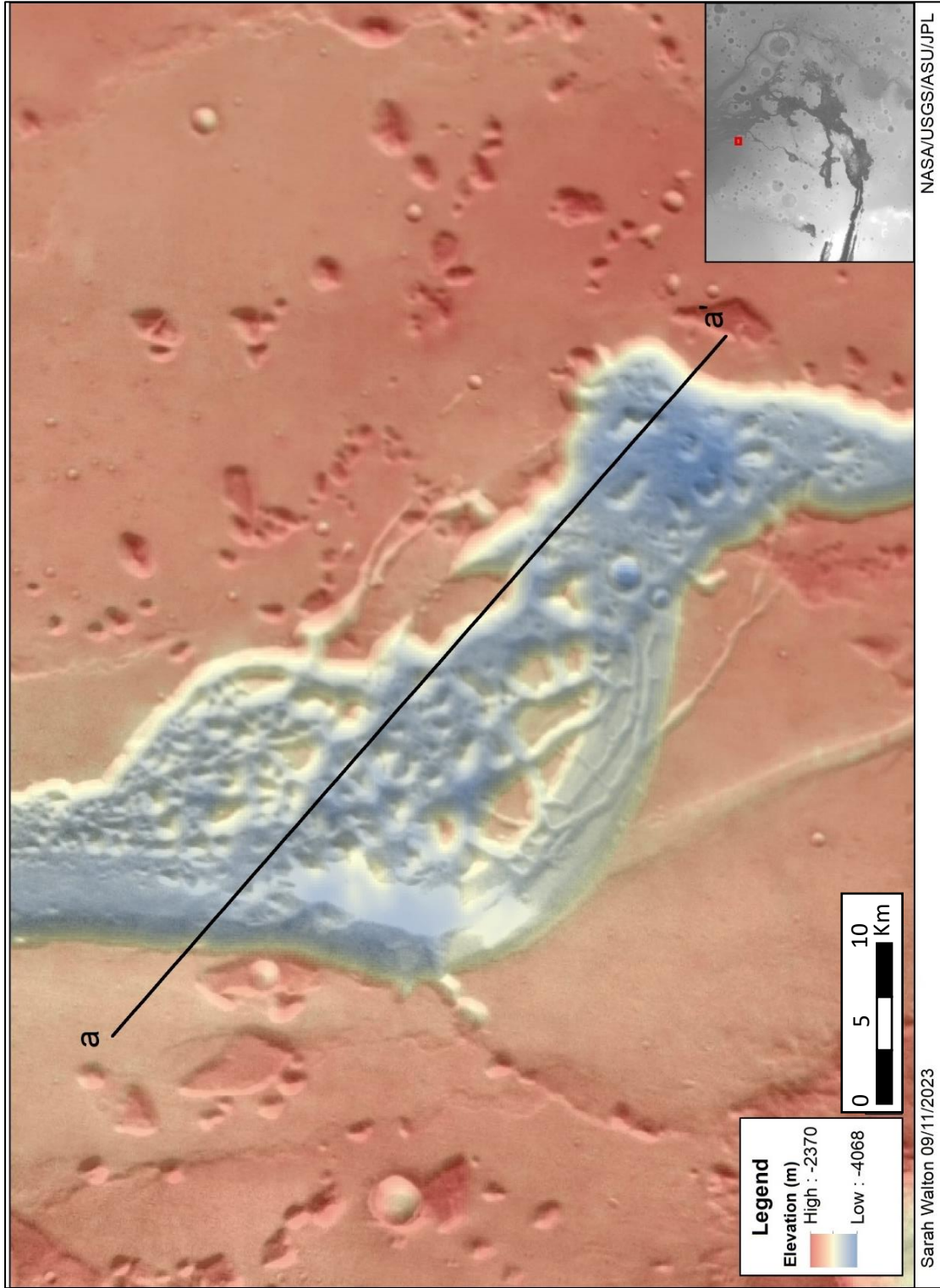


Figure 72: Topographic profile taken in Xanthe Chaos.

Xanthe Chaos Topographic Profile a – a'

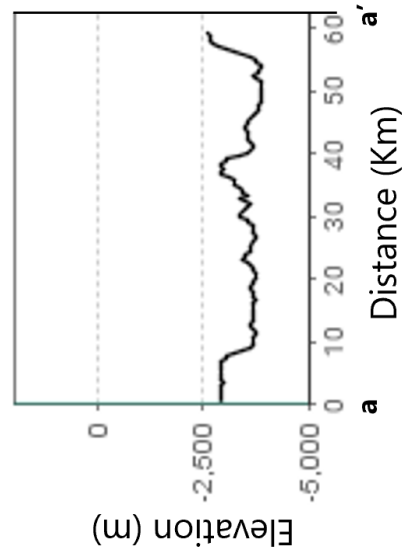


Figure 73: Topographic of Xanthe Chaos.

Slope Analysis

Slope analysis was performed within localized west, central, and east branches of NL for scale comparison to the chaotic terrains (Figures 74 -76). Slopes throughout NL mesa walls are nominally 25 – 45 degrees within slump features on mesa walls and vary between 0 - 15 degrees on the trough floor of NL. In areas in proximity to Valles Marineris, slope exceeds 45 degrees, where mesa walls become visibly steeper (Figure 76). Slopes within chaotic terrains (Figures 77 – 95) vary with locality and degradation state but do not exceed 45 degrees compared to the slopes seen within NL. Slopes are consistently 0 – 15 degrees, where high slopes are associated with mesa walls surrounded by relatively flat chaos floors.

Calculation of percent area per classification of slope break showed that NL has a higher percentage of area that surpasses 15-degree slopes, while the chaotic terrains show shallower average slopes (Tables 2 – 22). Both locations show a high percent area of 0 -2 degrees slope but may be bias due to flat areas surrounding the areas that may not be representative of the true nature of the features themselves. When plotting the percent area of each slope break of all sites against another, NL is anomalous with slopes of elevated value than the chaotic terrains (Figure 96). When comparing individual chaotic terrain slope analyses, four groups of chaotic terrains representing different stages of

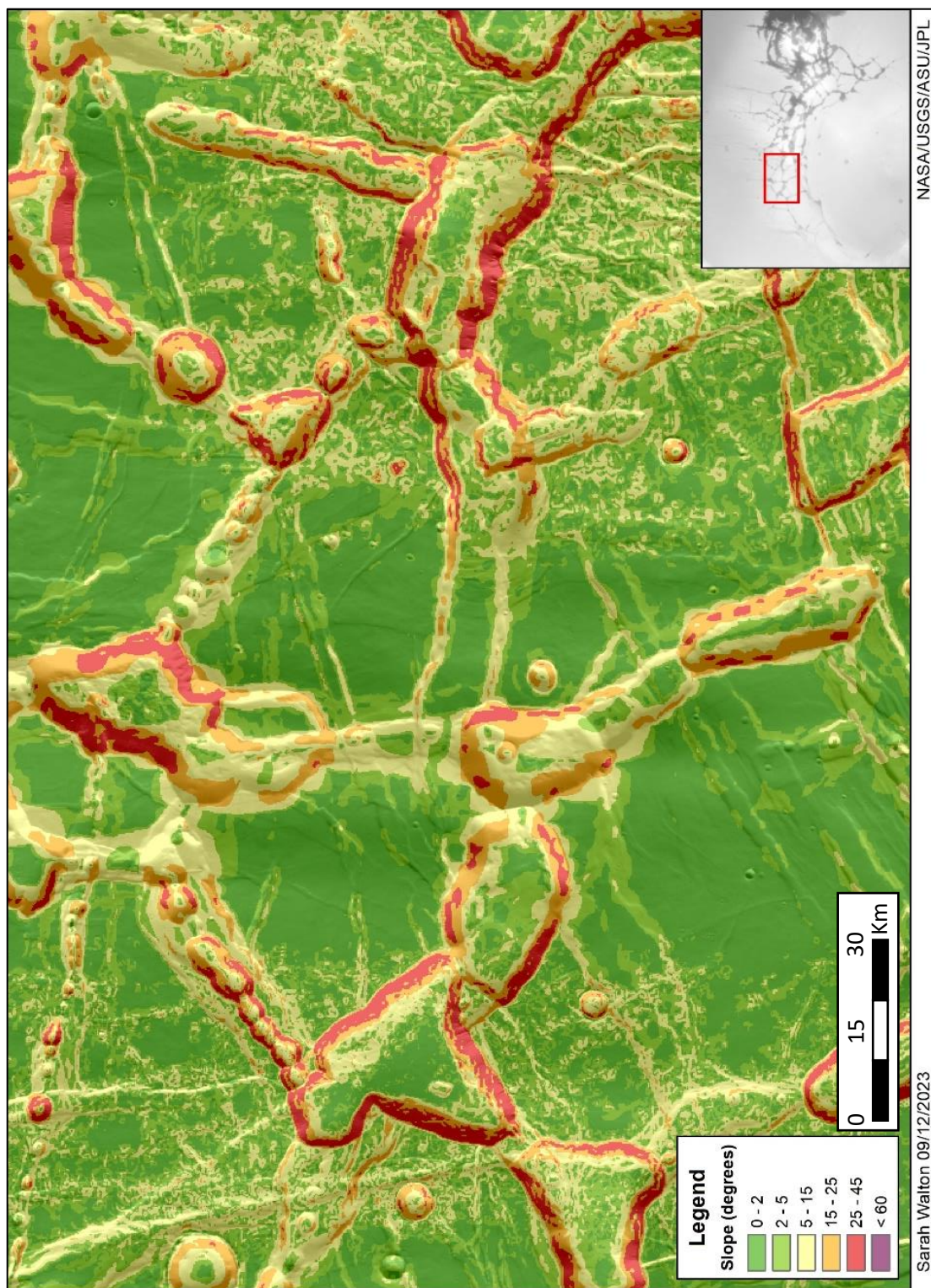


Figure 74: Slope profiles within west NL.

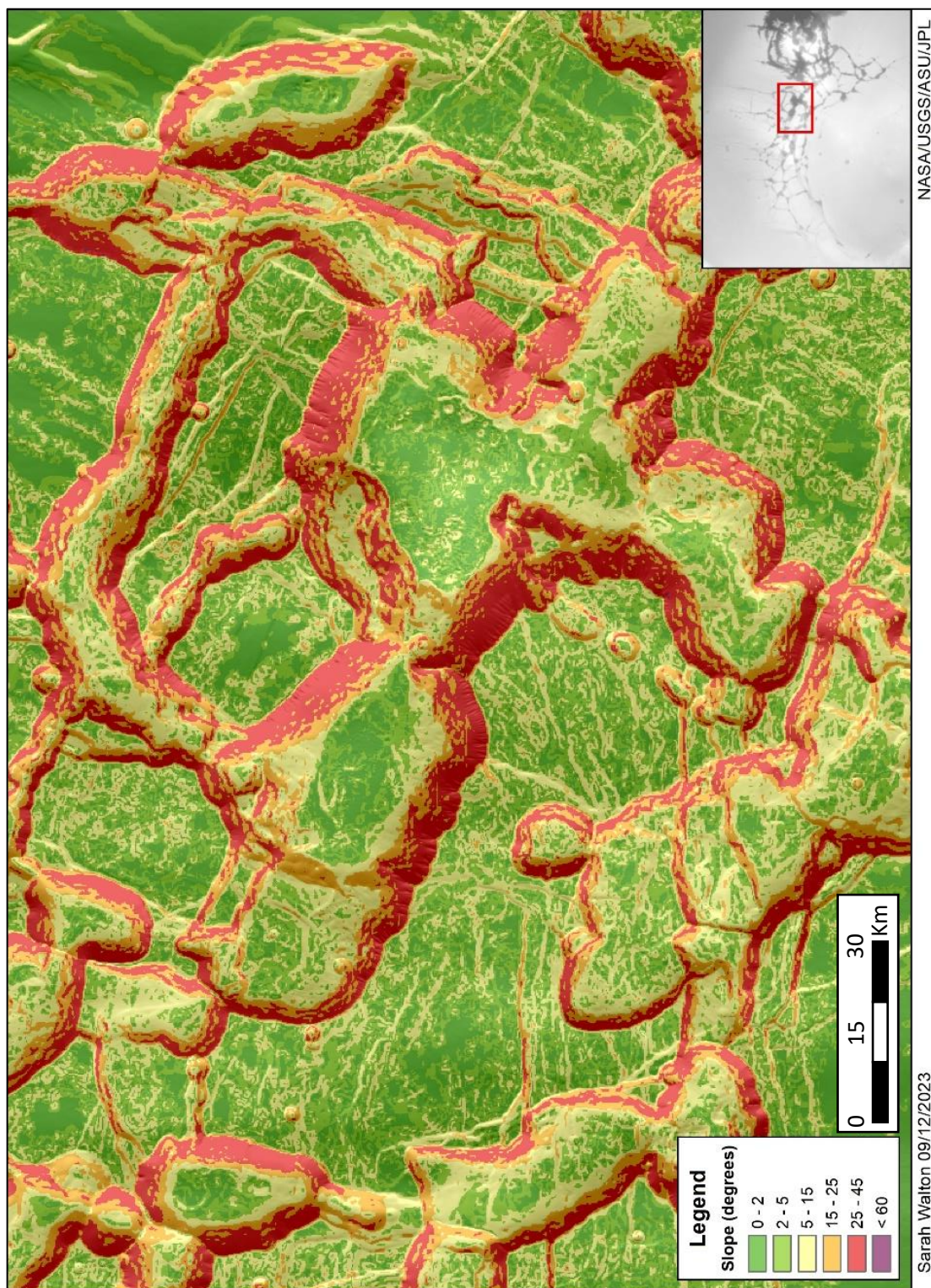


Figure 75: Slope profiles within central NL.

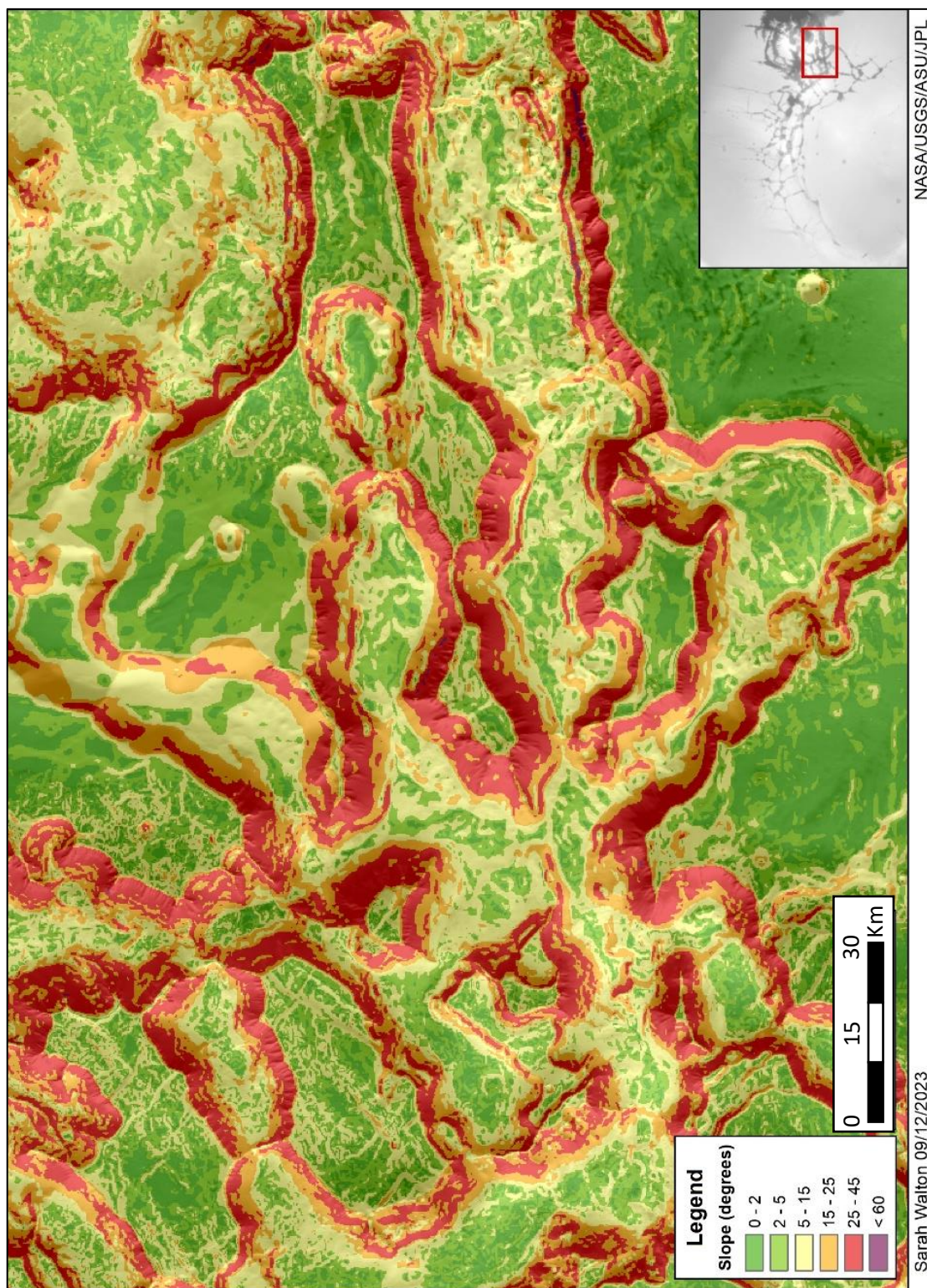


Figure 76 Slope profiles within east NL.

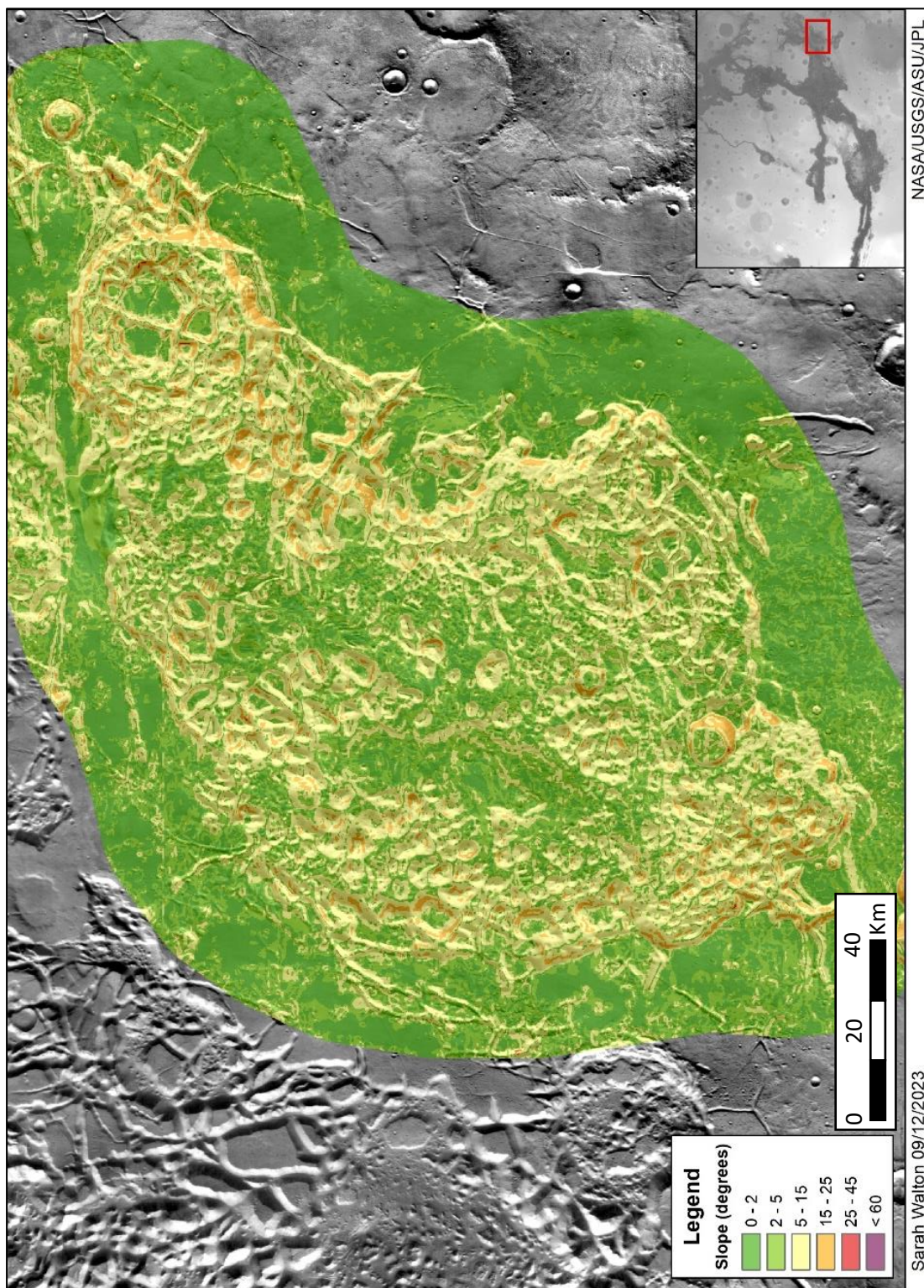


Figure 77: Slope profiles within Arsinoes Chaos.

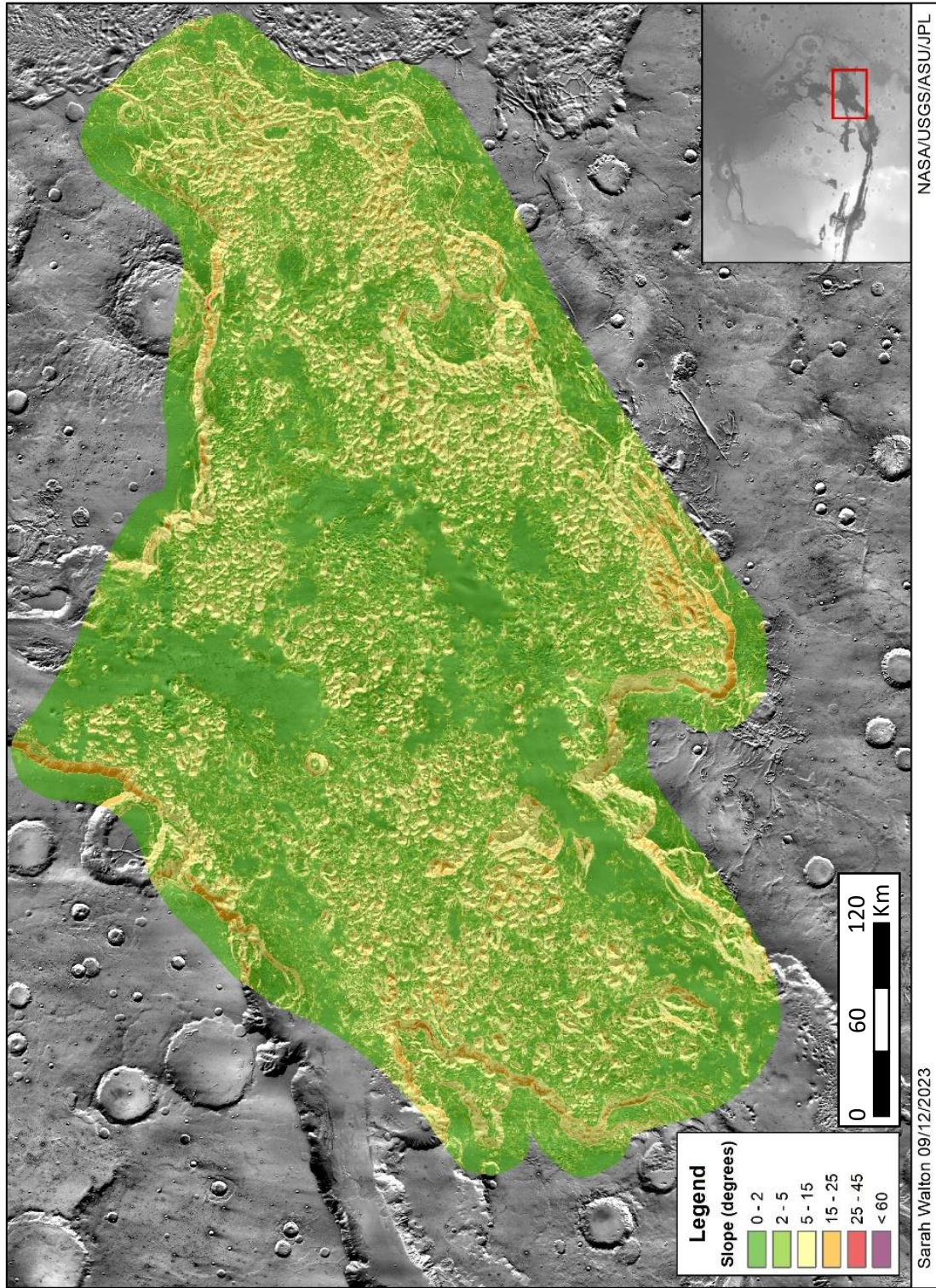


Figure 78: Slope profiles within Aurorae Chaos.

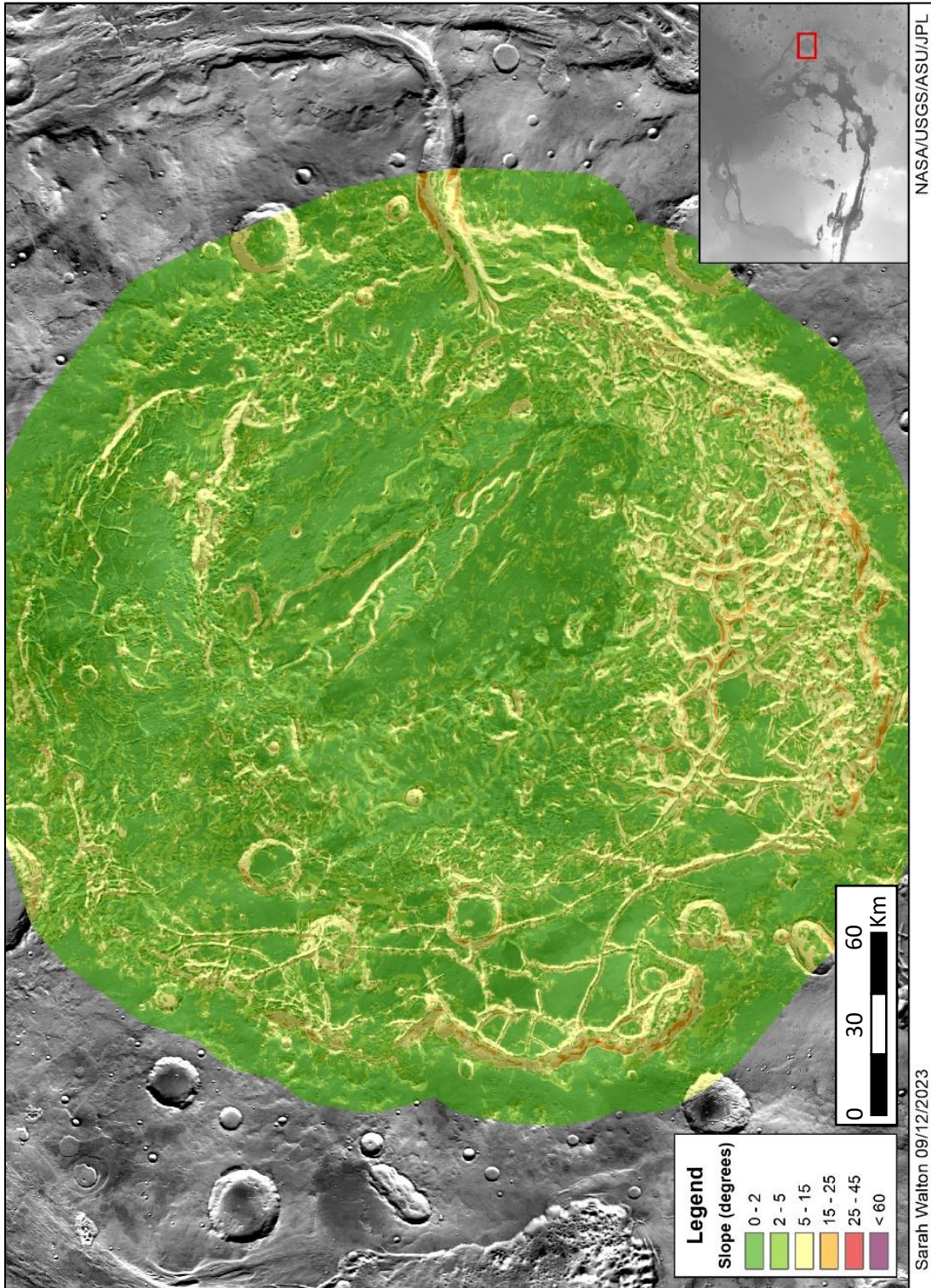


Figure 79: Slope profiles within Aram Chaos.

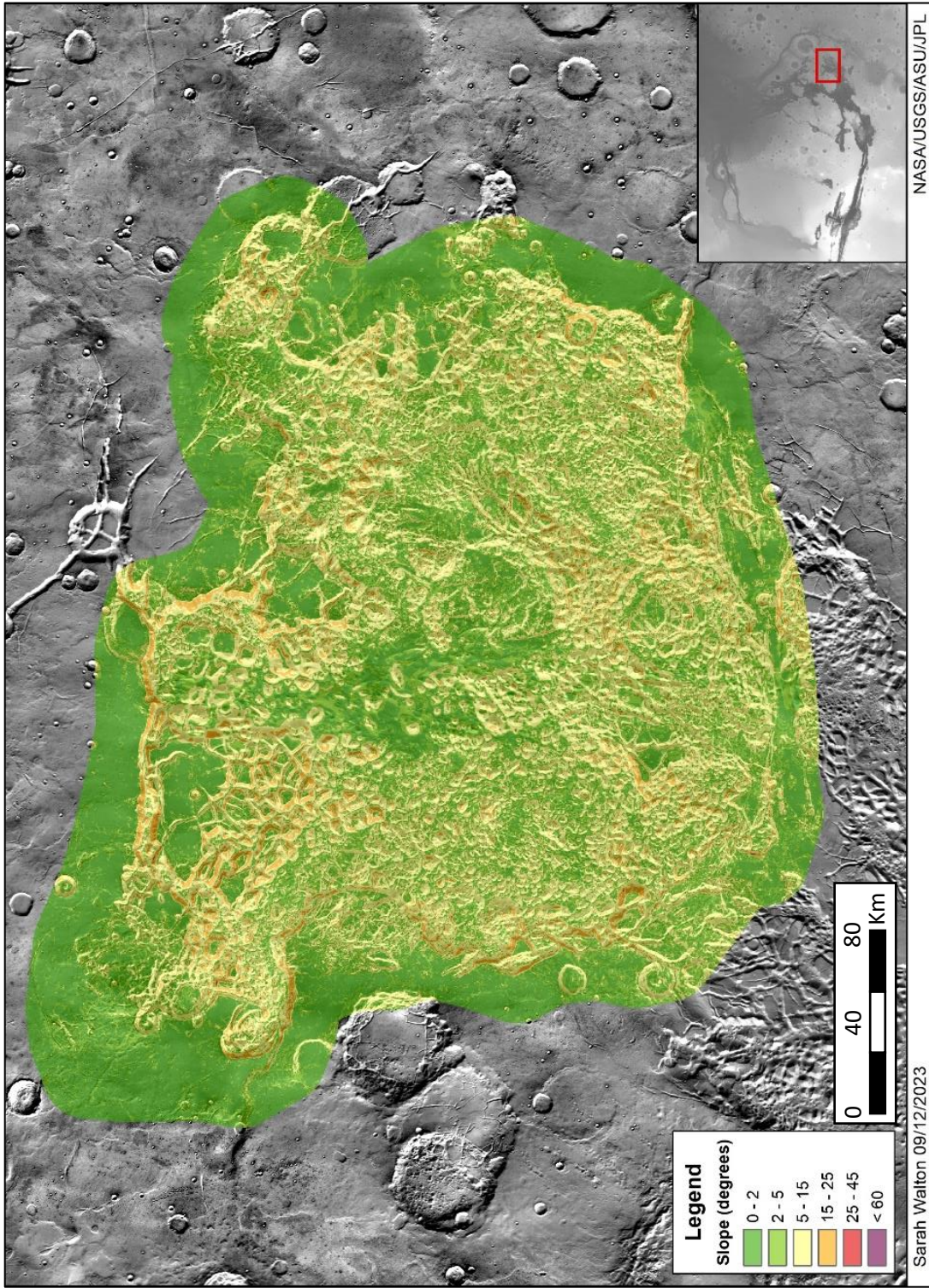


Figure 80: Slope profiles within Aureum Chaos.

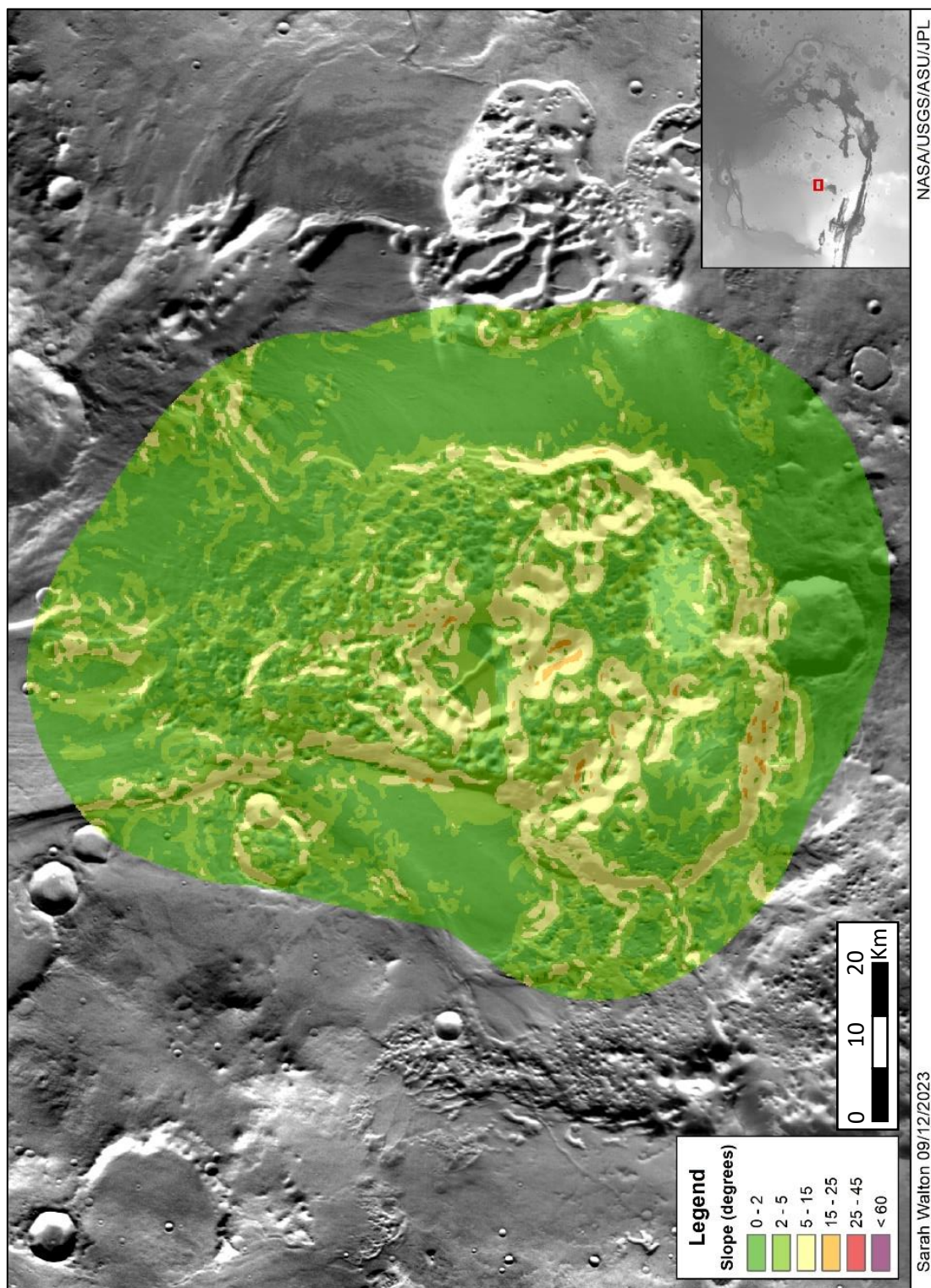


Figure 81: Slope profiles within Baetis Chaos.

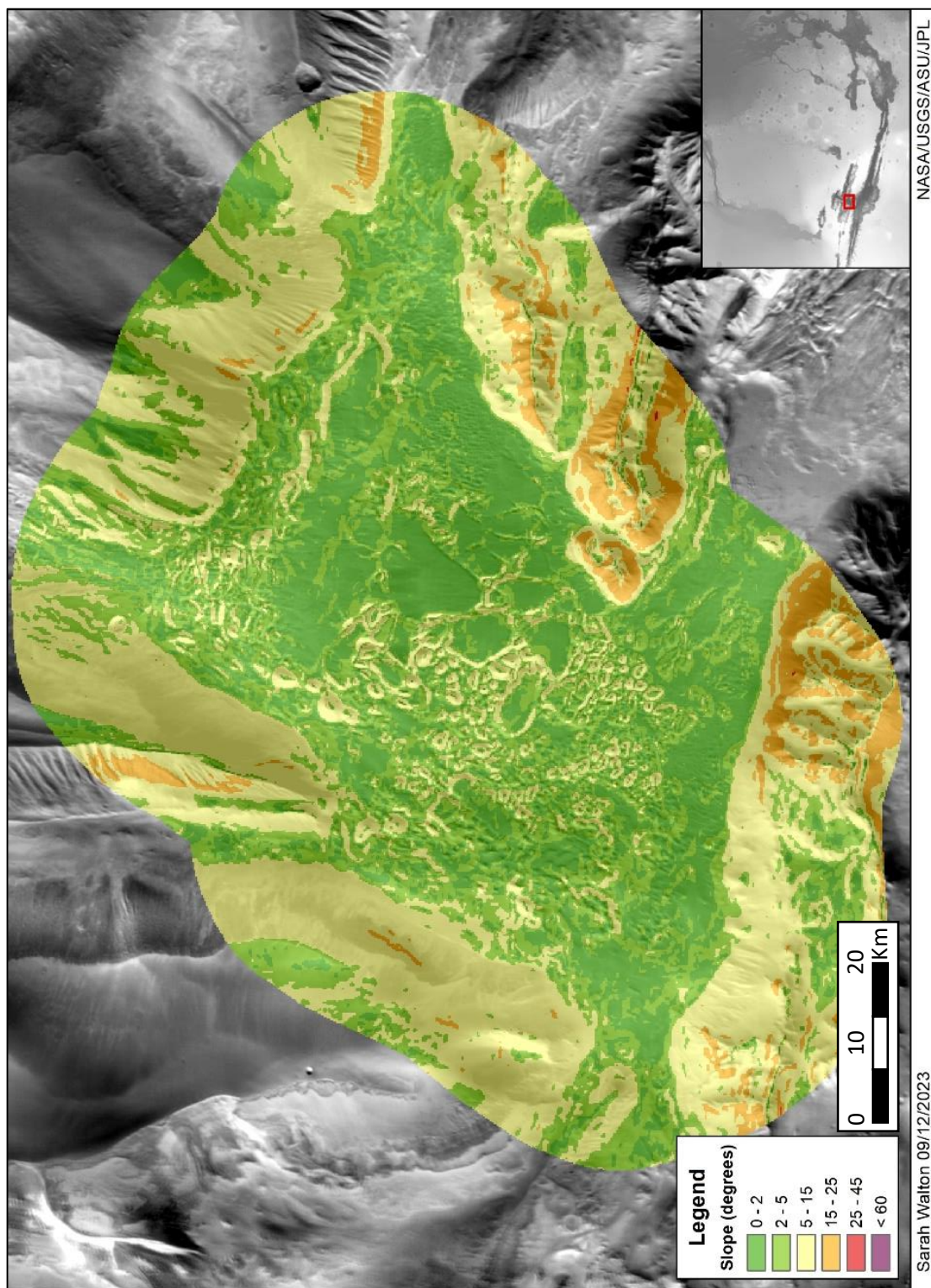


Figure 82: Slope profiles within Candor Chaos.

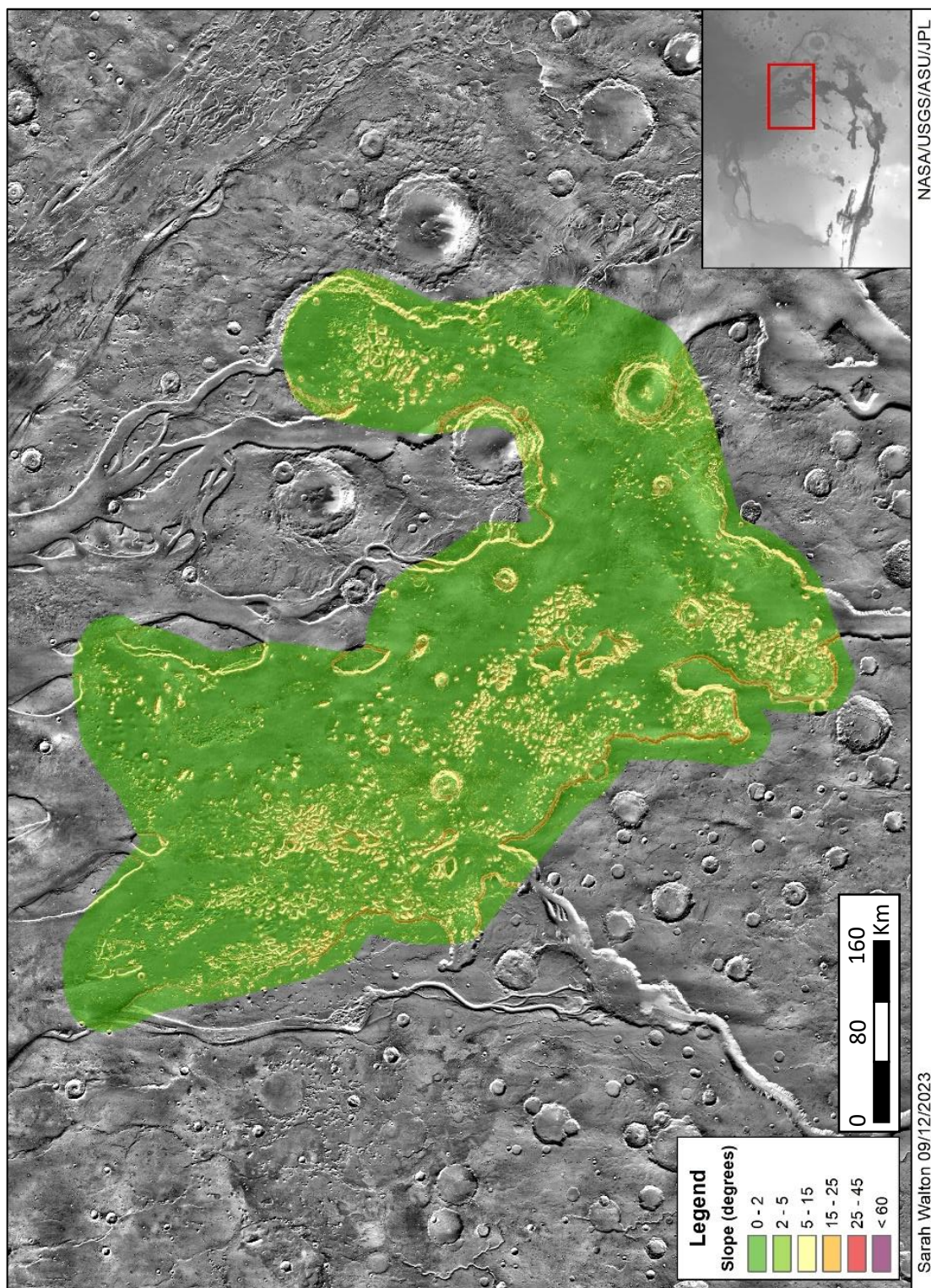


Figure 83: Slope profiles within Chryse Chaos.

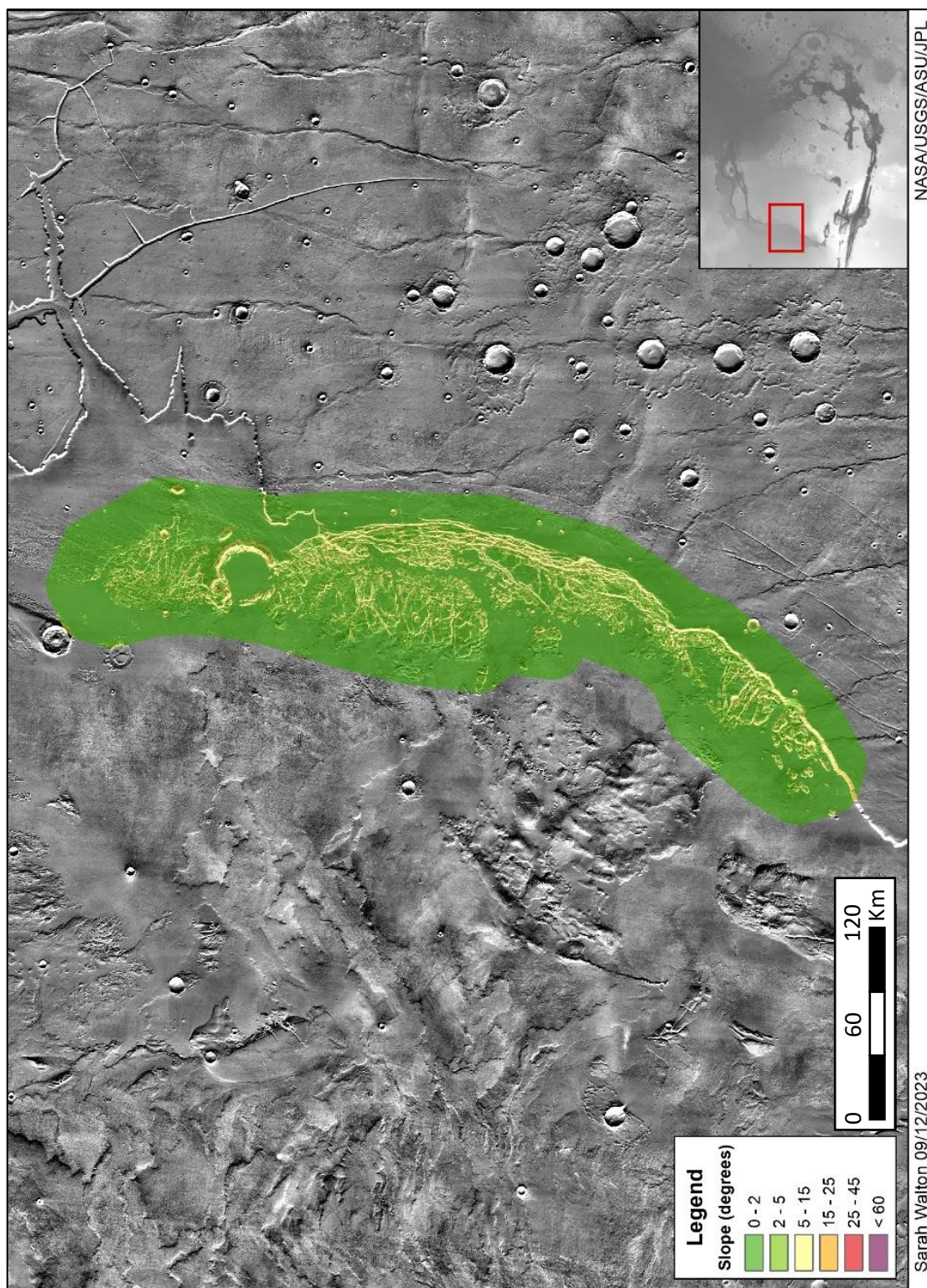


Figure 84: Slope profiles within Echus Chaos.

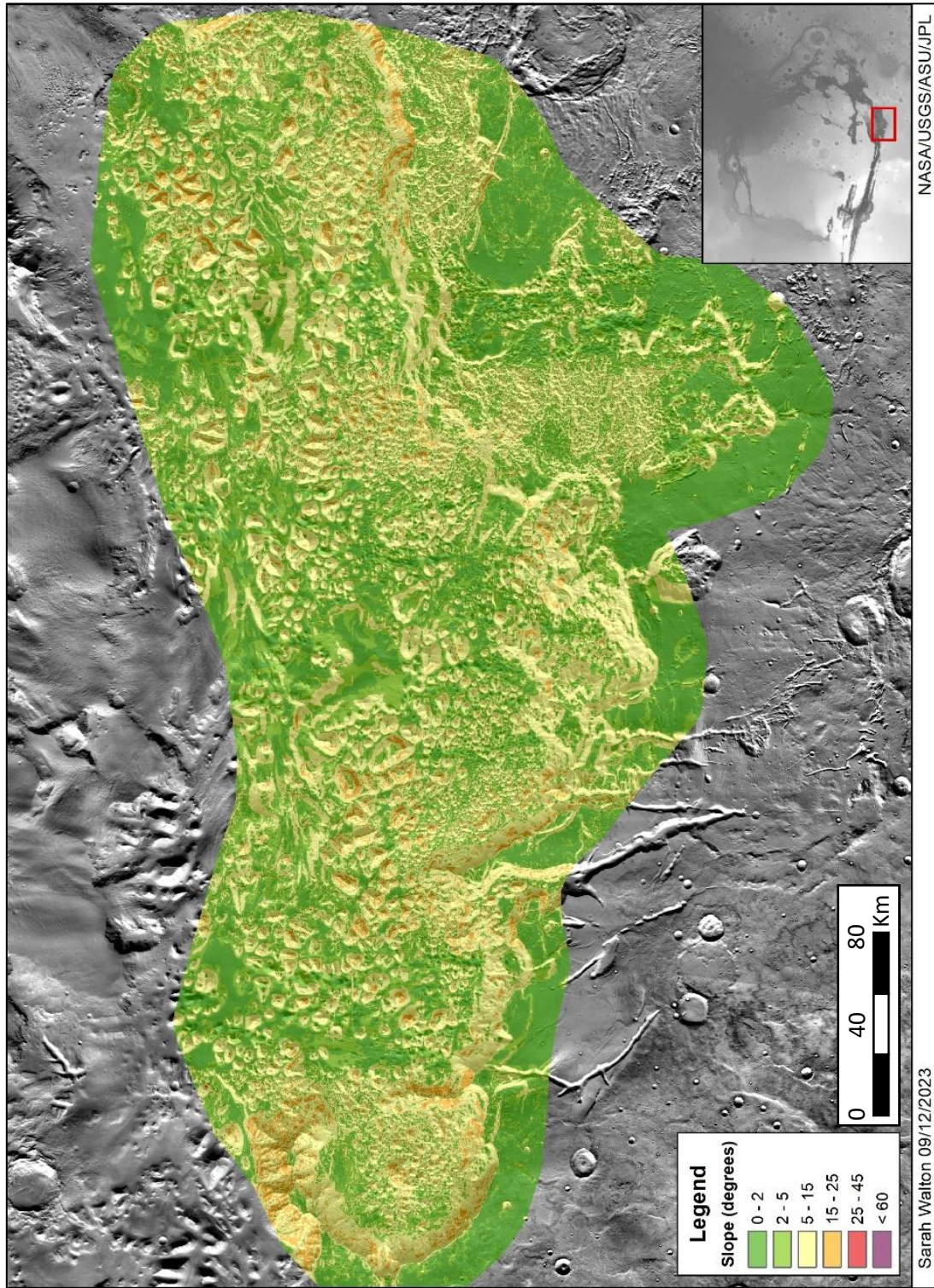


Figure 85: Slope profiles within Eos Chaos.

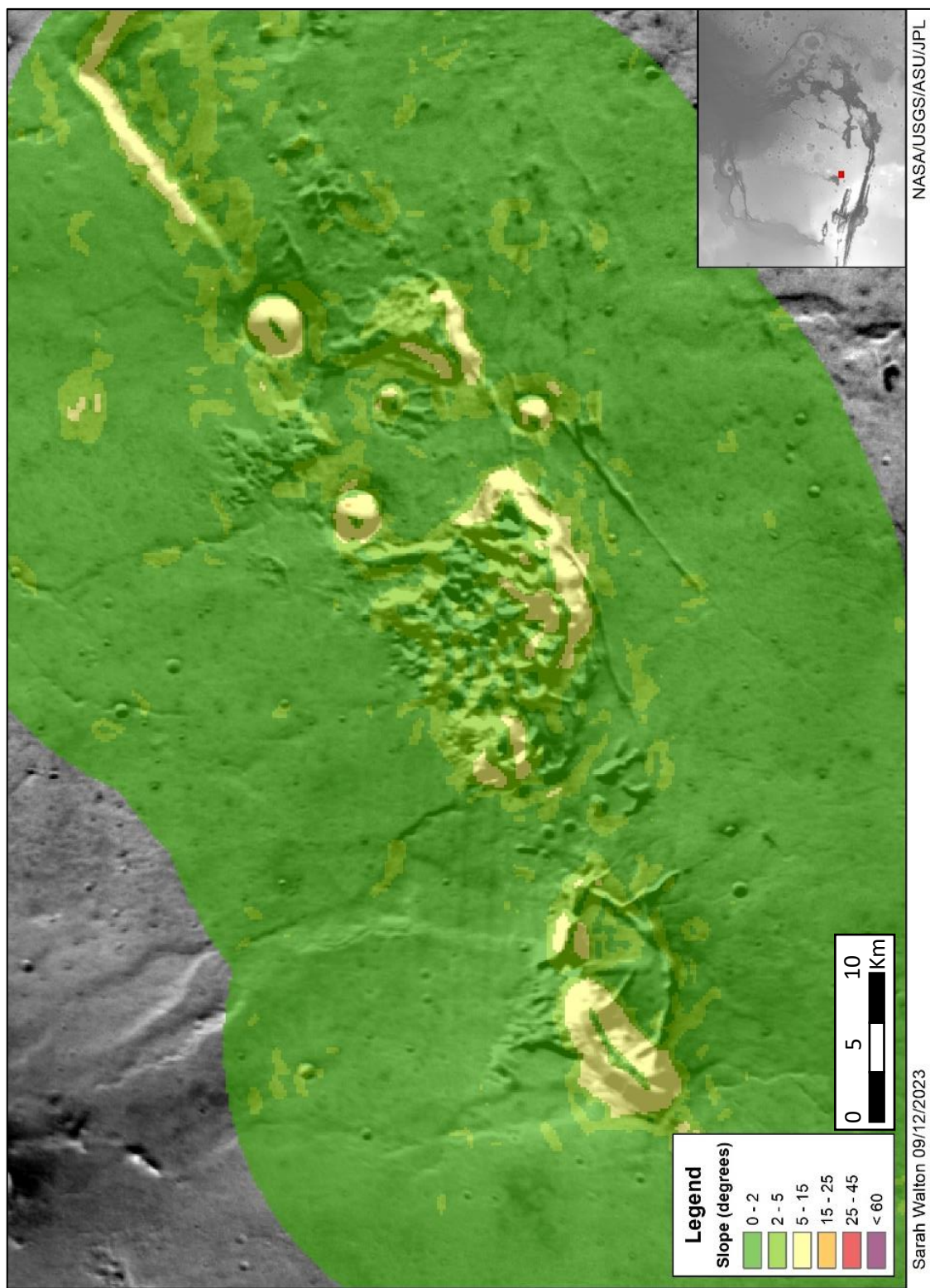


Figure 86: Slope profiles within Hydræ Chaos.

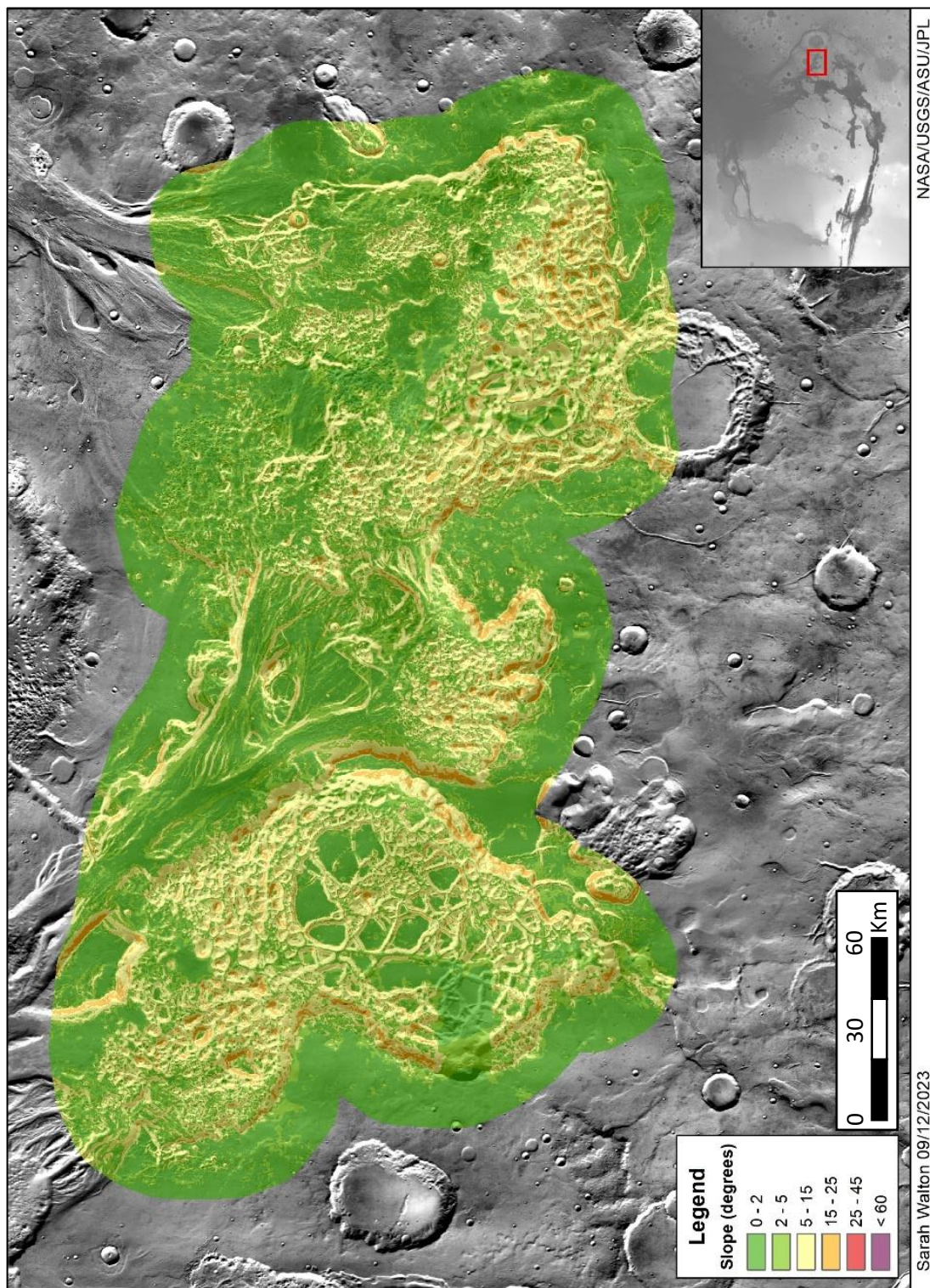


Figure 87: Slope profiles within Hydaspis Chaos.

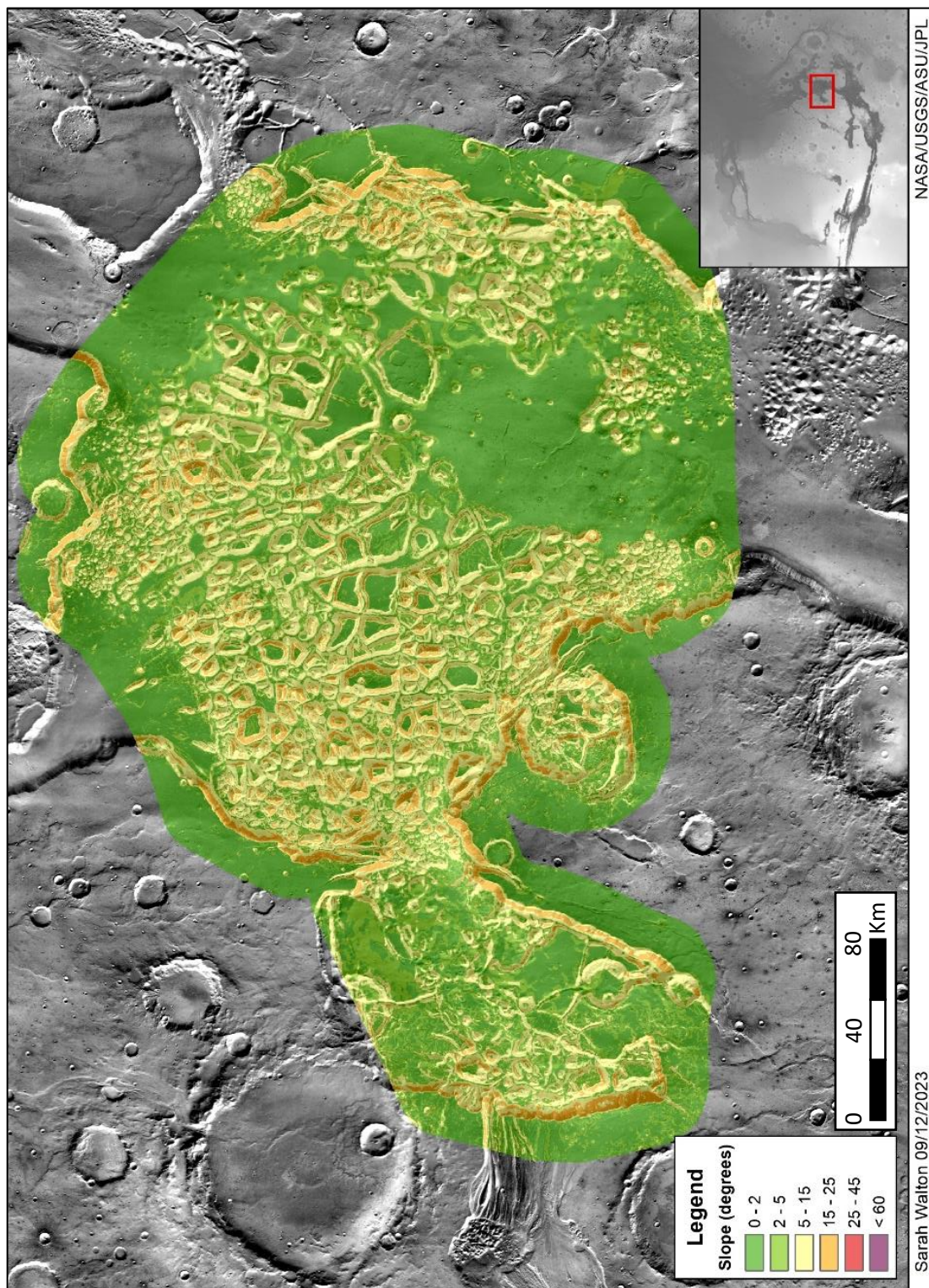


Figure 88: Slope profiles within Hydrates Chaos.

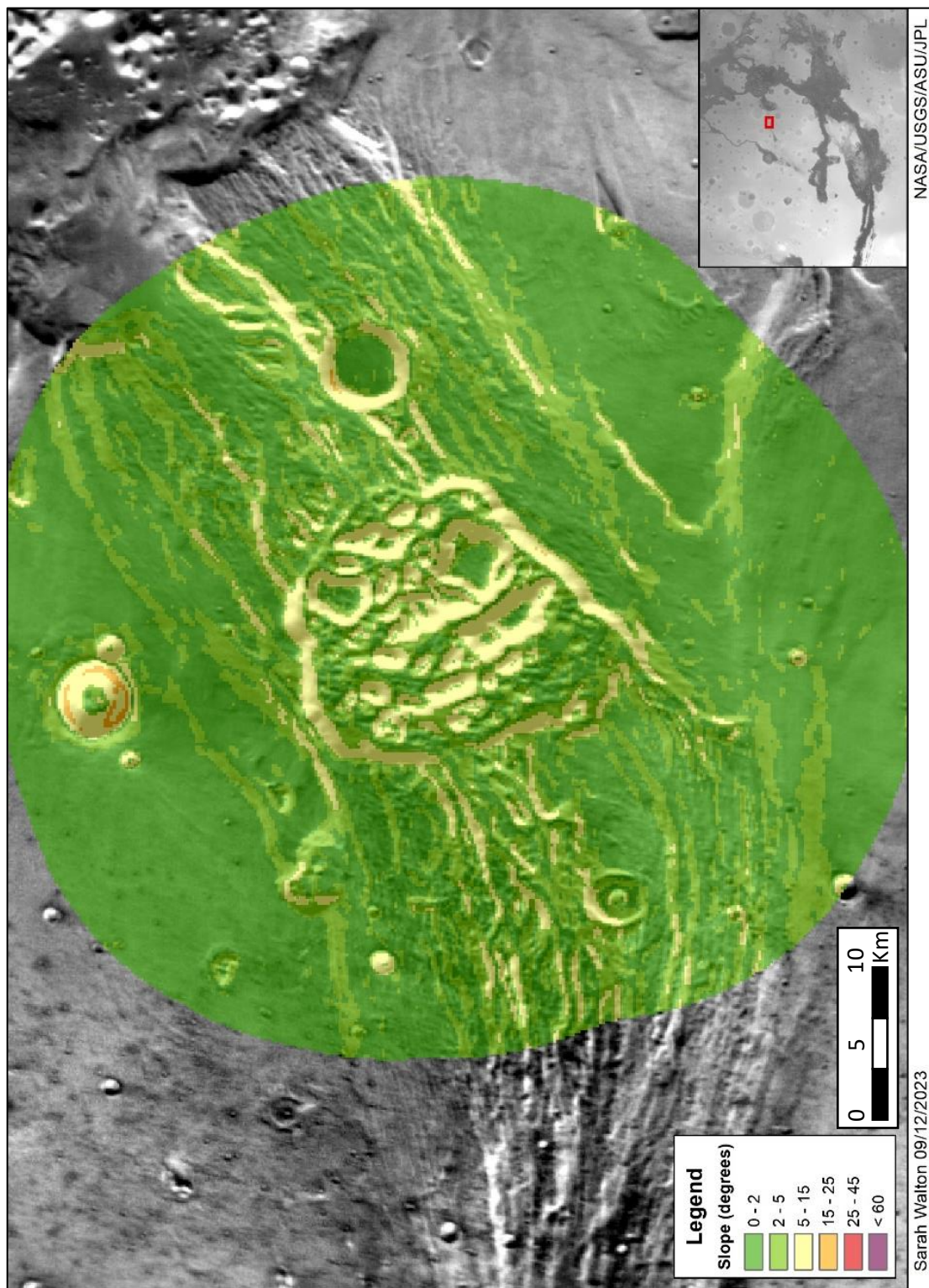


Figure 89: Slope profiles within lamuna Chaos.

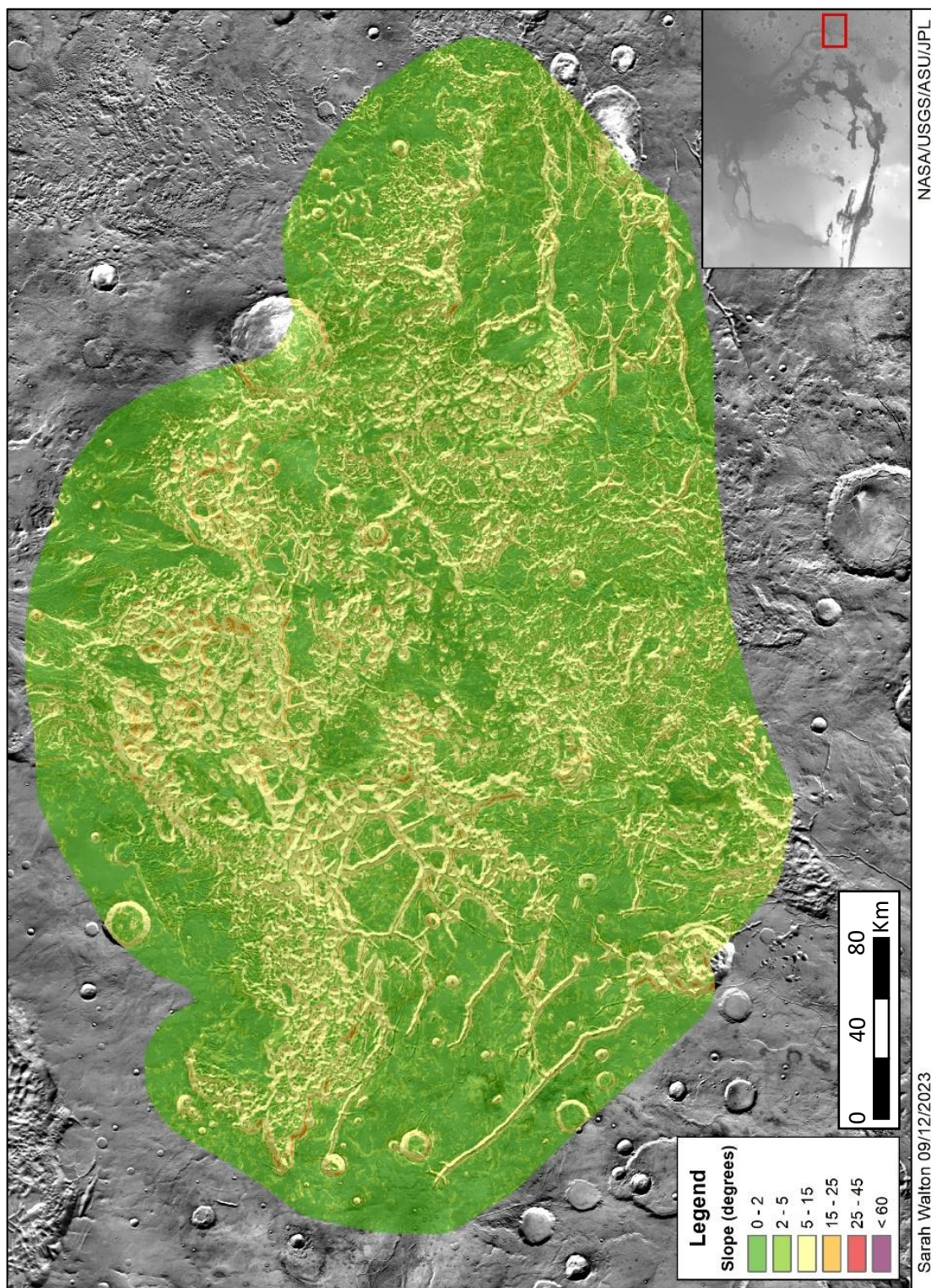


Figure 90: Slope profiles within Iani Chaos.

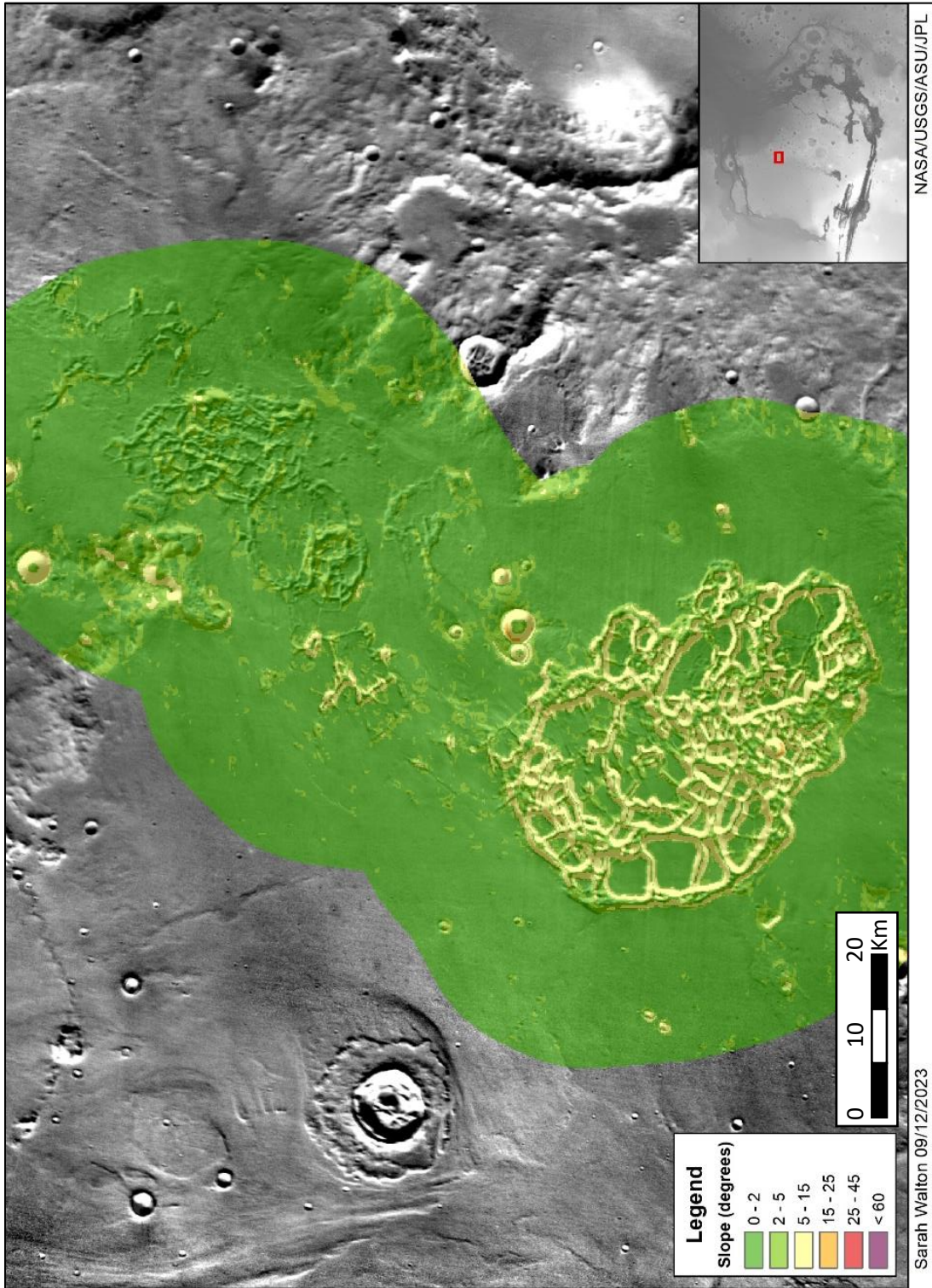


Figure 91: Slope profiles within Ister Chaos.

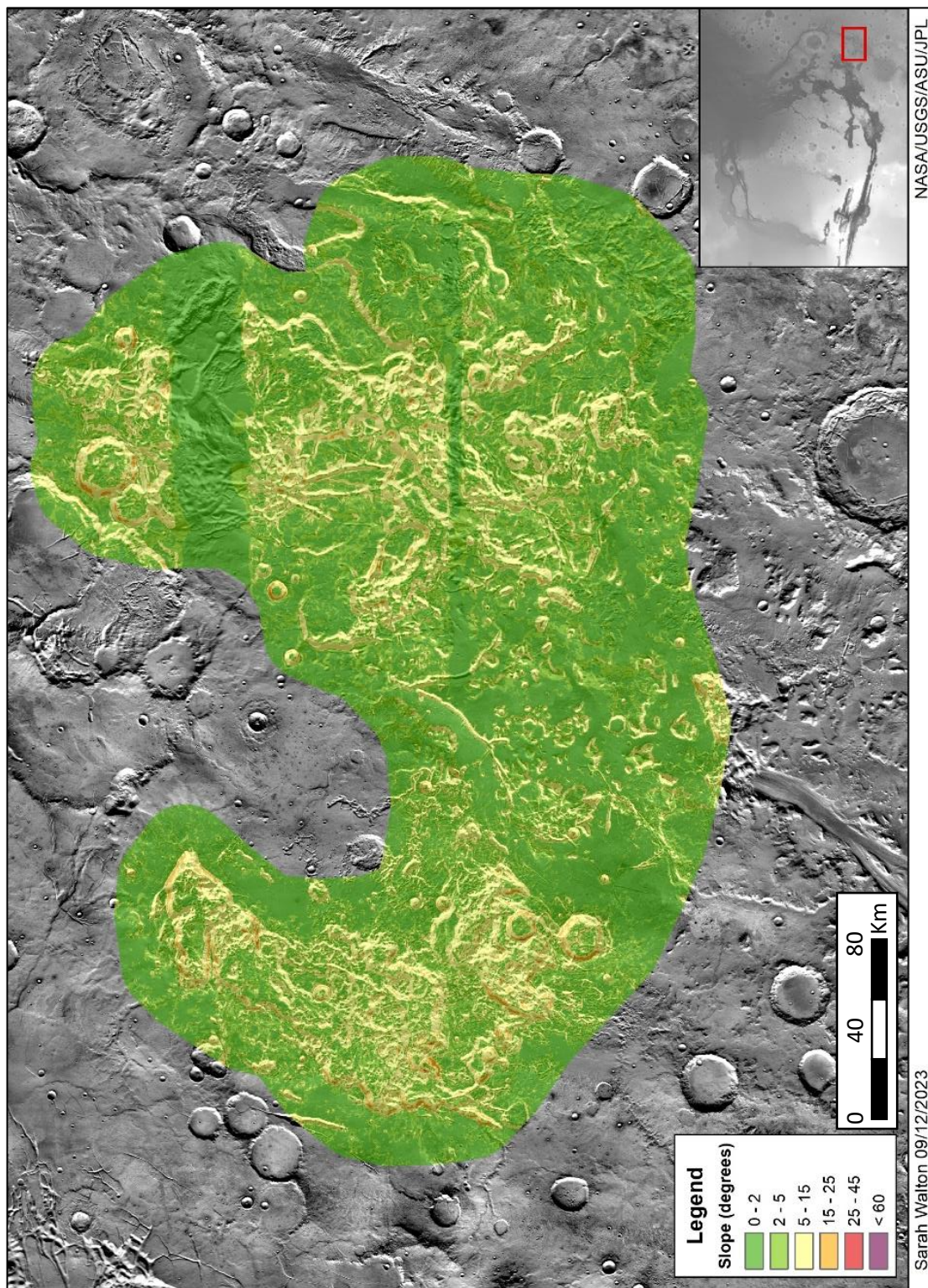


Figure 92: Slope profiles within Margaritifer Chaos.

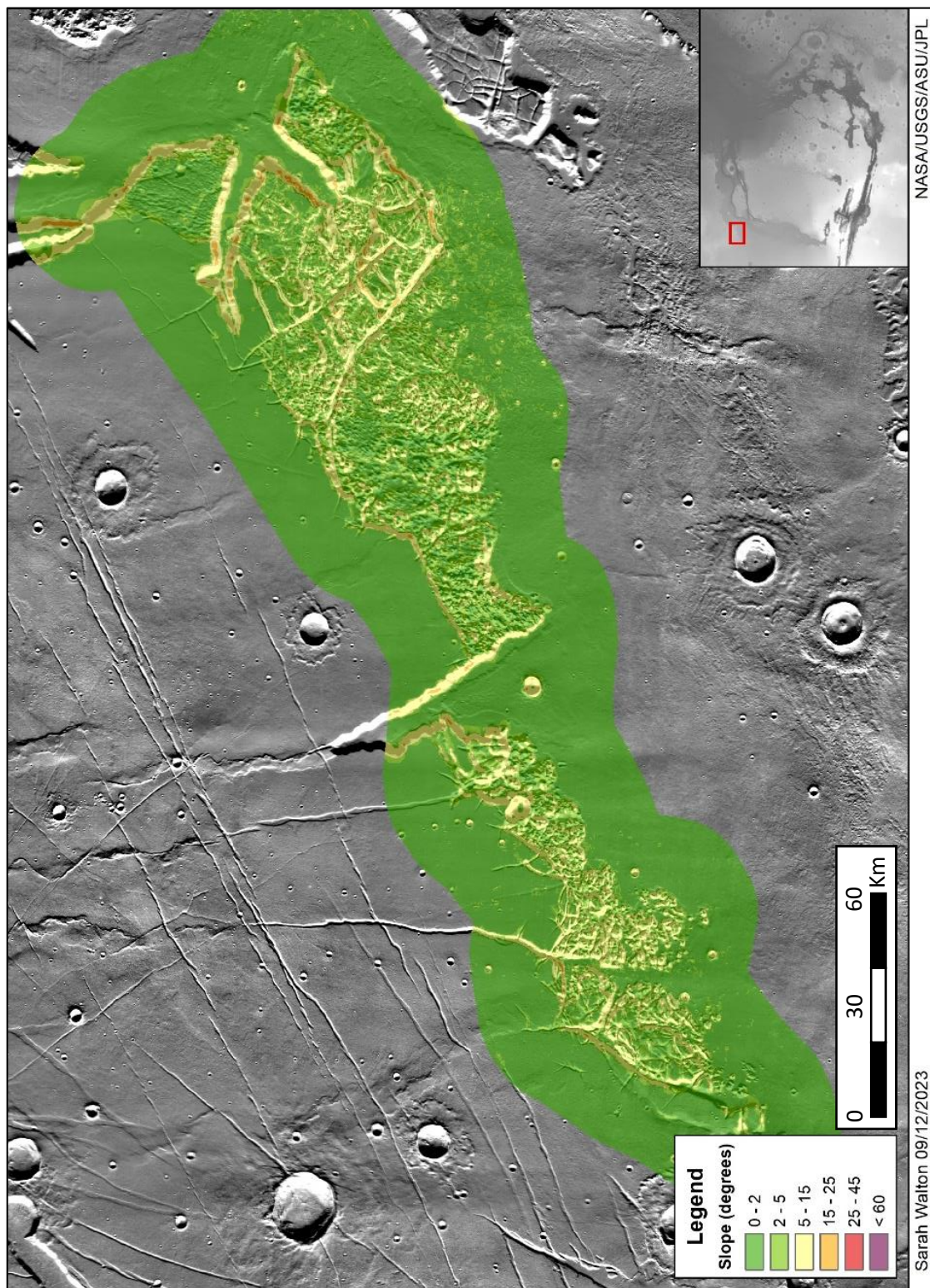


Figure 93: Slope profiles within Nilus Chaos.

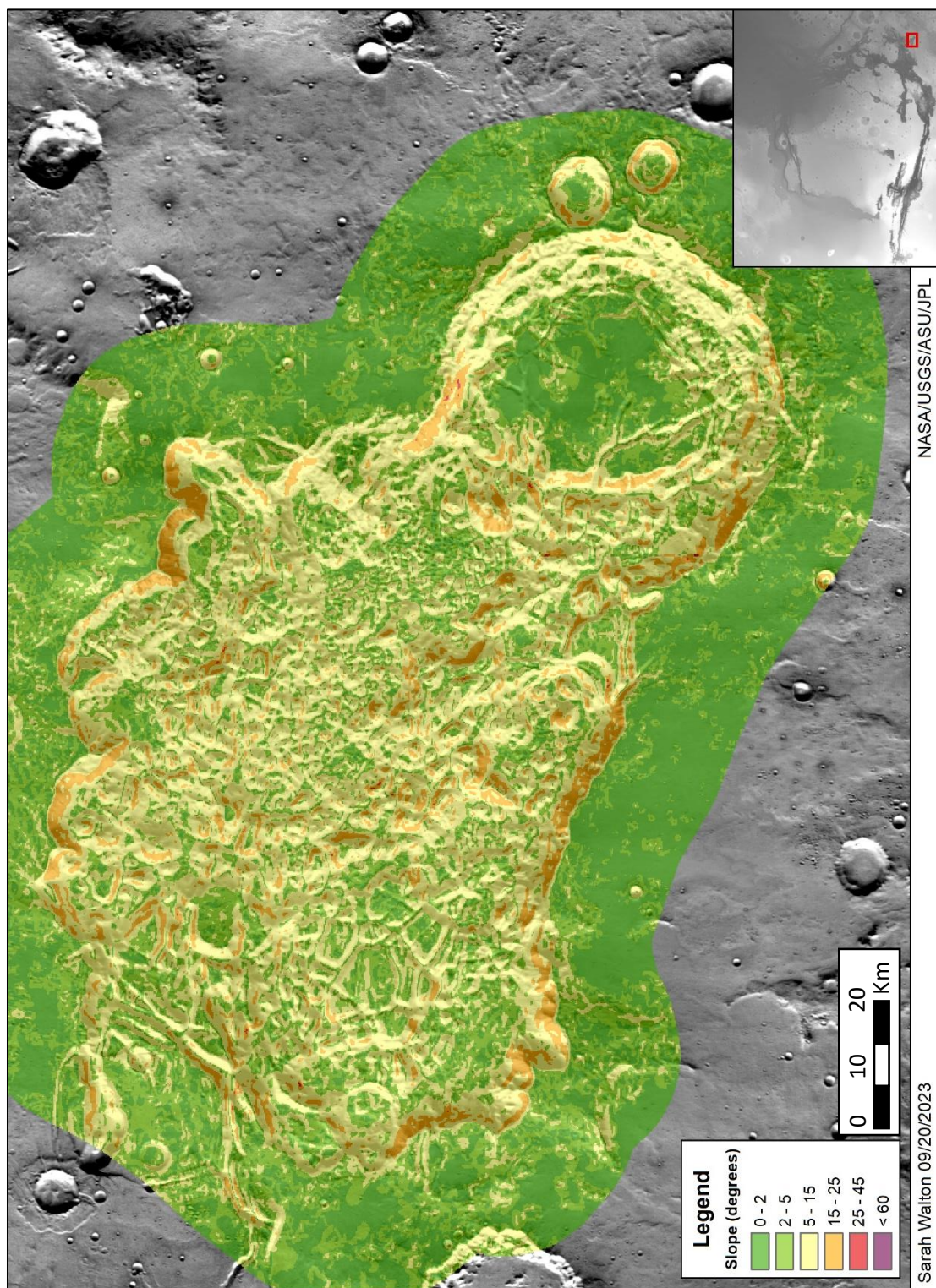


Figure 94: Slope profiles within Pyrrhae Chaos.

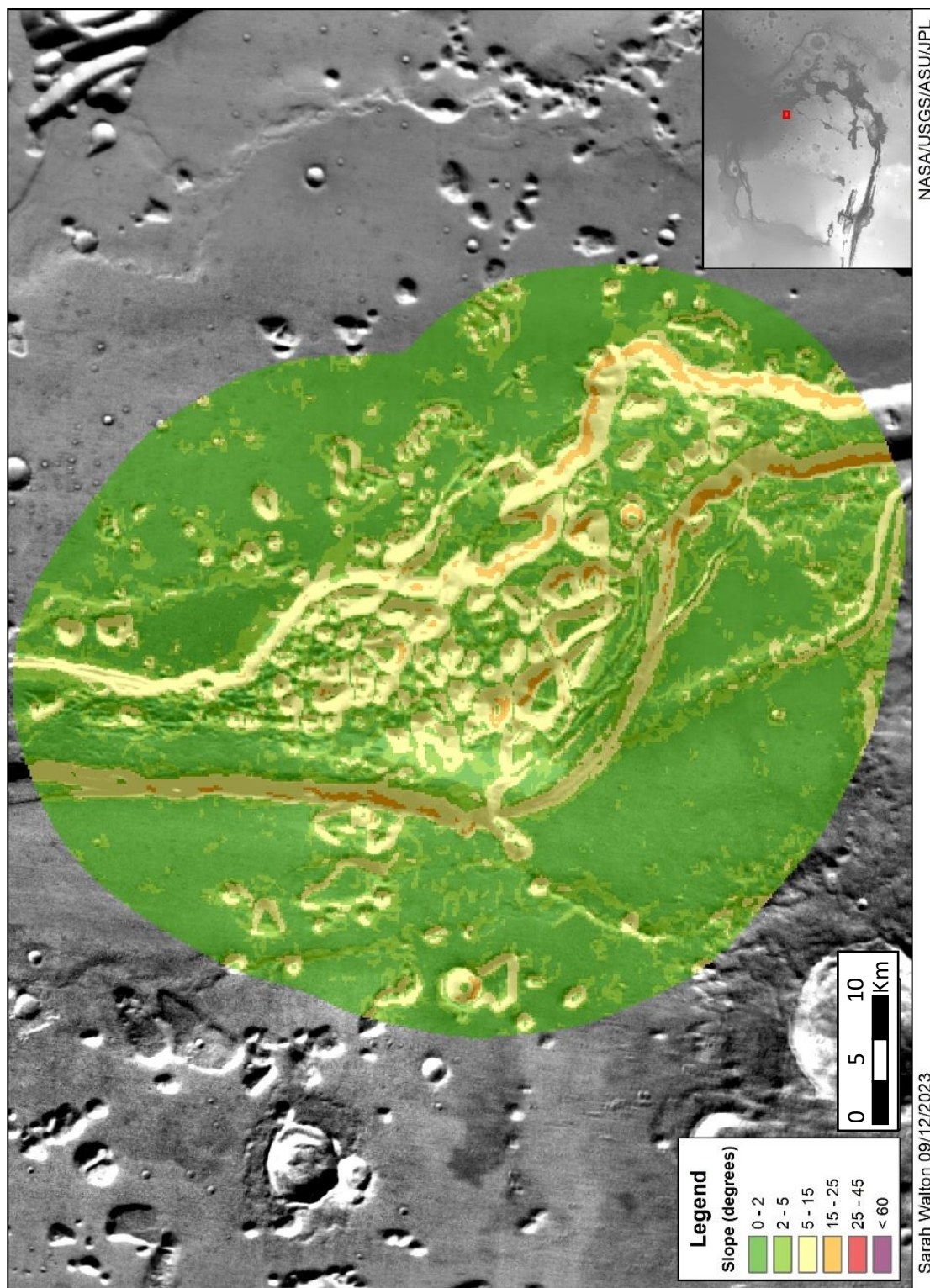


Figure 95: Slope profiles within Xanthe Chaos.

Table 2: Slope classifications measured by percent area within NL.

<i>Noctis Labyrinthus</i>		
Slope (deg.)	Shape Area (km ²)	Percent Area (%)
0 -2	276689.08	47.84
2 - 5	131991.25	22.82
5 - 15	95736.07	16.55
15 -25	41626.63	7.20
25 - 45	32213.66	5.57
45 - 60	70.76	0.01
Sum Shape Area (km²)	578327.45	

Table 3: Slope classifications measured by percent area within all chaotic terrains.

<i>Composite Chaotic Terrains</i>		
Slope (deg.)	Shape Area (km ²)	Percent Area (%)
2	546848.33	42.63
5	366064.50	28.54
15	335790.47	26.18
25	33878.40	2.64
45	113.94	0.01
60	0.00	0.00
Sum Shape Area (km²)	1282695.64	

Table 4: Slope classifications measured by percent area within Arsinoes Chaos.

<i>Arsinoes Chaos</i>		
Slope (deg.)	Shape Area (km²)	Percent Area (%)
0 -2	9046.93	27.88
2 - 5	9963.01	30.71
5 - 15	12135.35	37.40
15 -25	1296.07	3.99
25 - 45	4.48	0.01
45 - 60	0.00	0.00
Sum Shape Area (km²)	32445.84	

Table 5: Slope classifications measured by percent area within Aurorae Chaos.

<i>Aurorae Chaos</i>		
Slope (deg.)	Shape Area (km²)	Percent Area (%)
0 -2	71679.71	30.91
2 - 5	81615.60	35.20
5 - 15	71391.04	30.79
15 -25	7141.33	3.08
25 - 45	66.16	0.03
45 - 60	0.00	0.00
Sum Shape Area (km²)	231893.84	

Table 6: Slope classifications measured by percent area within Aram Chaos.

<i>Aram Chaos</i>		
Slope (deg.)	Shape Area (km²)	Percent Area (%)
0 -2	35434.53	45.13
2 - 5	27915.66	35.55
5 - 15	14419.71	18.36
15 -25	747.94	0.95
25 - 45	4.98	0.01
45 - 60	0.00	0.00
Sum Shape Area (km²)	78522.82	

Table 7: Slope classifications measured by percent area within Aureum Chaos.

<i>Aureum Chaos</i>		
Slope (deg.)	Shape Area (km²)	Percent Area (%)
0 -2	28997.09	28.27
2 - 5	28684.16	27.96
5 - 15	40346.46	39.33
15 -25	4532.81	4.42
25 - 45	13.47	0.01
45 - 60	0.00	0.00
Sum Shape Area (km²)	102573.98	

Table 8: Slope classifications measured by percent area within Baetis Chaos.

<i>Baetis Chaos</i>		
Slope (deg.)	Shape Area (km²)	Percent Area (%)
0 -2	3660.08	47.22
2 - 5	2714.84	35.02
5 - 15	1354.53	17.47
15 -25	22.38	0.29
25 - 45	0.00	0.00
45 - 60	0.00	0.00
Sum Shape Area (km²)	7751.83	

Table 9: Slope classifications measured by percent area within Candor Chaos.

<i>Candor Chaos</i>		
Slope (deg.)	Shape Area (km²)	Percent Area (%)
0 -2	2711.81	25.09
2 - 5	3055.34	28.26
5 - 15	4410.78	40.80
15 -25	630.63	5.83
25 - 45	1.33	0.01
45 - 60	0.00	0.00
Sum Shape Area (km²)	10809.90	

Table 10: Slope classifications measured by percent area within Chryse Chaos.

<i>Chryse Chaos</i>		
Slope (deg.)	Shape Area (km²)	Percent Area (%)
0 - 2	152658.41	65.37
2 - 5	46494.56	19.91
5 - 15	30445.26	13.04
15 - 25	3937.82	1.69
25 - 45	1.15	0.00
45 - 60	0.00	0.00
Sum Shape Area (km²)	233537.21	

Table 11: Slope classifications measured by percent area within Echus Chaos.

<i>Echus Chaos</i>		
Slope (deg.)	Shape Area (km²)	Percent Area (%)
0 - 2	37748.89	71.58
2 - 5	9315.58	17.67
5 - 15	5483.74	10.40
15 - 25	185.41	0.35
25 - 45	0.32	0.00
45 - 60	0.00	0.00
Sum Shape Area (km²)	52733.93	

Table 12: Slope classifications measured by percent area within Eos Chaos.

<i>Eos Chaos</i>		
Slope (deg.)	Shape Area (km²)	Percent Area (%)
0 -2	27910.23	25.55
2 - 5	33227.44	30.41
5 - 15	43774.14	40.06
15 -25	4336.96	3.97
25 - 45	9.58	0.01
45 - 60	0.00	0.00
Sum Shape Area (km²)	109258.35	

Table 13: Slope classifications measured by percent area within Hydaspiis Chaos.

<i>Hydaspiis Chaos</i>		
Slope (deg.)	Shape Area (km²)	Percent Area (%)
0 -2	21076.08	37.33
2 - 5	16236.37	28.76
5 - 15	17208.04	30.48
15 -25	1936.57	3.43
25 - 45	1.62	0.00
45 - 60	0.00	0.00
Sum Shape Area (km²)	56458.68	

Table 14: Slope classifications measured by percent area within Hydræ Chaos.

<i>Hydræ Chaos</i>		
Slope (deg.)	Shape Area (km²)	Percent Area (%)
0 -2	4134.45	84.98
2 - 5	587.54	12.08
5 - 15	143.10	2.94
15 -25	0.05	0.00
25 - 45	0.00	0.00
45 - 60	0.00	0.00
Sum Shape Area (km²)	4865.14	

Table 15: Slope classifications measured by percent area within Hydraotes Chaos.

<i>Hydraotes Chaos</i>		
Slope (deg.)	Shape Area (km²)	Percent Area (%)
0 -2	38271.62	38.80
2 - 5	23504.14	23.83
5 - 15	30894.92	31.32
15 -25	5973.10	6.06
25 - 45	3.60	0.00
45 - 60	0.00	0.00
Sum Shape Area (km²)	98647.39	

Table 16: Slope classifications measured by percent area within lamuna Chaos.

<i>lamuna Chaos</i>		
Slope (deg.)	Shape Area (km²)	Percent Area (%)
0 -2	1733.90	62.49
2 - 5	763.00	27.50
5 - 15	273.89	9.87
15 -25	3.93	0.14
25 - 45	0.00	0.00
45 - 60	0.00	0.00
Sum Shape Area (km²)	2774.72	

Table 17: Slope classifications measured by percent area within Iani Chaos.

<i>Iani Chaos</i>		
Slope (deg.)	Shape Area (km²)	Percent Area (%)
0 -2	40853.38	34.47
2 - 5	42520.02	35.87
5 - 15	33962.91	28.65
15 -25	1189.38	1.00
25 - 45	1.59	0.00
45 - 60	0.00	0.00
Sum Shape Area (km²)	118527.29	

Table 18: Slope classifications measured by percent area within Ister Chaos.

<i>Ister Chaos</i>		
Slope (deg.)	Shape Area (km²)	Percent Area (%)
0 -2	7501.51	76.75
2 - 5	1487.49	15.22
5 - 15	782.37	8.00
15 -25	3.05	0.03
25 - 45	0.00	0.00
45 - 60	0.00	0.00
Sum Shape Area (km²)	9774.43	

Table 19: Slope classifications measured by percent area within Margaritifer Chaos.

<i>Margaritifer Chaos</i>		
Slope (deg.)	Shape Area (km²)	Percent Area (%)
0 -2	39299.67	44.04
2 - 5	29531.64	33.10
5 - 15	19569.84	21.93
15 -25	822.49	0.92
25 - 45	2.54	0.00
45 - 60	0.00	0.00
Sum Shape Area (km²)	89226.19	

Table 20: Slope classifications measured by percent area within Nilus Chaos.

<i>Nilus Chaos</i>		
Slope (deg.)	Shape Area (km²)	Percent Area (%)
0 - 2	19562.45	69.07
2 - 5	5237.51	18.49
5 - 15	3410.65	12.04
15 - 25	112.50	0.40
25 - 45	0.15	0.00
45 - 60	0.00	0.00
Sum Shape Area (km²)	28323.26	

Table 21: Slope classifications measured by percent area within Pyrrhae Chaos.

<i>Pyrrhae Chaos</i>		
Slope (deg.)	Shape Area (km²)	Percent Area (%)
0 - 2	6623.56	27.93
2 - 5	6952.80	29.32
5 - 15	8859.24	37.36
15 - 25	1271.06	5.36
25 - 45	4.88	0.02
45 - 60	0.00	0.00
Sum Shape Area (km²)	23711.54	

Table 22: Slope classifications measured by percent area within Xanthe Chaos.

<i>Xanthe Chaos</i>		
Slope (deg.)	Shape Area (km²)	Percent Area (%)
0 - 2	1931.60	49.20
2 - 5	1040.71	26.51
5 - 15	884.01	22.52
15 - 25	69.65	1.77
25 - 45	0.00	0.00
45 - 60	0.00	0.00
Sum Shape Area (km²)	3925.96	

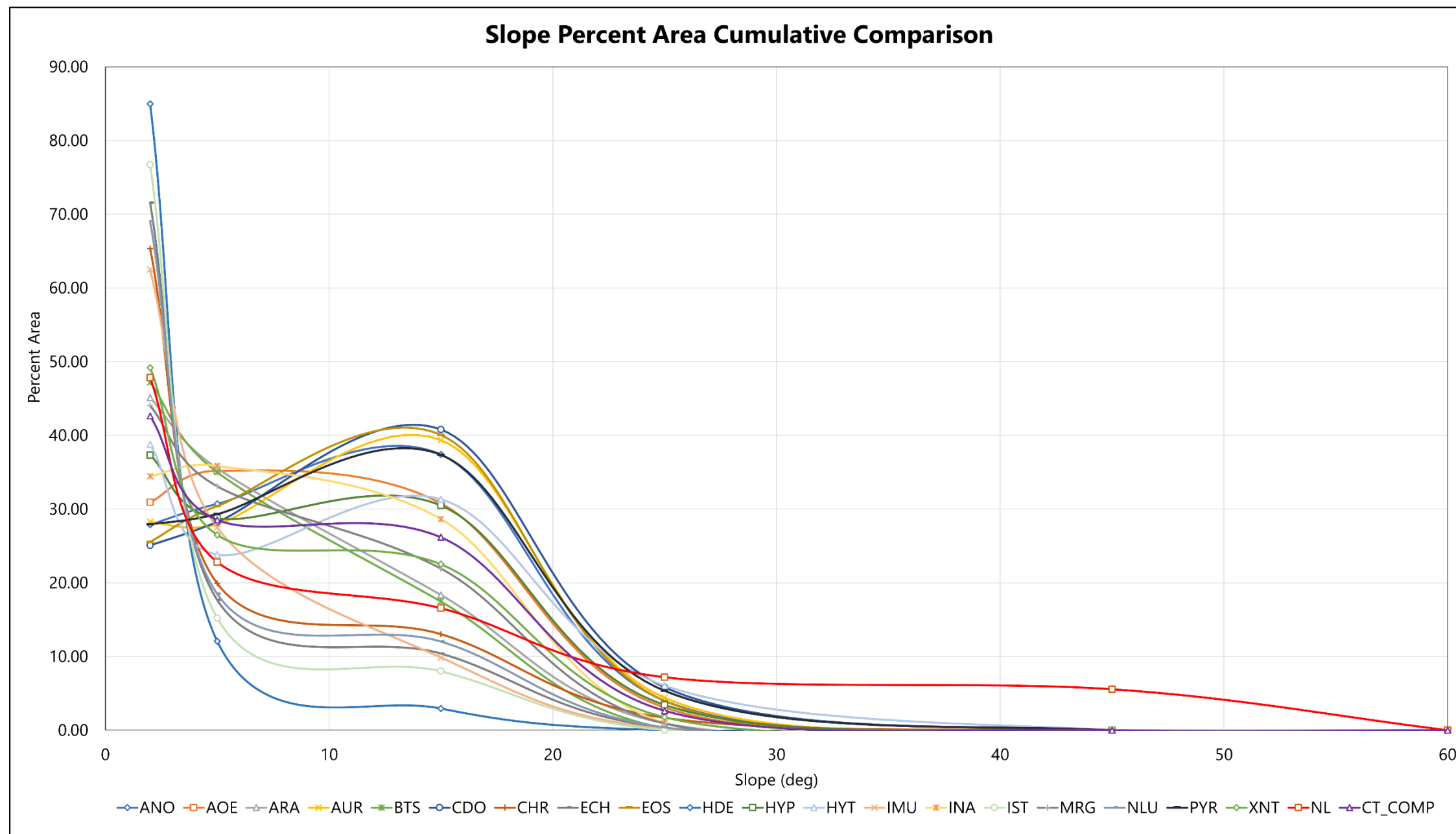


Figure 96: Cumulative plot of percent area for defined slope breaks at 2, 5, 15, 25, 45, and 60 degrees for all chaotic terrains and NL. Four maturities of chaotic terrains were able to be discerned from slope comparisons.

evolution and maturity can be discerned from the plots. Group 1 is the least evolved, or immature group, where the slopes are nominally between 15 and 30 degrees, with a sharp decrease in shallow slopes between 2 and 15 degrees comparatively (Figure 97). Group 1 includes Arsinoes Chaos, Aureum Chaos, Candor Chaos, Eos Chaos, and Pyrrhae Chaos. Group 2 chaotic terrains are slightly more evolved from a slope perspective, where the percentage of shallow slopes increases from Group 1 but does not show a distinct preference between slopes between 2 – 15 degrees and 15 – 30 degrees (Figure 98). Chaotic terrains classified into Group 2 are Aurorae Chaos and Iani Chaos. Group 3 chaotic terrains represent a more evolved group with medium maturity, where slopes dominantly fall between 2 – 15 degrees, with a decrease in slopes from 15 -30 degrees (Figure 99). The composite chaotic terrain dataset, with all percent area slope values of all chaotic terrains analyzed also falls within Group 3. Chaotic terrains within Group 3 are Aram Chaos, Baetis Chaos, Hydaspiis Chaos, Hydraotes Chaos, Margaritifer Chaos, and Xanthe Chaos. Group 4 chaotic terrains are the most evolved and mature chaotic terrains, showing a dominant percent area of slopes between 2 -15 degrees, and minimal slopes that exceed that threshold (Figure 100). These chaotic terrains are likely areas of high erosion rates, where the chaos floor has been widened significantly and positive relief features such as knobs or mesas are relatively sparse. Group 4 chaotic

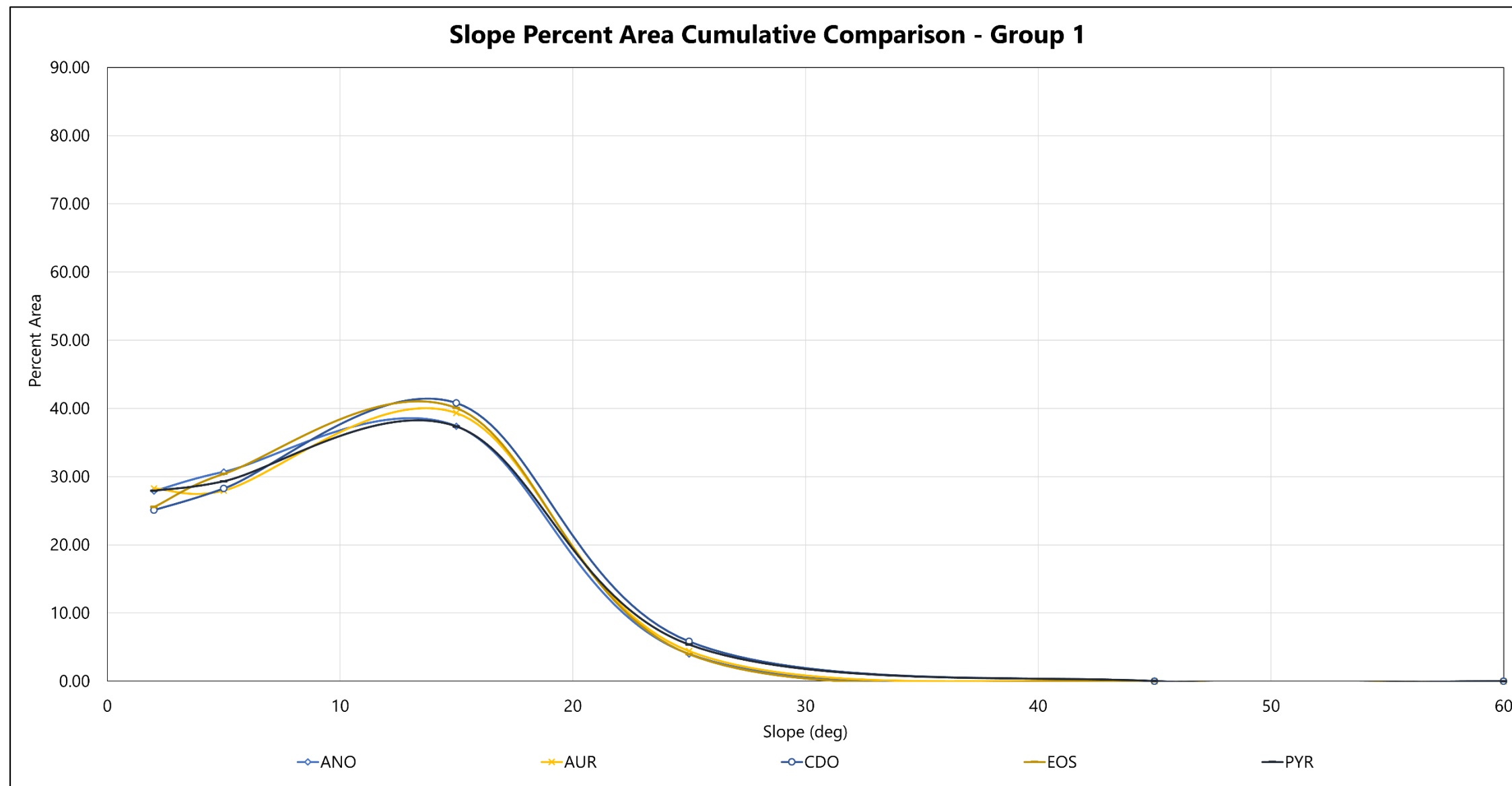


Figure 97: Group 1 of similar slope values within the chaotic terrains. This group represents immature or un-evolved chaotic terrains due to the low relative percentages of slopes between 2 and 15 degrees.

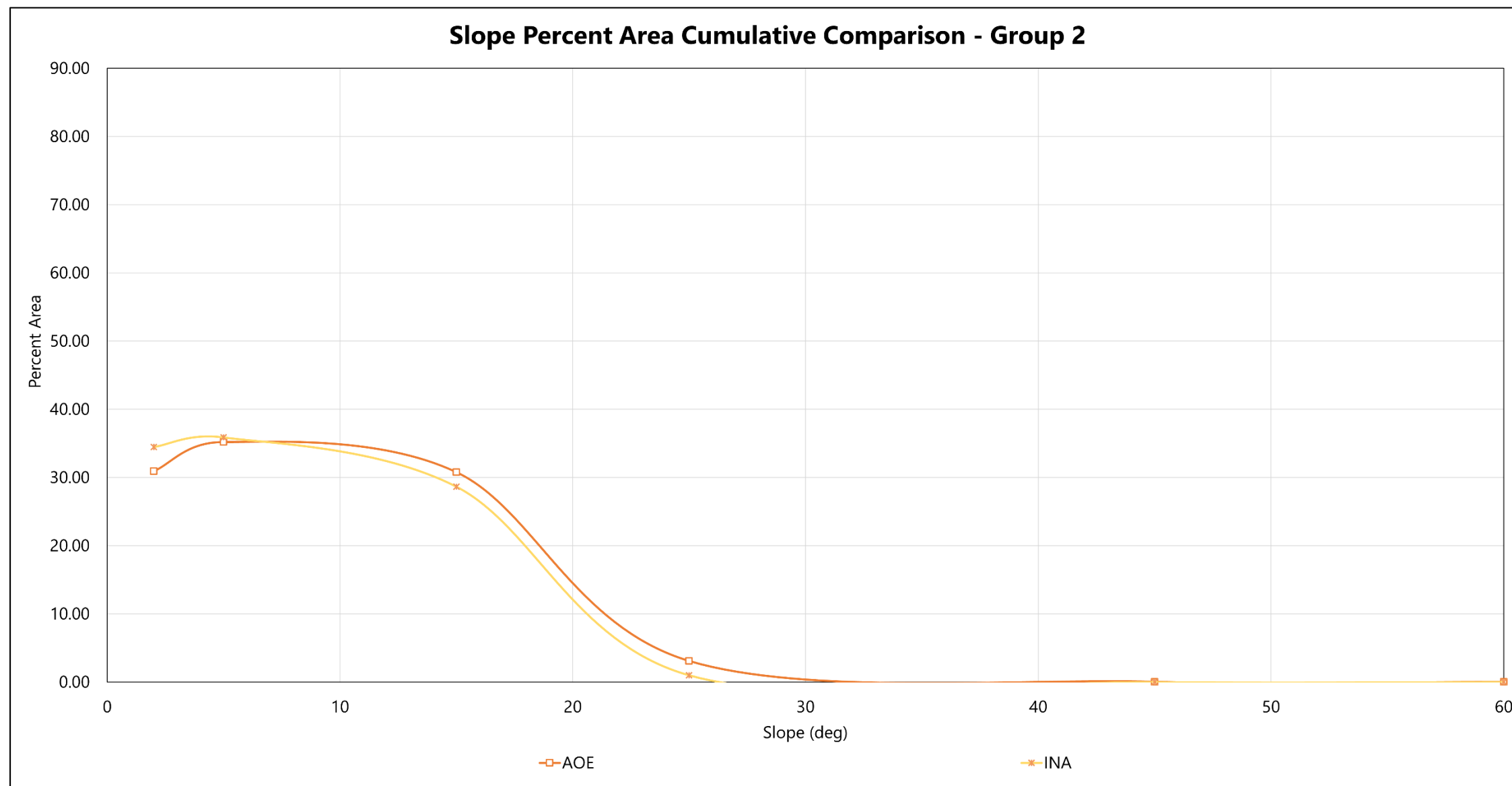


Figure 98: Group 2 of similar slope values within the chaotic terrains. This group represents a second group of immature or un-evolved chaotic terrains but is more evolved than group 1 due a higher number of slopes between .2 – 15 degrees.

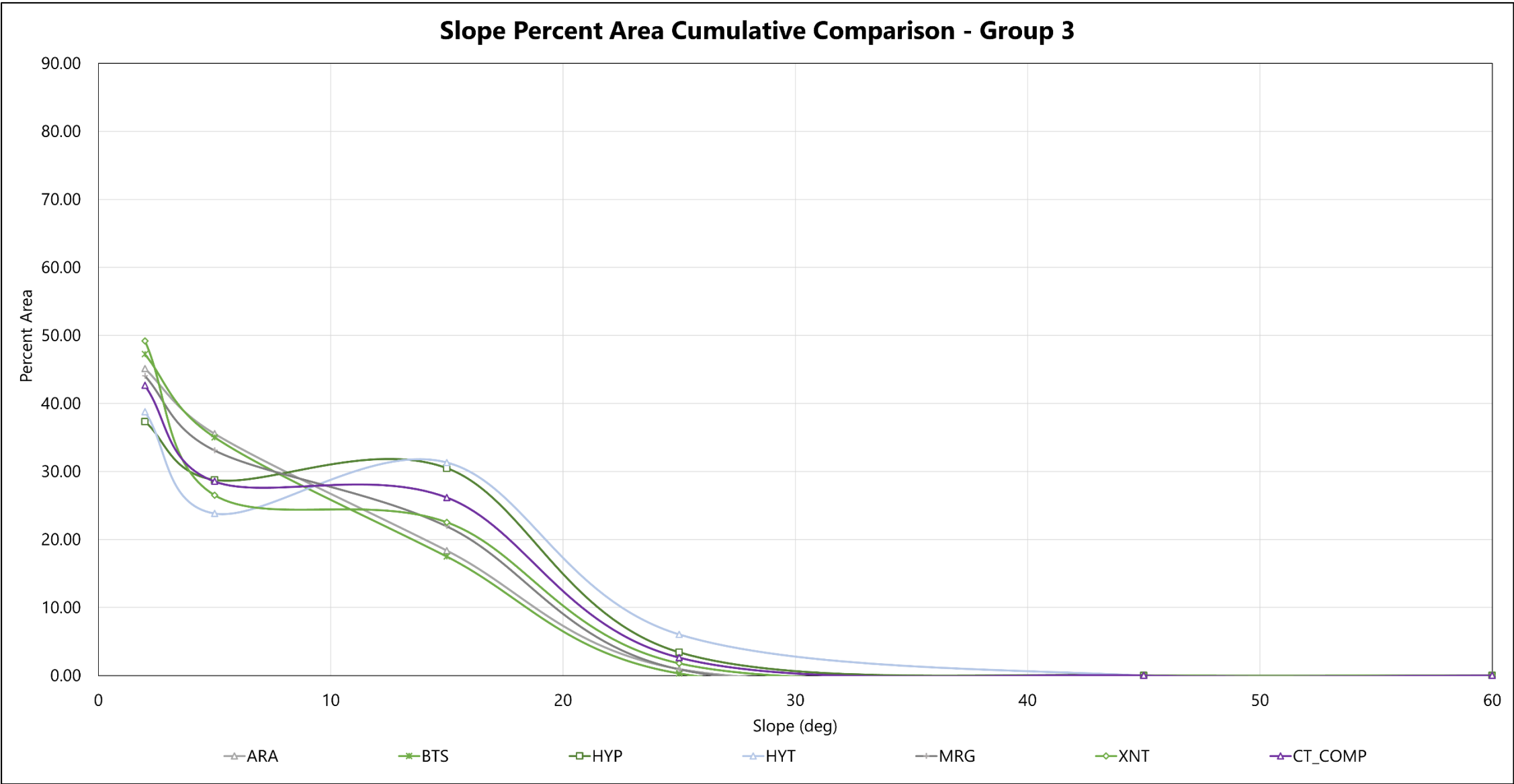


Figure 99: Group 3 of similar slope values within the chaotic terrains. This group represents a more evolved group of chaotic terrains with medium maturity, where slopes dominantly fall between 2 – 15 deg. The compiled dataset of all chaotic terrains also averages to this group.

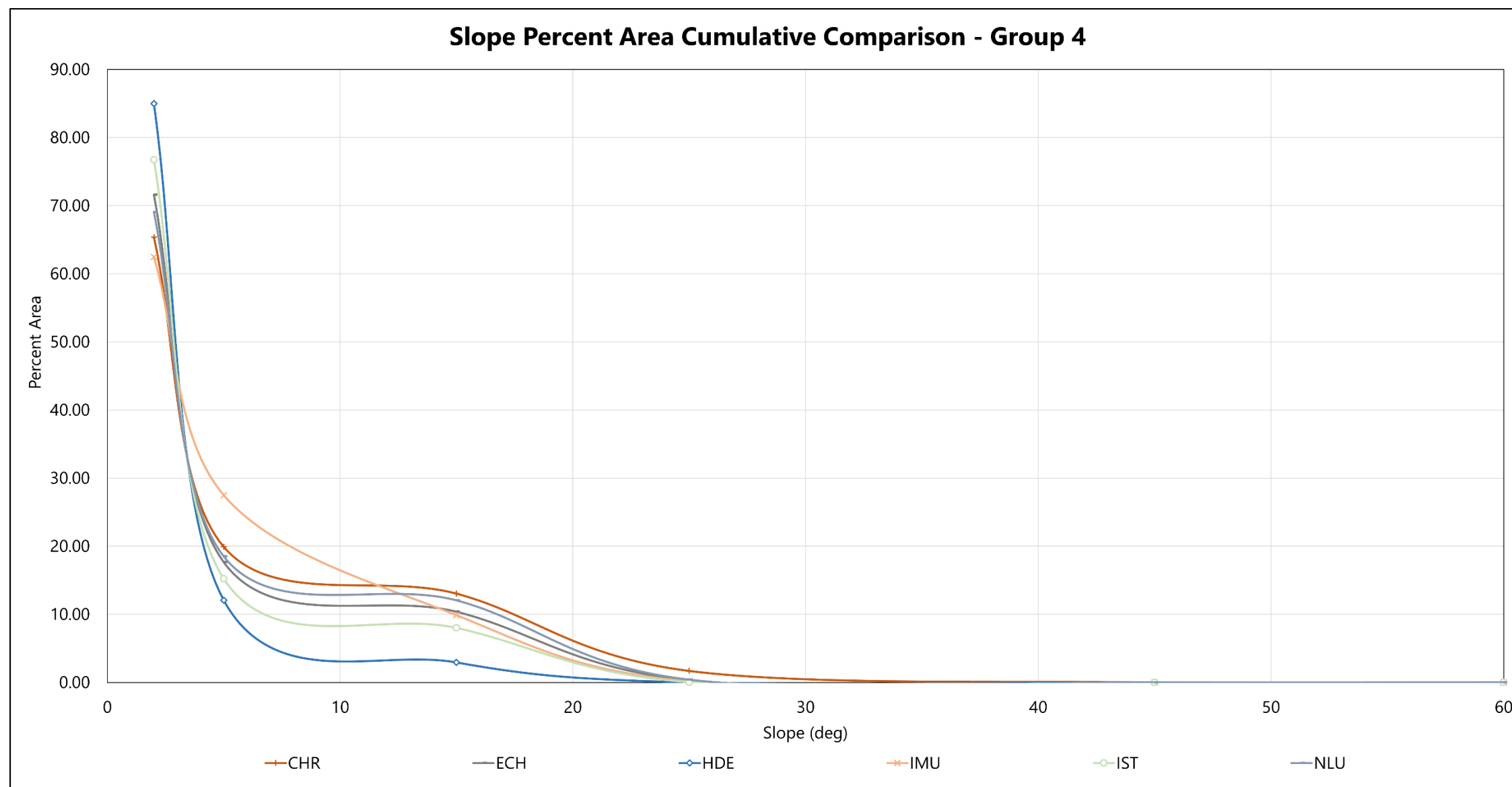


Figure 100: Group 4 of similar slope values within the chaotic terrains. This group represents the evolved, mature, chaotic terrains that are likely to have wide, eroded chaos floors as well as shallow mesa and knob walls.

terrains are Chryse Chaos, Echus Chaos, Hydrae Chaos, Iamuna Chaos, Ister Chaos, and Nilus Chaos.

NL does not fall into any of these slope groupings but shows a significantly different result when compared directly to the composite chaotic terrain dataset (Figure 101). The slope area percentages are relatively evenly distributed reaching 60 degrees, after an initial peak in slopes between 2 – 15 degrees. This initial peak in slope is likely attributed to the flat area surrounding the bulk of NL and the flat mesa plateaus within the network itself.

When defined slope groupings of chaotic terrains are mapped spatially, there is a correlation between proximity to the outflow channel mouth and slope group (Figure 102). Group 1, unevolved terrains are farther south and closer to breakout points, where generally larger slopes are found. Chaotic terrains increase in maturity moving north towards the mouth of the outflow channels, where Group 3 and Group 4, or the most evolved terrains, are found.

Lineament Analysis Phase I: Noctis Labyrinthus

Phase I of the lineament analysis for NL produced a rose diagram plot and mean vector statistics (Figure 103). NL shows a strong preference for a NNE

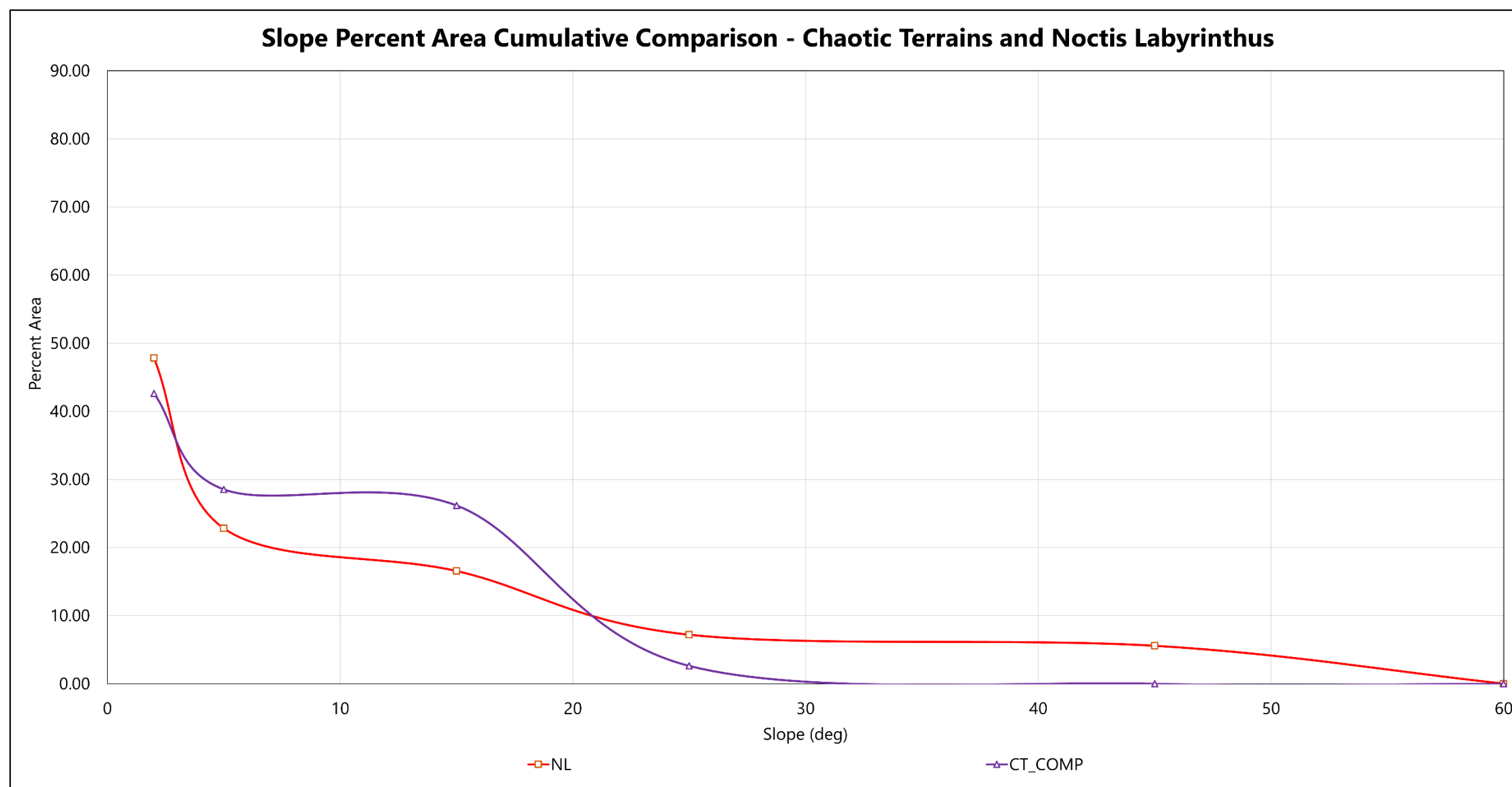


Figure 101: Comparative slope percent area of NL and composite chaotic terrain slopes. The bulk of chaotic terrain slopes are below 30 degrees, while slopes in NL are nominally > 60. These high slope values within NL are likely attributed to steep mesa walls, while low slope values are attributed to mesa plateaus, trough floors, and surrounding flat terrain.

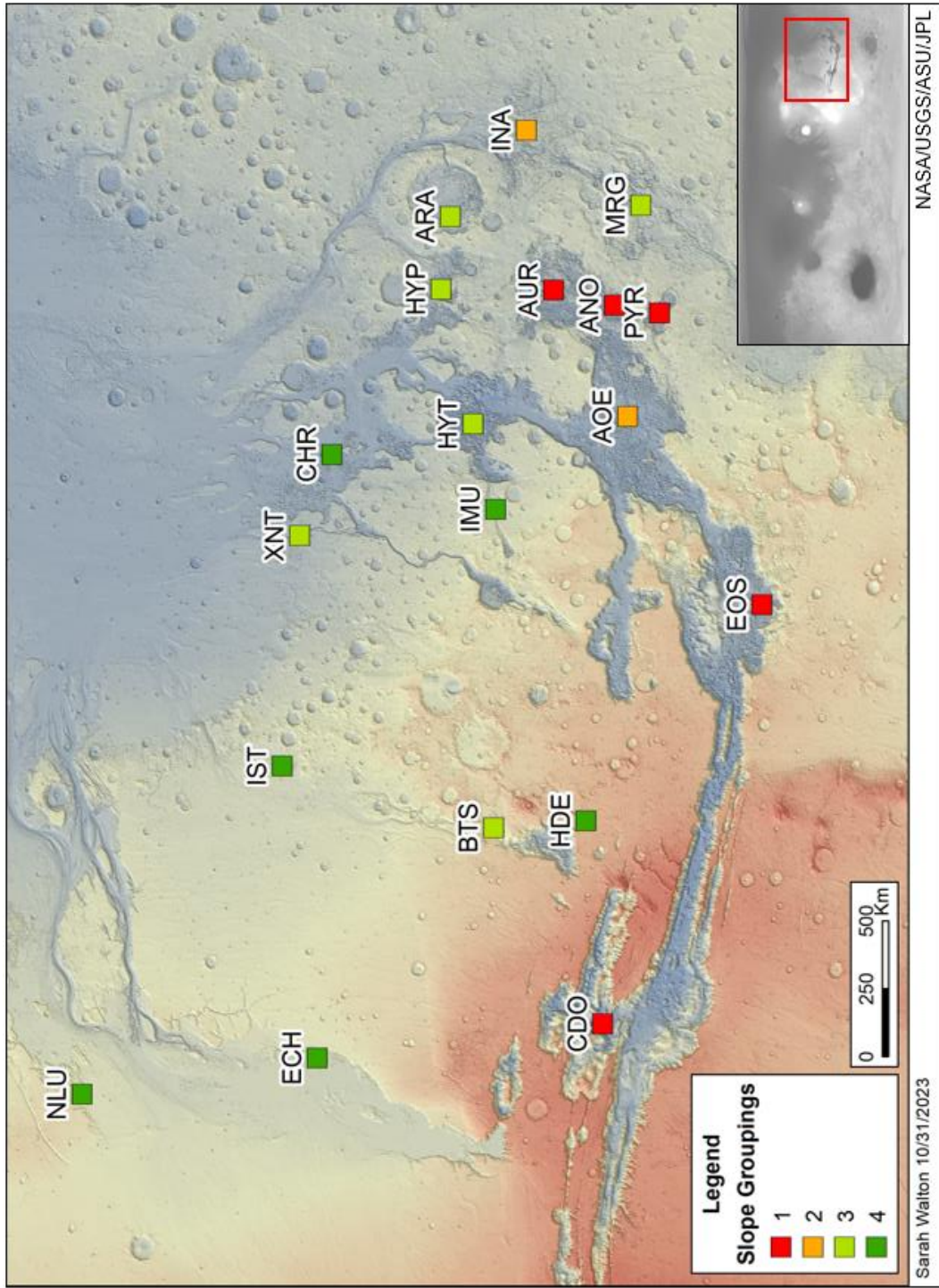


Figure 102: Groupings of chaotic terrains defined based on slope percent area analysis.

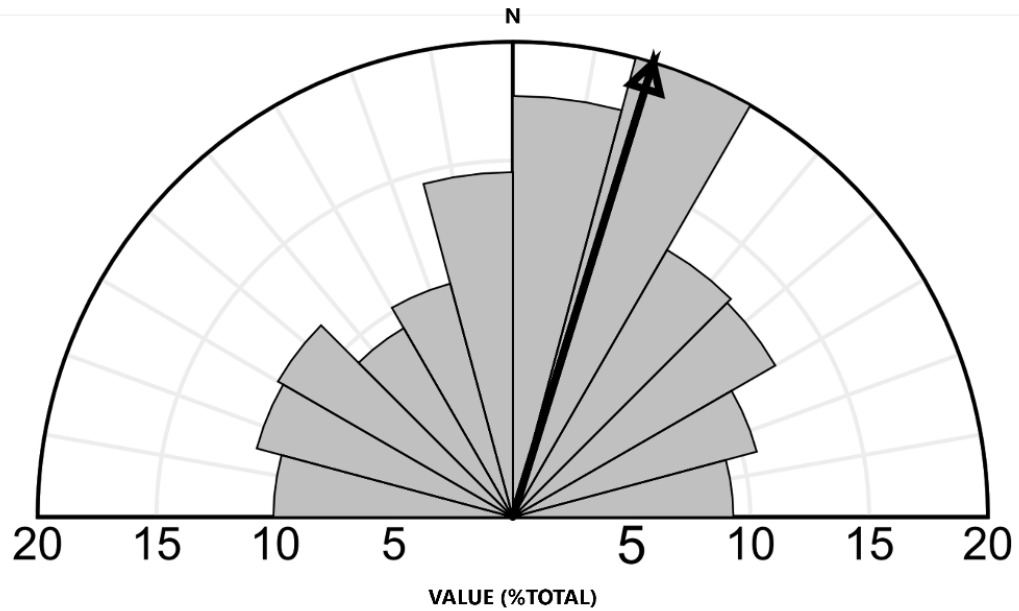
lineament direction, where digitized lines in the NNE direction are statistically the majority. The analysis also reveals lineaments in all directions, where each set of directional lines follow distinct spatial patterns. NL follows regional fracture patterns with preferential normal faulting occurring in three groups, NNE, NNW, and radial faulting (NE and NW group) (Figure 104).

Lineament Analysis Phase II: Chaotic Terrains

Phase II lineament analyses yielded rose diagram plot results from digitizing lines within the chaotic terrains. Lineaments from each individual chaos showed preferential lineament orientation locally but did not show minimal regional preferential orientation cumulatively (Figure 105). Figures 106 – 124 show rose diagram plots of lineament azimuths for each individual chaotic terrain. Features digitized differed from NL where within the chaotic terrains, mesas breaks and troughs along lineaments dominate features digitized, while in NL, normal faulting and smaller scale grabens were digitized. Breakout faulting (with a connection to subsidence) within the chaotic terrains was common throughout but did not exhibit cumulative areas of obvious fault trends.

Individually, the rose diagram analysis for chaotic terrains shows a trended lineament orientation towards the NW and NNW, where 14/19 analyzed terrains showed preference in those directions. This is also shown in the

Noctis Labyrinthus Lineament Rose Diagram



Map Code	Number of Lines	Max Value	Mean Vector
NL	1044	13.12261% between 021° and 030°	017.2° ± 04.1°

Figure 103: Rose diagram plot and statistics for digitized NL lineaments. Lineaments in NL show a preferential NNE direction.

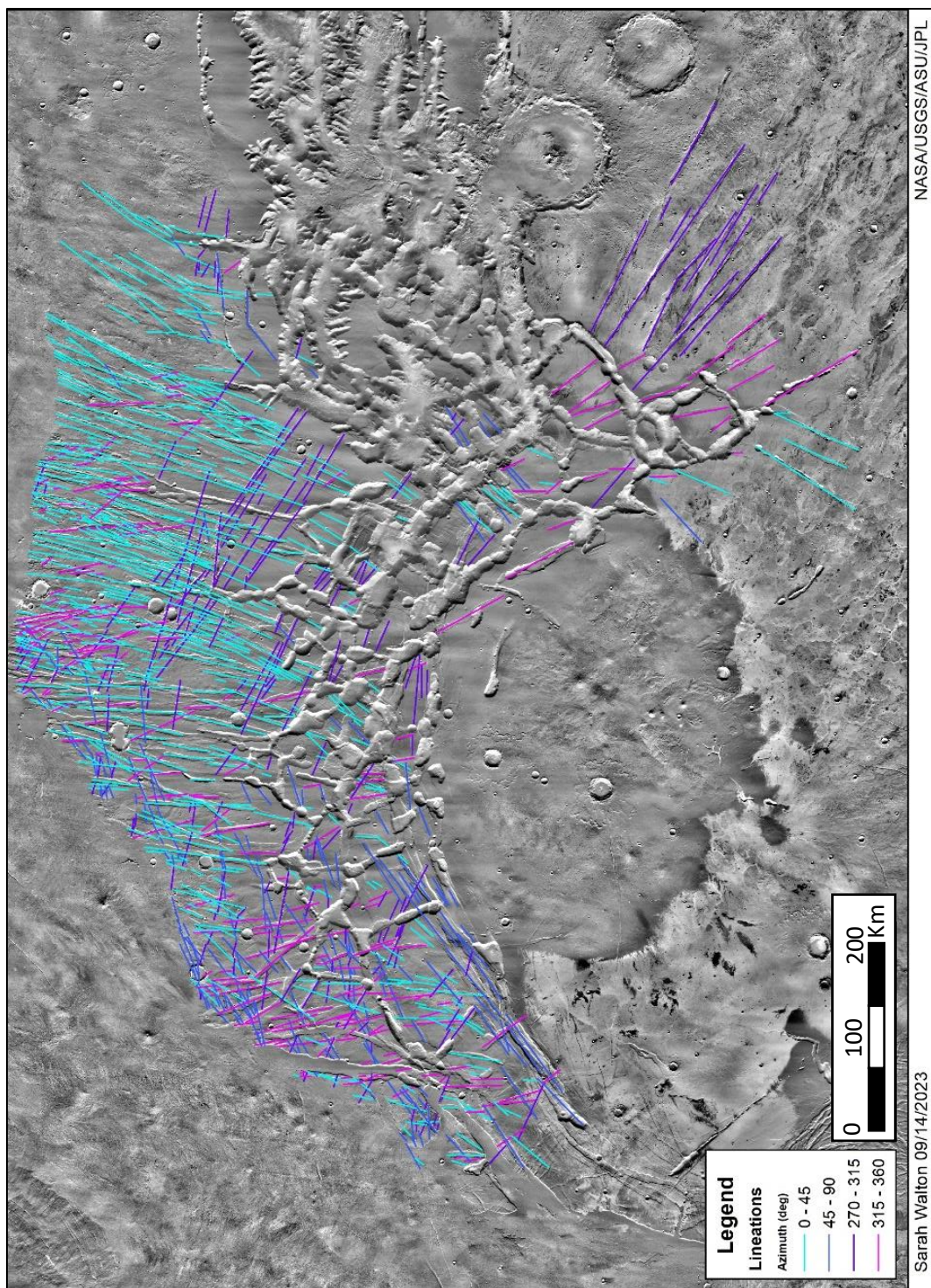
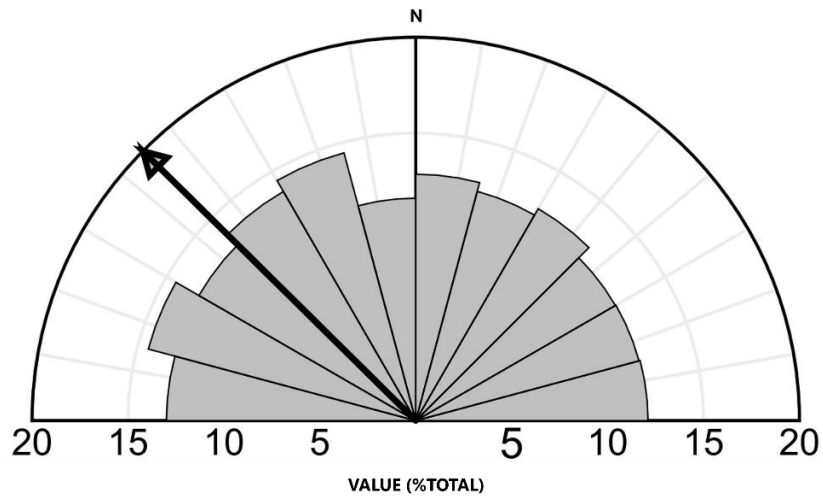


Figure 104: Results of the lineament analysis for NL. Three dominant regional fracture patterns are seen in the NNE, NNW and radial fractures (NW and NE directions).

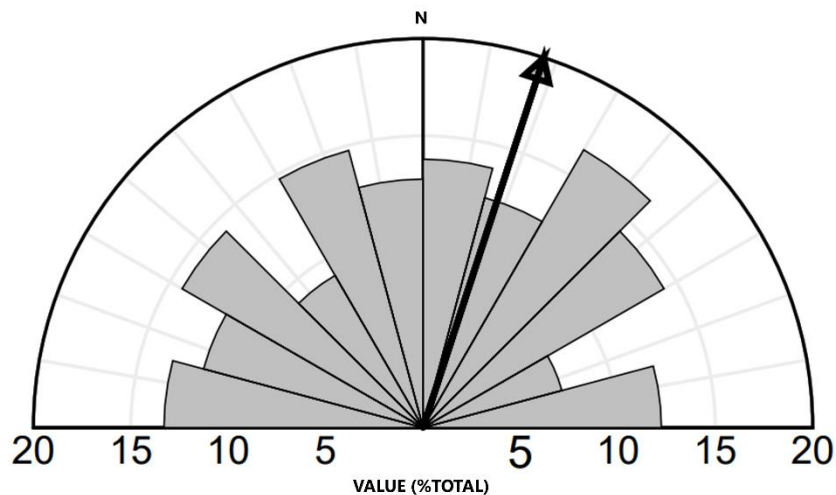
Chaotic Terrain Lineament Rose Diagram



Map Code	Number of Lines	Max Value	Mean Vector
All Chaos	2687	7.59211% between 331° and 340°	314.7° ± 12.1°

Figure 105: Cumulative rose diagram plot for all 19 analyzed chaotic terrains. The mean vector has a value of ~315 but does not show strong preferential orientation of lineaments within all chaos.

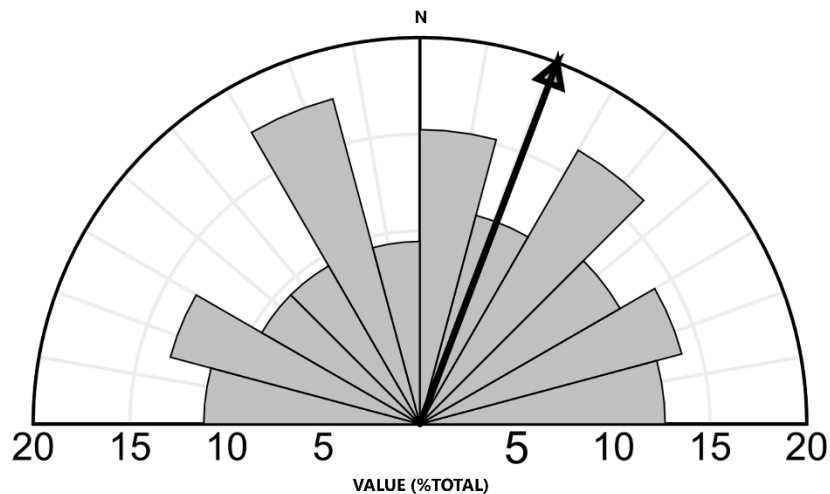
Arsinoes Chaos Lineament Rose Diagram



Map Code	Number of Lines	Max Value	Mean Vector
ANO	147	10.20408% between 041° and 050°	018.1° ± 45.0°

Figure 106: Cumulative rose diagram plot for Arsinoes Chaos.

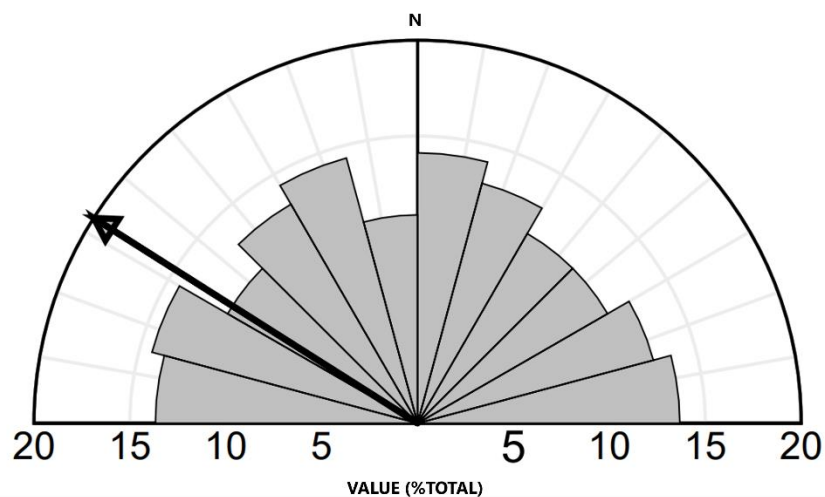
Aurorae Chaos Lineament Rose Diagram



Map Code	Number of Lines	Max Value	Mean Vector
AOE	112	12.5% between 031° and 040°	020.8° ± 52.2°

Figure 107: Cumulative rose diagram plot for Aurorae Chaos.

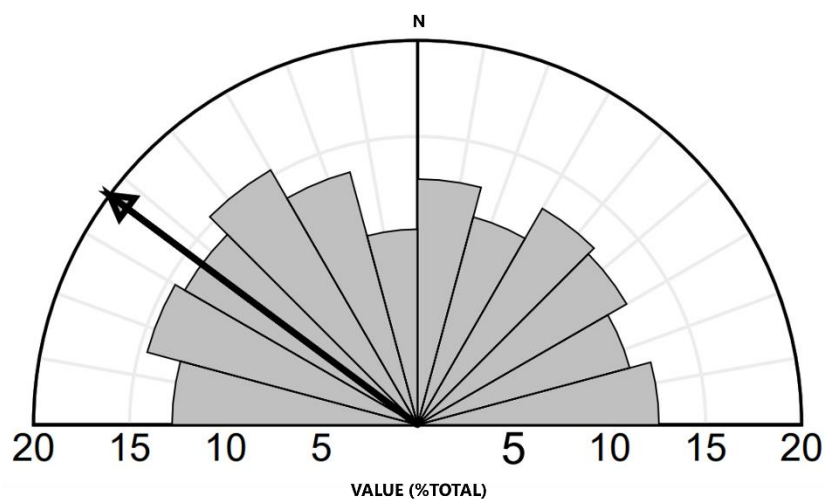
Aram Chaos Lineament Rose Diagram



Map Code	Number of Lines	Max Value	Mean Vector
ARA	321	7.165109% between 001° and 010°	302.4° ± 52.1°

Figure 108: Cumulative rose diagram plot for Aram Chaos.

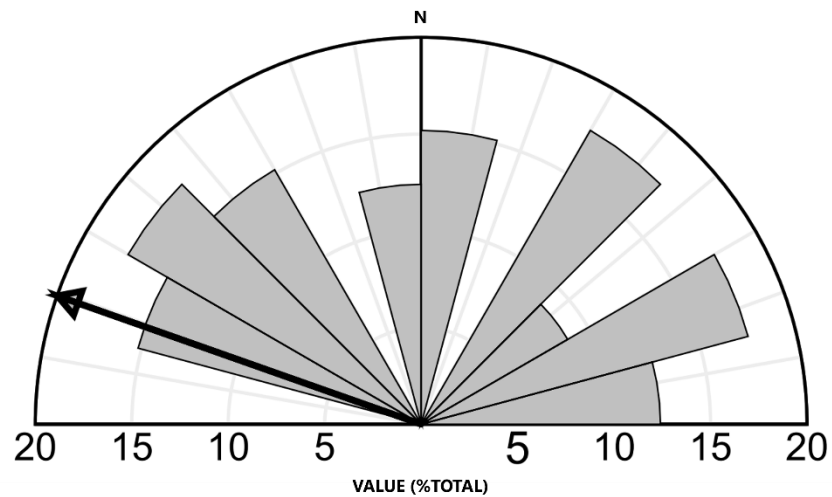
Aureum Chaos Lineament Rose Diagram



Map Code	Number of Lines	Max Value	Mean Vector
AUR	367	8.991826% between 321° and 330°	306.7° ± 22.7°

Figure 109: Cumulative rose diagram plot for Aureum Chaos.

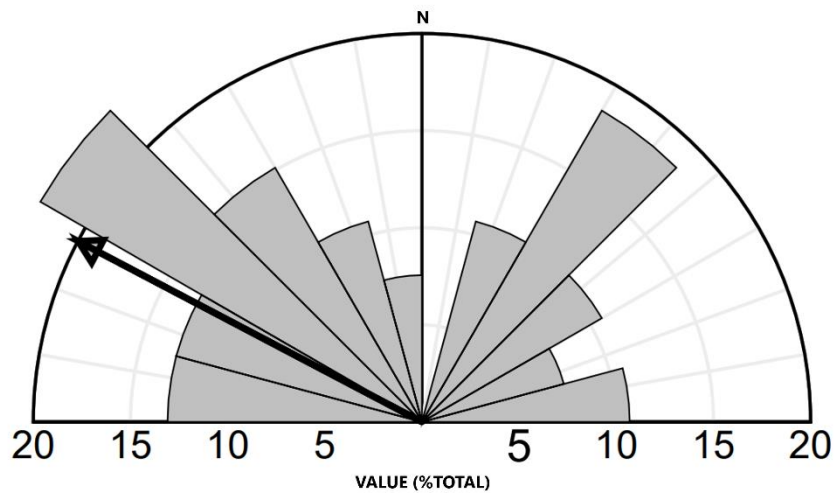
Baetis Chaos Lineament Rose Diagram



Map Code	Number of Lines	Max Value	Mean Vector
BTS	26	19.23077% between 311° and 320°	289.4° ± 123.1°

Figure 110: Cumulative rose diagram plot for Baetis Chaos.

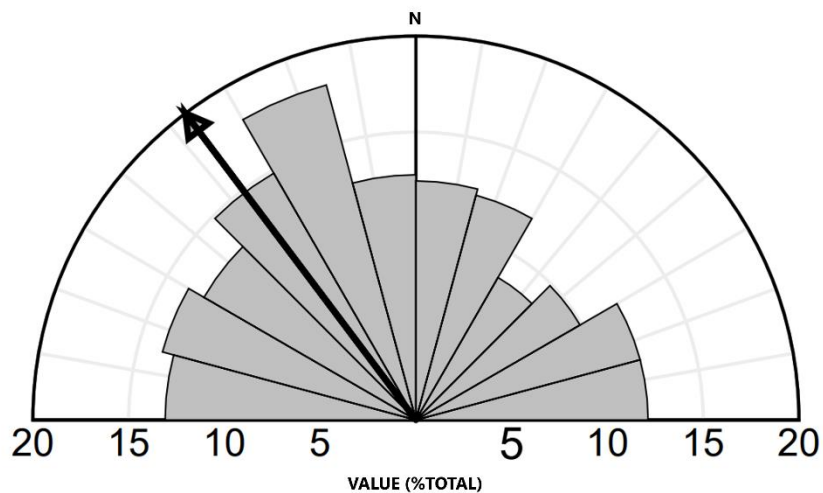
Candor Chaos Lineament Rose Diagram



Map Code	Number of Lines	Max Value	Mean Vector
CDO	35	17.14286% between 311° and 320°	297.7° ± 28.9°

Figure 111: Cumulative rose diagram plot for Candor Chaos.

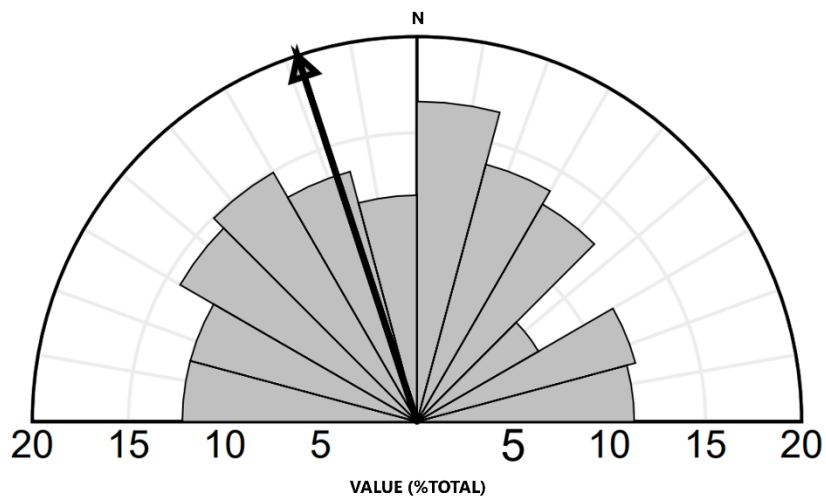
Chryse Chaos Lineament Rose Diagram



Map Code	Number of Lines	Max Value	Mean Vector
CHR	245	12.65306% between 331° and 340°	323.0° ± 13.9°

Figure 112: Cumulative rose diagram plot for Chryse Chaos.

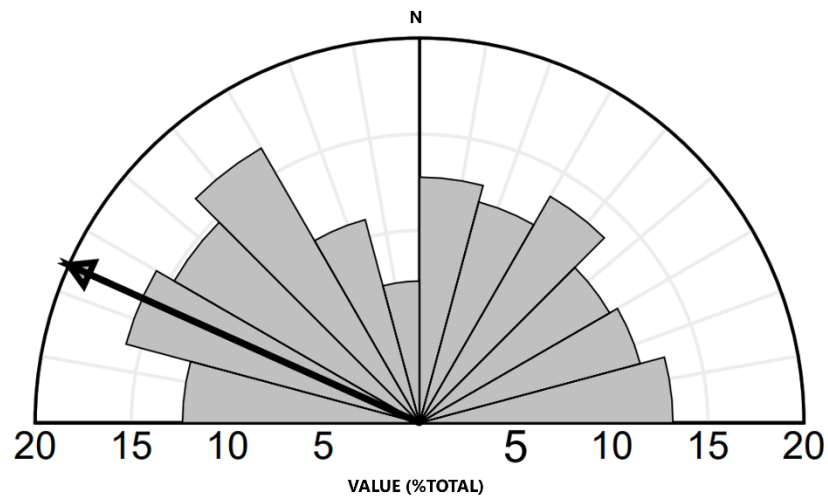
Echus Chaos Lineament Rose Diagram



Map Code	Number of Lines	Max Value	Mean Vector
ECH	188	10.10638% between 001° and 010°	341.9° ± 22.0°

Figure 113: Cumulative rose diagram plot for Echus Chaos.

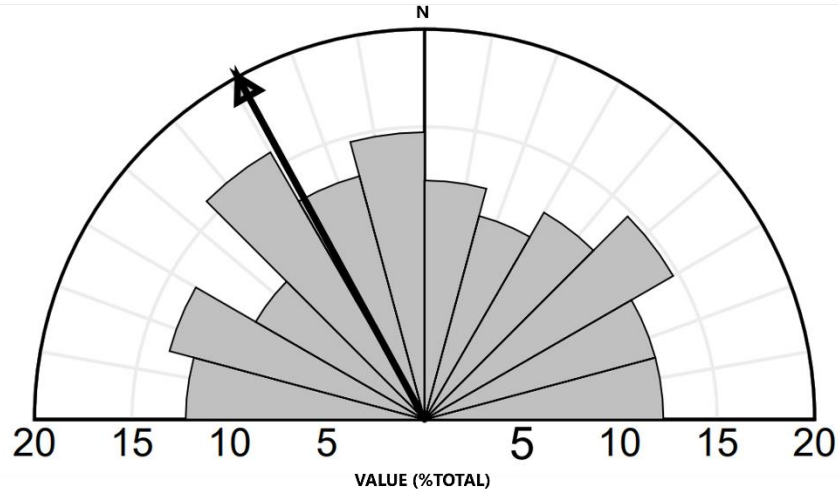
Eos Chaos Lineament Rose Diagram



Map Code	Number of Lines	Max Value	Mean Vector
EOS	184	8.695652% between 291° and 300°	294.2° ± 21.1°

Figure 114: Cumulative rose diagram plot for Eos Chaos.

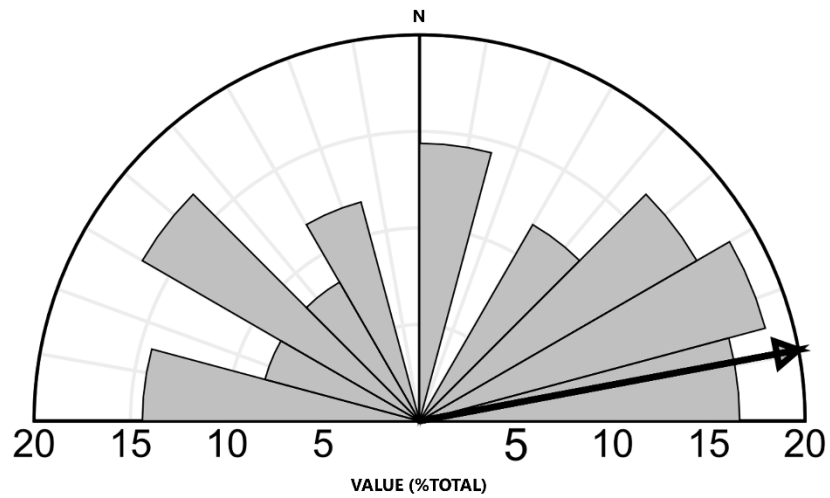
Hydaspis Chaos Lineament Rose Diagram



Map Code	Number of Lines	Max Value	Mean Vector
HYP	120	9.166667% between 041° and 050°	331.4° ± 110.0°

Figure 115: Cumulative rose diagram plot for Hydaspis Chaos.

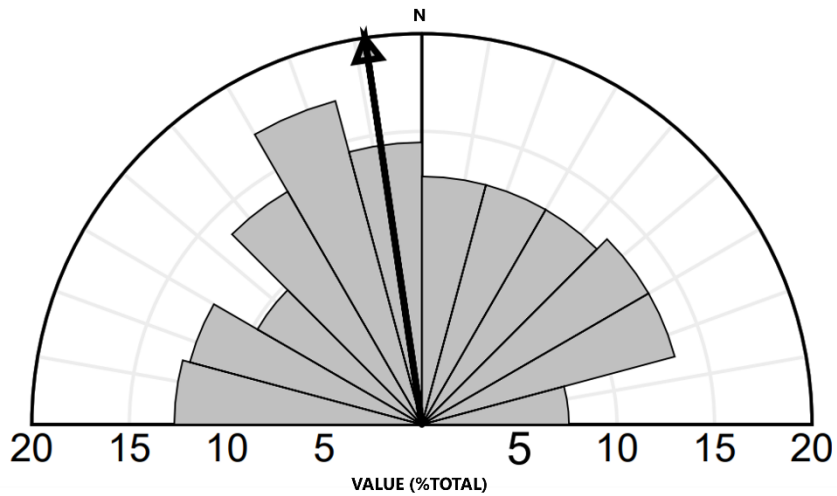
Hydrae Chaos Lineament Rose Diagram



Map Code	Number of Lines	Max Value	Mean Vector
HDE	29	13.7931% between 051° and 060°	079.4° ± 21.4°

Figure 116: Cumulative rose diagram plot for Hydrae Chaos.

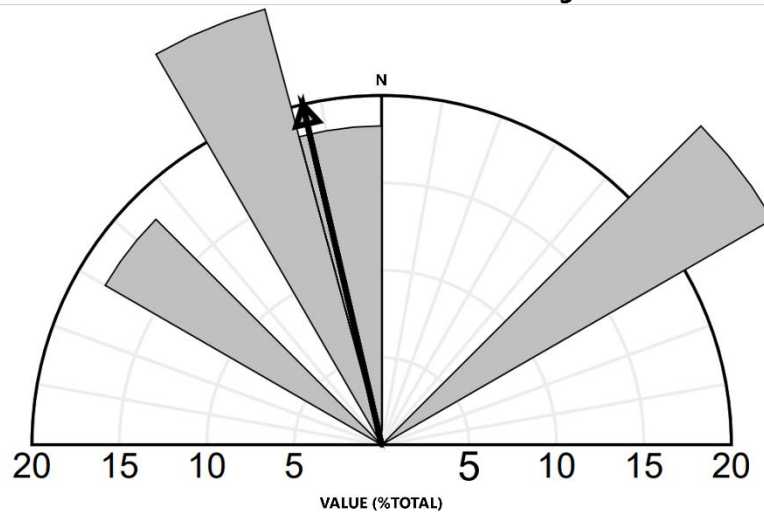
Hydraotes Chaos Lineament Rose Diagram



Map Code	Number of Lines	Max Value	Mean Vector
HYT	211	10.42654% between 331° and 340°	351.6° ± 21.0°

Figure 117: Cumulative rose diagram plot for Hydraotes Chaos.

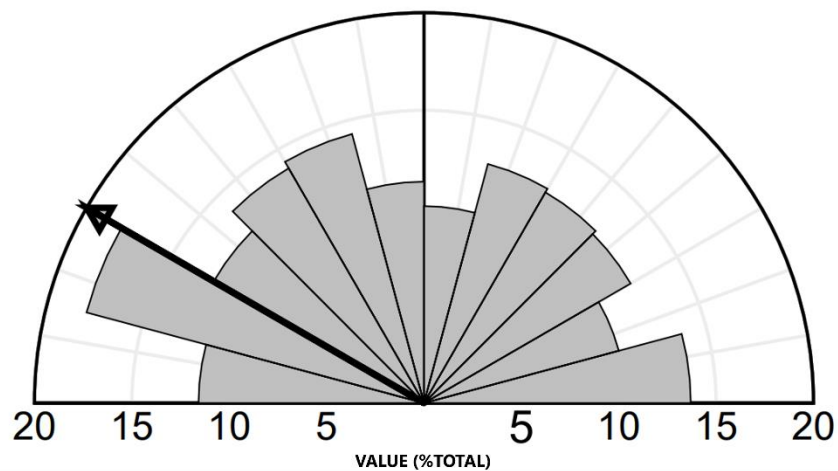
Iamuna Chaos Lineament Rose Diagram



Map Code	Number of Lines	Max Value	Mean Vector
IMU	6	33.33333% between 051° and 060°	347.0° ± 55.3°

Figure 118: Cumulative rose diagram plot for Iamuna Chaos.

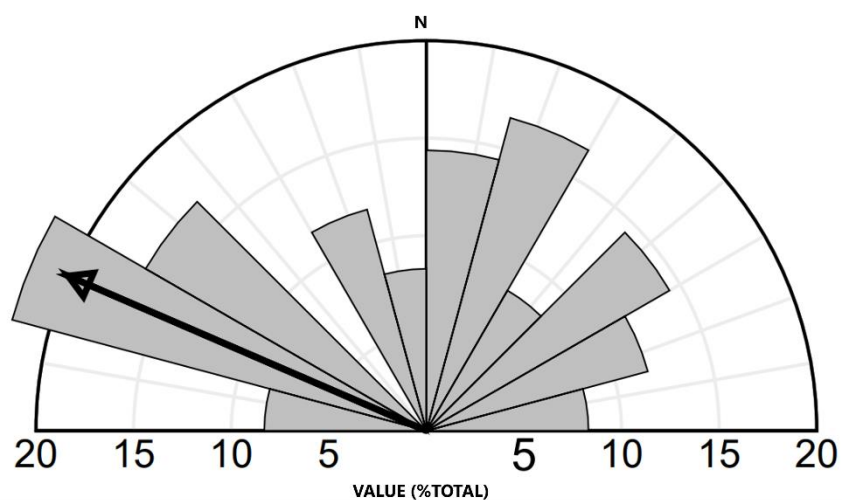
Iani Chaos Lineament Rose Diagram



Map Code	Number of Lines	Max Value	Mean Vector
INA	373	11.79625% between 291° and 300°	300° ± 17.1°

Figure 119: Cumulative rose diagram plot for Iani Chaos.

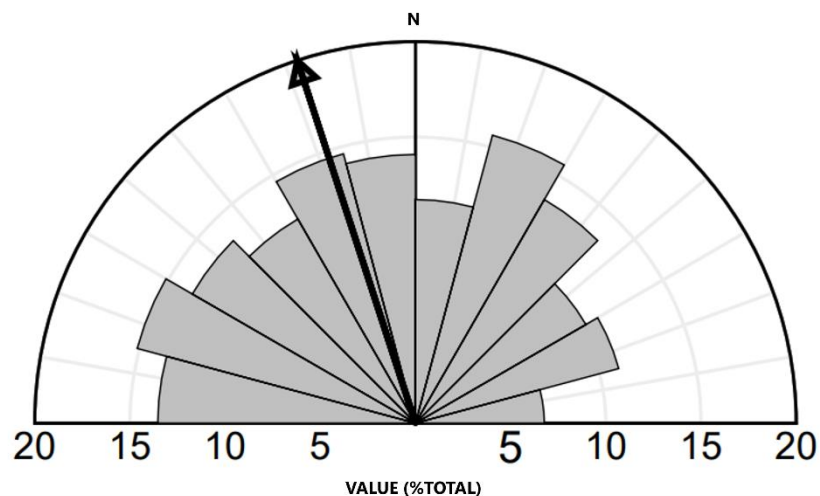
Ister Chaos Lineament Rose Diagram



Map Code	Number of Lines	Max Value	Mean Vector
IST	29	20.68966% between 291° and 300°	293.4° ± 117.6°

Figure 120: Cumulative rose diagram plot for Ister Chaos.

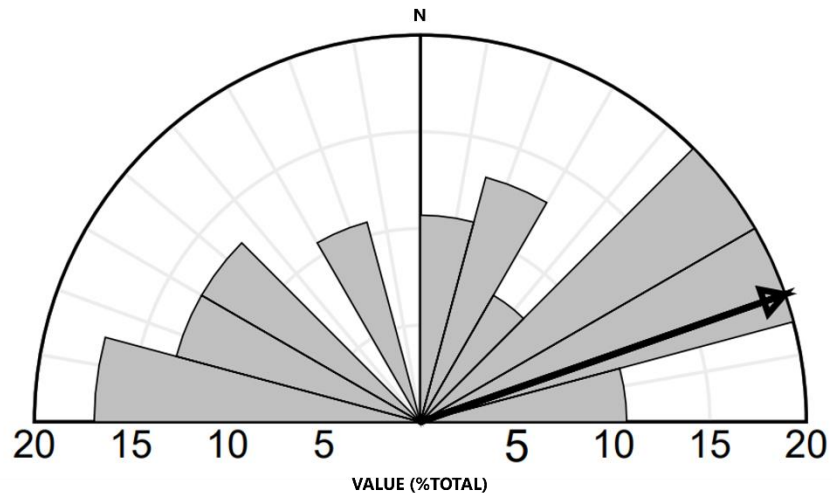
Margaritifer Chaos Lineament Rose Diagram



Map Code	Number of Lines	Max Value	Mean Vector
MRG	131	9.160305% between 021° and 030°	341.9° ± 29.0°

Figure 121: Cumulative rose diagram plot for Margaritifer Chaos.

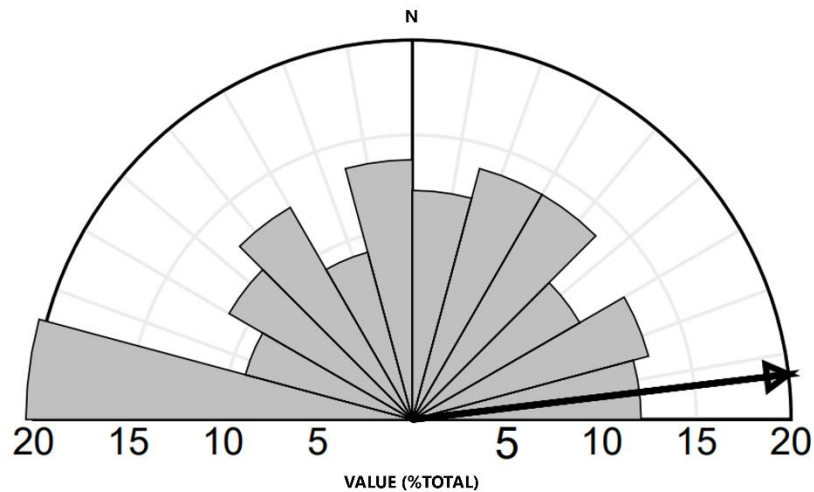
Nilus Chaos Lineament Rose Diagram



Map Code	Number of Lines	Max Value	Mean Vector
NLU	35	14.28571% between 051° and 060°	070.8° ± 15.1°

Figure 122: Cumulative rose diagram plot for Nilus Chaos.

Pyrrhae Chaos Lineament Rose Diagram



Map Code	Number of Lines	Max Value	Mean Vector
PYR	96	15.625% between 271° and 280°	083.2° ± 49.4°

Figure 123: Cumulative rose diagram plot for Pyrrhae Chaos.

Xanthe Chaos Lineament Rose Diagram

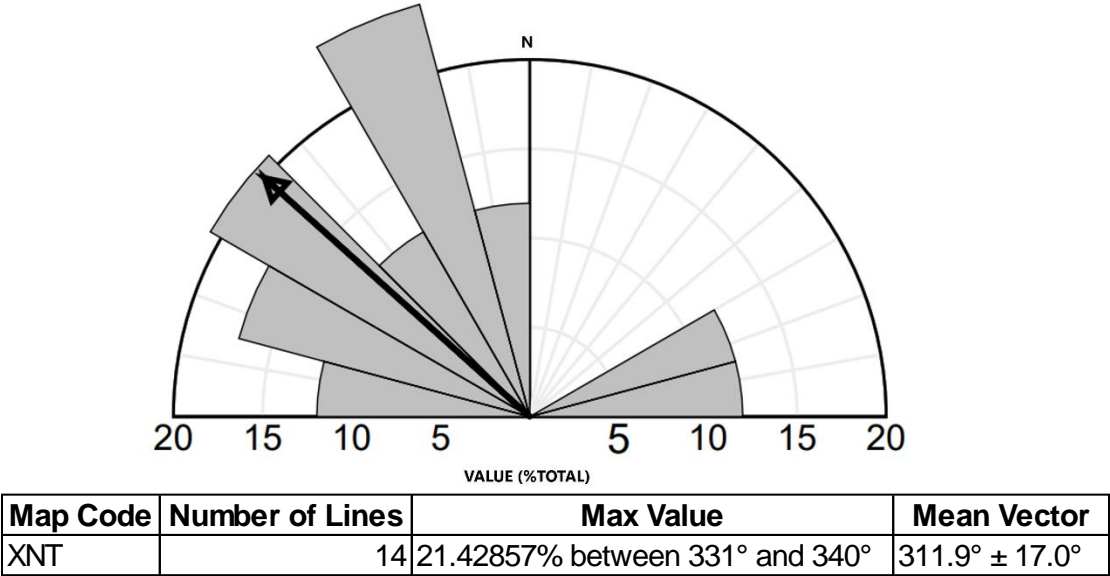


Figure 124: Cumulative rose diagram plot for Xanthe Chaos.

composite chaotic terrain rose diagram with a slight bias towards the NW, but lineaments are also well distributed across other orientation directions. Other observations include preference of 3/19 chaotic terrains showing dominant lineament directional preference towards the NE, and 2/19 showing lineament directional preference towards the NNE.

Lineament Analysis Phase III: Statistical Analyses

A statistical two sample Kolmogorov-Smirnov test was run using lineament azimuth values to determine the degree of dissimilarity between two lineament analyses (Tables 23 and 24). The result of NL lineaments compared to the composite chaotic terrain dataset yielded a p- value of < 0.05 , assuming we can reject the null hypothesis and the two datasets do not show a comparative degree of similarity (Figure 125). Running each individual chaotic terrain dataset against the lineaments of NL shows the same results, where the p-value never surpassed 0.05, suggesting there is no correlation between lineament azimuths within NL and the lineament azimuths within the chaotic terrains.

P-value results from the comparison of chaotic terrain lineament datasets against one another show expected results, where some terrains show varying degrees of similarity towards each other. This result is expected, as the chaotic terrains in theory, have similar formation and evolution mechanics. When

Table 23: P-value results from the two sample Kolmogorov-Smirnov test comparing the similarity between the azimuths of two lineament datasets. Each chaotic terrain, as well as a compiled chaotic terrain dataset, was tested against all other terrains and NL. A p-value above 0.05 (highlighted in red stripes) indicates the azimuths of two lineament datasets are similar from a statistical standpoint.

	ARA	ANO	AUR	AOE	BTS	CDO	CHR	ECH	EOS	HYP	HDE	HYT	IMU	INA	IST	MRG	NLU	PYR	XNT	CT Comp
NL	8.19E-89	1.95E-134	2.72E-77	1.38E-145	9.82E-172	1.23E-168	3.99E-105	9.76E-122	6.86E-123	3.40E-141	1.07E-170	6.14E-115	1.00E-178	2.25E-74	1.07E-170	8.56E-138	1.23E-168	1.89E-148	6.55E-176	0.00E+00
ARA		1.72E-05	0.72	1.48E-07	1.64E-14	1.16E-13	0.22	2.77E-03	1.67E-03	5.87E-07	3.17E-14	0.02	1.72E-16	0.39	3.17E-14	2.92E-06	1.16E-13	1.30E-08	1.10E-15	0.00E+00
ANO			2.98E-08	0.85	0.01	0.02	0.03	0.81	0.85	0.93	0.01	0.34	1.22E-03	4.68E-09	0.01	0.98	0.02	0.72	2.77E-03	0.00E+00
AUR				6.04E-11	2.93E-19	2.82E-18	0.01	1.32E-05	6.73E-06	2.70E-10	6.27E-19	2.33E-04	1.53E-21	1.00	6.27E-19	1.96E-09	2.82E-18	2.61E-12	1.30E-20	0.00E+00
AOE					0.13	0.22	1.10E-03	0.14	0.14	1.00	0.15	0.03	0.03	5.84E-12	0.15	1.00	0.22	1.00	0.06	0.00E+00
BTS						1.00	3.51E-08	1.15E-04	1.85E-04	0.07	1.00	5.86E-06	1.00	6.25E-20	1.00	0.03	1.00	0.31	1.00	0.00E+00
CDO							1.48E-07	3.29E-04	5.16E-04	0.14	1.00	1.97E-05	0.99	6.27E-19	1.00	0.06	1.00	0.49	1.00	0.00E+00
CHR								0.34	0.39	4.50E-03	5.70E-08	0.83	1.15E-09	4.50E-03	5.70E-08	0.01	1.48E-07	5.16E-04	4.68E-09	0.00E+00
ECH									1.00	0.31	1.46E-04	1.00	7.71E-06	2.53E-06	1.64E-04	0.51	2.94E-04	0.09	2.55E-05	0.00E+00
EOS										0.36	2.62E-04	1.00	1.51E-05	1.90E-06	2.62E-04	0.43	5.16E-04	0.11	4.26E-05	0.00E+00
HYP											0.09	0.09	0.02	7.31E-11	0.09	1.00	0.14	1.00	0.03	0.00E+00
HDE												8.83E-06	1.00	1.36E-19	1.00	0.04	1.00	0.36	1.00	0.00E+00
HYT													3.20E-07	7.95E-05	8.83E-06	0.18	1.97E-05	0.01	1.06E-06	0.00E+00
IMU														2.99E-22	1.00	0.01	1.00	0.09	1.00	0.00E+00
INA															1.36E-19	5.62E-10	6.27E-19	7.66E-13	2.63E-21	0.00E+00
IST																0.04	1.00	0.37	1.00	0.00E+00
MRG																	0.06	0.98	0.01	0.00E+00
NLU																		0.47	1.00	0.00E+00
PYR																			0.16	0.00E+00
XNT																				0.00E+00

Table 24: Simplified p-value results from Table 23.1. Red boxes reject the null hypothesis of similarity (p-value < 0.05), while green boxes indicate a p-value > 0.05, indicating the input datasets are not dissimilar.

	ARA	ANO	AUR	AOE	BTS	CDO	CHR	ECH	EOS	HYP	HDE	HYT	IMU	INA	IST	MRG	NLU	PYR	XNT	CT Comp
NL																				
ARA																				
ANO																				
AUR																				
AOE																				
BTS																				
CDO																				
CHR																				
ECH																				
EOS																				
HYP																				
HDE																				
HYT																				
IMU																				
INA																				
IST																				
MRG																				
NLU																				
PYR																				
XNT																				

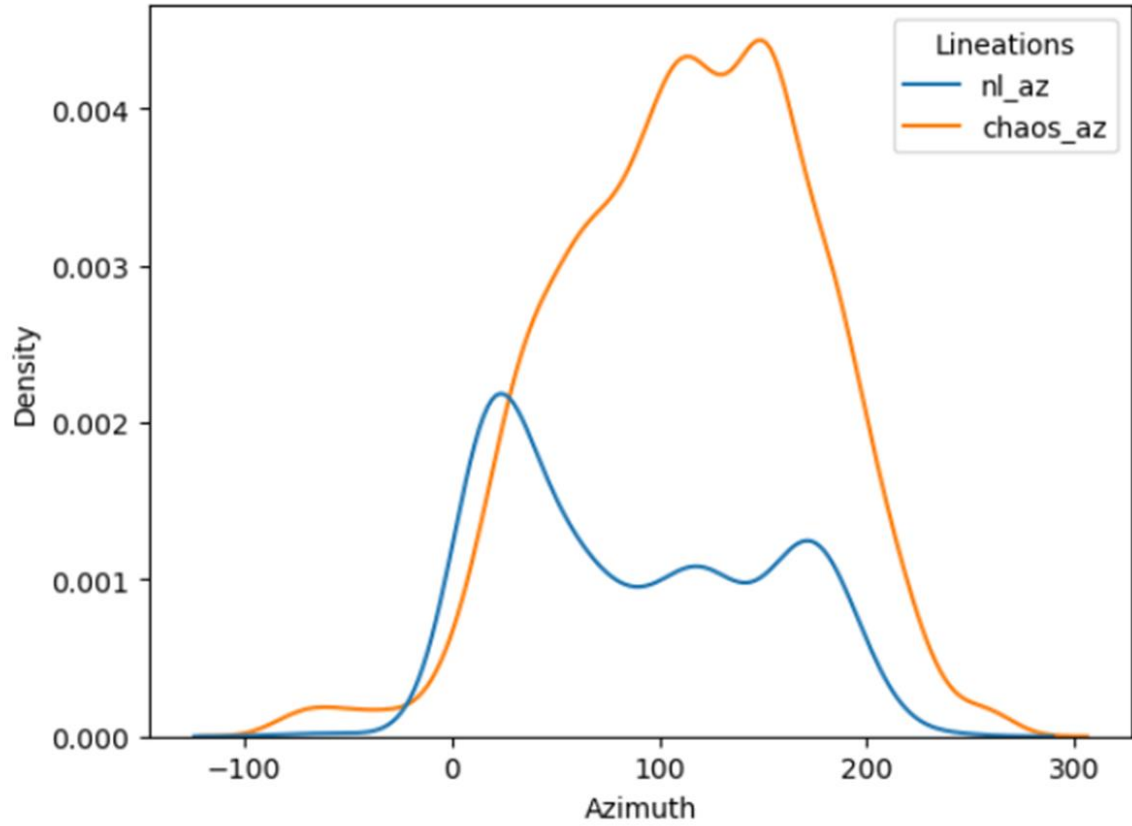


Figure 125: Result of the comparative two-sample Kolmogorov-Smirnov test between NL lineation orientations (nl_az) and chaotic terrain lineation orientations (chaos_az)

individual chaotic terrain datasets were compared against the composite dataset, no individual terrain showed similarity to the composite dataset, with p-values all < 0.05 .

Figure 126 shows groupings of similar lineament orientations based on the two sample Kolmogorov-Smirnov test. Chaotic terrains that showed similarity within the analysis towards each other were grouped into four related groups. These discrete groups seem to have a spatial relationship, in which some groups of lineament similarity are plotting in similar local areas. Group 1 consists of Aram Chaos, Iani Chaos, and Aureum Chaos. These three terrains are located within the same region, suggesting the control for lineament preference is related to locality. Group 2 consists of Eos Chaos, Aurorae Chaos, Iamuna Chaos, Arsinoes Chaos, Pyrrhae Chaos, Margaritifer Chaos, Echus Chaos, and Hydaspiis Chaos. Group 2 spatial pattern seems to be related except for Hydaspiis Chaos and Echus Chaos, which are apparent outliers. Group 3 consists of Candor Chaos, Hydrae Chaos, Baetis Chaos, Ister Chaos, and Xanthe Chaos. Group 3 follows a similar spatial pattern as seen in Group 1, in which the chaos' are located within the same local spatial position. Group 4 consists of Chryse Chaos and Hydraotes Chaos, which again are spatially located within the same area. With the exception of a few outliers (Echus Chaos and Hydaspiis Chaos), it appears that similar lineament orientation groups are related spatially.

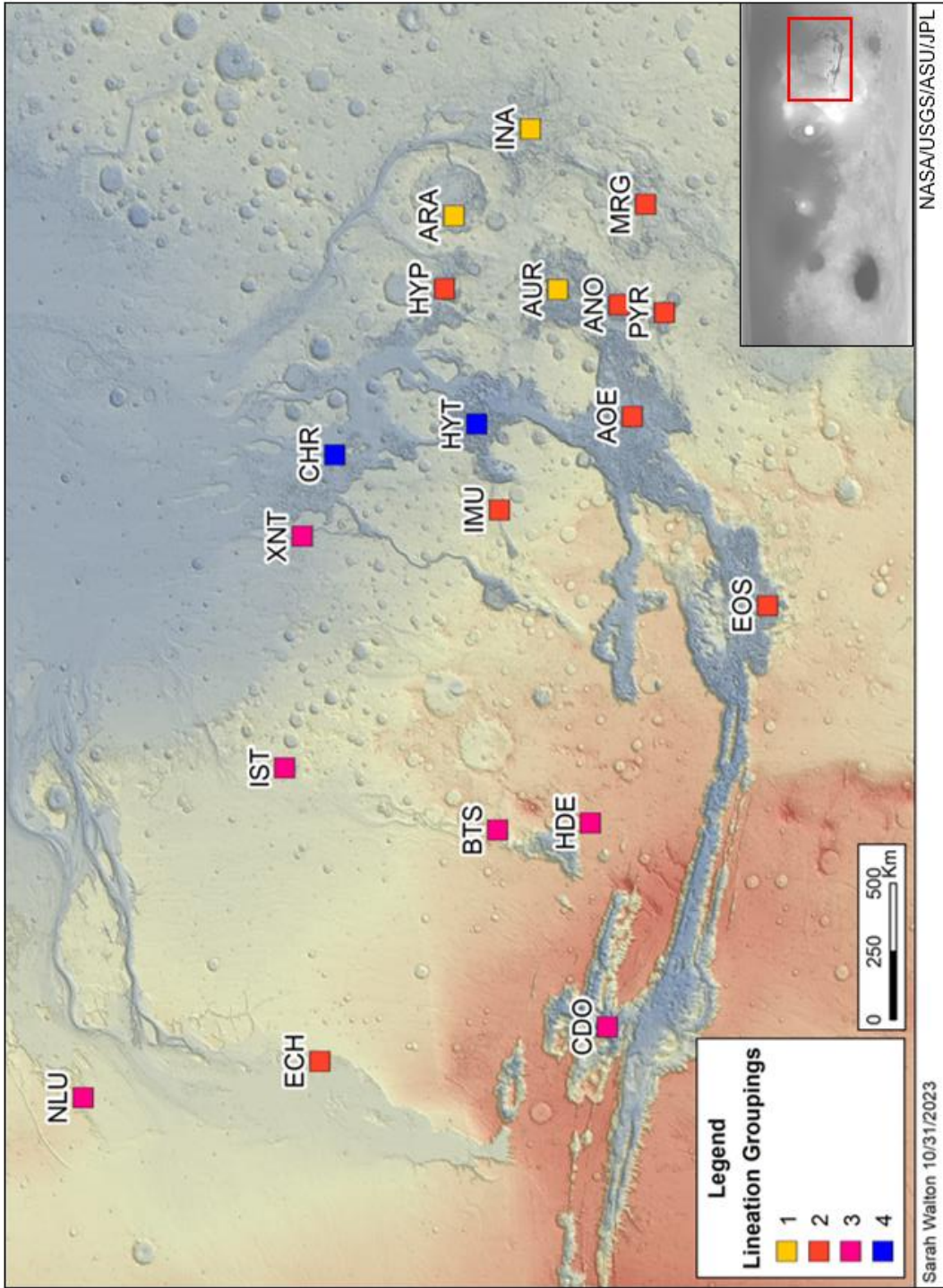


Figure 126: Groupings of chaotic terrains based on similarity of lineament orientation. Four discrete groups are defined.

Hydrated Mineral Mapping

Hydrated mineral mapping in NL shows less amounts of CRISM observations per analyzed area but shows hydrated sulfates as the dominate hydrated mineral group within the network. CRISM observations also found hydrated phyllosilicates and silica minerals to a lesser extent (Figure 127).

Hydrated mineral mapping in the chaotic terrains shows more data points per square area, where all hydrated mineral groups are represented well within the terrain (Figure 128). The dominant hydrated mineral group within the chaotic terrains are hydrated phyllosilicates, which are found scattered throughout the region. Hydrated sulfates are observed but less abundant.

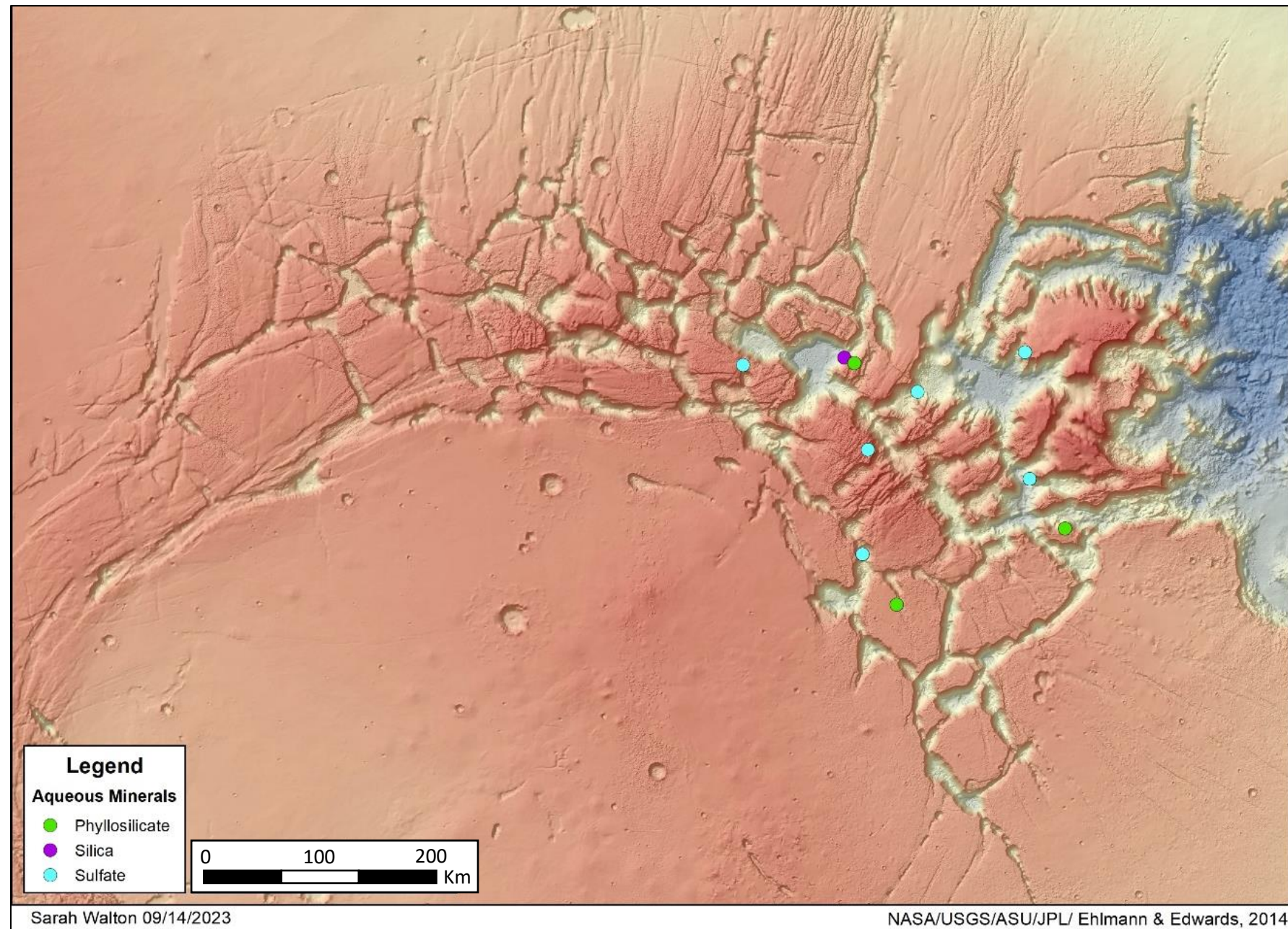


Figure 127: Hydrated mineral mapping within NL. Dominant observations are hydrated poly and mono- sulfates, although, hydrated silica (opal), and hydrated phyllosilicates are also detected.

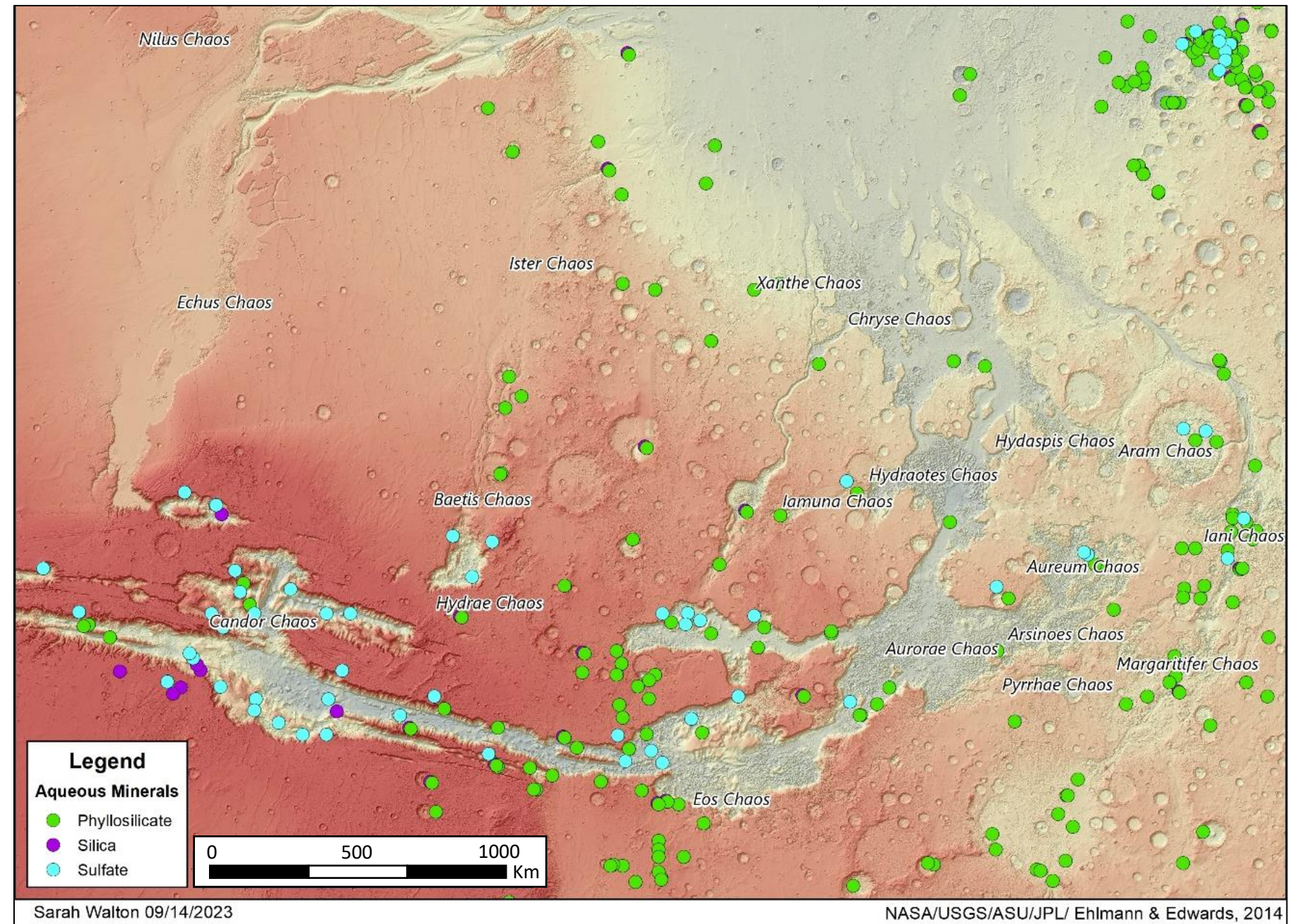


Figure 128: Aqueous mineral distribution within analyzed chaotic terrains. Hydrated phyllosilicates are the most abundant hydrated mineral within the region, with sulfates also appearing, and hydrated silica observations being confined to the Valles Marineris region.

DISCUSSION

Comparative Analyses

NL appears to follow regional fracture patterns with preferential normal faulting occurring in three phases; NNE, NNW, and radial faulting parallel to the Syria Planum volcanic province. This three-phase fracture pattern coincides with the regional tectonic story and follows spatial trends of troughs within NL. Cumulative chaotic terrain lineament analyses resulted in an inconclusive preferential fracture direction, where the rose diagram fails to highlight a population of interest. Individually, the 19 chaotic terrains show lineament preference but can be biased due to local fracture patterns unrelated to regional trends. Bias also arises based on the degree of degradation of an individual chaos. The more degraded a terrain is, with more evolved floors, smaller resolvable mesas and knobs, the lineament analysis yielded less digitized polylines per named terrain. Where chaotic terrain showed a less degree of degradation, with prominent mesas and knobs, digitization of lineaments produced a more robust analysis. Lineament statistical analysis of azimuths across NL and chaotic terrains demonstrated that lineaments within NL have no orientational similarity to that of any of the chaotic terrains analyzed. This strengthens the argument that

lineaments within NL are controlled by major regional pre-existing faulting (the three-phase fracture pattern).

When individual chaotic terrain lineament datasets were compared against each other, several groups appear to demonstrate similar spatial patterns between locations based on imagery analysis (Figure 126). This could be due to local fracturing controlling the development of mesas, knobs, and the chaos floors, but cannot be attributed to regional tectonic processes as is seen within NL. Breakout points in which the massive outflow channels are theorized to originate from, are likely found along local fault or fracture planes controlled by local tectonic regimes.

Topographically, slopes within chaotic terrains are much gentler compositely, but within each chaotic terrain, the slopes represent different stages of evolution and maturity of the morphology. Maturity can be defined as the degree of erosion undergone within the terrain. Terrains that fall within Group 1 and Group 2 of maturity are immature and are likely to have steep mesa walls and unevolved chaos floors. Terrains that fall within Group 3 or Group 4 of maturity are mature and are likely to have evolved, wide chaos floors. Mature chaotic terrains have undergone heavier periods of erosion, exposed more to the intense flowing breakout fluids that formed the outflow channels, and flattening the area. Immature chaotic terrains have undergone less intense erosion, where

morphology of the breakout points (steep mesa walls and narrow floors) have been preserved.

Spatially, slope groups defined increase in maturity and evolution with increasing latitudes and proximity to the outflow channel mouth (Figure 102). Groups 1 and 2 of unevolved chaotic terrains are found closer to Valles Marineris regions, whereas Groups 3 and 4 are located near to the mouths of the outflow channels. This could be due to differing amounts of fluid flowing through the chaotic terrains periodically. If several breakout points of massive fluid flow combined at the mouth of the channel to outflow into the northern lowlands, a chaotic terrain found at the mouth of the channel would be more evolved and show significantly lower slopes than those located closer to breakout points. This is what is seen in Groups 3 and 4, with decreasing maturity towards the breakout points south of the outflow channel mouth (Figure 102).

Results from the imagery showed a difference in the nature of digitized lineaments. Lineaments digitized within NL were typically grabens or normal faults, while lineaments within the chaotic terrain were typically mesas or knobs that aligned along a plane. Within some chaotic terrain such as Echus Chaos and Nilus Chaos on the western side of the study region, the floor between the mesas seemed to be controlled by pre-existing faults.

Differences in morphologies were primarily driven by scale constraints, where major morphologies identified within NL (troughs and mesas) are more evolved extensional features than within the chaos. Chaotic terrain mesas and floor features appear highly degraded at most localities, and where the floor was evolved, the mesas transitioned into knobs. Where the floor was juvenile, mesas were prominent and wide. Crater morphologies were expected at both sites, due to high crater density populations occurring in the Noachian-aged southern highland terrains. Low global-erosion rates will preserve craters at most scales, but dust in-fill is common and expected. Both sites also showed pit craters and pit chains along a plane, formed by subsidence.

Hydrated mineral mapping showed dominant phyllosilicate deposits within chaotic terrains but differing dominant sulfate deposits within NL. This may be due to the local volcanics within NL being active during a time of high sulfur deposition and then later re-worked by hydrothermal fluids into hydrated sulfates. Hydrated phyllosilicates on Mars are also usually associated with the flow of fluid altering the underlying surface. Outflow originating chaotic terrain breakout points would have created an environment more susceptible to the development of hydrated phyllosilicates than that of hydrated sulfates. LTD's are found at both localities but serve differing purposes in the stratigraphy. Within the chaos, LTD's serve as cap rocks for many of the mesas and knobs, while LTD's within NL are found layered within mesa walls and on the trough floors in a non-layered

deposit, but do not serve as cap rocks for the mesas. This could be due to the spatial position of both sites, with changes in lithologies from one site to another from local volcanic and depositional influences.

No obvious correlation can be made between slope, lineament, and hydrated mineral observations within the individual chaotic terrain datasets nor when compared to the NL dataset, suggesting that these two regions may be only related by similar morphologies seen in the imagery.

From the comparative analyses, it is evident that the main driver of differences in these two areas is the scale of features and degree of erosion. Chaotic terrains show eroded terrain at all localities caused by the outflow of massive amounts of fluid, while features within NL are more dominated by subsidence and faulting. More in depth comparison may come from analysis of NL trough features that may resemble the mesa and floor morphologies of the chaotic terrain. The formation of chaotic terrains was likely not controlled by regional faulting but may have been controlled by fractures in Noachian basement rocks caused by continuous bombardment. The formation of NL was controlled by pre-existing NNE and radial faulting resulting in extension and collapse of mesas. What remains unclear is the role of subsurface fluid in the formation of NL. From imagery, interpreted dolines seemed to have formed within certain trough localities (Figure 14), but it does not appear to be a widespread

regional phenomenon, while thermokarstic morphology is widespread and appears across most troughs. Kling and others (2021) note that troughs within NL have a mean width that is significantly larger than interpreted grabens and pit craters, leading to a conclusion in which hydrologic processes may have aided in the widening of the troughs. A simplified theory for the evolution of NL is proposed below:

1. Initial NNE and radial extension produced widespread grabens and normal faulting.
2. Formation of pit craters and pit chains from induced collapse over a subsurface void along a plane.
3. Cryosphere thaw and re-freeze promoted further subsidence within troughs and development of thermokarstic features.
4. Periodic subsurface fluid flow within NL induced preferential faulting within the subsurface as cyclic cryosphere changes occur with global climate changes and local volcanic activity.
5. Hydration of local mineral deposits through fluid flows within the subsurface.
6. Continued subsidence and widening of existing troughs.

A theory for the evolution of chaotic terrains analyzed is proposed below.

1. Basement Noachian terrain heavily fractured.

2. Initial fracturing and subsidence along un-oriented basement fractures due to massive breakout flow of subsurface fluid along pre-existing basement fractures
3. Differential erosion of now identified mesas and troughs by massive outflow of fluid.
4. Deposition/and or alteration of hydrated minerals
5. Cryosphere thaw and re-freeze cycles promote development of thermokarstic features.
6. Major subsidence ceases as periodic outflow episodes end.

CONCLUSIONS

Both NL and the chaotic terrains provide substantial insight into the nature of regional tectonics on Mars and how subsurface fluid and tectonic activity influenced the development of unique morphology across the planet. Although the spatial pattern of both NL and chaotic terrains are represented by similarly polygonal bounded mesas and a high-level morphology analysis shows that they share very similar morphologic patterns and features, there is no clear relationship between the origin of both feature types.

NL is dominated by a complicated intermixing of tectonic, hydrothermal, glacial, and volcanic processes. The network is controlled by regional faulting and extended due to collapse and subsidence caused by the removal of subsurface material. Results from the lineament comparison, confirmed with the initial assumption from imagery analysis, indicate that the chaotic terrains and NL are not orientated along similar lineament planes. Chaotic terrains do follow similar lineament patterns based on spatial position, where chaotic terrains located in proximity to one another are likely to have similar lineament orientations. Although locally related, chaotic terrains individually show no similarity to the lineament orientations found within NL. Thus, the chaotic terrains analyzed do not appear to be controlled along regional fractures but by local

breakout points of the outflow channels, possibly controlled by un-oriented highly fractured basement rock and related by similar spatial position.

Chaotic terrains can also be grouped maturity by slope and imagery. Terrains with dominate slopes greater than 15 degrees can typically be classified as immature or unevolved, where large amounts of erosion have not yet taken place within the boundaries of the chaotic terrains. These terrains are likely dominated by mesas and knobs, with little floor area. Chaotic terrains with a majority of slopes less than 15 degrees can be classified as mature or evolved, where large-scale erosion episodes widened and flattened the chaos floors. From slope analysis, the percent slope area classification can be related to proximity to outflow channel scarps and mouths, where unevolved or immature terrains are found farther from the channel scarps. This indicates the main diagenetic influence of the morphology seen within chaotic terrains as the amount and force of fluid passed through each terrain during episodic outflow events, and likely structurally controlled by local basement fracturing.

The formation of NL was heavily driven by regional tectonic extension, but periglacial and collapse morphologies seen within the network, points to a multi-phase evolution, in which extension induced collapse and the workings of a near-surface cryosphere interacting with period of volcanics allowed for the unique surface features seen throughout. Chaotic terrains are not a result of regional

tectonic extension and more indicative of large-scale fluvial events where fluid originating from local breakout points controlled by basement fracture patterns within the subsurface. Although different origins, these two regions show similar top-down polygonal fracturing at the surface and host several morphological similarities, suggesting a similar evolutionary history involving cryosphere fluid interactions. Limitations in data resolution and availability across these large areas constrain observable morphologic characteristics seen in the imagery and detected within elevation data.

FUTURE WORK

Contributions and Constraints

This research provides a global view of geologic processes that influenced the landscape of Mars and provides workable theories to the nature of these processes. Discussing large-scale geologic processes will further our understanding of differing terrestrial body evolution throughout geologic time and more importantly, the importance of fluid as a continuous diagenetic influence. Tectonic influences on terrestrial bodies that lack a continuous global plate tectonic cycle allows for the evolution of large-scale unique structures that may be present on similar bodies. The study of preserved geomorphologies on Mars allows for the characterization of early planetary geology and processes that may serve as early-Earth analogs. Similar studies influence how geologic observations are performed on planetary bodies, how instrumentation suites are developed for planetary exploration, and aid in selecting sites for further in-situ observations.

General constraints lie in the availability of data collected by instrumentation aboard orbiters. Unlike sites on the surface that have been investigated by in-situ methods, both NL and the chaotic terrains have difficult terrain that makes it near impossible to traverse in-situ. This limits the information

obtained to orbiters and is restricted to specific resolution parameters of the CTX camera and the MOLA DEM datasets. It is worth noting, CRISM ceased operations as of April 2023, so new investigations of Martian surface mineralogy will be separated from the MRO mission completely. With higher resolvable data, more information about the geology of Mars will be achieved, but without that data, interpretations and mapping of the Martian surface is constrained to the limitations of current data. Availability of data will only come with time, as future missions to Mars will support the collection of higher resolution of data. Locally, constraints within the difficult terrain of both sites are the large number of slumps and landslide debris associated with subsidence. These structures at their core are directly related to collapse, so heavy debris is expected. This debris is likely overprinting underlying key morphology and geology of importance to further the theories of evolution of both unique features.

The scale of features of the study area also provides a significant constraint in the resolvability of small-scale features. NL alone is over ~1,000km wide which is about the distance from San Francisco, CA to Salt Lake City, UT here on Earth. Without in-depth observations within the study area and the nature of this study being very high-level, key observations within small morphologies may be overlooked.

High-resolution CTX DEM Generation

The global digital elevation model that was used for this research is available at 200m resolution, but further DTM generation using stereo pair images from the CTX camera can produce an astonishingly low ~6 m per pixel resolution. Low resolution DTM generation with the AMES Stereo Pipeline and ISIS processing for NL is possible but was not performed due to time constraints. Future efforts to understand the geomorphic relationship between NL and chaotic terrains may consider generating DTM's for the entire study area, which would employ a large task effort to do so. Mapping and analysis of the area using CTX derived DTM's would allow for a characterization of the terrain at a smaller scale, resolving regional features and trends not well recognized at larger resolutions. Furthermore, detailed analysis of HiRISE imagery which resolves sub-meter features could be of merit to further characterize this region. Lack of data currently leads to a scattering of image products available, barring the entire region to be characterized in this manner.

In-Depth Analysis

A low-level, in-depth analysis of each study area within this research is warranted due to the complicated nature of the morphologies. Using HiRISE ~30cm resolution data would provide an astonishingly close look at sub-meter

geomorphic features of interest, but again, was not preferred for this high-level look due to lack of a continuous dataset.

REFERENCES

- Anderson, R.C., Dohm, J.M., Golombek, M.P., Haldemann, A.F.C., Franklin, B.J., Tanaka, K.L., Lias, J., & Peer, B., (2001), Primary centers and secondary concentrations of tectonic activity through time in the western hemisphere of Mars: *Journal of Geophysical Research: Planets*, v. 106, p. 20563–20585, doi:10.1029/2000JE001278.
- Andrews-Hanna, J. C., & Bottke, W. B., (2017), Mars During the Pre-Noachian. NASA/ADS.
<https://ui.adsabs.harvard.edu/abs/2017LPICo2014.3078A/abstract>
- Baioni, D., Murana, A., & Hajna, N.Z., (2014), Karstic morphology in northern Sinus Meridiani, Mars: *Geosciences Journal*, v. 18, p. 261–268, doi:10.1007/s12303-014-0003-0.
- Banerdt, W.B., Phillips, R.J., Sleep, N.H., & Saunders, R.S., (1982), Thick shell tectonics on one-plate planets: Applications to Mars: *Journal of Geophysical Research*, v. 87, p. 9723, doi:10.1029/JB087iB12p09723.
- Bouley, S., Baratoux, D., Paulien, N., Missenard, Y., & Saint-Bézar, B., (2018), The revised tectonic history of Tharsis: *Earth and Planetary Science Letters*, v. 488, p. 126–133, doi:10.1016/j.epsl.2018.02.019.
- Carr, M.H., (1979), Formation of Martian flood features by release of water from confined aquifers: *Journal of Geophysical Research*, v. 84, p. 2995, doi:10.1029/JB084iB06p02995
- Carr, M.H., (1995), The Martian drainage system and the origin of valley networks and fretted channels: *Journal of Geophysical Research*, v. 100, p. 7479, doi:10.1029/95je00260.
- Carr, M.H., & Head, J.W., (2010), Geologic history of Mars: *Earth and Planetary Science Letters*, v. 294, p. 185–203, doi:10.1016/j.epsl.2009.06.042.
- Chapman, M.G., and Tanaka, K.L., 2002, Related Magma–Ice interactions: possible origins of chasmata, chaos, and surface materials in Xanthe, Margaritifer, and Meridiani Terrae, Mars: *Icarus*, v. 155, p. 324–339, doi:10.1006/icar.2001.6735

- Christensen, P.R.; Engle, E.; Anwar, S.; Dickenshied, S.; Noss, D.; Gorelick, N.; Weiss-Malik, M.; JMARS – A Planetary GIS, <http://adsabs.harvard.edu/abs/2009AGUFMIN22A..06C>
- Clifford, S.M., (1993), A model for the hydrologic and climatic behavior of water on Mars: *Journal of Geophysical Research*, v. 98, p. 10973, doi:10.1029/93JE00225.
- Clifford, S.M., Lasue, J., Heggy, E., Boisson, J., McGovern, P., & Max, M.D., (2010), Depth of the Martian cryosphere: Revised estimates and implications for the existence and detection of subpermafrost groundwater: *Journal of Geophysical Research*, v. 115, p. E07001, doi:10.1029/2009JE003462.
- Dickson, J.L., Ehlmann, B.L., Kerber, L.H., & Fassett, C.I. (2023). Release of the global ctx mosaic of mars: an experiment in information-preserving image data processing.
- Edwards, C. S., K. J. Nowicki, P. R. Christensen, J. Hill, N. Gorelick, and K. Murray (2011), Mosaicking of global planetary image datasets: 1. Techniques and data processing for Thermal Emission Imaging System (THEMIS) multi-spectral data, *J. Geophys. Res.*, 116, E10008, doi:10.1029/2010JE003755. <http://dx.doi.org/10.1029/2010JE003755>
- Ehlmann, B.L., Berger, G., Mangold, N., Michalski, J.R., Catling, D.C., Ruff, S.W., Chassefière, E., Niles, P.B., Chevrier, V., & Poulet, F., (2013), Geochemical Consequences of Widespread Clay Mineral Formation in Mars' Ancient Crust: *Space Science Reviews*, v. 174, p. 329–364, doi:10.1007/s11214-012-9930-0.
- Ehlmann, B.L., & Edwards, C.S., (2014). Mineralogy of the Martian surface: *Annual Review of Earth and Planetary Sciences*, v. 42, p. 291–315, doi:10.1146/annurev-earth-060313-055024.
- Ferguson, R. L, Hare, T. M., & Laura, J. (2018). HRSC and MOLA Blended Digital Elevation Model at 200m v2. Astrogeology PDS Annex, U.S. Geological Survey. http://bit.ly/HRSC_MOLA_Blend_v0
- Glotch, T.D. & Rogers, A.D., (2007). Evidence for aqueous deposition of hematite- and sulfate-rich light-toned layered deposits in Aureum and Iani Chaos, Mars: *Journal of Geophysical Research*, v. 112, doi:10.1029/2006je002863.

- Holo, S.J., Kite, E.S., & Robbins, S.J., (2018), Mars obliquity history constrained by elliptic crater orientations: *Earth and Planetary Science Letters*, v. 496, p. 206–214, doi:10.1016/j.epsl.2018.05.046.
- International Astronomical Union Working Group for Planetary System Nomenclature. "Gazetteer of Planetary Nomenclature." (Accessed March 01, 2023). <http://planetarynames.wr.usgs.gov/>.
- Johnston, J. G., Boston, P. J., & Stafford, K. W., (2006), Assessment of Karst Landform Potential on Mars. NASA/ADS.
- Kling, C.L., Byrne, P.K., Atkins, R.M., & Wegmann, K.W., (2021), Tectonic deformation and volatile loss in the formation of noctis Labyrinthus, Mars: *Journal of Geophysical Research: Planets*, v. 126, doi:10.1029/2020je006555.
- Kling, C. L., Byrne, P. K., Wyrick, D. Y., Wegmann, K. W., & Drive, F., (2018), Spatial and Temporal Relationships of Pit Craters and Graben within Noctis Labyrinthus, Mars. NASA/ADS.
- Kreslavsky, M.A., Head, J.W., & Marchant, D.R., (2008), Periods of active permafrost layer formation during the geological history of Mars: Implications for circum-polar and mid-latitude surface processes: *Planetary and Space Science*, v. 56, p. 289–302, doi:10.1016/j.pss.2006.02.010.
- Malin, M. C., et al. (2007), Context Camera Investigation on board the Mars Reconnaissance Orbiter, *J. Geophys. Res.*, 112, E05S04, doi:10.1029/2006JE002808.
- Mège, D., Cook, A. C., Garel, E., Lagabriele, Y., & Cormier, M.-H. (2003), Volcanic rifting at Martian grabens, *J. Geophys. Res.*, 108, 5044, doi:10.1029/2002JE001852, E5.
- Murchie, S. et al., (2007), Compact Reconnaissance Imaging Spectrometer for Mars (CRISM) on Mars Reconnaissance Orbiter (MRO): *Journal of Geophysical Research*, v. 112, p. E05S03, doi:10.1029/2006JE002682.
- NASA Jet Propulsion Laboratory Mars Reconnaissance Orbiter - NASA:, <https://mars.nasa.gov/mro/> (accessed September 2023).
- NASA/John Hopkins University Applied Physics Laboratory CRISM Web Site:, <http://crism.jhuapl.edu/index.php> (accessed September 2023).

- Nimmo, F., & Tanaka, K., (2005), Early Crustal Evolution of Mars: Annual Review of Earth and Planetary Sciences, v. 33, p. 133–161, doi:10.1146/annurev.earth.33.092203.122637.
- Reese, C.C., (2004), Magmatic evolution of impact-induced Martian mantle plumes and the origin of Tharsis: Journal of Geophysical Research, v. 109, p. E08009, doi:10.1029/2003JE002222.
- Rodriguez, J.A.P. et al., (2005), Control of impact crater fracture systems on subsurface hydrology, ground subsidence, and collapse, Mars: Journal of Geophysical Research, v. 110, doi:10.1029/2004je002365.
- Rodriguez, J.A.P. et al., (2016), Groundwater flow induced collapse and flooding in Noctis Labyrinthus, Mars: Planetary and Space Science, v. 124, p. 1–14, doi:10.1016/j.pss.2015.12.009.
- Schubert, G., Solomon, S., Turcotte, D.L., Drake, M.J., & Sleep, N., (1990), Origin and thermal evolution of Mars: v. 1.
- Sharp, R.P., (1973), Mars: Fretted and chaotic terrains: Journal of Geophysical Research, v. 78, p. 4073–4083, doi:10.1029/jb078i020p04073.
- Sharp, R.P., & Malin, M.C., (1975), Channels on Mars: GSA Bulletin, v. 86, p. 593–609, doi:10.1130/0016-7606(1975)86<593:COM>2.0.CO;2.
- Stafford, K.W., & Boston, P.J., (2005), Theoretical Evaporite Karst Development on Mars, in 36th Lunar and Planetary Science Conference Proceedings.
- Tanaka, K.L. & Davis, P.A., (1987), History and Morphology of Faulting in the Noctis Labyrinthus-Claritas Fossae Region of Mars:
- Tanaka, K.L., & Davis, P.A., (1988), Tectonic history of the Syria Planum province of Mars: Journal of Geophysical Research, v. 93, p. 14893–14917, doi:10.1029/jb093ib12p14893.
- Tanaka, K.L., Skinner, J.A., Jr., Dohm, J.M., Irwin, R.P., III, Kolb, E.J., Fortezzo, C.M., Platz, T., Michael, G.G., & Hare, T.M., (2014), Geologic map of Mars: U.S. Geological Survey Scientific Investigations Map 3292, scale 1:20,000,000, pamphlet 43 p., <https://dx.doi.org/10.3133/sim3292>
- Thollot, P., Mangold, N., Ansan, V., Le Mouélic, S., Milliken, R.E., Bishop, J.L., Weitz, C.M., Roach, L.H., Mustard, J.F., & Murchie, S.L., (2012), Most Mars minerals in a nutshell: Various alteration phases formed in a single environment in Noctis Labyrinthus: Journal of Geophysical Research: Planets, v. 117

- Ward, W.R., (1973), Large-Scale variations in the obliquity of Mars: *Science*, v. 181, p. 260–262, doi:10.1126/science.181.4096.260.
- Watters, T. R., & Schultz, R. A., (2010), *Planetary Tectonics* (Cambridge Planetary Science, Series Number 11) (1st ed.). Cambridge University Press.
- Wise, D.U., Golombek, M.P., & McGill, G.E., (1979), Tectonic evolution of Mars: *Journal of Geophysical Research*, v. 84, p. 7934, doi:10.1029/JB084iB14p07934.
- Yin, A., (2012), An episodic slab-rollback model for the origin of the Tharsis rise on Mars: Implications for initiation of local plate subduction and final unification of a kinematically linked global plate-tectonic network on Earth: *Lithosphere*, v. 4, p. 553–593, doi:10.1130/L195.1.

VITA

Sarah A. Walton graduated from William B Travis High School in Richmond, Texas in 2017. She attended Stephen F. Austin State University, earning her Bachelor of Science in Geology in August of 2021. Sarah continued her education at Stephen F. Austin State University expected to earn her Master of Science in Geology in December of 2023. She has completed an internship with NASA Jet Propulsion Laboratory working with Martian rover GIS data products in 2022. Sarah is currently employed performing contract work in planetary mapping and GIS mission operations at NASA Johnson Space Center.

Permanent Address: 15240 Highway 3 Apt 704

Webster TX 77598

Style Manual: Geological Society of America (GSA)

This thesis was typed by Sarah A. Walton.